

Settore Concorsuale: 02/C1 - Astronomia, Astrofisica, Fisica della Terra e dei Pianeti
Settore Scientifico Disciplinare: FIS/05 - Astronomia e Astrofisica

The structure and evolution of
Gamma-Ray Bursts:
mapping explosive transients at
high angular resolution

Dottorato di Ricerca in Astrofisica

Candidato:

Stefano Giarratana

Supervisore:

Dr. Marcello Giroletti

Coordinatore Dottorato:

Prof. Dr. Andrea Miglio

Ciclo XXXVI

Esame finale Anno 2024

To my Family

Abstract

Gamma-Ray Bursts (GRBs) are brief flashes of γ -rays (keV – MeV) that last from a fraction of second up to a few hundreds of seconds, during which a significant amount of isotropic equivalent energy is released (ranging from 10^{48} to 10^{54} erg). Occurring at cosmological distances (the farthest GRB was identified at $z = 9.2$), these explosive transients are historically divided into long- and short-duration GRBs based on the total duration of the initial γ -ray emission. Long GRBs, which last more than 2 s, are associated with the catastrophic explosion of an isolated massive star, as confirmed by their connection with Supernova events. In contrast, short GRBs, which last less than 2 s, are believed to result from the merger of two neutron stars or a neutron star and a black hole, as indicated by the landmark discovery of joint gravitational waves and electromagnetic signatures in GW170817 / GRB 170817A.

Regardless of the distinct production channels, both scenarios lead to the formation of a highly magnetised neutron star or a spinning, stellar-mass black hole. This central engine is thought to accrete material and launch two oppositely directed relativistic jets, piercing through the “vestige” of the progenitor, either the stellar envelope for long GRBs or the pre-merger ejecta for short GRBs. These jets then expand into the material surrounding the burst, producing the brief γ -ray emission through magnetic reconnections or internal shocks. As the GRB outflow expands, it interacts with the circum-burst environment through external shocks, accelerating electrons to relativistic energies. These electrons cool down via synchrotron emission, producing the long-lived afterglow emission that extends from γ -rays down to the radio band.

To investigate the launch and subsequent evolution of the GRB jet, the circum-burst medium, and the nature of the progenitor, a standard model based on an ultra-relativistic expanding outflow is commonly employed. This model relies on global (the isotropic equivalent energy, the circum-burst density, . . .), microphysical (the electron distribution index, the fractions of internal energy retained by the magnetic field and the electrons) and geometrical (viewing angle, aperture angle) parameters. However, even sophisticated models face degeneracy in the multi-dimensional parameter space. To alleviate or possibly break the degeneracy, broad-band observations across the electromagnetic spectrum are crucial. For nearby events, deviations from the simplified model can be detected, requiring further independent information to precisely constrain the involved physics. In particular, the Very Long Baseline Interferometry technique (VLBI) at radio wavelengths has proven to be a unique asset, providing direct evidence of apparent superluminal expansion (for on-axis GRBs), centroid displacement of the outflow (for slightly off-axis GRBs) and the first confirmation that merger events can launch successful jets. VLBI offers unique and complementary insights into the dynamics, geometry and structure of GRB jets that cannot be obtained through other methods or bands.

Throughout the Ph.D. program, I employed radio and VLBI observations to characterise and constrain the outflow, the circum-burst medium, and the properties of the progenitors of GRBs. This included studies on individual events, which are important to test the predictions of current models, GRB host galaxies, which are fundamental to constrain the nature of the progenitor through the characterisation of the surrounding environment, and the statistical properties of GRB afterglows, in order to verify the existence of potential GRB sub-populations.

Concerning radio and VLBI studies of single bursts, I analysed two remarkable GRBs.

In the case of GRB 201015A, a comprehensive analysis of the multi-wavelength afterglow emission was conducted, comparing it with predictions from the standard GRB model. The combination of radio, optical, and X-ray data allowed us to constrain key physical parameters of the outflow and characterise the profile of the circum-burst medium. Despite achieving sub-milliarcsecond angular resolution with our VLBI observation, the relatively faint brightness of the afterglow prevented us from measuring the size of the outflow. Additionally, we could not verify whether the very high energy (≥ 100 GeV) emission originated from synchrotron self-Compton, synchrotron or external inverse Compton processes, as very high energy data were not publicly available at the time of our analysis.

On 2023 October 9, the brightest GRB ever recorded, GRB 221009A, triggered all satellites equipped for transient detection. Proposed models failed at convincingly reproducing the observed multi-wavelength afterglow emission. To shed light on the dynamics and the geometry of the outflow, we conducted VLBI observations with the European VLBI Network and the Very Long Baseline Array, ranging from 40 to 262 days post-burst. Our campaign provided robust evidence of apparent superluminal expansion of the GRB ejecta. Specifically, the observed size evolution could be reconciled with a combination of reverse shock and forward shock in the case of a circum-burst medium with a wind-like profile, provided that the two shocks dominate the emission at different frequencies and at different times.

Complementary to the study of individual bursts, exploring the properties of galaxies hosting GRBs is fundamental to unveil the nature of GRB progenitors. We conducted dedicated observations with the European VLBI Network and the *e*-MERLIN of J1304+2938, initially identified as the candidate host galaxy of the long GRB 200716C. Combining multi-scale observations, comprising our VLBI campaign and radio surveys with lower angular resolution, enabled us to ascribe the observed emission to highly star-forming regions within the galaxy. The derived high star formation rate (approximately $\sim 300 M_{\odot} \text{ yr}^{-1}$) supported the hypothesis of GRB 200716 being a long-duration GRB located in J1304+2938. An alternative scenario, based on the analysis of the prompt emission, proposed that GRB 200716C is a short-duration burst lensed by an intermediate-mass black hole located within J1304+2938, which would be a foreground galaxy. Although our observations did not reveal a compact emitting region, we could not exclude the presence of an isolated intermediate-mass black hole, as radio emission from these sources is predicted to be fainter than the upper limits currently achievable.

Finally, statistical afterglow studies are essential to identify potentially different channels for GRB production. Recently, it was proposed and favoured in the literature that two populations of GRBs may exist based on the radio emission of their afterglow. While GRBs with a detected afterglow in radio were termed radio-bright, or radio-loud GRBs, those bursts without a detected radio afterglow were classified as radio-dark, or radio-quiet. In this scenario, the dichotomy was directly linked to different progenitors. Specifically, radio-bright GRBs would result from the collapse of massive stars in interacting binary systems, while radio-dark GRBs would originate from the collapse of isolated massive stars. We selected and analysed a sample of radio-bright and radio-dark *Swift* GRBs. The selection of a sample with uniform biases strongly supported the hypothesis that the apparent dichotomy is a spurious effect primarily driven by instrumental factors, particularly the limited sensitivity of both γ -ray and radio facilities.

The Thesis is structured as follows. In the introductory part, Chapter 1 provides an overview of the scientific context of GRBs, while Chapter 2 delves into the standard, simplified model firstly proposed to explain the observed emission from these explosive transients. The basics of radio interferometry and VLBI are introduced in Chapter 3. Following the general framework, the analysis of GRB 201015A and GRB 221009A is detailed in Chapter 4 and 5, respectively. Chapter 6 is dedicated to the investigation of the candidate host galaxy of GRB 200716C. The ongoing statistical study on the population of radio afterglows is outlined in Chapter 7. Lastly, the main results are summarised and discussed in Chapter 8.

Contents

Abstract	iii
1 Gamma-Ray Bursts	1
1.1 The discovery of Gamma-Ray Bursts	1
1.2 Prompt emission	2
1.3 The Afterglow phase	6
1.4 Short Gamma-Ray Bursts	9
1.4.1 Host Galaxies	10
1.4.2 Kilonovae	11
1.4.3 Gravitational Waves	13
1.5 Long Gamma-Ray Bursts	15
1.5.1 Host Galaxies	15
1.5.2 Supernovae	16
1.5.3 Very High Energy emission	17
2 The standard model for GRBs	21
2.1 Compactness problem	21
2.2 Synchrotron emission	22
2.3 Three reference frames	24
2.4 Prompt emission	26
2.4.1 Dynamics	26
2.4.2 Spectrum	29
2.5 Afterglow model	30
2.5.1 Dynamics of the forward shock	30
2.5.2 Break Frequencies	32
2.5.3 Spectrum of the forward shock	34
2.5.4 Reverse shock	35
2.6 Non-spherical ejecta	38
3 Radio Interferometry	41
3.1 Basic Principles	41
3.2 Calibration	51
3.3 Compact Arrays	53
3.3.1 The Karl G. Jansky Very Large Array	53
3.3.2 MeerKAT	54
3.4 Very Long Baseline Interferometry	55
3.4.1 The enhanced Multi-Element Remotely Linked Interferometer Network	56
3.4.2 The European VLBI Network	57
3.4.3 The Very Long Baseline Array	57
3.4.4 The Long Baseline Array	57

4	GRB 201015A	61
4.1	Introduction	61
4.2	Observations	62
4.2.1	VLA Observations at 6 GHz	62
4.2.2	<i>e</i> -MERLIN observations at 1.5 GHz	62
4.2.3	<i>e</i> -MERLIN observations at 5 GHz	62
4.2.4	EVN observations at 5 GHz	63
4.2.5	Optical observations and public data	63
4.2.6	X-ray observations and public data	64
4.3	Results	64
4.3.1	Radio	64
4.3.2	Optical	65
4.3.3	X-rays	66
4.4	Broadband modelling	67
4.4.1	ISM profile	68
4.4.2	Wind-like profile	70
4.4.3	Intrinsic host galaxy extinction	70
4.5	Discussion	70
4.5.1	Additional emission components	72
4.5.2	High-resolution observations	73
4.5.3	Host galaxy	73
4.6	Conclusions	74
5	GRB 221009A	75
5.1	Introduction	75
5.2	VLBI observations and data reduction	76
5.2.1	European VLBI Network	76
5.2.2	Very Long Baseline Array	76
5.3	Methods	77
5.3.1	Source flux density, size and average apparent expansion velocity estimate	77
5.3.2	Source size evolution model fitting	78
5.3.3	FS and RS size evolution and proper motion model	78
5.4	Results	79
5.4.1	Source size expansion	79
5.4.2	Apparent proper motion	80
5.5	Discussion	80
5.6	Conclusions	86
5.7	Appendices	86
5.7.1	EVN observation strategy and data reduction	86
5.7.2	Circular Gaussian fits to source visibilities	87
5.7.3	Tests on the evolution of the flux density and the size	89
5.7.4	Projected size and proper motion model of the FS and RS	90
6	The candidate host galaxy of GRB 200716C	97
6.1	Introduction	97
6.2	Observations	98
6.2.1	Multi-wavelength archival data	98
6.2.2	European VLBI Network and <i>e</i> -MERLIN follow up	98
6.2.3	Spectroscopy from the Telescopio Nazionale Galileo	99
6.3	Results	101

6.4	Discussion	102
6.4.1	The radio-loud AGN	102
6.4.2	The extreme star formation	103
6.4.3	J1304+2938 and GRB 200716C	105
6.5	Conclusions	106
6.6	Appendices	106
6.6.1	Photometric data	106
6.6.2	Luminosities of the GRB host galaxies	109
7	Radio afterglows of <i>Swift</i> Gamma-Ray Bursts	111
7.1	Introduction	111
7.2	The <i>Swift</i> GRB sample	113
7.3	Results	117
7.4	Discussion and conclusions	118
8	Conclusions and prospects	125
	Bibliography	129

Chapter 1

Gamma-Ray Bursts

1.1 The discovery of Gamma-Ray Bursts

During the Cold War, a group of military satellites known as *Vela* was deployed by the United States with the primary objective of monitoring compliance with the 1963 Partial Test Ban Treaty, which specifically prohibited participating nations from conducting nuclear tests in the upper atmosphere or outer space. Between July 1967 and 1972, the satellites identified and recorded 16 flashes of γ -rays that exhibited unique characteristics not observed in any known nuclear weapon signatures [1]. Soon it became clear that the flashes originated from astrophysical phenomena: they were referred to as Gamma-Ray Bursts (GRBs henceforth). Nevertheless, the poor angular resolution of γ -ray facilities and the rapid evolution of these transient events made it impossible to constrain the actual distance of GRBs. As a consequence, a precise localisation of the emission remained beyond reach for two decades, hindering any conclusive insights into the nature of their progenitors. Many models were proposed, either locating GRB within the Milky Way [2] or postulating a cosmological origin [3, 4].

A fundamental contribution to the debate on the origin of these phenomena was provided by the Burst And Transient Source Experiment (BATSE) on board the Compton Gamma-Ray Observatory that was launched in 1991. BATSE showed that GRBs have an isotropic sky distribution (Fig. 1.1), but at the same time it revealed that the cumulative peak flux distribution deviated from a power-law with index of $-3/2$ expected for a population of sources with a uniform distribution. This deviation, attributed to the absence of relatively faint bursts, served as a significant indicator of the cosmological origin of GRBs [5]. The definitive solution was facilitated by the the Italian-Dutch X-ray satellite *BeppoSAX* during the late 1990s: this satellite played a crucial role by delivering precise and rapid localisation, thereby enabling a quick follow up of GRBs at different wavelengths. In 1997 the remarkable discovery of the X-ray emission originating from a GRB was reported [6], followed by the detection of optical [7] and radio [8] counterparts. That same year, a few absorption lines were observed in the spectra of GRB 970508, revealing an intervening system along the line of sight of the GRB at a redshift of $z = 0.835$ [9]. This observation confirmed the cosmological nature of GRBs, establishing them as the most powerful explosions known in the Universe, second only to the Big Bang itself.

The existence of such powerful explosions triggered the curiosity of the scientific community. The transient and non-repeating nature of GRBs led to the prevailing idea that a cataclysmic event involving extreme objects was somehow required. As early as 1981, the KONUS experiment on the Venera space probes suggested that the temporal and spectral distribution of GRBs was bimodal [10]. These results were subsequently confirmed with the ISEE-3 experiment [11] and further refined utilising an extensive sample encompassing over 2700 GRBs observed with BATSE [12]. This delineated the categorisation of GRBs into two distinct classes, separated by a minimum in the distribution of duration located at around 2s (Fig. 1.2). Specifically, long

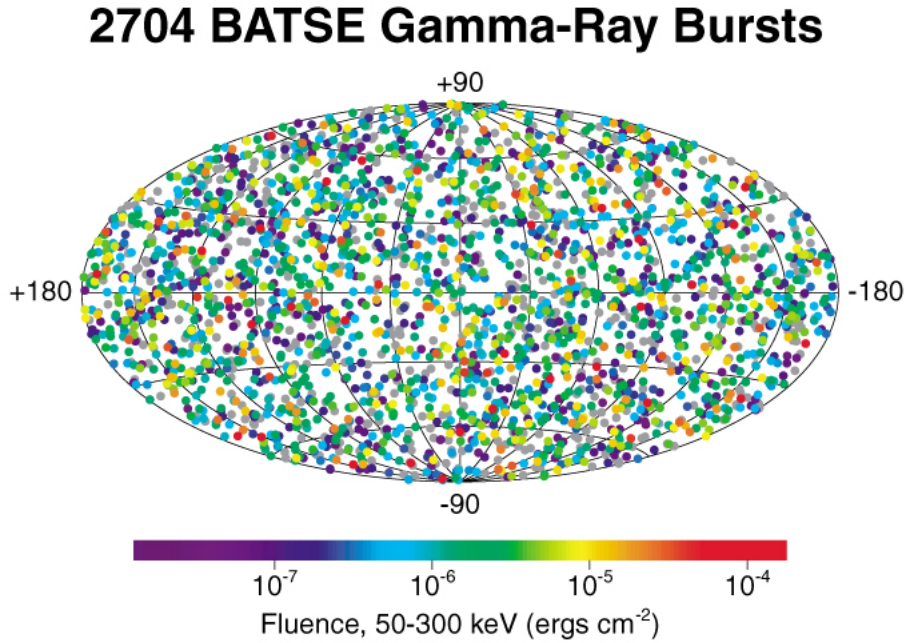


Figure 1.1: Isotropic sky distribution of 2074 GRBs detected by BATSE. The burst are color coded by the measured fluence (i.e. flux integrated over the event duration). Figure taken from <https://heasarc.gsfc.nasa.gov/docs/cgro/batse/>.

GRBs extend beyond 2s in duration, while short GRBs last less than 2s. Furthermore, short GRBs exhibit a higher peak energy within their spectral profiles when compared to long GRBs, so that they are harder. As both long and short GRBs show an isotropic sky distribution, the different temporal and spectral properties point towards a different progenitor for the two classes. Over the last two decades, comprehensive and thorough studies of GRBs spanning the whole electromagnetic spectrum have revealed that short and long GRBs differ not only in their prompt γ -ray emission, but also in their subsequent afterglow emission and their host galaxy properties (see, e.g., [13–18]). These results provided compelling evidence for the different origin of the two classes: at present, the prevailing explanation states that short GRBs are ascribed to the merger of a compact binary system involving two neutron stars (NS) or a NS and a black hole (BH), while long GRBs are generated in the catastrophic collapse of a single massive star at the end of its life.

After fifty-seven years since their initial discovery, numerous questions continue to remain unanswered. Are all long-duration GRBs produced in the collapse of a single massive star? What is the mechanisms behind the very high energy emission observed in some GRB afterglows? What is the angular structure of the relativistic outflow? In this Thesis I will discuss the fundamental and unique role played by radio observations in addressing these challenges and disclosing the extreme physics underlying GRBs. The subsequent chapters will provide a concise examination of both the observational evidence and the standard model employed to explain the extreme physics underlying GRBs. Nevertheless, it is essential to acknowledge that a comprehensive review of this subject extends beyond the goal of this Thesis. For a more comprehensive and detailed account, interested readers are encouraged to refer to, e.g., [13, 16, 19–25].

1.2 Prompt emission

Prior to the discovery of a multi-wavelength afterglow [6–8], GRBs were primarily recognised as brief, highly variable bursts of γ -rays. This initial phase of emission, which is observed from

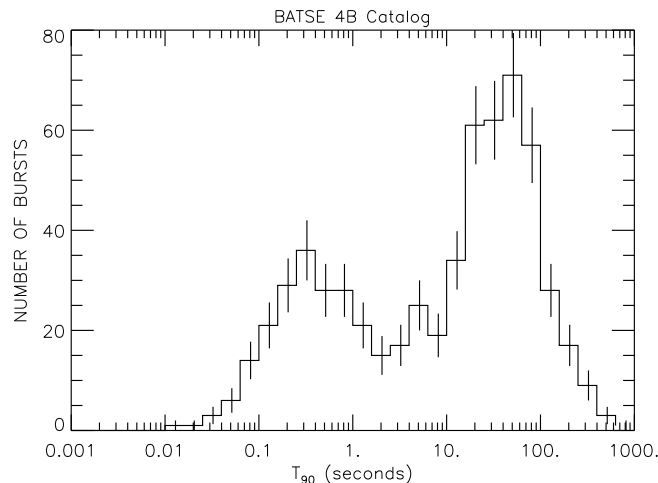


Figure 1.2: Duration distribution of the BATSE 4B Catalog. The duration parameter used is T_{90} , which is the time over which a burst emits from 5% to 95% of its total measured counts. The distribution is clearly bimodal, with a minimum at around 2 s. Figure taken from <https://gammaray.nsstc.nasa.gov/batse/grb/duration/>.

several hundred keV to a few tens of MeV, is referred to as the prompt emission. The light curve of the prompt emission, i.e. the flux as a function of time, exhibits substantial diversity in duration and shape among different bursts: most GRBs show 100% variation in flux on a time scale much shorter than the total burst duration. For some long bursts, the variability can have a time scale of a few milliseconds [22]. For roughly 80% of GRBs the light curve of the prompt emission is a composite of individual pulses (see, e.g., GRB 910503 in Fig. 1.3), while the remaining 20% show a smooth structure, typically with a one single pulse shape (GRB 910711 in Fig. 1.3) that can be described with a Fast-Rise-Exponential-Decay (FRED) function [22]. The total duration of a burst is conventionally quantified using the T_{90} parameter, which is the time interval encompassing the 5th to 95th percentiles of the total counts recorded in the energy range of the instrument. As previously mentioned in Section 1.1, the distribution of T_{90} is bimodal (Fig. 1.2; [10–12]), and this result holds even if the T_{90} is not an intrinsic measure, as its definition relies on the observed photon counts and therefore the T_{90} depends on the sensitivity of the satellites and on the considered energy band. Historically, GRBs have been classified as long if $T_{90} \geq 2$ s, or short if $T_{90} < 2$ s. Nevertheless, recent discoveries suggest that this duration-based classification does not always map to the progenitor: for instance, GRB 200826A had a duration of ~ 1.1 s (30–500 keV), but it showed a photometric excess fully consistent with an associated supernova (SN), indicative of a single massive star collapse [26]; conversely, GRB 211211A had a T_{90} duration larger than 50 s (15–350 keV), but it showed a photometrically confirmed kilonova (KN), indicative of a NS merger origin [27]. The latter burst was also noteworthy for its high-energy emission (>0.1 GeV) observed by the *Fermi* satellite during the afterglow phase [28]. Additionally, a GRB can also show a precursor, namely one or more fainter pulses preceding the main burst, as observed, for instance, in GRB 990316A (Fig. 1.3). Lastly, some GRBs exhibit an extremely prolonged γ -ray emission that extends beyond durations of 1000 s. These events have been proposed to belong to a distinct class known as ultra-long GRBs whose progenitors may differ from the conventional single massive star collapse [29, 30].

As for the light curve, the prompt emission exhibits a wide range of different spectra. The overall spectrum is non-thermal. If the spectral energy distribution (SED) is defined as $E^2 N_E(E)$, where $N_E(E)$ is the photon flux as a function of the observed energy E , the typical SED of the prompt emission is a peaked function (Fig. 1.4) and the energy corresponding to the maximum is called E_p . In order to fit the SED, a phenomenological function was introduced in 1993 by

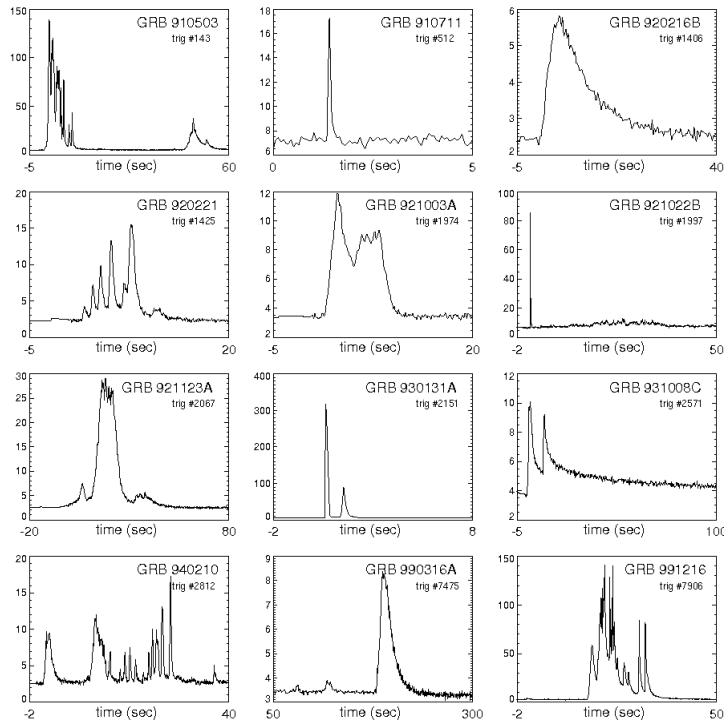


Figure 1.3: Total number of counts in time for twelve GRBs from the BATSE Catalogue. The large diversity of temporal structure and variability associated with these bursts is evident. Figure taken from <http://gammaray.msfc.nasa.gov/batse/grb/catalog/>. Credits: D. Perley.

[31]: known as Band function, it employs two power laws that are smoothly joined at a break energy $(\tilde{\alpha} - \tilde{\beta})E_0$:

$$N_E(E) = A \begin{cases} \left(\frac{E}{100 \text{ keV}}\right)^{\tilde{\alpha}} \exp\left(-\frac{E}{E_0}\right), & \text{if } E \leq (\tilde{\alpha} - \tilde{\beta})E_0 \\ \left[\frac{(\tilde{\alpha} - \tilde{\beta})E_0}{100 \text{ keV}}\right]^{\tilde{\alpha} - \tilde{\beta}} \exp(\tilde{\beta} - \tilde{\alpha}) \left(\frac{E}{100 \text{ keV}}\right)^{\tilde{\beta}}, & \text{if } E \geq (\tilde{\alpha} - \tilde{\beta})E_0 \end{cases} \quad (1.1)$$

where $N_E(E)$ is the photon flux in units of photons $\text{cm}^{-2} \text{s}^{-1} \text{keV}^{-1}$ in the energy bin dE ; A is the normalisation factor at 100 keV in units of photons $\text{cm}^{-2} \text{s}^{-1} \text{keV}^{-1}$; $\tilde{\alpha}$ and $\tilde{\beta}$ are the low-energy and high-energy power law indices, respectively; E_0 is the break energy in units of keV. The notation for the power law indices in Eq. 1.1 follows [22], in order to distinguish the prompt parameters $\tilde{\alpha}$ and $\tilde{\beta}$ from the afterglow parameters α and β , which will be discussed later. Even if there is no theoretical model that can predict the spectral shape of the Band function, it still provides an excellent fit to most of the observed spectra (Fig. 1.4). For most of the observed values of $\tilde{\alpha}$ and $\tilde{\beta}$, the peak energy with the Band function is $E_p = (\tilde{\alpha} + 2)E_0$ [22].

Conversely, when the peak energy E_p lies outside the energy range covered by the γ -ray instrument, the spectrum is typically modeled using a single power law with an exponential cutoff, often referred to as CPL:

$$N_E(E) = A \left(\frac{E}{100 \text{ keV}}\right)^{\tilde{\alpha}} \exp\left(-\frac{E}{E_0}\right) \quad (1.2)$$

Based on theoretical considerations (see Chapter 2) the prompt γ -ray emission is expected to be produced via synchrotron cooling of a population of relativistic electrons [22]. According to this scenario, the slope of the low energy tail is predicted to be $\tilde{\alpha} = -3/2$ in the fast cooling regime; notwithstanding, GRBs exhibit a low-energy slope $\tilde{\alpha} \sim -1$ on average (see, e.g., [31, 33]). More recently, a second break occurring at roughly 3 - 20 keV has been successfully incorporated

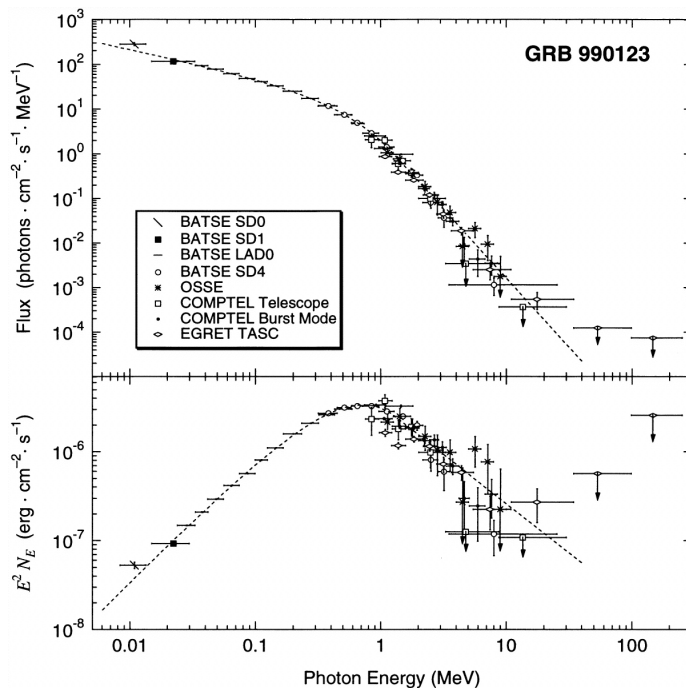


Figure 1.4: Photon flux $N_E(E)$ (upper panel) and SED ($E^2 N_E(E)$; lower panel) of GRB 990123 as observed by the Compton Gamma-Ray Observatory detectors. The dashed line is the fitting Band function. Figure taken from [32].

into the fitting model of many GRB SEDs [34–37]. The inclusion of a second break provides a solution that is consistent with the synchrotron expectations.

Finally, if the redshift z is known, the isotropic equivalent energy E_{iso} can be calculated from the SED [38]:

$$E_{iso} = \frac{\int_{E_1}^{E_2} 4\pi D_L^2 N_E(E) E dE}{(1+z)^2} \quad (1.3)$$

where E_1 and E_2 are the lower and upper limits in energy (usually 1 - 10⁴ keV); $N_E(E)$ is the best fit Band model to the time-integrated and redshift-corrected SED; D_L is the luminosity distance. The $(1+z)^2$ factor comes out from the cosmological time dilation and the spectral redshift [38].

The peak energy E_p and the isotropic equivalent energy E_{iso} are fundamental parameters to quantify the energetics of the burst, which in turn relies on the characteristics of the progenitor. In the early 2000s, many authors tried to constrain the prompt emission parameters in order to reveal the origin of the observed γ - and X-ray radiation. Notably, a significant breakthrough was achieved in 2002, when a correlation between the peak energy and the isotropic equivalent energy was established through the analysis of twelve *BeppoSAX* long GRBs with known redshifts. The correlation, known as the Amati relation, asserts that $E_p(1+z) \propto E_{iso}^{0.52 \pm 0.06}$ [38]. The Amati relation was later confirmed and extended with the inclusion of long GRBs and X-ray flashes detected by more recent satellites. The theoretical interpretations ascribe the Amati relation to geometrical effects or to dissipative mechanisms within the photosphere of the fireball (see, for instance, [39] and reference therein). Subsequently, in 2004, a more stringent relation was identified between the intrinsic peak energy and the total energy, accounting for GRB collimation effects, i.e. $E_\gamma = (1 - \cos\theta_j)E_{iso}$ with θ_j being the opening angle of the GRB jet. The relation, now recognised as the Ghirlanda relation, states that $E_p(1+z) \propto E_\gamma^{0.706 \pm 0.047}$ [40]. Concurrently, the Yonetoku relation was introduced, postulating that $L_{52} \propto [E_p(1+z)]^{2.0 \mp 0.2}$, with L_{52} representing total luminosity in units of 10⁵² erg s⁻¹ [41]. In addition to the role they

play in understanding GRB physics, these relations represent an independent method to derive cosmological parameters [39, 42, 43].

As I will discuss in Chapter 2, following the collapse of a single massive star (in the context of long GRBs) or the merger of two compact objects (for short GRBs), two jets with opposite directions are launched. These jets pierce through the stellar envelope (long GRBs) or the material ejected before the merger (short GRBs); if the jets are sufficiently energetic, they dig the envelope and the blast wave generated from this interaction can propagate through the circum-burst medium. The origin of the prompt emission is attributed to internal shocks occurring within the outflow. These internal shocks accelerate the ejected electrons up to relativistic energies: the observed γ -ray emission is due to the cooling of the relativistic electrons. As the outflow expands, it interacts with the environment surrounding the burst, producing the afterglow emission through external shocks. The connection between the prompt and the afterglow phases is therefore evident. In Chapter 7, I will delve into recent studies concerning the relationship between the prompt emission properties and the subsequent radio emission during the afterglow phase: these studies are crucial to shed light on the progenitor systems, whose nature remains still elusive.

1.3 The Afterglow phase

Long awaited from theoretical considerations, the first X-ray and optical afterglows were discovered in GRB 970228 [6, 7]. The same year, the first radio counterpart was found in GRB 970508 [8]. Following the prompt γ - and X-ray emission, a multi-wavelength, continuum and long-lasting afterglow emission is, in fact, expected. For long GRBs, it has been observed that approximately 95% are detected in X-rays, around 70% in the optical and merely 30% in radio [44, 45]. Similarly, for short GRBs detected by the NASA's Neil Gehrels *Swift* Observatory (*Swift*) around 76% have detected X-ray afterglows but only 11% are detected in radio [46]. This discrepancy, which has been usually explained with different sensitivities of telescopes across different bands, has recently been proposed to indicate a dichotomy in the population of long GRBs analogous to what is observed in Active Galactic Nuclei, i.e. radio-loud and radio-quiet GRBs. The latter classification has been proposed to point at different progenitors: one of the possible explanations argues that radio-loud GRBs may originate from massive stars collapsing in interacting binary systems, while radio-quiet GRBs hail from the collapse of isolated massive stars [47]. Thus, observations of GRB afterglows are fundamental as they carry crucial information on the surrounding environment and, consequently, on the progenitor. In Chapter 7 a comprehensive statistical analysis of radio afterglows of long GRBs will be presented.

In Fig. 1.5, a schematic representation of the afterglow light curve across different bands is provided. It is important to emphasise that these illustrations are presented solely for explanatory purposes and actual light curves can exhibit greater complexity. Concerning the X-rays (upper left panel), the afterglow light curve is characterised by five main components [48]: (I) an initial steep decay at very early times, with a slope of roughly 3; (II) a shallower decay, with a typical slope of ~ 0.5 ; (III) a subsequent decay with a power law index of ~ 1.2 ; (IV) a late decay with a typical slope of approximately ~ 2 . Phase (II), known as plateau, and phase (V), called flare (dotted line), are observed only in a fraction of bursts. They are usually associated with late time energy injection from the central engine (a BH or a NS). Phase (0) is the X-ray prompt emission. Finally, the onset of phase (IV) marks the jet break. The latter phenomenon is often interpreted as a geometrical effect due to the non-spherical shape of the ejecta (see Section 2.6 for a detailed explanation).

Regarding the optical (upper right panel), the light curve usually exhibits (0) an early, single power law rise, which marks the onset of the observable emission; (I) a subsequent single power-law decay, characterised by an index between 1 and 2; (II) a post-jet break decay with a

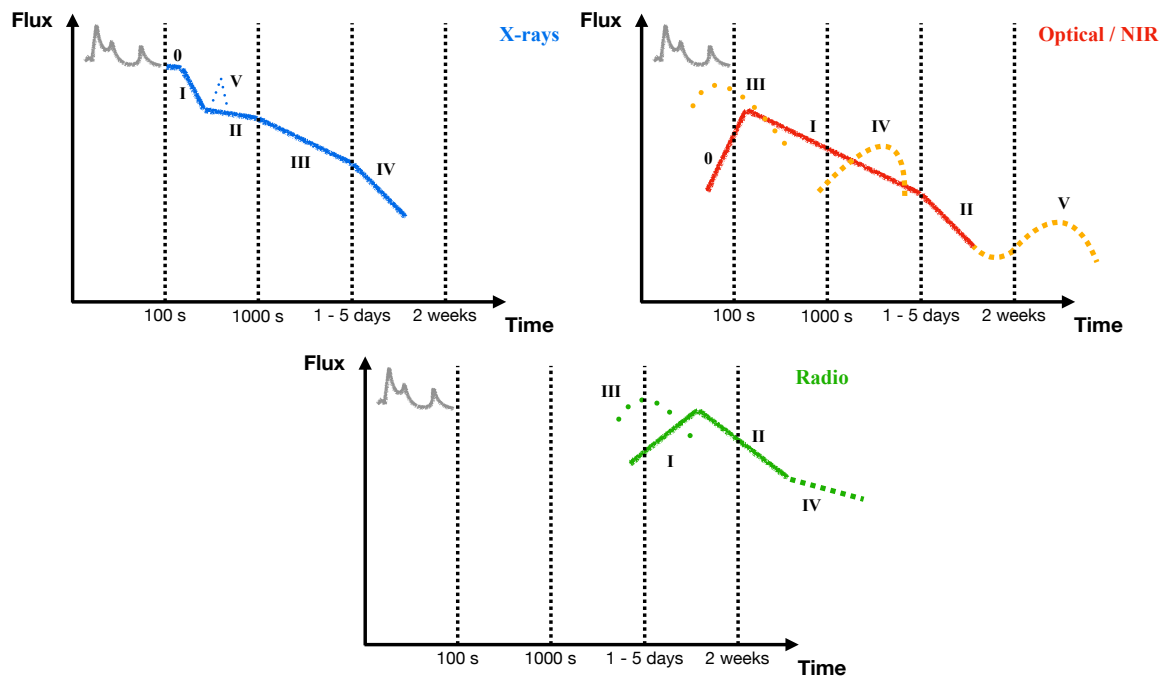


Figure 1.5: Sketch of the afterglow light curves, namely the flux density in time, in X-rays (upper left), optical (upper right) and radio (lower). For each band, the prompt γ -ray emission is shown with a grey line. The coloured solid lines are the continuum light curves expected for a forward shock. The exhaustive description of the different phases for each band is provided in the text. Figures inspired by G. Ghirlanda.

steeper slope. For some bursts, an early bump may be observed (indicated with a dotted orange line, phase III). This bump can be explained within the framework of the standard model for GRBs as originating from reverse shock emission (Chapter 2). Within a few days post-burst, the emission of a Kilonova can be detected in the case of a short GRB (phase IV, dashed orange line). Conversely, in the context of long GRBs, the contribution from a SN can be predominant at later stages (phase V, dashed orange line).

Moving to the radio domain, the afterglow typically becomes observable at later times, extending over days, weeks, or even years in some cases (for instance, GRB 171205A [49]). The radio light curve can be tentatively characterised by two primary phases: (I) an initial rise with index between 0 and 2; (II) a decay with index between 1 and 2. Analogous to the optical regime, the radio light curve can manifest an early bump linked to reverse shock (dotted line, phase III). In later stages, a shallower decay phase has been observed for a handful of GRBs (phase IV), which has been attributed to the transition of the GRB outflow to a non-relativistic expansion. Finally, at early stages radio afterglows may also show some fluctuations that are suppressed at later times. These fluctuations have been attributed to interstellar scintillation effects [50–52]. In fact, radio waves are perturbed by the ionised interstellar medium in the Milky Way [50, 51], inducing frequency-dependent variability in the observed flux. While diffractive scintillation arises from the interference between rays diffracted by small-scale irregularities in the ionised interstellar medium, perturbations of the wavefront by large-scale inhomogeneities give rise to refractive scintillation. Diffractive scintillation, which is narrow-band and highly variable, occurs only when the apparent source size is smaller than a characteristic scale, known as the diffractive angle. Consequently, diffractive scintillation diminishes as the GRB outflow expands. Conversely, refractive scintillation, which has a limited effect and acts on longer timescales, is broadband and less sensitive to the source size [51]. Both diffractive and refractive scintillation effects have been observed in GRBs (GRB 970508 [8, 53]; GRB 070125 [54]; GRB 130427A [55]; GRB 160625B [56]; GRB 161219B [57]). In most cases, the attenuation of scintillation has been

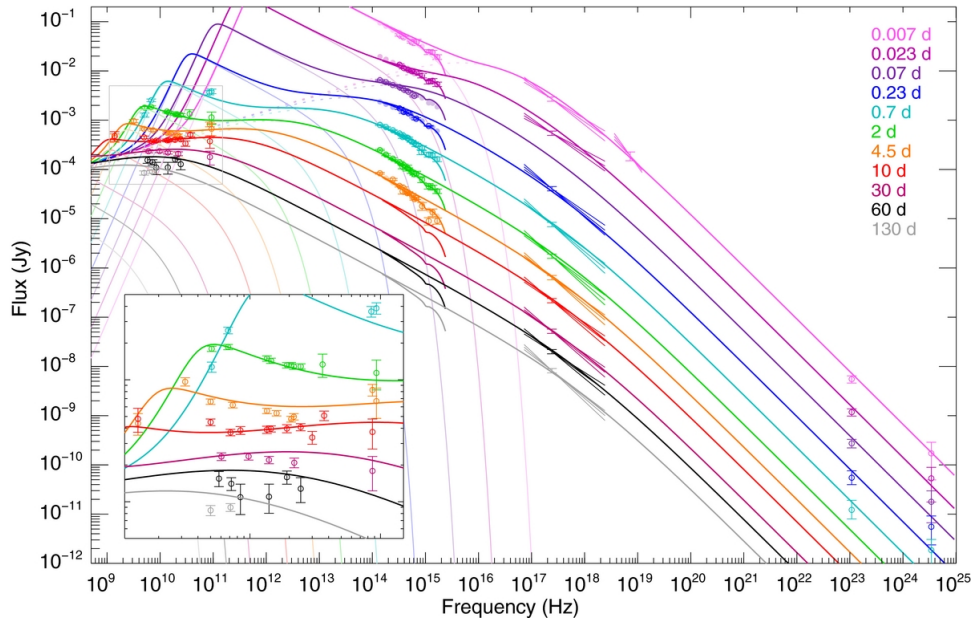


Figure 1.6: Afterglow emission of GRB 130427A, spanning 16 orders of magnitude in frequency (from 10^9 Hz to 10^{25} Hz). Open points with error bars are measurements, while solid lines represent the standard model prediction. Each colour marks a coeval epoch (from 0.007 days to 130 days). The inset shows a magnified version of the radio part of the SED at $t > 0.7$ days. Figure taken from [58].

used to unveil the expansion of the GRB outflow and to estimate a size of approximately 10^7 cm a few days or weeks post-burst.

From the observational evidence of the light curves the prevailing suspected radiative mechanism is synchrotron emission. This interpretation is also confirmed by the afterglow spectrum that, contrary to the prompt emission, can span up to 18 orders of magnitude, ranging from the very high energies (> 100 GeV) to X-rays, optical and near infrared (NIR), down to the radio. In fact, simultaneous observations across the electromagnetic spectrum revealed that the SED can be fitted with several power law segments, which join at specific break frequencies that can be precisely reproduced by synchrotron emission from a population of relativistic electrons (Chapter 2). In Fig. 1.6 an example taken from [58] is shown. The modelling curves for the SED of GRB 130427A, which are computed from a standard model including both forward and reverse shocks, can explain the afterglow emission over 16 orders of magnitude in frequency and 4 orders of magnitude in time.

Despite the success of the standard model for GRBs, the last few years have witnessed the opening of a new, exciting window in GRB spectrum, whose explanation requires an extension of models and, in turn, of our understanding. In 2019, the Major Atmospheric Gamma-ray Imaging Cherenkov Telescopes (MAGIC) reported the first detection of very high energy emission from a long GRB, specifically GRB 190114C [59]. In the same year, very high energy emission was reported from the afterglow of GRB 180720B, starting ten hours after the end of the prompt emission phase [60]. Following these breakthrough discoveries, other four additional long GRBs have been proposed to exhibit very high energy emission, namely GRB 190829A, GRB 201015A, GRB 201216C and GRB 221009A. This emission has been seen at either early epochs (e.g. GRB 190114C, 300 GeV – 1 TeV [61], GRB 201216C [62] and GRB 221009A, 200 GeV - 7 TeV [63]) or at later times deep in the afterglow phase (e.g. GRB 180720B, 100–400 GeV [60] and GRB 190829A, 180 GeV – 3.3 TeV [64]).

Studying this emission component provides the opportunity to constrain the physical characteristics of the emitting region and/or the shocked accelerated particles. Nonetheless, the detection of very high energy emission is challenged by pair production from the interaction

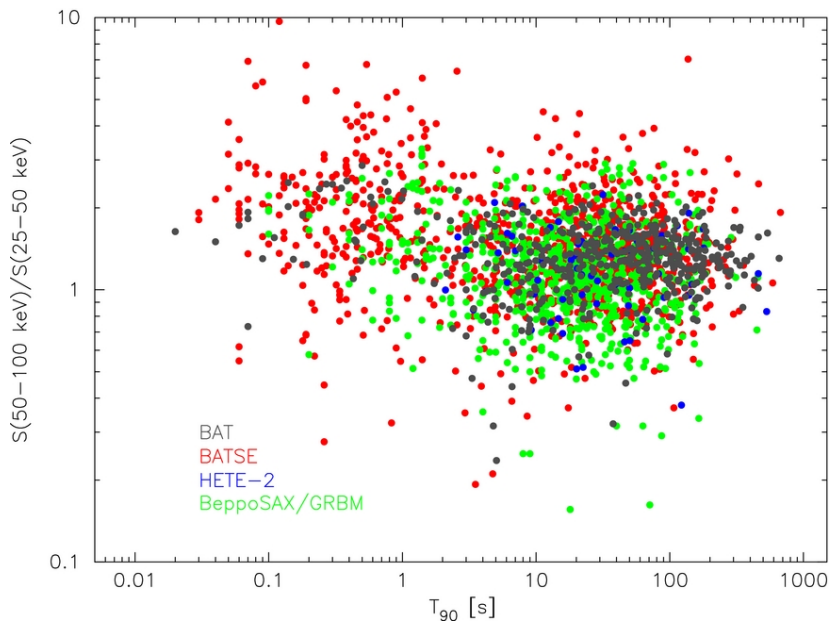


Figure 1.7: Hardness ratio, i.e. fluence ratio between the 50–100 keV and the 25–50 keV bands, as a function of T_{90} duration for BAT (dark gray), BATSE (red), HETE-2 (blue), and *BeppoSAX* (green) GRBs. Short GRBs ($T_{90} < 2$ s) exhibit a higher hardness ratio than long ones ($T_{90} > 2$ s). Figure taken from [65].

between very high energy photons and the extra-galactic background light, leading to a substantial attenuation of the very high energy photons with increasing distance. Consequently, the detection of very high energy photons from sources beyond redshift 1.5 is considered improbable. Based on the very few events detected so far, it seems that the very high energy emission characterises both very energetic events, such as GRB 180720B and GRB 190114C, and low-energy events, such as GRB 190829A and GRB 201015A, but any possible peculiarities of very high energy detected bursts will become clearer as the sample of events increases. What is the origin of the very high energy emission? To answer the question, high-quality, broadband observations of nearby GRB afterglows are needed. In Chapter 4 I will present the multi-wavelength analysis of GRB 201015A carried out during my Ph.D course.

1.4 Short Gamma-Ray Bursts

The classification of GRBs into two distinct classes has been widely proved over the past two decades. In addition to their shorter T_{90} duration, short GRBs are also characterised by higher spectral hardness when compared to long GRBs. This difference is highlighted by the generally larger ratio between the fluence, namely the flux integrated over the event duration, at higher and lower energy bands, as depicted in Fig. 1.7 from [65]. Broadly speaking, short GRBs exhibit fainter luminosities, with isotropic equivalent energies typically ranging from 10^{48} to 10^{52} erg [66]. Furthermore, their average spectroscopic redshift is around $z \sim 0.5$ [17], placing them closer in terms of distance compared to the average range for long GRBs.

The distinction between short and long GRBs is not solely confined to their prompt emission features. In fact, this idea is reinforced when considering the burst environment, their afterglow properties and their multi-messenger emissions. These aspects will be presented in the following sections.

1.4.1 Host Galaxies

The launch of the *Swift* satellite in 2005 marked a breakthrough in GRB science. Because of its sensitivity and reduced slewing time, it was possible for the first time to detect an X-ray afterglow for a short GRB [67]. Together with the afterglow emission, a host galaxy candidate was detected for the same burst, GRB 050509B, opening a new window on the study of the environment of the progenitors. Many other host galaxies of short GRBs have been identified afterwards, but the initial comprehensive studies on short GRB host galaxies were limited to those cases in which a detection in the optical was available [14, 68]. Nevertheless, it was immediately clear that short GRB hosts were not drawn from the same parent population of long GRB hosts, but rather from the underlying field galaxy distribution [14]. Through multi-band optical and NIR observations of a small sample of three GRB host galaxies, it was initially posited that short GRBs might be originating from compact binary mergers situated relatively close to their star-forming regions within the host galaxy [68]. However, a subsequent work based on a larger sample of 10 short GRB host galaxies observed with the *Hubble Space Telescope* (HST) revealed that [69]:

- short GRBs host galaxies are, on average, larger by a factor of ~ 2 than the hosts of long GRBs.
- Approximately 75% of short GRB hosts are young, star-forming galaxies. Nevertheless, some short GRBs originated in older, quiescent host galaxies, implying that the progenitors of short GRBs exhibit a wide range of formation timescales [17].
- The projected physical offset between the position of short GRBs and the centre of their host galaxies range from 1 to 50 kpc, with a median of about 5 kpc, which is roughly 4 times larger than for long GRBs [70]. More recently, the median physical offset increased up to 7.7 kpc [18]. This is in agreement with the expected distribution of compact binaries.

These results were confirmed and further refined by subsequent analyses of larger samples [15, 17, 18, 70]. Additionally, it was found that short GRBs do not spatially trace star formation or stellar mass, which is in agreement with the general notion that NS–NS or NS–BH binaries may be ejected from their birth sites due to the natal kicks generated in the binary formation process [15]. Moreover, it was recently proposed that the physical offset from the host centre decreases with increasing redshift [17, 70]. If confirmed, this could be an evidence of two formation channels in short GRBs. The majority (around 80%) of short GRB progenitors would belong to a population of binaries that originates in young, star-forming regions and merge in a short time. Conversely, a small fraction of compact binaries, which are found predominantly in older, closer, quiescent galaxies, would exhibit longer delay times between the formation and the merger. Other possible explanations for the redshift evolution include a larger size of low- z galaxies, or selection biases in the sample [70].

Concerning the overall properties of short GRB hosts, a recent study involving a sample of 69 host galaxies yielded important median quantities for the stellar population within the galaxies [17]. Specifically, the authors found that $\log(M_*/M_\odot) = 9.69^{+0.75}_{-0.65}$, $\text{SFR} = 1.44^{+9.37}_{-1.35} M_\odot \text{ yr}^{-1}$, $t_m = 0.8^{+2.71}_{-0.53} \text{ Gyr}$, $\log(Z/Z_\odot) = -0.38^{+0.44}_{-0.42}$ and $A_v = 0.43^{+0.85}_{-0.36} \text{ mag}$ (68% confidence), where M_* is the total stellar mass, SFR is the star formation rate, t_m is mass-weighted age, Z_* is the stellar metallicity and A_v is the total dust attenuation. The average spectroscopic redshift found is $z = 0.47^{+0.58}_{-0.25}$. The wide ranges of ages, metallicities and SFRs corroborate the general idea that short GRB progenitors form in a plethora of different environments. Interestingly, no relation was found between the aforementioned host properties (stellar mass, SFR, age, metallicity and dust attenuation) and the circumburst density, the GRB projected physical offset and the optical afterglow [17]. Nonetheless, the authors suggested that most short GRBs in quiescent hosts exhibit shorter T_{90} durations and lower fluences than those in star-forming galaxies [17].

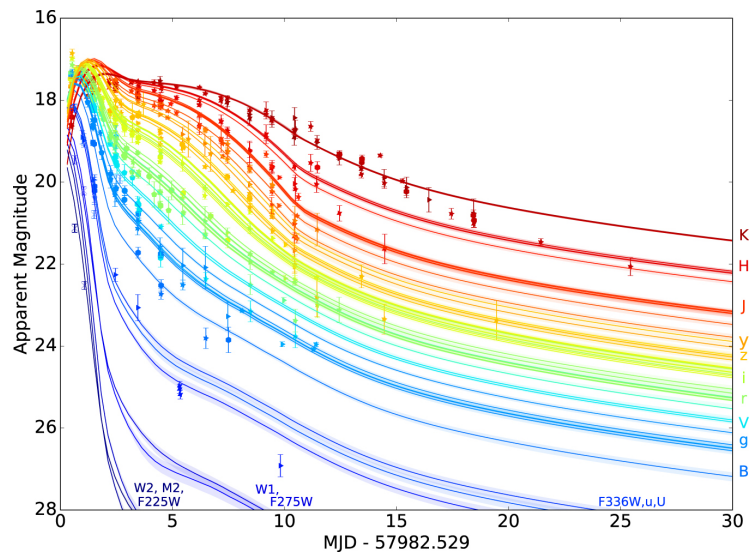


Figure 1.8: Optical light curve of AT 2017gfo. Figure taken from [80].

Finally, it is worth noticing that the optical emission of host galaxies might be affected by dust obscuration, hence the SFR derived with optical estimators may be underestimated. On the contrary, radio and sub-millimeter observations are not affected by dust and they represent a valuable tool to determine the level of obscured star formation and the overall properties of host galaxies [71]. However, less than ~ 15 short GRBs have a radio counterpart (e.g. [46]) and even less have an associated host galaxy detected in this band. Therefore, even though radio can play a fundamental role, studies of host galaxies in this band are hitherto hindered by the paucity of detections. The advent of new, more sensitive facilities such as the Square Kilometre Array (SKA) and the next generation Very Large Array (ngVLA), will provide us with an unprecedented view on the environment of short GRBs.

1.4.2 Kilonovae

The tidal forces experienced during the spiralling phase by a NS in close binary system with another NS or a BH lead to ejection of small fraction of matter (10^{-3} - $0.1 M_{\odot}$) with a sub-relativistic velocity [72–74]. Due to emission of gravitational waves, the orbit decays and the compact objects will eventually merge. The coalescence, which produces a highly magnetised NS or a spinning stellar mass BH, releases further material into the surrounding medium. The expanding material ejected before and after the merger event is endowed with significant quantities of neutron-rich elements whose radioactivity provides a long-term heat source [75]. It has been suggested that, if the ejected matter consists mainly of r-process nuclei, NS mergers could account for the observed abundance of r-process elements in our Galaxy [73]. The overall process is expected to produce a short-lived optical/NIR transient similar to, but dimmer than, an ordinary supernova, known as Kilonova [75, 76]. Therefore, the detection of a Kilonova (KN hereafter) can be considered as a signpost of a compact binary merger involving at least one NS.

The first evidence for such an event came precisely from the observation of GRB 130603B [77, 78]. The optical and NIR emission associated with this short GRB at $z = 0.356$ was significantly brighter than what would be expected from the extrapolated contribution of the afterglow, supporting the hypothesis of a merger origin for short GRBs [79]. The observed properties of the KN could be reproduced by a simple KN model with an ejected mass of 0.03 - $0.08 M_{\odot}$ and a velocity of 10 - 30% the speed of light [78].

Simulations of binary mergers predict that the ejected material might be divided into two

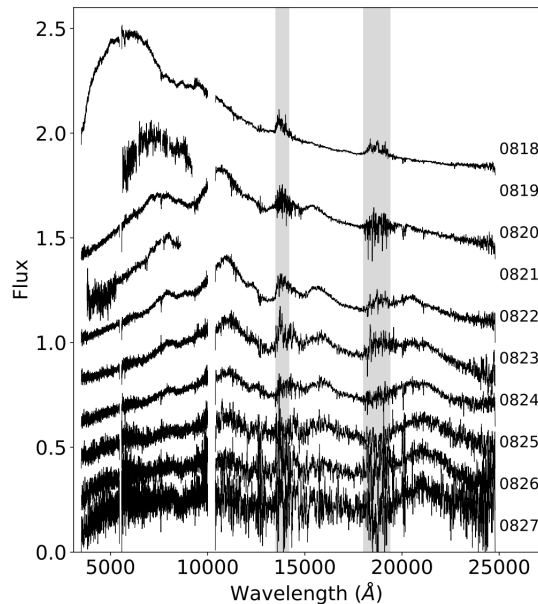


Figure 1.9: Evolution of the spectrum of AT 2017gfo. The epoch of each spectrum is reported on the right (in the MMDD format). Figures taken from [81].

components: an outer, lanthanide-free region that produces a brief (~ 2 d), bluer optical transient and an inner region rich in lanthanides, which produces a longer (~ 10 d), redder transient (see, e.g., [82]). The dearth of available data with enough quality hindered the quest for the blue and the red regions until 2017. The discovery of a KN emission, named AT 2017gfo, associated with the multi-messenger event GW 170817 / GRB 170817A represented a major breakthrough: an extensive campaign in the optical and NIR, including the Rapid Eye Mount (REM) telescope, the ESO Very Large Telescope (VLT) and the ESO VLT Survey Telescope (ESO-VST), with an almost daily cadence provided for the first time ever the spectral evolution of a KN emission [81]. In Fig. 1.8, the optical light curve of AT 2017gfo from [80] is shown, while the spectral evolution from [81] is presented in Fig. 1.9. The first spectrum reveals a black-body emission with temperature of roughly 5000 K [81]. Subsequently, the shape of the spectrum changes dramatically and broad absorption lines appear. The evolution of the spectrum is consistent with predicted KN emission: at first, the expanding material is optically thick, and the blue lanthanide-free black body emission is observed; later on, the spectrum is dominated by the contribution of new atomic species produced in the nucleo-synthesis [81, 83]. The derived mass for the ejecta was around $0.03 - 0.05 M_{\odot}$.

More recently, a third KN was detected in GRB 211211A, a long GRB at $z = 0.0763$ [27]. Observations of GRB 211211A could be reproduced by a KN model that includes a red (lanthanide-rich), a ‘purple’ (with an intermediate opacity) and a blue (lanthanide-free) components. The total ejected mass derived was $0.05 M_{\odot}$. The fact that this KN was detected in a long GRB questioned the accepted idea that long GRBs originate in the collapse of a single massive star. In fact, this burst represented the first compelling evidence that at least some long GRBs hail from compact binary mergers.

As the kilonova expands, it will eventually interact with the surrounding medium, producing a KN afterglow by shocking the ambient gas (see, e.g., [84, 85]). This interaction is expected to produce a rebrightening of the radio afterglow, making it detectable for years after the GRB. The emission from a KN afterglow will provide fundamental constraints on the velocity distribution and the total energy of the material ejected before and during the merger [85]. Hitherto, only one candidate for a KN afterglow in the X-rays has been proposed [86, 87]. With the improved

sensitivity and surveying capabilities of the next generation of radio observatories, such as the SKA and the ngVLA, it will be possible not only to detect the KN afterglow of short GRBs for decades, but also to discover new orphan afterglows, i.e. off-axis GRBs for which we cannot observe the prompt γ -ray emission. Therefore, future radio facilities represent a fundamental asset to independently characterise and constrain the outflow of a KN, its circum-burst medium and the rate of compact binary mergers.

1.4.3 Gravitational Waves

After almost 100 years from Einstein’s prediction, gravitational waves (GW) were detected from the coalescence of a binary BH pair, initially with the Laser Interferometer Gravitational-Wave Observatory (LIGO; [88]) and later using the combined LIGO-Virgo global 3-detector network [89]. These milestones opened the era of GW astronomy. The General Relativity theory postulates that a GW signal produced by two compact objects in a close orbit should increase in frequency and strength as the objects approach each other; this is known as a chirp signal (see Figure 1.10). The shape of this chirp signal strongly depends on the properties and the nature of the binary. The main parameters to consider are intrinsic, such as the initial masses, the spin angular momenta and the tidal deformability of the two objects, and extrinsic, namely the localisation of the GW event in the sky, the luminosity distance and the orientation of the binary angular momentum. As GW signals are swamped in gaussian noise, they can be detected only with the matched filtering technique: a template of the expected waveform is used to filter the data in order to identify any possible signal drowned in the data that is similar to the predicted template.

On 2017 August 17, a GW signal from a NS binary coalescence was detected by Advanced LIGO and Advanced Virgo (Figure 1.10; [90, 91]). After 1.74 ± 0.05 s, a short GRB was detected by *Fermi*–GBM [92]. Soon after the optical counterpart was found [93], while the X-ray and radio emissions were detected 9 [94] and 16 days post burst [95], respectively. The extensive, multi-wavelength campaign that followed provided the most detailed light curves and spectra for a short GRB to date (see, e.g., [96]). The event, known as GW170817 / GRB 170817A, was also associated with the first spectroscopically confirmed KN, AT 2017gfo. This impressive discovery signposted the dawn of “multi-messenger” astrophysics with GW. Combining the electromagnetic and the GW information, it was possible to constrain in an unprecedented way the progenitors, the geometry and the structure of the GRB. From the GW signal a primary mass between 1.36 and 1.89 M_{\odot} , a secondary mass between 1.00 and 1.36 M_{\odot} and a total mass of $2.77^{+0.22}_{-0.05} M_{\odot}$ were derived [97]. The spin angular momenta were less constrained, with the dimensionless value χ_i ranging from 0 to 0.61 [97]. Finally, the system was found to be inclined with respect to the observer’s line of sight of roughly 150° .

Concerning the electromagnetic counterpart, the prompt γ -ray light curve of GRB 170817A consisted of a spike of 0.5 s, followed by a lower-significance tail of softer emission, with total duration of $T_{90} = (2.0 \pm 0.5)$ s. The peak energy of the spectrum and the isotropic equivalent energy were $E_p = (185 \pm 62)$ keV and $E_{iso} = (3.6 \pm 0.9) \times 10^{46}$ erg (10–1000 keV), respectively. As highlighted by [96], the fact that GRB 170817A is significantly less energetic than cosmological short GRBs is in agreement with an off-axis configuration of the binary system. In fact, while the GW signal is maximised when the plane of the orbit is inclined, with an observer’s angle of 30° , the GRB emission is considerably suppressed.

The later afterglow emission of GRB 170817A showed a single power law spectrum from the X-rays down to the radio. Such a behaviour can be explained by an optically thin synchrotron emission from a population of relativistic electrons: in fact, if the minimum injection frequency lies below the observed radio band and the electron cooling frequency is above the X-rays (see Chapter 2), the very same synchrotron regime is observed at every wavelength. Even though

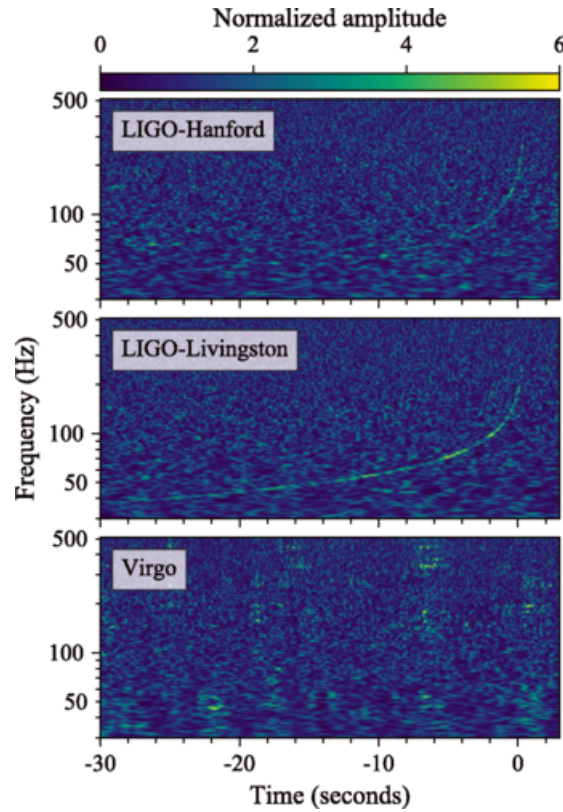


Figure 1.10: Time vs frequency representations of the GW signal from GW 170817, observed by the LIGO-Hanford (top), LIGO-Livingston (middle), and Virgo (bottom) detectors. Times are shown relative to 2017 August 17, 12:41:04 UTC. The chirp signal is clearly visible in LIGO-Hanford and LIGO-Livingston data. Figure taken from [90].

under these circumstances the break frequencies could not be constrained properly, the spectrum provided the most precise measurement of the electron distribution index ever, $p = 2.166 \pm 0.026$ [96]. The slowly rising flux, uniquely unveiled by the radio observations between 1 and 7 months as shown in Figure 1.11, invoked either a highly collimated jet with an angular structure or an isotropic outflow with a distribution of its radial velocity profile. In fact, simulations of NS-NS mergers show that when a jet pierces through a pre-ejected denser material a mildly relativistic, wide-angle cocoon is produced. If the jet has enough energy, it can successfully drill the matter and a highly collimated ultra-relativistic outflow emerges. That being the case, the final outcome is a system with a jet and a cocoon. Conversely, if the energy content is not sufficient, the jet is quenched and a pure cocoon is produced.

For GRB 170817A, the two models could be distinguished only by exploiting the high angular resolution provided by the Very Long Baseline Interferometry (VLBI). In particular, VLBI observations with the High Sensitivity Array (HSA) showed the apparent superluminal motion of the centroid of the radio emission with a velocity $v_{app} = (4.1 \pm 0.5)c$ between 75 and 230 d [101], where c is the speed of light. Moreover, global-VLBI observations involving 32 radio telescopes all over the world constrained the apparent size of the unresolved radio source to < 2.5 mas at 270.4 d post burst (90% confidence level, [100]). Overall, these measurements ruled out a quasi-spherical outflows and provided the first direct evidence that NS-NS mergers are able to launch highly collimated relativistic jets that pierce through the material spread around by the merger, as first posited by [3, 79].

GW 170817 / GRB 170817A represented a breakthrough with deep implications on many scientific areas. However, this event occurred in a galaxy at 40 Mpc [102], while the median redshift for short GRB is 0.64 (68% confidence level, [17]). Therefore, to probe the population of cosmological short GRBs, both GW and electromagnetic facilities with higher sensitivities are

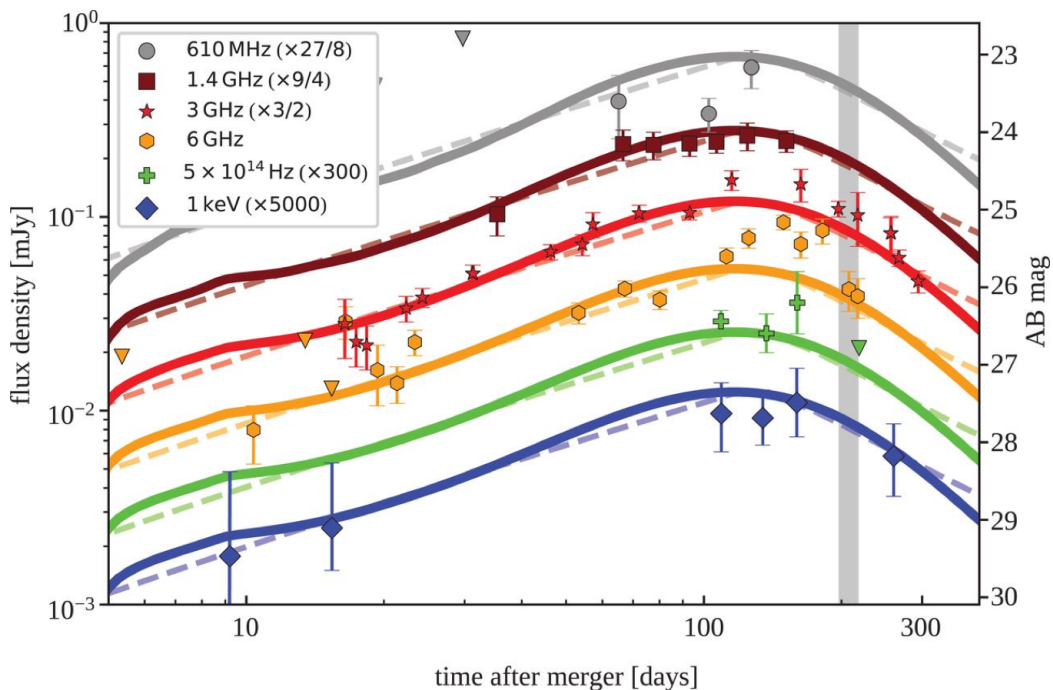


Figure 1.11: Multi-frequency light curve of GRB 170817A. Fluxes are re-scaled for the ease of the presentation. The intermediate epochs (25-100 days) are sampled by radio observations when the flux density has a shallow rise. This evidence required the introduction of a velocity profile in the the simplest cocoon model [98] or an angular-structured jet model [99]. Only with VLBI observations it was possible to distinguish between the two of them. Figure taken from [100].

required. The ongoing fourth observing run (O4) of the LIGO, Virgo and KAGRA network is meant to extend the accessible horizon up to 200 Mpc. The expected detection rate is 10_{-10}^{+52} for NS-NS mergers and 1_{-1}^{+91} for NS-BH mergers, providing new opportunities for multi-messenger studies of these extraordinary sources.

1.5 Long Gamma-Ray Bursts

In comparison to short GRBs, long GRBs exhibit a wider range of spectroscopic redshifts, spanning from $z \sim 0.008$ to $z = 8.1$ [103, 104], with an average value of $z \approx 2$ [16]. Additionally, they are generally more energetic, with isotropic equivalent energies that typically range from 10^{48} to 10^{54} erg [22]. In many cases, long GRBs have been associated with SN events [105]. Moreover, in the last few years afterglow emission of long GRBs has been detected up to teraelectronvolt (TeV) energies. In the next sections I will present the latest and most relevant observational discoveries concerning long GRBs. While the collapse of an isolated massive star should result in the emission of GWs, the precise GW waveform remains uncertain as it relies on poorly understood explosion mechanisms. At the time of writing, no empirical evidence of such GW emission has been found; thus, GW emission associated to long GRBs will not be discussed.

1.5.1 Host Galaxies

The environment surrounding GRBs provides fundamental clues to trace the origin of their progenitor back. Optical/NIR photometry and spectroscopy have been extensively employed to gauge stellar masses, SFRs, dust extinctions and metallicities of the galaxies hosting GRBs. One of the first, pioneering attempt to characterise the circum-burst medium included a sample of 46

galaxies observed in these bands, spanning a redshift between 0 and 6.3 [106]. The authors found that GRB hosts are generally small, star-forming galaxies with low metallicity. The derived SFRs ranged from $0.01 M_{\odot} \text{yr}^{-1}$ to $36 M_{\odot} \text{yr}^{-1}$, with a median at $2.5 M_{\odot} \text{yr}^{-1}$. The metallicity for host galaxies at $z < 1$ was between a tenth of solar to solar [106], in agreement with the hypothesis that the production of a burst is heavily suppressed in more metal-rich environments [107]. Subsequent studies have corroborated these properties [108, 109]. Specifically, a median redshift of 2.14 ± 0.18 for *Swift* GRB hosts was found [110].

To establish a connection between long GRBs and other astrophysical transients, their host galaxies have been compared with those associated with different explosive phenomena. Interestingly, it was found that long GRB hosts are not statistically different from galaxies harbouring core-collapse SNe [111] or Hydrogen-poor superluminous SN [112], although they tend to be smaller, less massive and less luminous [113, 114]. If long GRBs are associated to SNe, it may be expected that they are unbiased tracer of the SFR over the cosmic time. Although a conclusive picture has not been drawn yet, the current understanding suggests that long GRBs tend to avoid massive galaxies [113] and they prefer the bright, inner regions of their hosts [114, 115]. Therefore, long GRBs do not appear to be an unbiased tracer of the cosmic star formation history. Nevertheless, the SFR derived with optical estimators, such as the $H\alpha$, $H\beta$, or NII emission lines, may be affected by dust absorption.

As previously highlighted, radio and sub-millimeter observations play a crucial role in assessing the obscured star formation [71] and exploring interactions between the host galaxy and the surrounding intergalactic medium [116, 117]. In fact, by comparing the SFR derived from the radio with the value provided by optical estimators, it is possible to determine the amount of dust within the host galaxy [71, 118]. The first study of the radio properties of GRB host galaxies comprising 20 sources revealed that the SFR inferred from the radio measurements exceeds the values determined from the optical by an order of magnitude, suggesting significant dust obscuration [118]. Conversely, the observations of five GRB host galaxies at $z < 0.5$ showed a radio-derived SFR $< 15 M_{\odot} \text{yr}^{-1}$, in agreement with the values inferred from optical estimators, suggesting little dust obscuration [119]. The latter result was subsequently confirmed using a complete sample of 30 hosts with $z < 1$, including those from the The Optically Unbiased Gamma-Ray Burst Host (TOUGH) sample [110] and sources compiled from the literature [120]. The authors found that at least $\sim 63\%$ of GRB hosts have SFR $< 100 M_{\odot} \text{yr}^{-1}$ and at most $\sim 8\%$ can have SFR $> 500 M_{\odot} \text{yr}^{-1}$. Surprisingly, $\gtrsim 88\%$ of the $z \lesssim 1$ GRB hosts have UV dust attenuation $A_{UV} < 6.7 \text{ mag}$ and $A_V < 3 \text{ mag}$, suggesting that the majority of GRB host galaxies are not heavily obscured by dust.

Other studies tackled this problem [116, 117, 121–125] and, although they generally agree with the hypothesis of little dust obscuration, a conclusive result is still pending due to the dearth of detected sources: among the approximately 87 host galaxies that have been observed in the radio, only 20 have a confirmed detection, corresponding to a $\sim 23\%$ detection rate [126]. As a consequence, important questions regarding whether or not long GRBs are unbiased tracers of the cosmic star formation history, or if they provide insight into a particular formation channel of young massive stars, remain elusive [71, 127].

1.5.2 Supernovae

The association of SN events with many long GRBs is undoubtedly one of the strongest evidence that short and long GRBs hail from different progenitors. The optical emission of GRB is generally dominated by the contribution from the afterglow phase, produced in the interaction between the ejecta and the surrounding environment. In order to detect the signature of a SN, the optical afterglow has to fade rapidly [128]. At present, a SN has been identified in coincidence with many long GRBs, while only a handful of short GRBs have shown a KN

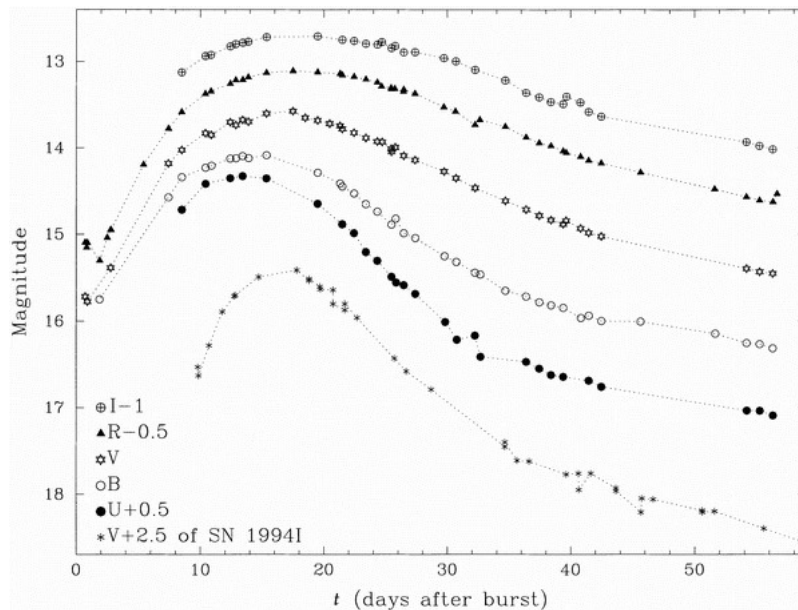


Figure 1.12: Optical light curves of SN1998bw at I , R , V , B , U bands. The flux has been rescaled for the sake of presentation. The light curve of the Type Ic SN 1994I is shown for comparison. Figure taken from [105].

emission, suggesting that the majority of long GRB are produced in the catastrophic explosion of massive, single stars, such as Wolf-Rayet stars [129].

The first discovery of a SN coincident with the position of a GRB occurred for GRB 980425 [105]. The SN, named SN 1998bw, was identified within a spiral arm of the galaxy ESO 184-G82 ($z = 0.00856$) and it was classified as a highly luminous type Ic SN (Fig. 1.12). The optical light curve could be adequately explained by the core collapse of a massive carbon-oxygen star, occurring concurrently with the GRB. Notably, the radio emission of SN 1998bw exhibited an unusually high luminosity at its peak, with a total radio flux reaching approximately 50 mJy [130]. The interpretation of the radio light curve required the propagation of a shock through the supernova ejecta at relativistic velocities [130]. Consequently, the radio emission provided the first observational evidence that GRB are associated with the production of relativistic shock waves. Given that GRB 980425 had a total γ -ray energy of approximately 9×10^{47} erg, it fell within the low luminosity tail of the GRB energy distribution [105]. Therefore, the detection of a SN in coincidence with such a low luminous GRB was primarily due to its close proximity.

In the same year, a SN linked to GRB 980326 was reported. The overall optical light curve consisted of a transient coincident with the afterglow phase of a GRB, succeeded by a rebrightening associated to a SN. The observed emission could only be explained by assuming a cosmological origin of the GRB [128]. Subsequently, further connections between SNe and GRBs were established, including SN that closely resembled SN1998bw (e.g., GRB 030329; [131, 132]) as well as those significantly different from it (e.g., GRB 011121; [133]). The diversity in SN characteristics suggests that SNe associated with GRBs may exhibit a wide range of properties. Since then, numerous additional associations have been confirmed, further supporting the collapsar origin for long GRBs.

1.5.3 Very High Energy emission

The primary emission mechanism responsible for GRB radiation is widely believed to be synchrotron radiation. In fact, the broadband afterglow phase has been successfully explained from the high energies to X-rays, optical and NIR, down to radio with the synchrotron emission of electrons. Over the last two decades, it has been suggested that emission at very high

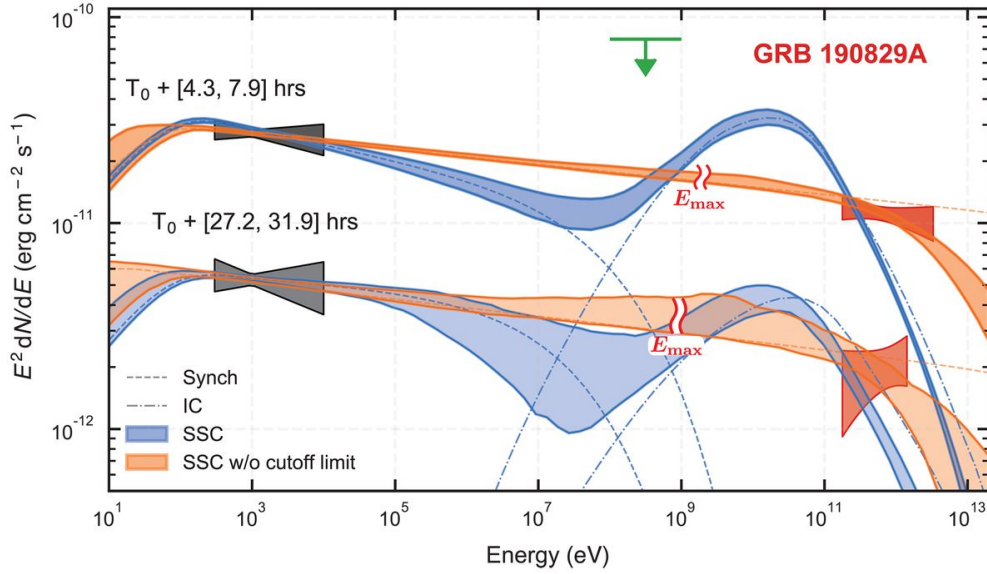


Figure 1.13: Spectra of GRB 190829A including *Swift*-XRT (black region), *Fermi*-LAT (green arrow) and H.E.S.S. (red region) data for two nights of observations. The shaded areas represent the best fit predicted by a model dominated by the synchrotron emission (light blue) and a standard SSC model (orange). The synchrotron component within the SSC model is indicated by dashed curves, while the dashed-dotted curves show the inverse Compton component. Figure taken from [64].

energies (VHE, >100 GeV) may result from inverse Compton scattering [134]. The detection of an additional VHE component in the afterglow spectrum presents an invaluable piece of information essential for discerning the physical conditions of the emitting region and/or the shocked, accelerated particles.

The first print of inverse Compton scattering of synchrotron photons was reported in GRB 090902B and GRB 090926A, in which the GeV light curve flattened and the LAT spectrum hardened, a feature expected when the peak of the inverse Compton scattering of synchrotron photons reaches the band of LAT (20 - 300 GeV; [135]). In 2013, the identification of a 95 GeV photon at 244s post-burst in GRB 130427A further challenged the hypothesis of a single mechanism governing the emission observed from GeV to radio frequencies [135]. Until 2018, the quest for a VHE component yielded only upper limits (see, e.g., [136]). As mentioned before, the detection of VHE emission is hindered primarily by pair production caused by the interaction between VHE photons and the extra-galactic background light. This interaction leads to a substantial attenuation of the VHE photons with increasing distance. At $z \sim 2$, the Universe becomes opaque to VHE photons.

Finally, in 2019 the MAGIC telescopes detected photons ranging between 300 GeV and 1 TeV in GRB 190114C [59], from approximately 50s to 10^3 s post-burst. The observed emission, consistent with being generated during the afterglow phase, could not be accurately modelled with a single component emitting synchrotron radiation. This discovery opened a new era of VHE studies on GRBs. In the same year, the H.E.S.S. collaboration reported the detection of VHE emission between 100 and 400 GeV from the afterglow of GRB 180720B, ten hours after the end of the prompt emission phase [60]. Subsequently, three more GRBs were detected at VHE with high significance. GRB 190829A exhibited emission between 180 GeV and 3.3 TeV from 4 to 56 hr post-burst [64]. GRB 201216C was detected after about 57s post-burst by the MAGIC telescopes [62]. Lastly, the outstanding GRB 221009A was detected within 3000s post-burst by the Large High Altitude Air Shower Observatory (LHAASO) between 200 GeV and 7 TeV [63].

The most natural interpretation for the VHE emission is the synchrotron self-Compton (SSC) process. This occurs when synchrotron photons are Compton up-scattered by a factor γ_e^2 , where γ_e is the Lorentz factor of the electrons, by the same population of electrons that emit them. Other potential explanations include standard synchrotron emission and external inverse Compton (EIC). A single component dominated by synchrotron radiation can account for the VHE emission if either the forward shock has a high bulk Lorentz factor, of the order of 100, hours post-burst, which is in contrast with the standard hydrodynamic predictions, or an unconventional distribution of accelerated electrons [64]. For GRB 190829A, the VHE emission detected by the H.E.S.S. telescopes was first interpreted as synchrotron emission (Fig. 1.13; [64]). However, multi-wavelength follow-up studies agreed on an SSC emission origin [137–139]. Lastly, if the accelerated electrons encounter a photon field external to the jet, these seed photons can be up-scattered through inverse Compton. This process, known as EIC, is expected to occur in the presence of late time accretion events [140], a cocoon [141] or a KN, in the case of a short GRB [28]. As previously mentioned, multi-wavelength follow-up campaigns represent a fundamental asset in discriminating between the proposed emission mechanisms.

Chapter 2

The standard model for GRBs

In this chapter, I present the standard model generally employed to explain the observed emission of GRBs. It is thought that GRBs are produced in the dissipation of kinetic energy through internal processes due to shocks. A thorough description of the standard model for GRBs is beyond the goal of this Thesis, hence I provide a summary of the physical configuration and the emission mechanisms. For detailed information, interested readers are encouraged to refer to [22, 23, 142–144]. First, I present the argument for which we know that GRBs are ultra-relativistic sources in Section 2.1. In Section 2.2, I derive useful formulas for the synchrotron emission of a population of relativistic electrons. These formulas will be used in Section 2.4 and 2.5 to explain the prompt and afterglow model, respectively. I present the three reference frames involved in the model, together with the relations between quantities as viewed by different observers in Section 2.3. Lastly, in Section 2.6 I briefly discuss well-known deviations from the simplified picture exposed in this chapter. Throughout the chapter, I used the notation Q_x to indicate a quantity Q in units of 10^x .

2.1 Compactness problem

Regardless of the nature of the sources that produce GRBs, from a simple argument it is clear that GRB are produced by the dissipation of kinetic energy of an ultra-relativistic fireball. The variability observed in the prompt γ -ray emission has a typical timescale of $\delta t = 1 - 100$ ms and 10 ms - 1 s for short and long GRBs, respectively. To ensure causal connection, the linear scale of the emitting region must be of the order of $R \simeq c\delta t \simeq 10^7 - 10^8$ cm, where c is the speed of light. Given a burst with a luminosity distance d_L from the observer and an observed flux F , the photon density inside the fireball will be

$$n_\gamma \simeq \frac{3E_{iso}}{\epsilon 4\pi R^3} \simeq \frac{3d_L^2 F \delta t}{\epsilon c^3 \delta t^3} \simeq \frac{3d_L^2 F}{\epsilon c^3 \delta t^2}$$

where ϵ is the characteristic energy of the photons, approximately 1 MeV. At these energies, the main interaction is photon - photon annihilation, for which the optical depth is

$$\tau_{\gamma\gamma} = \xi \sigma_T n_\gamma R \simeq 10^{15}$$

where σ_T is the Thomson cross section, ξ is the probability that a photon interacts with another photon whose energy is sufficient for pair creation. With such a high pair opacity, the spectrum of GRBs should display a sharp cut-off at high energies, which is in contrast with the observed high energy emission.

The aforementioned paradox is solved if one assumes that the fireball is expanding at relativistic speed towards the observer. That being the case, two corrections must be included

[22]. First, the energy ϵ of the photon in the fireball rest frame decreases by a Γ factor, where Γ is the bulk Lorentz factor of the ejecta. This means that the energy threshold for pair annihilation increases by Γ^2 , namely the energy ϵ_{rel} a photon needs to annihilate another photon of energy ϵ_1 is $\epsilon_{rel} = \Gamma^2 \epsilon$. Second, the size of the source becomes $R_{rel} = \Gamma^2 c \delta t = \Gamma^2 R$ (see, e.g., [23]). Assuming that the photon distribution N follows a power law of the type $N \propto \epsilon^{-\beta}$, the optical depth in the relativistic case becomes

$$\tau_{\gamma\gamma,rel} = \xi \sigma_T n_{rel} R_{rel} = \xi \sigma_T \frac{3d_L^2 F}{\epsilon_{rel} c R^2 \Gamma^4} R \Gamma^2 \propto \xi \sigma_T \frac{3d_L^2 \epsilon_{rel}^{-\beta}}{c^2 \delta t \Gamma^2} \propto \xi \sigma_T \frac{3d_L^2 \epsilon^{-\beta} \Gamma^{-2\beta-2}}{c^2 \delta t}$$

where I used the fact that $F/\epsilon_{rel} \propto N \propto \epsilon_{rel}^{-\beta} = (\epsilon \Gamma^2)^{-\beta}$. It follows that $\tau_{\gamma\gamma,rel} \propto \tau_{\gamma\gamma} \Gamma^{-2\beta-2}$ and with $\Gamma \simeq 100$, the fireball becomes optically thin to photon - photon annihilation. Therefore, GRBs must be ultra-relativistic.

2.2 Synchrotron emission

Observations of both prompt and afterglow broadband emission reveal a non-thermal spectrum, which can be explained with synchrotron emission from a population of electrons that have been accelerated up to relativistic energies. The latter radiative mechanism was extensively explored in the last five decades, hence the interested reader can refer to, e.g., [145–147] for detailed information. In this section I provide a general overview to derive the main relations required in GRB models.

Let's start with the motion of an electron with mass m_e and electromagnetic charge e in a magnetic field B . If the electron is moving with a relativistic velocity β and Lorentz factor $\gamma = 1/\sqrt{1-\beta^2}$, the total emitted radiation P' will be [145]

$$P' = \frac{2e^4 B'^2 \gamma^2 \beta^2 \sin^2 \alpha}{3m_e c^3} \quad (2.1)$$

where α is the angle between the velocity of the particle and the magnetic field lines, known as pitch angle. I will use a single quote mark when referring to quantities as measured in the comoving frame. The frequency of the rotation of the electron around the magnetic field lines is

$$\omega_B = \frac{eB'}{m_e \gamma c} \quad (2.2)$$

While the distribution of the emitted radiation is isotropic in the comoving frame, an external observer sees a pulse of radiation with a length smaller than the rotation frequency, which is $2\pi/\omega_B$, due to the relativistic beaming effect. Therefore, the spectrum will extend over a frequency range larger than $\omega_B/2\pi$.

In order to compute the spectrum of the synchrotron emission of a population of electrons as viewed in the observer's reference frame, one needs to derive the emitted power per unit frequency $P'(\omega)$ first. From [145] one can write

$$P'(\omega) = \frac{dW'}{dt' d\nu'} = C_1 F\left(\frac{\omega}{\omega_{crit}}\right) \quad (2.3)$$

where C_1 is a constant, $F\left(\frac{\omega}{\omega_{crit}}\right)$ is a function that is not known *a priori* and ω_{crit} is the critical angular frequency [145, 146], defined as

$$\omega_{crit} \equiv \frac{3}{2} \gamma^3 \omega_B \sin \alpha = \frac{3\gamma^2 e B' \sin \alpha}{2m_e c} \quad (2.4)$$

By introducing the variable $x = \omega/\omega_{crit} = \nu/\nu_{crit}$, the total emitted power can be written as

$$P' = \int_0^\infty P'(\omega)d\omega = C_1 \int_0^\infty F\left(\frac{\omega}{\omega_{crit}}\right)d\omega = \omega_{crit}C_1 \int_0^\infty F(x)dx \quad (2.5)$$

Inserting eq. (2.1) and (2.4) into eq. (2.5), it is possible to derive the constant C_1 :

$$C_1 = \frac{4 e^3 B' \beta^2 \sin \alpha}{9 m_e c^2} \frac{1}{\int_0^\infty F(x)dx} \quad (2.6)$$

Since the factor $\int_0^\infty F(x)dx$ is a normalisation factor of a function that is not known, we can set it to be

$$\int_0^\infty F(x)dx = \frac{8\pi}{9\sqrt{3}} \quad (2.7)$$

This arbitrary choice is motivated by the requirement that the total energy loss (integrated over the frequency) of a charge particle in a magnetic field is [146]:

$$-\frac{dE}{dt} = 2\sigma_T c U_{mag} \beta^2 \gamma^2 \sin^2 \alpha \quad (2.8)$$

where $U_{mag} = B'^2/8\pi$ is the energy density of the magnetic field. Therefore, the radiated power per electron per unit frequency is

$$P'(\omega) = C_1 F\left(\frac{\omega}{\omega_{crit}}\right) = \frac{\sqrt{3} e^3 B' \sin \alpha}{2\pi m_e c^2} F\left(\frac{\omega}{\omega_{crit}}\right) = \frac{1}{2\pi} P'(\nu) \quad (2.9)$$

The next step is to integrate over a distribution of pitch angles. To do so, I assume an isotropic distribution of angles, as the magnetic field lines can be considered sufficiently tangled that there is no preferred orientation for the velocity vector. Therefore, the isotropic distribution of pitch angles takes the form

$$f(\alpha) = \frac{1}{2} \sin \alpha \quad (2.10)$$

and the isotropic radiated power per electron per unit frequency becomes [142]

$$P'_{ISO} = \frac{\sqrt{3} e^3 B'}{2m_e c^2} F_{ISO}(x) \quad (2.11)$$

where the isotropic synchrotron function is

$$F_{ISO} = 2 \int_0^{\frac{\pi}{2}} f(\alpha) \sin \alpha F(x) d\alpha = 2 \int_0^{\frac{\pi}{2}} \frac{1}{2} \sin^2 \alpha F(x) d\alpha \quad (2.12)$$

where the factor 2 comes from the fact that the integral is symmetric, and therefore it can be computed in the first quadrant. Lastly, P'_{ISO} needs to be integrated over a distribution of electron energies, as every electron in the shell will have a different Lorentz factor γ_e and hence a different critical frequency. From standard acceleration processes in shocks, we expect the distribution to follow a power law between two extreme values γ_p and γ_t :

$$N_\gamma = \frac{N_0}{\gamma_p} \left(\frac{\gamma_e}{\gamma_p}\right)^{-q} \quad \text{with} \quad \gamma_p \leq \gamma_e \leq \gamma_t \quad (2.13)$$

where N_0 is a normalisation factor. If the electrons are adiabatic, q is the usual electron distribution index p , γ_p is the injection energy γ_i and γ_t is the cooling energy γ_c . Conversely, if the electrons are radiative, i.e. they efficiently cool in a timescale much shorter than the

remnant age [143], $q = 2$, $\gamma_p = \gamma_c$ and $\gamma_t = \gamma_i$. Imposing that the total probability of having an electron with energy between γ_p and γ_t is one, we get the normalisation N_0 :

$$N_0 = \frac{q - 1}{1 - \left(\frac{\gamma_t}{\gamma_p}\right)^{1-q}} \quad (2.14)$$

and therefore the average radiated power per unit frequency per unit electron becomes [142]

$$P'_{PL}(x) = \frac{\sqrt{3}e^3 B'}{m_e c^2} F_{PL}(x) \quad \text{erg/cm}^2/\text{s}/\text{Hz}/e^{-1} \quad (2.15)$$

where

$$F_{PL}(x) = \int_{\gamma_p}^{\gamma_t} F_{ISO} \frac{N_0}{\gamma_p} \left(\frac{\gamma_e}{\gamma_p}\right)^{-q} d\gamma_e \quad (2.16)$$

The total emitted power per unit frequency can be derived by multiplying the average power of a single electron provided in eq. (2.15) by the total number of accelerated electrons N_e . However, as it will be clear in Section 2.4 and 2.5, I will focus on the maximum flux density, which gives the normalisation for the spectrum as viewed by an external observer. To derive this quantity, I shall consider the maximum of the average radiated power. The maximum of eq. (2.15), located at x_p , can be written as [142]:

$$P'_{\nu_p} = -\frac{dE'}{dt'd\nu'} = \phi \frac{\sqrt{3}e^3 B'}{m_e c^2} \quad (2.17)$$

where $\phi = F_{PL}(x_p)$. In order to obtain the maximum flux density in the observer's frame, which is going to be used as a normalisation factor for the light curves and spectra in Sections 2.4 and 2.5, many ingredients must be considered. First, the flux density is defined as

$$F = -\frac{dE}{dt dA d\nu d\Omega} \quad (2.18)$$

where $dA = 4\pi d_L^2$ is the unit surface that receives the radiation. While the quantity dE/dt is a Lorentz invariant, $d\nu = \Gamma d\nu'/(1+z)$ and $d\Omega \simeq d\Omega'/\Gamma^2$ [145]. Therefore, the maximum flux density in the observer's rest frame will be:

$$F_{\nu_p} = \frac{N_e P_{\nu_p}}{4\pi d_L^2 d\Omega} = \frac{\sqrt{3}\phi e^3 B'}{4\pi d_L^2 m_e c^2} N_e \Gamma(1+z) \quad (2.19)$$

2.3 Three reference frames

Since GRBs are ultra-relativistic, even in the simplest model for their emission three reference frames must be considered: the central engine, the moving shell ejected from the engine and the observer. The physical quantities as viewed in the reference frames are different and they are related through Lorentz transformations. Throughout the section, I will denote quantities in the comoving frame with a single quote mark, while quantities as viewed by the central engine and the observer will be marked with the subscript *eng* and *obs*, respectively.

If two photons are emitted from a shell with a width $\Delta R \lll R$ at a distance R from the central engine, the time interval between the emission of the two photons is $\Delta t'_e = t'_{2,e} - t'_{1,e}$ in the comoving rest frame. However, as the shell is expanding, for non-comoving reference frames, i.e. the central engine and the observer, the two photons are emitted at different locations. In order to link the same quantity as viewed in the three reference frames, I must consider just as many ingredients: the causal connection, the propagation of the photons and the cosmological redshift.

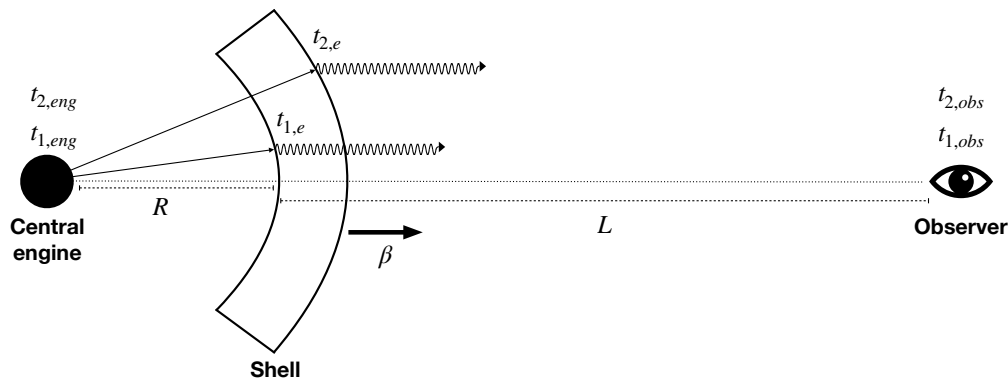


Figure 2.1: Schematic representation of the three reference frames: the central engine, the shell ejected by the central engine, the observer. The shell is expanding with relativistic velocity β . Detailed explanation of the figure is provided within the text.

First, the shell is in causal connection with the central engine, hence the observed time interval between the emission of two photons as measured in the central engine reference frame $\Delta t_e = t_{2,e} - t_{1,e}$ is not equal to the actual time interval between the two signals in the same reference frame, $\Delta t_{eng} = t_{2,eng} - t_{1,eng}$. In Figure 2.1 a schematic representation of the physical configuration is provided. The relation between the two times can be derived:

$$\begin{cases} t_{1,eng} = t_{1,e} - R/c \\ t_{2,eng} = t_{2,e} - R/c - \beta \Delta t_e \end{cases} \quad (2.20)$$

where β is the speed of the shell in units of speed of light c . Combining the equations in the system (2.20) one gets:

$$\Delta t_{eng} = t_{2,eng} - t_{1,eng} = t_{2,e} - t_{1,e} - \beta \Delta t_e = (1 - \beta) \Delta t_e \quad (2.21)$$

If $\beta \lesssim 1$, as it is expected for GRBs, then $1 - \beta \simeq 1/(2\Gamma^2)$ and therefore

$$\Delta t_{eng} = \frac{\Delta t_e}{2\Gamma^2} \quad (2.22)$$

Concerning the propagation of photons, let's consider that two photons are emitted at different angles with respect to the straight line connecting the observer with the central engine, i.e. the line of sight. In the observer's frame, the time interval between the detection of the two photons $\Delta t_{obs} = t_{2,obs} - t_{1,obs}$ is clearly different from the time interval between the emission of the two photons by the shell $\Delta t_e = t_{2,e} - t_{1,e}$ (always observed in the observer's reference frame). Following the argument presented before, one can derive the relation between Δt_{obs} and Δt_e :

$$\begin{cases} t_{1,obs} = t_{1,e} + L/c \\ t_{2,obs} = t_{2,e} + L/c - \beta \cos \theta \Delta t_e \end{cases} \quad (2.23)$$

where θ is the angle at which the photon is emitted, with respect to the line of sight of the observer, and L is the distance between the shell and the observer (see Figure 2.1). Combining the equations, it follows that:

$$\Delta t_{obs} = t_{2,obs} - t_{1,obs} = (1 - \beta \cos \theta) \Delta t_e \quad (2.24)$$

Since the path δr travelled by the shell in a time δt in the observer's frame is $\delta r = \beta c \delta t$, then:

$$R = \frac{\beta c \Delta t_{obs}}{1 - \beta \cos \theta} \simeq 2\Gamma^2 c \Delta t_{obs} \quad (2.25)$$

where I used the standard approximation $\beta \lesssim 1$ and $\theta \ll 1$. It is worth noting that, since c is finite, photons received by the observer at a particular time t are not radiated simultaneously, but come from a distorted ellipsoid which is determined by the integral

$$t = \int \frac{1 - \beta \cos \theta}{\beta c} dr = \text{const} \quad (2.26)$$

The third reference frame is the comoving frame of the expanding shell. Times in this frame can be derived from the reference frame of the central engine by simply introducing the Lorentz transformation

$$\Delta t' = \frac{\Delta t_{eng}}{\Gamma} \quad (2.27)$$

The last ingredient that must be considered is the redshift, which is needed to link the central engine to the observer's frame. From the expansion of the Universe it is known that

$$\frac{\delta t_0}{\delta t_1} = \frac{a(t_0)}{a(t_1)} = 1 + z \quad (2.28)$$

where δt are the time intervals as measured at a given cosmic time t , $a(t)$ is the scale factor, t_0 is the cosmological time when the photon is observed, i.e. in the observer's frame, and t_1 is the cosmological time when the photon is emitted, i.e. in the reference frame of the central engine. By combining eq. (2.28) with eq. (2.21) and (2.24), it is possible to derive the relation between the observer and the central engine, with the caveat that Δt_e in eq. (2.21) is different from Δt_e in eq. (2.24), as they are measured in different cosmological times:

$$\begin{cases} \Delta t_{obs} = (1 - \beta \cos \theta) \Delta t_e(t_0) \\ \Delta t_{eng} = (1 - \beta) \Delta t_e(t_1) \end{cases} \quad (2.29)$$

which leads to

$$\Delta t_{obs} = \left(\frac{1 - \beta \cos \theta}{1 - \beta} \right) (1 + z) \Delta t_{eng} \quad (2.30)$$

If $\theta \ll 1$ then $\Delta t_{obs} \approx \Delta t_{eng}(1 + z)$, and therefore the central engine and the observer measure the same quantities, except for a factor $(1 + z)$.

2.4 Prompt emission

2.4.1 Dynamics

It is thought that the prompt emission hails from the dissipation of kinetic energy through internal processes, such as the collision between two shells of ejected material. In the standard prescription, a central engine, which can be a stellar-mass black hole or a highly magnetised neutron star, launches multiple shells in two opposite directions. When a faster shell catches up with a slower one, inner shocks arise. The electrons are accelerated at the shock front up to

relativistic energies. The prompt emission observed in γ -rays is due to synchrotron emission of these particles that are cooling down after being accelerated.

Nevertheless, for the sake of the explanation, I start with a single shell of material ejected by the central engine. For the moment, I am not considering the redshift of the source, as this has a small impact on the final result. This means that the quantities as viewed by the observer and the central engine are the same (Section 2.3). In the first stage, the shell is accelerated by radiation pressure. The acceleration ends when all the internal energy is converted into kinetic energy. The expansion of the shell is considered adiabatic, as only a little portion of energy is converted into electromagnetic radiation. If the expansion is adiabatic, two conservation laws can be used. First, the total luminosity $L = 4\pi R^2 F$ can be written as

$$L = 4\pi R^2 cn\epsilon = \Gamma^2 4\pi R^2 cT'^4 \sigma_B \quad (2.31)$$

where n is the number density of electrons, ϵ is the average internal energy per electron, T' is the temperature of the shell and σ_B is the Stefan - Boltzmann constant. In eq. (2.31), I used the fact that $n = n'\Gamma$, $\epsilon = \Gamma mc^2$ and $n'mc^2 = \sigma_B T'^4$ for the Stefan - Boltzmann law.

Second, for an adiabatic expansion the following law holds:

$$T'V'^{\frac{1}{3}} = \text{const} \quad (2.32)$$

As $V' \propto R^3$ [144], the equation becomes

$$T'R = \text{const} \quad (2.33)$$

Combining eq. (2.31) with eq. (2.33) one gets

$$\begin{cases} \left(\frac{\Gamma}{\Gamma_0}\right)^2 \left(\frac{R}{R_0}\right)^2 \left(\frac{T}{T_0}\right)^4 = 1 \\ \left(\frac{T}{T_0}\right) \left(\frac{R}{R_0}\right) = 1 \end{cases} \quad (2.34)$$

where the subscript 0 is used to refer to values at the initial time. Note that, whatever the factor required to convert the temperature from the comoving to the observer's frame is, the same factor is cancelled out in the ratio. Therefore:

$$\begin{cases} T = T_0 \frac{R_0}{R} \\ \Gamma = \Gamma_0 \frac{R}{R_0} \end{cases} \quad (2.35)$$

When all the internal energy is converted into kinetic energy, the acceleration stops. The time at which this happens is usually referred to as the saturation point. At the saturation point, the bulk Lorentz factor and the saturation radius are

$$\begin{cases} \Gamma_s = \frac{E}{Mc^2} \\ R_s = R_0 \Gamma_s \end{cases} \quad (2.36)$$

where E and M are the total energy and mass of the shell, respectively. After the saturation point, the outflow is expanding at a constant speed, i.e. $\Gamma \approx \text{const}$, while its temperature is decreasing as $T \propto R^{-\frac{2}{3}}$ [144]. The latter phase of the evolution is called coasting phase. During the coasting phase, the shell becomes transparent to electromagnetic radiation. The differential optical depth is a Lorentz invariant, hence I consider here the quantities in the comoving frame, i.e. $d\tau = \alpha' ds'$, where α' and ds' are the absorption coefficient and the differential length of the path travelled by a photon. From eq. (2.24) and eq. (2.27) one gets $dR'_{obs} = \Gamma(1 - \beta \cos \theta) dR_{obs}$. The absorption coefficient can be written as $\alpha' = n'_p \sigma_T$, where n'_p is the number density of

protons in the shell. I am considering protons instead of electrons as the total mass (see below) is dominated by protons, while the number of protons and electrons is considered to be the same in this simplified picture. Therefore, the differential optical depth in a relativistic expansion takes the form:

$$d\tau = n'_p \sigma_T \Gamma (1 - \beta \cos \theta) dR \quad (2.37)$$

Taking $\theta \simeq 0$, the differential optical depth becomes $d\tau \simeq n'_p \sigma_T dR / (2\Gamma)$. The radius R_{ph} at which the shell becomes optically thin can be derived by integrating the latter equation and imposing $\tau = 1$:

$$R_{ph} \simeq \frac{L\sigma_t}{8\pi m_p c^3 \Gamma^3} \approx 7 \times 10^{12} L_{52} \Gamma_{s,2}^{-3} \text{cm} \quad (2.38)$$

from which it is clear that the point at which the electromagnetic radiation can escape is far away from the central engine.

So far, I have considered a single, expanding shell. If a second shell of material is ejected after a time δt with velocity larger than that of the first shell, i.e. $\beta_2 > \beta_1$, they collide, producing internal shocks that can dissipate the kinetic energy of the outflow. Let's consider two shells with $\Gamma_1, \Gamma_2, m_1, m_2, \beta_1, \beta_2$, where $\Gamma_2 > \Gamma_1$:

$$\begin{cases} R_1(t) = c\beta_1 t \\ R_2(t) = c\beta_2(t - \delta t) \end{cases} \quad (2.39)$$

If both Γ_1 and Γ_2 are constant, the time t_{is} and the radius R_{is} at which the shells collide are given by:

$$t_{is} = \frac{\beta_2 \delta t}{\beta_2 - \beta_1} \quad (2.40)$$

and

$$R_{is} = R_1(t_{is}) = \frac{c\beta_1\beta_2}{\beta_2 - \beta_1} \delta t \quad (2.41)$$

After the collision, the two shells move as one. A simple, rough estimate of R_{is} can be obtained in the case of $\Gamma_2 \gg \Gamma_1 \gg 1$. With the latter approximation, $t_{is} \approx 2\Gamma_1^2 \delta t$, hence R_{is} takes the form

$$R_{is} \simeq 2\Gamma^2 c \delta t \approx 6 \times 10^{13} \delta t_{-1} \Gamma_{1,2}^2 \quad (2.42)$$

Lastly, the final bulk Lorentz factor Γ of the merged shell can be derived from the conservation of energy and momentum in a perfectly inelastic collision:

$$\begin{cases} \Gamma_1 m_1 c^2 + \Gamma_2 m_2 c^2 = \Gamma m c^2 + \epsilon \\ \Gamma_1 m_1 c \beta_1 + \Gamma_2 m_2 c \beta_2 = \Gamma m c \beta + \frac{\epsilon}{c} \end{cases} \quad (2.43)$$

where ϵ is the internal energy converted in the collision. By solving eq. (2.43), Γ can be found:

$$\Gamma = \frac{\Gamma_1 m_1 + \Gamma_2 m_2}{\sqrt{m_1^2 + m_2^2 + 2m_1 m_2 \Gamma_{rel}}} \quad (2.44)$$

where $\Gamma_{rel} \equiv \Gamma_1 \Gamma_2 (1 - \beta_1 \beta_2)$.

2.4.2 Spectrum

So far, I have presented the global dynamics of the GRB outflow. In order to derive the expected spectrum, the microphysics of the blast wave must be taken into account. While the solutions for a blast wave linking thermodynamics and microphysics of the shock were presented in [148], here I start from a population of accelerated electrons, ignoring the details of the acceleration processes. Therefore, the expected distribution of electrons will follow a power law, as in eq. (2.13). First, I assume that the prompt emission is produced in a fast cooling regime, i.e. the electrons efficiently cool in a timescale much shorter than the remnant age [143]. This translates into $\gamma_c < \gamma_i$, where γ_c is the Lorentz factor above which electrons cool rapidly and γ_i is the minimum Lorentz factor at which electrons are injected. This assumption is motivated by observational evidence. The continuity equation of electrons in the energy space is:

$$\frac{\partial N_\gamma}{\partial t} + \frac{\partial(\dot{\gamma}N_\gamma)}{\partial \gamma} = Q(\gamma, t) \quad (2.45)$$

where N_γ is the number of electrons, γ is the Lorentz factor of one electron, Q is the source function above γ_i . In a steady-state system approximation and in the fast cooling regime, eq. (2.45) becomes:

$$\dot{\gamma}N_\gamma = \text{const} \quad (2.46)$$

and therefore:

$$N_\gamma \propto \dot{\gamma}^{-1} \propto \gamma^{-2} \quad (2.47)$$

where I used the fact that $\dot{\gamma} \propto \gamma^2$, from eq. (2.1). However, the most energetic electrons will cool rapidly, emitting energy at their characteristic synchrotron frequency, which is $\propto \gamma^2$. For a population $N_\gamma \propto \gamma^{-p}$ of electrons injected at $\gamma > \gamma_i$, each “generation” of electrons has a different cooling frequency. The integrated distribution will be the superposition of these generation of electrons. Therefore, the distribution of electrons is [143]:

$$N_\gamma \propto \begin{cases} \gamma^{-2} & (\gamma_c < \gamma < \gamma_i) \\ \gamma^{-p-1} & (\gamma > \gamma_i) \end{cases} \quad (2.48)$$

where γ_c is the Lorentz factor above which the oldest generation of electrons cools.

In order to get the spectrum, namely the flux density as a function of frequency, I consider that $dF_\nu \propto \nu dN_\nu$. Moreover, it is clear from eq. (2.4) that $\nu_{crit} \propto \gamma^2$. Thus, γ_c and γ_i can be related to some break frequencies ν_c and ν_i , respectively. By combining these ingredients with eq. (2.48), it is possible to derive the spectrum of the prompt emission as a combination of several power laws that join together at the break frequencies ν_c and ν_i :

$$F_\nu = F_{\nu_c} \begin{cases} \left(\frac{\nu}{\nu_c}\right)^{\frac{1}{3}} & (\nu < \nu_c) \\ \left(\frac{\nu}{\nu_c}\right)^{-\frac{1}{2}} & (\nu_c < \nu < \nu_i) \\ \left(\frac{\nu}{\nu_i}\right)^{-\frac{p}{2}} \left(\frac{\nu_i}{\nu_c}\right)^{-\frac{1}{2}} & (\nu > \nu_i) \end{cases} \quad (2.49)$$

where F_{ν_c} is given by eq. (2.19) for $\nu_p = \nu_c$. The slope of the power law for $\nu < \nu_c$ is given by the emission from a single electron at low energies. In Figure 2.2 a representation of the electron distribution (left panel) and the expected spectrum (right panel) is shown. Therefore, the slope of the low energy tail in the photon spectrum, which is given by F_ν/ν , is predicted to be $\tilde{\alpha} = -3/2$ in the fast cooling regime. However, as mentioned in Section 1.2, GRBs exhibit a low-energy slope $\tilde{\alpha} \sim -1$ on average [31, 33]. More recently, a second break occurring at roughly

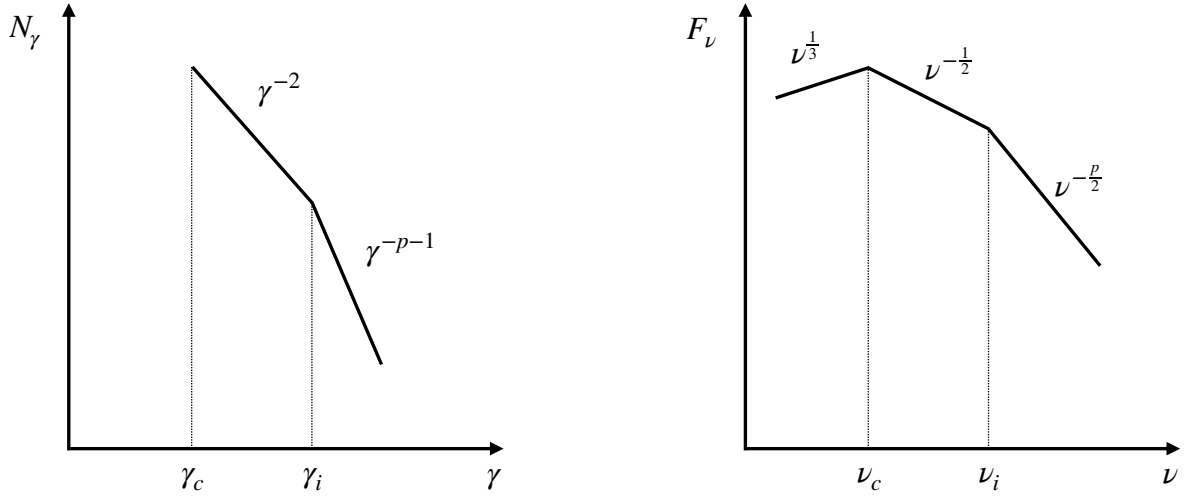


Figure 2.2: Schematic representation of the distribution of electrons in the fast cooling regime (left panel) and the flux density as a function of frequency expected from the same population (right panel).

3 - 20 keV has been successfully incorporated into the fitting model of many GRB SEDs [34–37]. The inclusion of a second break provides a solution that is consistent with the synchrotron expectations.

2.5 Afterglow model

In the simplified model presented so far, two (or multiple) shells interact to produce the observed γ -ray prompt emission. After the interaction through internal shock, the two shells “merge” and expand as one. The outflow sweeps up material from the low-density environment surrounding the burst. As the ejecta are still ultra-relativistic, their interaction with the circumburst medium produces both a forward shock (FS), which propagates outwards throughout the environment, and a reverse shock (RS), which propagates backwards and compresses the ejecta. Electrons at each shock front are accelerated up to relativistic energies and produce a broadband emission through synchrotron cooling. The superposition of the FS and the RS emitting components gives birth to the afterglow phase of the GRB, which can be detected from VHE down to optical, NIR and radio.

2.5.1 Dynamics of the forward shock

In order to derive a simplified version of the FS dynamics, many approximations are required. In this section I follow the standard prescription from [142, 143]. First, I assume that the energy carried out by the emitted photons is a negligible fraction of the total energy of the ejecta. Therefore, the expansion can be considered adiabatic. The total energy of the outflow E , which encompasses the internal E_{int} and the rest mass E_{rest} energies, can be written as

$$E = E_{int} + E_{rest} = E_{int} + Mc^2 = \Gamma Mc^2 \quad (2.50)$$

where Γ is the bulk Lorentz factor, M is the total mass of the ejecta. The ratio between the two energy components becomes $E_{int}/E_{rest} = \Gamma - 1$, if the internal energy is assumed to be negligible compared with the rest mass energy. As the outflow expands, it sweeps up material from the surrounding medium. From the conservation laws of energy and momentum

$$\begin{cases} M\Gamma_0 + m(r) = (M + m(r))\Gamma + \Gamma \frac{E_{diss}}{c^2} \\ \sqrt{\Gamma_0^2 - 1}M = \sqrt{\Gamma^2 - 1} \left[(M + m(r)) + \frac{E_{diss}}{c^2} \right] \end{cases} \quad (2.51)$$

where $m(r)$ is the swept mass as a function of the distance r , Γ_0 is the initial bulk Lorentz factor, Γ is the Lorentz factor at the distance r , E_{diss} is the energy dissipated in the process. Eq. (2.51) leads to [143]

$$\begin{cases} M\Gamma_0 + m(r) = M\Gamma + \Gamma^2 m(r) \\ \frac{E_{diss}}{c^2} = (\Gamma^2 - 1)m(r) \end{cases} \quad (2.52)$$

An extended formula for the swept-up material can be derived if one assumes that the external medium particle density depends only on the radius:

$$\begin{cases} dm(r) = 4\pi r^2 n(r) m_p dr \\ n(r) = Ar^{-s} \end{cases} \quad (2.53)$$

where m_p is the proton mass, which is the dominating contribution in the total mass of surrounding medium, A is a constant, s is the coefficient of the density profile, which is usually taken to be either $s = 0$ or $s = 2$ if the surrounding environment has a homogeneous or a wind-like density profile, respectively. Therefore, the swept-up mass at the radius r takes the form [143]:

$$m(r) = \frac{4\pi}{3-s} m_p n(r) r^3 \quad (2.54)$$

Starting from eq. (2.52) and eq. (2.54), the bulk Lorentz factor Γ as a function of r can be derived [143]:

$$\Gamma(r) = \frac{1}{2} \left\{ \sqrt{4 \left(\frac{r}{r_0} \right)^{3-s} + \left[\frac{2}{\Gamma_0} \left(\frac{r}{r_0} \right)^{3-s} \right]^2 + 1} - 1 \right\} \Gamma_0 \left(\frac{r}{r_0} \right)^{s-3} \quad (2.55)$$

where r_0 is the deceleration radius, defined as the distance at which the swept-up material equals M/Γ_0 [143]:

$$r_0 = \left(\frac{3-s}{4\pi} \frac{E}{Am_p c^2 \Gamma_0^2} \right)^{\frac{1}{3-s}} \quad (2.56)$$

The constant A in eq. (2.53) can be calculated in the homogeneous and in the wind-like external density profile [143]:

$$A = \begin{cases} n_\star & \text{cm}^{-3} \\ 3 \times 10^{35} A_\star & \text{cm}^{-3} \end{cases} \quad (2.57)$$

where n_\star is the constant particle density in the homogeneous case, A_\star is a scale factor computed for the wind of a Wolf-Rayet star [143, 149]. Inserting eq. (2.57) into eq. (2.56), the expression for r_0 becomes [143]

$$r_0 \simeq \begin{cases} 1.3 \times 10^{17} E_{53}^{\frac{1}{3}} \Gamma_{0,2}^{-\frac{2}{3}} n_\star^{-\frac{1}{3}} \text{ cm} & (s=0) \\ 4 \times 10^{15} E_{53} \Gamma_{0,2}^{-2} A_\star^{-1} \text{ cm} & (s=2) \end{cases} \quad (2.58)$$

where I used the fact that $L \simeq \Gamma M c^3 / R$. The relation between quantities, with a particular emphasis on times, has been presented in Section 2.3. To derive the evolution of the spectrum of the afterglow phase, the time dependence of the main physical quantities must be inferred. First, from eq. (2.22) and eq. (2.55) one can obtain the expression for the earliest time T a photon emitted by the outflow at time t can reach the observer:

$$T = \frac{r_0}{2(4-s)c\Gamma_0^2} \left[\left(\frac{r}{r_0} \right)^{4-s} + 3 - s \right] \quad (2.59)$$

The latter expression, when combined with eq. (2.55) and eq. (2.58), leads to [143]

$$(s=0) \quad \begin{cases} r_{18}(T) \propto E_{53}^{\frac{1}{4}} n^{-\frac{1}{4}} T_d^{\frac{1}{4}} \text{ cm} \\ \Gamma(T) \propto E_{53}^{-\frac{1}{8}} n^{\frac{1}{8}} T_d^{-\frac{3}{8}} \\ n(T) = n_* \text{ cm}^{-3} \end{cases} \quad (2.60)$$

$$(s=2) \quad \begin{cases} r_{18}(T) \propto E_{53}^{\frac{1}{2}} A_*^{-\frac{1}{2}} T_d^{\frac{1}{2}} \text{ cm} \\ \Gamma(T) \propto E_{53}^{\frac{1}{4}} A_*^{-\frac{1}{4}} T_d^{-\frac{1}{4}} \\ n(T) \propto E_{53}^{-1} A_*^2 T_d^{-1} \text{ cm}^{-3} \end{cases} \quad (2.61)$$

where T_d is the time in the observer's frame expressed in units of days post-burst. Note that, as seen in Section 2.3, I am not including the redshift. Even if the latter has a negligible effect on the final result, a precise derivation of eq. (2.60) and (2.61) should take into account the fact that the central engine and the observer refer to different reference frames. Furthermore, it is worth noticing that eq. (2.60) returns the well-known result that $\Gamma(T) \propto T^{-3/8}$ for an external medium with a homogeneous density profile.

2.5.2 Break Frequencies

While for the prompt emission the time evolution of the break frequencies is much longer than the emission itself, and therefore they can be considered as fixed in time, the afterglow is long lasting. This means that the afterglow phase of GRBs is one of the few physical phenomena in which not only a full synchrotron spectrum can be observed over many orders of magnitudes in frequency, but also that the spectrum is changing in time. Therefore, for the afterglow spectra the time evolution of the main break frequencies must be derived. Following the same argument exposed in Section 2.4, I assume that the distribution of injected electrons can be described by a single power law $N_\gamma \propto \gamma^{-p}$ for $\gamma > \gamma_i$, as observational evidence strongly supports the idea that the afterglow emission is in a slow cooling regime. The minimum Lorentz factor of the injected electron is:

$$\gamma_i = \frac{m_p}{m_e} \epsilon_e (\Gamma - 1) \quad (2.62)$$

where ϵ_e is the energy retained by the electrons. The synchrotron emission from such a distribution of electrons peaks at the observer frame frequency [142, 146]:

$$\nu_i = \frac{3x_p}{4\pi} \frac{e}{m_e c} \gamma_i^2 B' \Gamma \quad (2.63)$$

where x_p is a factor calculated in [142] that corrects eq. (2.4). Once again, I am not including the redshift, which would have a small effect. The magnetic field behind the shock front is [143]:

$$\frac{B'^2}{8\pi} = 4\epsilon_B m_p c^2 n(r) (\Gamma - 1) \left(\Gamma + \frac{3}{4} \right) \quad (2.64)$$

where ϵ_B is the energy retained by the magnetic field. From eq. (2.60), (2.61) and (2.62), it is possible to rewrite eq. (2.63) as [143]:

$$\nu_{i,13} \propto \begin{cases} \epsilon_{e,-1}^2 \epsilon_{B,-2} E_{53}^{\frac{1}{2}} T_d^{-\frac{3}{2}} \text{ Hz} & (s=0) \\ \epsilon_{e,-1}^2 \epsilon_{B,-2}^{\frac{1}{2}} E_{53}^{\frac{1}{2}} T_d^{-\frac{3}{2}} \text{ Hz} & (s=2) \end{cases} \quad (2.65)$$

Therefore, the maximum flux of the afterglow emission is usually found in the optical within the first few days after the initial GRB.

The relativistic electrons cool radiatively through synchrotron emission and inverse-Compton scattering of the synchrotron photons on a timescale [143]:

$$t'_{rad} = \frac{6\pi}{Y+1} \frac{m_e c}{\sigma_T} \frac{1}{\gamma B'^2} \quad (2.66)$$

in the comoving frame, where Y is the Compton parameter and the Klein-Nishina effect was neglected. The age t' of the outflow can be approximately calculated as [143]:

$$t' \simeq \frac{1}{c} \int_0^r \frac{dr}{\Gamma} \simeq \frac{2}{5-s} \frac{r}{\Gamma} \quad (2.67)$$

By equating (2.66) and (2.67), the Lorentz factor of the electrons above which cooling is important takes the form [143]:

$$\gamma_c = \frac{3\pi}{Y+1} (5-s) \frac{m_e c^2 \Gamma}{\sigma_T B'^2 r} \quad (2.68)$$

Using eq. (2.63) and (2.68), the frequency ν_c above which electrons cool efficiently can be derived [143]:

$$\nu_{c,14} \propto \begin{cases} (Y+1)^{-2} \epsilon_{B,-2}^{-\frac{3}{2}} n_0^{-1} E_{53}^{-\frac{1}{2}} T_d^{-\frac{1}{2}} \text{ Hz} & (s=0) \\ (Y+1)^{-2} \epsilon_{B,-2}^{-\frac{3}{2}} A_{\star}^{-2} E_{53}^{\frac{1}{2}} T_d^{\frac{1}{2}} \text{ Hz} & (s=2) \end{cases} \quad (2.69)$$

Therefore, ν_c is usually found in the X-rays and optical. It is worth noticing that, while for a homogeneous density profile ν_c is moving towards lower frequency in time, for a wind-like density profile the cooling frequency is increasing with time.

Lastly, for the afterglow phase another break frequency should be taken into account. In fact, synchrotron emission is accompanied by absorption: photons at low energies interact with the ultra-relativistic electrons that absorb them. In this process, known as synchrotron self-absorption, the electrons gain energy at the expense of the photons. The frequency ν_a below which the outflow is optically thick to this process is called synchrotron self-absorption frequency. The expression for ν_a can be derived from the optical depth. First, the optical depth at a given frequency can be written as [143]:

$$\tau_a(\nu) = \tau_i \left(\frac{\nu}{\nu_i} \right)^{-5/3} \quad (2.70)$$

where τ_i is the optical depth to synchrotron self-absorption at the injection break [143]:

$$\tau_i = \frac{5}{3-s} \frac{enr}{B' \gamma_i^5} \quad (2.71)$$

where e is the electron charge. Imposing that $\tau_a(\nu_a) = 1$ in eq. (2.70), the time evolution of ν_a can be derived [143]:

$$\nu_{a,9} \propto \begin{cases} E_{53}^{\frac{1}{5}} \epsilon_{e,-1}^{-1} \epsilon_{B,-2}^{\frac{1}{5}} n_0^{\frac{3}{5}} \text{ Hz} & (s=0) \\ E_{53}^{-\frac{2}{5}} \epsilon_{e,-1}^{-1} \epsilon_{B,-2}^{\frac{1}{5}} A_{\star}^{\frac{6}{5}} T_d^{-\frac{3}{5}} \text{ Hz} & (s=2) \end{cases} \quad (2.72)$$

Thus, ν_a is usually found in the radio. It is worth noticing that ν_a decreases faster if the outflow is interacting with a wind-like environment rather than a homogeneous external medium.

2.5.3 Spectrum of the forward shock

Observational evidence suggests that the afterglow is in a slow cooling regime. Therefore, the number of accelerated electrons in the afterglow phase can be described with two power laws joined together:

$$N_\gamma \propto \begin{cases} \gamma^{-p} & (\gamma_i < \gamma < \gamma_c) \\ \gamma^{-p-1} & (\gamma > \gamma_c) \end{cases} \quad (2.73)$$

Following the argument seen in Section 2.4, the flux density can be calculated from $dF \propto \nu dN$. From eq. (2.73), one gets that $F_\nu \propto \nu^{-(p-1)/2}$ for $\nu_i < \nu < \nu_c$ and $F_\nu \propto \nu^{-p/2}$ for $\nu > \nu_c$. However, the self-absorption frequency must be considered at low frequencies. While there could be many combinations for the order of ν_a , ν_i and ν_c , GRB afterglows usually show two possible combinations, i.e. $\nu_a < \nu_i < \nu_c$ or $\nu_i < \nu_a < \nu_c$. Here I derive the spectrum for these two scenarios only. A proper derivation, including many more possible scenarios, can be found in [150].

Starting from the radiative transfer equation, in the optically thick regime $F_\nu \propto S_\nu$, where $S_\nu = j_\nu/\alpha_\nu$ is the source function, j_ν and α_ν are the emission and the absorption coefficient, respectively. Considering the scenario with $\nu_i < \nu_a$ first, the emission coefficient j_ν can be written as [146]

$$j_\nu = \int_0^\infty P_\nu N_\gamma d\gamma = \frac{\sqrt{3}}{m_e c^2} e^3 B' \sin \alpha \left(\frac{3eB' \sin \alpha}{4\pi m_e c \nu} \right)^{(p-1)/2} C \int_0^\infty F(x) x^{(p-3)/2} dx \quad (2.74)$$

where x and $F(x)$ were defined in eq. (2.5) and C is a normalisation factor for eq. (2.73). The integral can be solved following [145]. Therefore, the emission coefficient depends on the frequency as $j_\nu \propto \nu^{-(p-1)/2}$.

The expression for the absorption coefficient α_ν was provided by [145]:

$$\alpha_\nu = \frac{c^2(p+2)}{8\pi\nu^2} \int_0^\infty P_\nu \frac{N_\gamma}{\gamma} d\gamma = \frac{c^2(p+2)}{8\pi\nu^2} \frac{\sqrt{3}}{2m_e c^2} e^3 B' \sin \alpha \left(\frac{4\pi m_e c \nu}{3eB' \sin \alpha} \right)^{-p/2} C \int_0^\infty F(x) x^{(p-2)/2} dx \quad (2.75)$$

where I followed the derivation proposed by [146]. Thus, the absorption coefficient depends on the frequency as $\alpha_\nu \propto \nu^{-(p+4)/2}$. Combining eq. (2.74) and (2.75), it follows that $F_\nu \propto \nu^{5/2}$. It is worth noticing that the proportionality index is not equal to the usual 2 obtained with the Rayleigh-Jeans approximation, as this is not a thermal spectrum. In fact, I have implicitly assumed that a particular frequency is preferentially absorbed by those electrons that can emit it, since for each emission process there is a corresponding and related absorption process [146, 147]. This means that the equivalent of a Maxwellian temperature can be associated to each frequency, even if the electrons are not in thermal equilibrium. The final spectrum is the superposition of the contributions from electrons with different ‘‘temperatures’’ [147].

The latter argument does not hold in the other scenario I am considering, i.e. $\nu_a < \nu_i$. In this case, it can be assumed that most of the photons are emitted and absorbed by electrons with Lorentz factor γ_i . Thus, it is not possible to associate a different temperatures to different frequencies. Since there is only one temperature, i.e. the one corresponding to ν_i , the expected slope will follow the Rayleigh-Jeans approximation. In fact, while the emission coefficient is the same as in eq. (2.74), the absorption coefficient becomes:

$$\alpha_\nu = \frac{c^2(p+2)}{8\pi\nu^2} \int_0^\infty P_\nu \frac{N_\gamma}{\gamma} d\gamma \propto \frac{j_\nu}{\nu^2} \quad (2.76)$$

where I used the fact that γ can be considered as constant, hence it can be taken outside the integral, which in turn takes the same form of eq. (2.74). Combining eq. (2.74) with (2.76), it is found that $F_\nu \propto \nu^2$, as expected from the Rayleigh-Jeans approximation.

The final spectrum of the afterglow is the combination of the aforementioned power laws, joined together at the break frequencies [150]:

$$F_\nu = F_{\nu_a} \begin{cases} \left(\frac{\nu_i}{\nu_a}\right)^{\frac{5}{2}} \left(\frac{\nu}{\nu_i}\right)^2 & (\nu < \nu_i) \\ \left(\frac{\nu}{\nu_a}\right)^{\frac{5}{2}} & (\nu_i < \nu < \nu_a) \\ \left(\frac{\nu}{\nu_a}\right)^{-\frac{(p-1)}{2}} & (\nu_a < \nu < \nu_c) \\ \left(\frac{\nu_c}{\nu_a}\right)^{-\frac{(p-1)}{2}} \left(\frac{\nu}{\nu_c}\right)^{-\frac{p}{2}} & (\nu > \nu_c) \end{cases} \quad (2.77)$$

for $\nu_i < \nu_a$, while in the $\nu_a < \nu_i$ scenario it can be described by the following equation:

$$F_\nu = F_{\nu_i} \begin{cases} \left(\frac{\nu_a}{\nu_i}\right)^{\frac{1}{3}} \left(\frac{\nu}{\nu_a}\right)^2 & (\nu < \nu_a) \\ \left(\frac{\nu}{\nu_i}\right)^{\frac{1}{3}} & (\nu_a < \nu < \nu_i) \\ \left(\frac{\nu}{\nu_i}\right)^{-\frac{(p-1)}{2}} & (\nu_i < \nu < \nu_c) \\ \left(\frac{\nu_c}{\nu_i}\right)^{-\frac{(p-1)}{2}} \left(\frac{\nu}{\nu_c}\right)^{-\frac{p}{2}} & (\nu > \nu_c) \end{cases} \quad (2.78)$$

where the normalisation constants are given by eq. (2.19). A schematic representation of the two scenarios considered is provided in Figure 2.3. The model provided here will be used in Chapter 4 to explain the observed multi-wavelength afterglow emission of GRB 201015A. In fact, fitting the GRB spectrum at different epochs with the latter equations directly constrain the microphysics of the blast wave, providing a direct insight into the physics of the ejecta. Nevertheless, even this simple model encounters challenges due to degeneracies within the multi-dimensional parameter space. Consequently, recent years have seen a concerted effort to seek complementary information. Possible solutions to partially mitigate this degeneracy have emerged from polarisation measurements, GWs and VLBI studies.

2.5.4 Reverse shock

The FS model has been successful in reproducing almost all GRB afterglows, proving that this phase hails from the interaction between the GRB ejecta and its surrounding environment. However, deviations from a single emission component were observed in recent years [56, 58, 151–160]: another component at earlier times seems necessary to explain the emission in the optical and in the radio. This emission component is thought to arise from the RS, i.e. a shock that propagates back into the ejecta. In fact, both a FS and a RS are expected when a relativistic outflow interacts with its ambient medium [161, 162].

Considering a shell that expands into the circum-burst environment, the system can be divided into four regions during the RS crossing:

- the unshocked surrounding medium (region 1, hereafter);

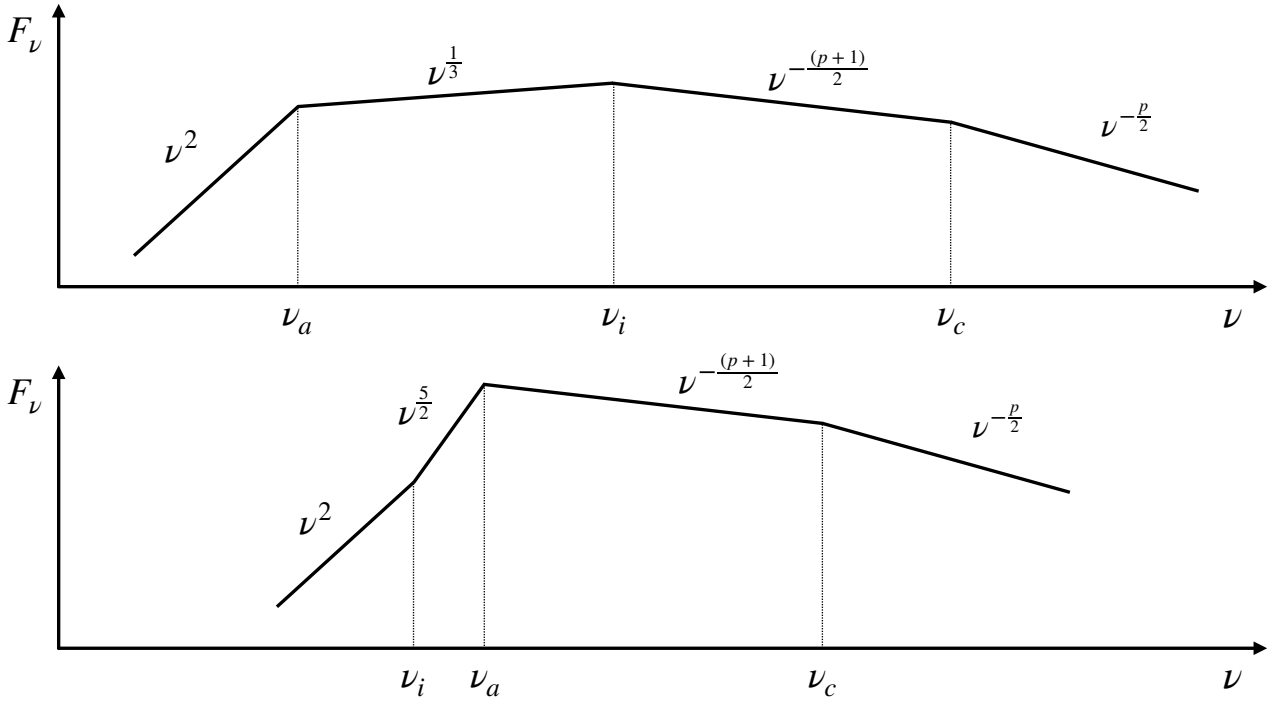


Figure 2.3: Expected spectra for the afterglow emission according to the order of the three break frequencies. Figure inspired by [150].

- the surrounding medium shocked by the FS (region 2);
- the GRB ejecta shocked by the RS (region 3);
- the unshocked GRB ejecta (region 4).

Synchrotron emission is expected from regions 2 and 3. Here I focus on region 3, which evolves through two phases, i.e. before and after the RS crossing time, T_{cross} . The overall dynamics can be studied by introducing the ξ_{rs} parameter, defined as [163]:

$$\xi_{rs} \equiv \left(\frac{l}{\Delta R} \right)^{1/2} \Gamma_0^{-(4-s)/(3-s)} \quad (2.79)$$

where ΔR is the width of the shell, Γ_0 is the initial bulk Lorentz factor, s is defined in eq. (2.53) and

$$l = \left(\frac{(3-s)E}{4\pi A m_p c^2} \right)^{1/(3-s)} \quad (2.80)$$

is the Sedov length, namely the distance at which the rest mass energy of the circum-burst swept-up material equals the initial energy E of the shell. The coefficient A was defined in eq. (2.53). If $\xi_{rs} \ll 1$, or, equivalently, if the density of the shell is low, the RS is ultra-relativistic and it considerably decelerates the shell. The latter is called “thick” shell regime. Conversely, if the shell is dense enough, i.e. $\xi_{rs} \gg 1$, the RS is Newtonian and it is too weak to slow down the shell [164]. The latter case is called “thin” shell regime. Between these two limits, if $\xi_{rs} \simeq 1$, the RS can be considered semi-relativistic [163].

Combining the density profile of the surrounding medium with the density of the shell (thin or thick), it is possible to derive the dynamics of the latter for different regimes and hence the light curves. First, the electrons in the shell are accelerated at the shock front. Therefore, eq. (2.73) can be used for the number distribution, as the emission is expected to be in a slow cooling regime. Similarly to what I showed before for the prompt and the FS emission, the light

curves and the spectra can be derived once the evolution of the break frequency is determined. In the following derivation I do not include the self-absorption frequency. Therefore, I consider only the minimum injection frequency ν_i and the cooling frequency ν_c , with $\nu_i < \nu_c$. Moreover, I focus the discussion in the case of a homogeneous surrounding medium, i.e. $s = 0$. The following expressions hold for the thick shell regime [164]:

$$\begin{cases} \nu_i \propto t^0 \\ \nu_c \propto t^{-1} \end{cases} \quad (t < T_{cross}) \quad (2.81)$$

$$\begin{cases} \nu_i \propto t^{-73/48} \\ \nu_c \propto t^{1/16} \end{cases} \quad (t > T_{cross}) \quad (2.82)$$

and hence the flux density dependence on time takes the form:

$$F_\nu(t < T_{cross}) \propto \begin{cases} t^{1/2} & (\nu_i < \nu < \nu_c) \\ t^0 & (\nu > \nu_c) \end{cases} \quad (2.83)$$

$$F_\nu(t > T_{cross}) \propto \begin{cases} t^{-17/36} & (\nu < \nu_i) \\ t^{-(73p+21)/96} & (\nu_i < \nu < \nu_{cut}) \\ 0 & (\nu > \nu_{cut}) \end{cases} \quad (2.84)$$

where ν_{cut} is proportional to ν_c and refers to the frequency above which no further electron is accelerated and therefore no further emission is expected [164].

Conversely, for the thin shell regime [164]:

$$\begin{cases} \nu_i \propto t^6 \\ \nu_c \propto t^{-2} \end{cases} \quad (t < T_{cross}) \quad (2.85)$$

$$\begin{cases} \nu_i \propto t^{-54/35} \\ \nu_c \propto t^{4/35} \end{cases} \quad (t > T_{cross}) \quad (2.86)$$

and the flux density follows the subsequent time evolution, approximately:

$$F_\nu(t < T_{cross}) \propto \begin{cases} t^{(6p-3)/2} & (\nu < \nu_c) \\ t^{(6p-5)/2} & (\nu > \nu_c) \end{cases} \quad (2.87)$$

$$F_\nu(t > T_{cross}) \propto \begin{cases} t^{-16/35} & (\nu < \nu_i) \\ t^{-(27p+7)/35} & (\nu_i < \nu < \nu_{cut}) \\ 0 & (\nu > \nu_{cut}) \end{cases} \quad (2.88)$$

A detailed derivation is beyond the scope of this Thesis. For a complete analysis of the RS emission, interested readers are referred to, e.g., [161–164] and reference therein. Additionally, the scenario involving a wind-like density profile in the circum-burst environment was extensively addressed by [165]. It is worth mentioning that, regardless of the density profile of the surrounding medium, a key observational feature emerges: the RS is expected to dominate at early times (~ 1 day) in the optical and in the radio, producing an initial peak observed in the light curves at these wavelengths. When optical and radio observations are available at both early and late times, it is possible to model the afterglow light curves as a composite of RS emission, which dominates at $\lesssim 1$ day, and FS emission, which dominates after ~ 1 day post-burst. While FS emission offers valuable insights into the microphysics of the shocked material surrounding the burst (region 2), the RS provides a direct window into the physical conditions within the GRB ejecta (region 3). Therefore, the two components are complementary to fully probe the GRB dynamics.

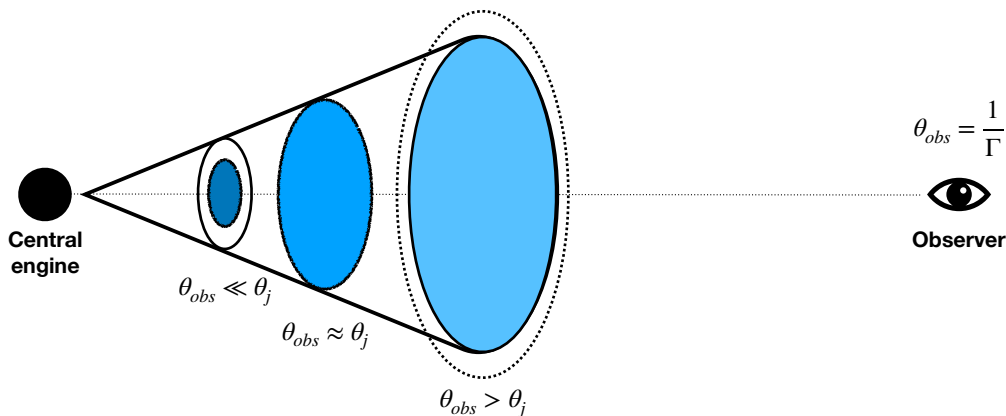


Figure 2.4: Schematic representation of the jet break. From left to right: first, $\theta_{obs} = 1/\Gamma \ll \theta_j$; as the bulk Lorentz factor decreases, the observable portion of the cone θ_{obs} increases, until $\theta_{obs} \approx \theta_j$ and the observer can see the whole jet; lastly, when the GRB ejecta have decelerated enough, $\theta_{obs} = 1/\Gamma > \theta_j$. Figure inspired by G. Ghirlanda.

2.6 Non-spherical ejecta

Hitherto, I have implicitly assumed that the emitting region is spherically symmetric. Even if this assumption is useful as a first order approximation, observational evidence suggests that GRBs are highly collimated. In fact, as explained in Section 1.3, for some bursts a steepening in the light curve is observed from the X-rays down to the radio. The latter can be naturally explained by assuming a jetted emission. Figure 2.4 shows the geometrical configuration that leads to a jet break. Considering the case in which the GRB is a top-hat jet, i.e. a cone with sharp edges, pointing directly towards the observer, the latter can only see a fraction $\theta_{obs} = 1/\Gamma < \theta_j$ of the outflow due to the relativistic beaming (blue region on the left in Figure 2.4), with θ_j being half the GRB jet opening angle. As the ejected matter expands, its bulk Lorentz factor Γ decreases, reducing the relativistic effects and increasing the observable portion of the outflow. The decrease in flux is partially compensated with the increase of θ_{obs} : although the observer records less flux per unit angle, the overall angle accessible to them increases. When $\Gamma = 1/\theta_j$ is reached, the observer sees the entire base of the GRB cone. For $\Gamma < 1/\theta_j$, the observer sees not only the entire outflow but also a portion of the sky which is not contributing to the total flux (area encompassed by the dashed line in Figure 2.4), i.e. they lose flux with respect to the isotropic case. This manifests itself as an achronic, steeper decay in the light curve. If the material is ejected within a uniform cone with opening angle θ_j , the total energy of the GRB becomes $E_\gamma = (1 - \cos \theta_j) E_{iso}$ [23], leading to less extreme values.

Nevertheless, even top-hat jet models present some drawbacks. First, a perfect cone structure seems unrealistic, given that the outflow interacts with the dense medium that surrounds the central engine (pre-merger ejecta for a short GRB; stellar envelope for long GRBs) and with the external low-density environment afterwards, producing different shocks that change the radial and lateral structure of the outflow [166]. Second, a top-hat jet does not predict the observed clustering of $E_\gamma \simeq \theta^2 E_{iso}$ at around 10^{51} erg [167–169]. It was this latter feature in GRBs that led the community to search for a unifying scenario where all jets share a universal structure. Two analytical functions were proposed for the jet structure: a power law with $dE/d\Omega \propto \theta^{-2}$ and a Gaussian with $dE/d\Omega \propto \exp(-(\theta/\theta_c)^2/2)$, where θ_c is half the “core” opening angle of

the jet [166]. The need for structures more sophisticated than a simple cone with sharp edges became clear with GW 170817 / GRB 170817A: a structured jet was the only feasible scenario to explain the shallow evolution of the afterglow light curve at different wavelengths (see, e.g., [96]), the proper motion [101] and the size probed by VLBI images [100]. Even if it is generally very hard to pinpoint signatures of a jet structure in standard GRB observations, this new, exciting field in GRB science can provide unique information about the jet-launching mechanism and the interaction between the jet and the surrounding environment that could not be probed otherwise. For the nearest events, VLBI plays a fundamental role to constrain the jet structure [100, 137].

Chapter 3

Radio Interferometry

3.1 Basic Principles

In contrast to other wavelengths, the energy carried by radio photons is insufficient to induce a photoelectric effect. Consequently, conventional detectors relying on this interaction, such as the Charge Coupled Device (CCD), cannot be used. For this reason, radio astronomy employs antennas to catch the wave nature of light: an antenna is a passive device that converts electromagnetic radiation into electrical currents in conductors. The two main types of antennas are single dishes, typically used for $\nu \gtrsim$ a few hundreds MHz, and dipole antennas, generally employed for $\nu \lesssim$ a few hundreds MHz. Both categories share a common basic functioning principle, which is Fraunhofer's diffraction. In fact, taking a single dish as an example, its surface acts as a narrow circular slit in a diffraction experiment [170].

First, the reciprocity theorem states that an antenna can be treated equivalently either as a receiving device or as a transmitting system [170]. Consequently, the response of a receiving antenna is equal to the emission of a transmitting antenna and the surface of a dish can be considered as narrow slit with aperture D that produces the light and illuminates an observer at a distant point A. For Huygens–Fresnel's principle, every point on a wavefront is itself a source of spherical waves, and the secondary waves emanating from different points interfere. Therefore, each point dx of the surface of the antenna acts like an antenna. Figure 3.1 shows a schematic representation of the one-dimensional configuration considered here. The electric field generated by the aperture element from x to $x+dx$ can be written as $g(x) = A(x)e^{-i(\phi-\omega t)}$, where $A(x)$ is the amplitude of the wave, ϕ is the phase and $\nu = \omega/2\pi = c/\lambda$ is the frequency. From the equations of Fraunhofer's diffraction, the electric field at the observer point A is [170]

$$df = g(x)e^{-i\omega t}dx = g(x)e^{-i2\pi r(x)/\lambda}dx \quad (3.1)$$

where $r(x)$ is the distance between the aperture element at the position x and the observer in A. In order to derive the transmitting (and, therefore, the response) pattern of the antenna, I assume that [170]:

- light rays are parallel, because we are in the far-field approximation. An aperture element in x emits a radiation that travels a distance $r = R + x \sin \theta$ to reach the observer in A (see Figure 3.1);
- the angle θ is small, i.e. $\theta \ll 1$, and therefore $l \equiv \sin \theta \simeq \theta$ and $r \simeq R + xl$

When $\theta \neq 0$, the phase xl/λ varies linearly across the aperture and different parts of the aperture add constructively or destructively to the total electric field $f(l)$. Defining $u = x/\lambda$ and integrating eq. (3.1) over the whole aperture, the total electric field $f(l)$ takes the form

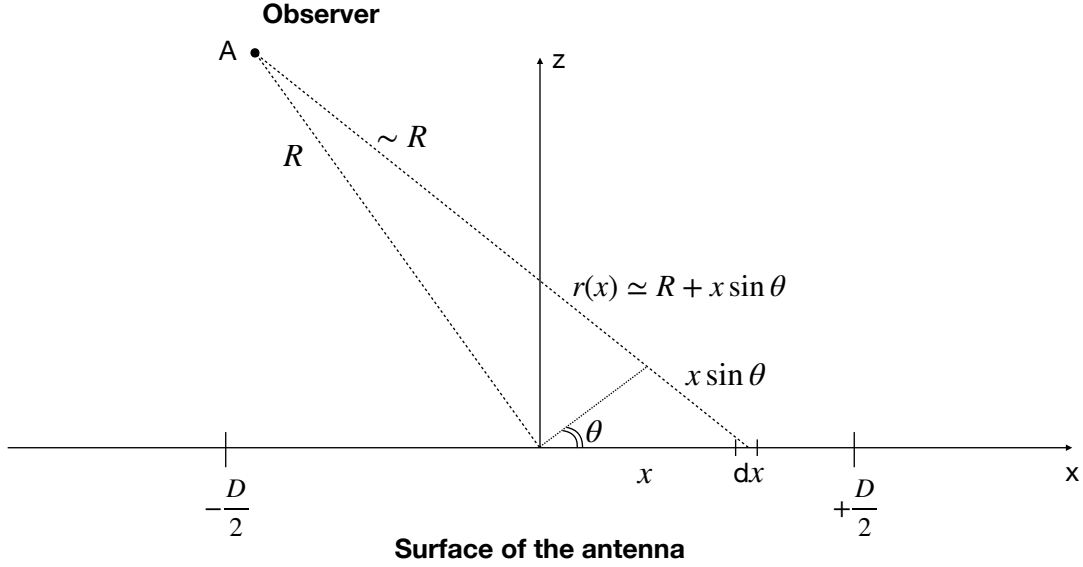


Figure 3.1: Schematic representation of a one-dimensional antenna with length D that is illuminating a distant observer.

[170]:

$$f(l) = \int_{-D/2}^{+D/2} g(u) e^{-i2\pi lu} du = \left(\frac{D}{\lambda}\right) \frac{\sin\left(\frac{\pi l D}{\lambda}\right)}{\frac{\pi l D}{\lambda}} = \frac{D}{\lambda} \operatorname{sinc}\left(\frac{l D}{\lambda}\right) \quad (3.2)$$

Consequently, in the far field approximation the electric field pattern $f(l)$ of an antenna with a diameter D is the Fourier transform of the electric field distribution $g(u)$ generated by the aperture. From the reciprocity theorem, eq. (3.2) gives the response of an antenna illuminated by a point source located at a position A far from the dish. Lastly, according to the Poynting flux theorem, the power pattern of a transmitting antenna is $P(l) \propto f^2(l)$, hence [170]

$$P(l) \approx \left(\frac{D}{\lambda}\right)^2 \operatorname{sinc}^2\left(\frac{\theta D}{\lambda}\right) \quad (3.3)$$

Eq. (3.2) and (3.3) can be generalised to two dimensions. It can be demonstrated that

$$f(l, m) \propto \int_{-D_y/2}^{+D_y/2} \int_{-D_x/2}^{+D_x/2} g(u, v) e^{-i2\pi(lu + mv)} du dv \quad (3.4)$$

where $v \equiv y/\lambda$, x and y are the two dimensions of the aperture. The power pattern of a rectangular aperture with dimension D_x and D_y is [170]:

$$P(l, m) \approx \frac{4\pi D_x D_y}{\lambda^2} \operatorname{sinc}^2\left(\frac{\theta_x D_x}{\lambda}\right) \operatorname{sinc}^2\left(\frac{\theta_y D_y}{\lambda}\right) \quad (3.5)$$

For a circular aperture, the power pattern is the conventional Airy's disc.

The analogue of the power pattern for a receiving antenna is called the point-source response, or beam. The beam is characterised by a main lobe (or primary beam) and some minor lobes. Figure 3.2 shows an example of the beam. The response of the antenna, i.e. the sensitivity, is maximum at the centre of the main lobe, known as phase centre, it goes to zero when the beam

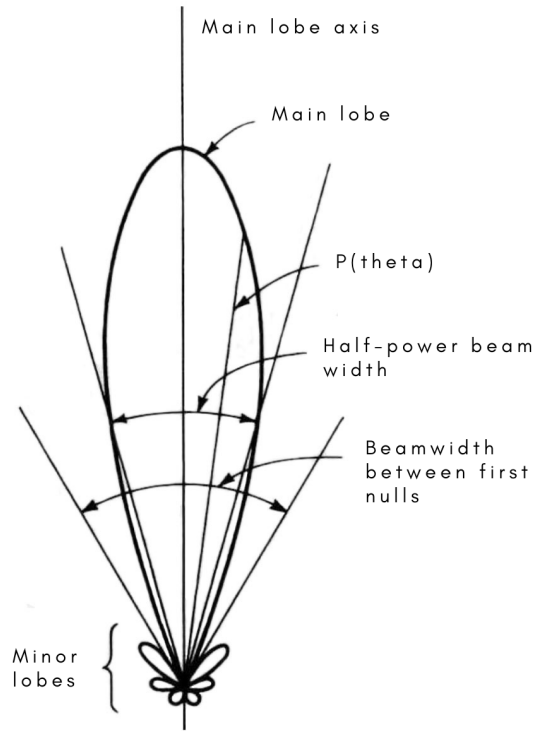


Figure 3.2: Power response of a single dish antenna illuminated by a point-like source, known as primary beam. Credits: D. Darling.

pattern is zero and progressively decreases along the minor lobes. The beam width is generally taken as the full width at half maximum of eq. (3.3) and it can be demonstrated that [170]

$$\theta_{beam} \approx \frac{\lambda}{D} \quad (3.6)$$

The beam width of an antenna represents its angular resolution, which is limited by diffraction. It is clear from eq. (3.6) that larger telescopes have a smaller θ_{beam} and therefore higher resolving power. Nevertheless, since single dishes cannot be arbitrarily large because of engineering and economic reasons, astronomers use more antennas to simulate a larger aperture than that provided by a single dish. The latter technique is called radio interferometry.

The simplest radio interferometer is a pair of radio telescopes whose voltage outputs are correlated, i.e. multiplied and averaged in time. Let's consider two identical dishes separated by the baseline vector \vec{b} of length b that points from antenna 1 to antenna 2, as shown in Figure 3.3. Both dishes point towards the same direction, specified by the unit vector \vec{s} . The angle between \vec{b} and \vec{s} is indicated with θ . Within this geometrical configuration, the wavefront of the radiation coming from a distant source reaches antenna 2 first. After a time τ_g , the same wavefront reaches antenna 1. The time interval τ_g is known as geometric delay [170]:

$$\tau_g = \frac{b \cos \theta}{c} \quad (3.7)$$

In order to derive the correlated response, I assume that the band $\Delta\nu$ of the receiver is quasi-monochromatic, namely $\Delta\nu \ll 2\pi/\tau_g$ centred at a frequency $\nu = \omega/2\pi$. The output voltages of antenna 1 and 2 at the time t are [170]:

$$\begin{cases} V_1 = V \cos[\omega(t - \tau_g)] \\ V_2 = V \cos(\omega t) \end{cases} \quad (3.8)$$

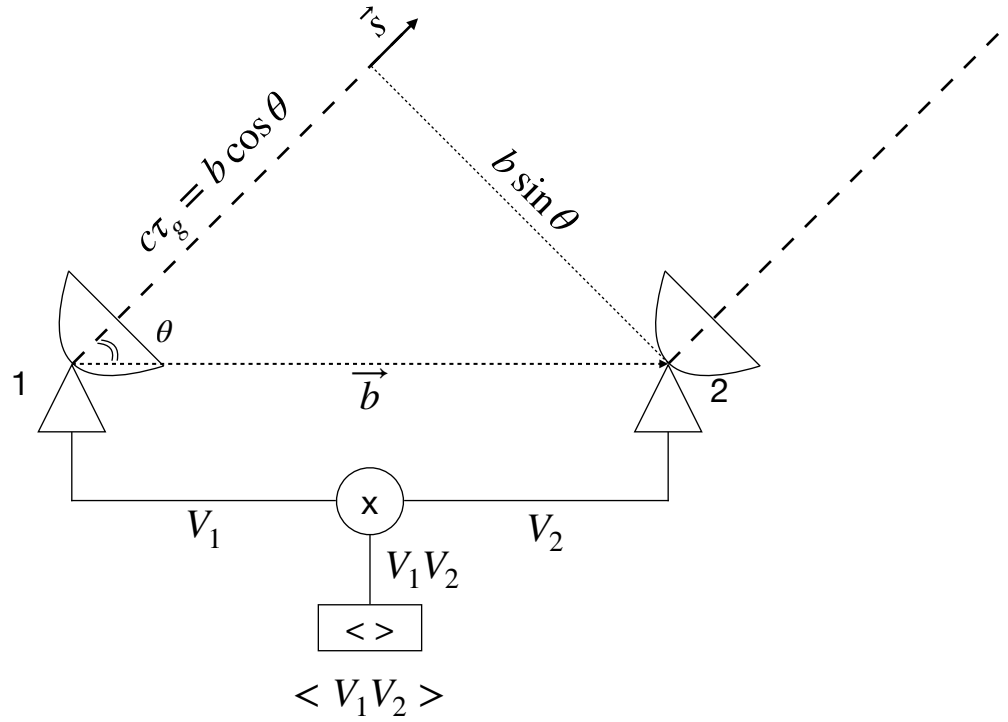


Figure 3.3: Schematic representation of the geometric delay for an interferometer with two identical dishes. The incoming light from a distant source is shown in bold dashed lines.

where V is the amplitude of the voltage. The correlator multiplies V_1 and V_2 to get [170]

$$V_1 V_2 = V^2 \cos[\omega(t - \tau_g)] \cos(\omega t) = \frac{V^2}{2} [\cos(2\omega t - \omega\tau_g) + \cos(\omega\tau_g)] \quad (3.9)$$

where I used Werner's trigonometric formulas, and it takes the time average over a time interval Δt long enough to remove the high frequency term $\cos(2\omega t - \omega\tau_g)$, i.e. $\Delta t \gg (2\omega)^{-1}$. The final output of the correlator is, therefore, [170]

$$R \equiv \langle V_1 V_2 \rangle = \frac{V^2}{2} \cos(\omega\tau_g) \quad (3.10)$$

The output voltage varies sinusoidally with time as the antennas track the source on the sky. In fact, τ_g is not constant due to the rotation of Earth. This sinusoids are called fringes. The phase of the fringes $\phi = 2\pi \cos \theta b / \lambda$ varies with θ .

In order to derive the total power, let's consider the Fourier space. The response of an interferometer is the Fourier transform (FT, hereafter) of the double pulse, i.e. the radiation detected by each antenna, multiplied by the FT of the rectangle function, which represents the response of each antenna as found in eq. (3.2). Figure 3.4 shows the different contributions in the final response of an interferometer, both in space/time domain and in the Fourier space. First, the signal detected by each antenna is a δ function. The FT of a double δ function is a cosine. However, since the surface of the antennas is not infinitely large, from eq. (3.2) the response of each antenna is a sinc function. Consequently, the final response in the Fourier space is a cosine modulated by a sinc function (see Figure 3.4). The total power is [170]:

$$P(\theta) \propto \text{sinc}^2\left(\frac{D}{\lambda} \cos \theta\right) \cos^2\left(2\pi \frac{b}{\lambda} \cos \theta\right) \quad (3.11)$$

From Figure 3.4 and eq. (3.11) it can be noticed that the baseline b determines the cosine, so that the resolution of the interferometer, while the diameter D of the single antenna determines

the primary beam of the interferometer, known as field of view (FOV). The FOV is the angular size from the phase centre to the first zeroes of the response of a single antenna¹.

Figure 3.4 shows the final response of an interferometer made of two identical dishes. The first peak, given by the peak of the cosine function modulated by the sinc function, is called synthesised beam, or dirty beam, and it provides the angular resolution of the interferometer. However, the other side lobes in the modulated cosine function are still significant. If the interferometer observes a point source at the phase centre (i.e. the source position is coincident with the maximum response of each antenna), the final image will consist of a point-like source at the phase centre, surrounded by many other sources which correspond to the response of the side lobes in the modulated cosine function. Figure 3.5 shows the dirty image of a point-like source or, equivalently, the dirty beam of an interferometer with N antennas. Each panel is composed of two figures: on the left the (u, v) -plane is shown (see below for the explanation), while on the right the resulting dirty beam is presented. In order to reduce the impact of the side peaks and, therefore, get a single point-like source in the image, multiple antennas and a longer exposure time are needed. In fact, a multi-element interferometer with N antennas produces $N(N - 1)/2$ unique responses. Each interferometer pair presents its own sinusoid at a frequency proportional to the fringe angular spacing, which is different for each pair. The instantaneous synthesised beam projected on the sky is the arithmetic mean of the individual responses of the two-element interferometers that compose the whole N -element interferometer. As N increases, the synthesised beam rapidly approaches a Gaussian and the secondary peaks are less and less significant. Figure 3.5 shows the effects of increasing N , while Figure 3.6 shows the effects of a longer time exposure for an array with 8 antennas.

It is worth noticing that each baseline is sensitive to emission from objects with angular sizes comparable to the fringe spacing $\Delta\theta \approx \lambda/(b \sin \theta)$. Consequently, longer baselines are sensitive to compact emission, such as point-like sources, and insensitive to extended emission, such as clusters of galaxies, extended jets, etc. Emission from sky regions larger than $\Delta\theta$ are not detected by the longer baselines. Conversely, shorter baselines are primarily sensitive to extended objects. Therefore, a perfect interferometer should ideally have a large number N of rather small (smaller D means larger FOV), well spaced (different baselines b) antennas. The latter is the driving idea behind the SKA and the ngVLA projects.

If a source is extended and it has a sky brightness distribution $I_\nu(\vec{s})$ at the frequency $\nu = \omega/2\pi$, the response $R_c = (V^2/2) \cos(\omega\tau_g)$ is computed by treating the extended source as the collection of independent point sources [170]:

$$R_c = \int I_\nu(\vec{s}) \cos\left(\frac{2\pi\vec{b} \cdot \vec{s}}{\lambda}\right) d\Omega \quad (3.12)$$

where $d\Omega$ is the solid angle covered by the source. Eq. (3.12) gives the cosine correlator output, namely the symmetric part of the source brightness distribution, which can be written as the sum of even (symmetric) and odd (antisymmetric) parts: $I_\nu = I_E + I_O$. The sine correlator output is given by the following expression [170]:

$$R_s = \int I_\nu(\vec{s}) \sin\left(\frac{2\pi\vec{b} \cdot \vec{s}}{\lambda}\right) d\Omega \quad (3.13)$$

The combination of eq. (3.12) and (3.13) gives the complex visibility [170]:

$$\mathcal{V} = R_c - iR_s = Ae^{-i\phi} = \int I_\nu(\vec{s}) e^{-i2\pi\frac{\vec{b} \cdot \vec{s}}{\lambda}} d\Omega \quad (3.14)$$

¹Therefore, for a single antenna the FOV and the angular resolution coincide.

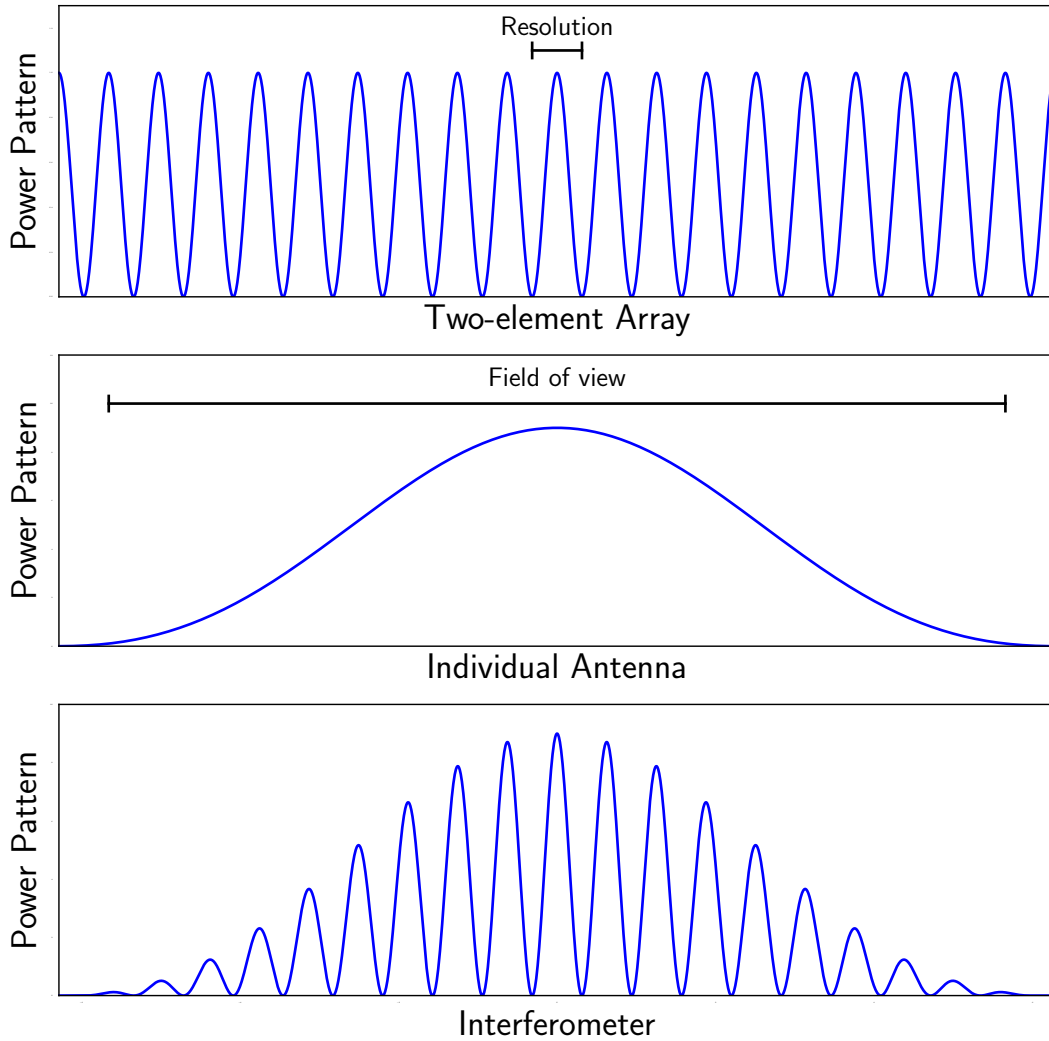


Figure 3.4: Upper panel: power pattern (in arbitrary units) of an array of two infinitely large dishes or, vice versa, the power recorded by two infinitely large dishes illuminated by a point source. The cosine function is the FT of two Dirac δ functions. Middle panel: response of each individual antenna with a diameter D . Lower panel: final power pattern of the interferometer. The response of the two-element array is modulated by the response of each antenna, given the fact that the two dishes have a limited size. The final resolution, given by the baseline, and field of view, determined by the single antenna response, are indicated.

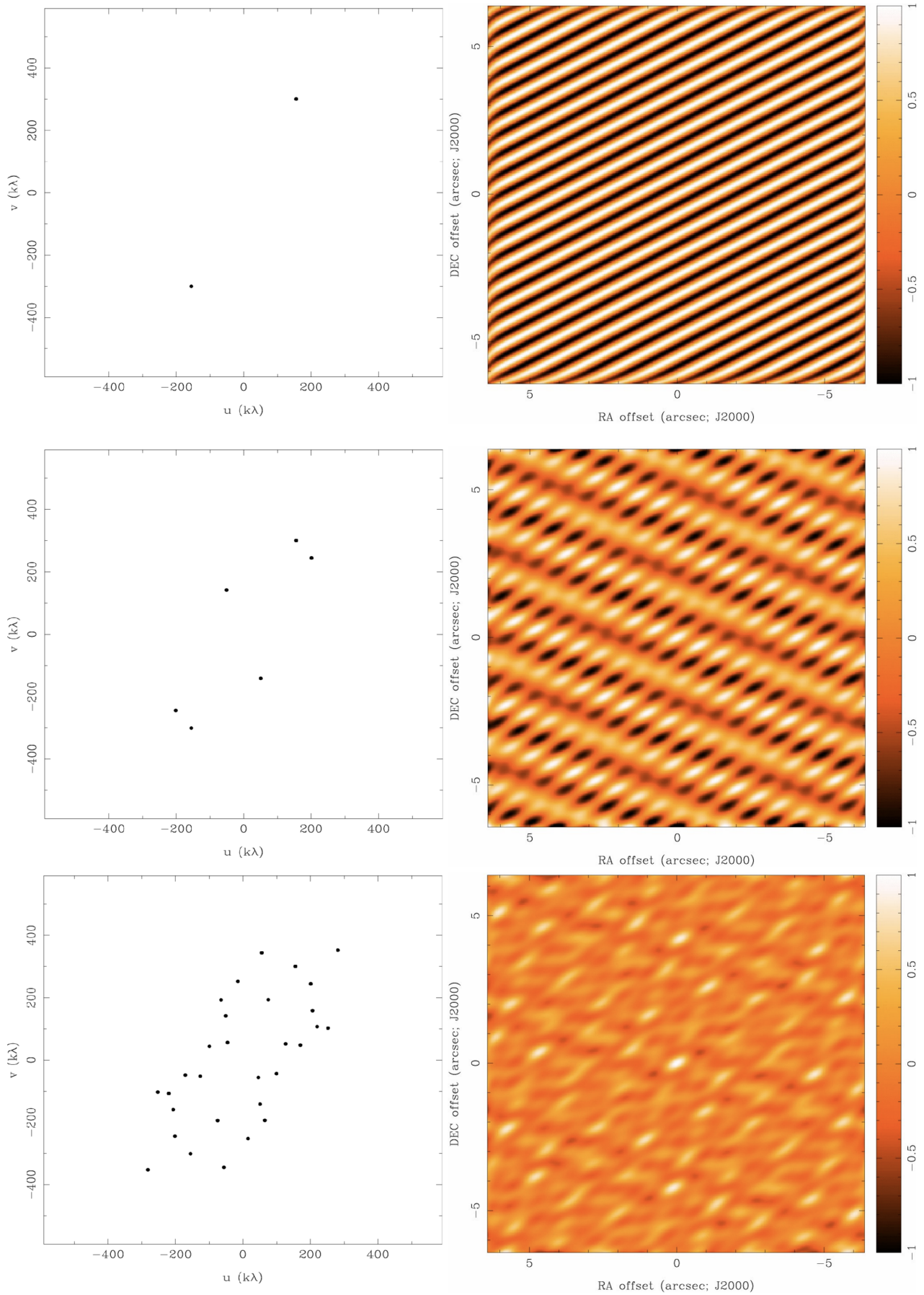


Figure 3.5: (u, v) -plane (left) and dirty beam (right) of an array with 2 (upper panel), 3 (middle panel) and 6 (lower panel) antennas. Credits: D.J. Wilner.

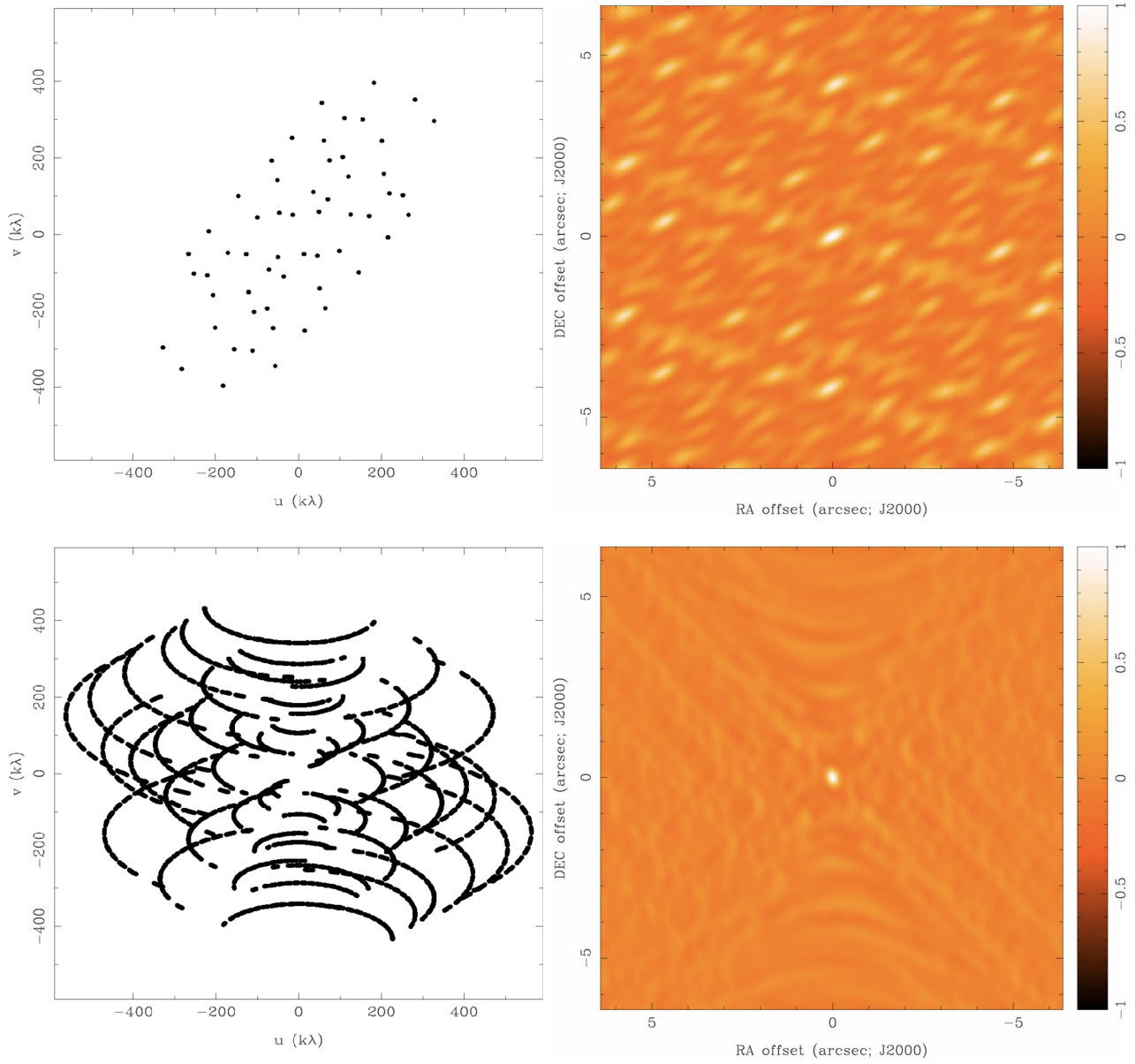


Figure 3.6: Effects of a longer exposure time on the (u, v) -plane (left) and dirty beam (right) of an array with 8 antennas. The upper panel shows the response for a single integration time T_{int} , while the lower panel shows the result for $T_{tot}/T_{int} = 480$. Credits: D.J. Wilner.

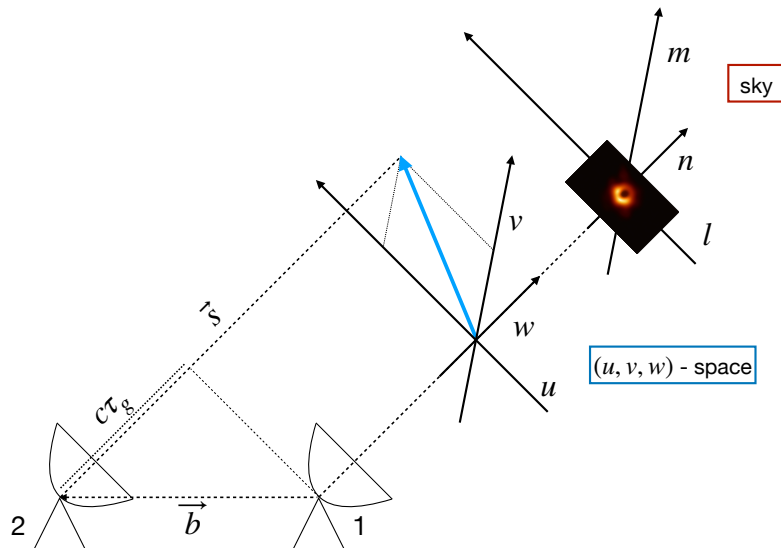


Figure 3.7: (u, v, w) and (l, m, n) coordinate systems. The w and n coordinates, which are generally ignored, are shown for the sake of completeness. The (u, v) -plane is the two-dimensional slice of the (u, v, w) -space. The visibility vector, shown as a blue arrow, is the projection of the baseline vector \vec{b} onto the (u, v) -plane. Credits for the sky image: EHT collaboration.

where $A = (R_c^2 + R_s^2)^{1/2}$ and $\phi = \tan^{-1}(R_s/R_c)$ are the amplitude and the phase of the complex visibility. Eq. (3.14) is a direct result of the van Cittert—Zernike’s theorem, which states that observed output is the FT of the brightness distribution of the source. The sine and cosine correlators represent the polarisations of the instrument. Radiotelescopes usually employ circular (R and L) or linear (X and Y) polarisations.

The natural coordinate system for expressing eq. (3.14) is the (u, v) -plane. The baseline vector \vec{b} can be specified by three coordinates, (u, v, w) , where w is in the direction of the source, u and v belong to the plane perpendicular to w . Figure 3.7 shows the geometrical configuration of the coordinate system. For an interferometer, the (u, v) -plane is the spatial distribution of the baselines, in units of λ , as seen from the source at infinity. The complex visibility of eq. (3.14) becomes [170, 171]:

$$\mathcal{V} = \int \int \int I_\nu(l, m, w) e^{-i2\pi(lu+mv+nw)} dl dm dn \simeq \int \int I_\nu(l, m) e^{-i2\pi(lu+mv)} dl dm \quad (3.15)$$

where w can be ignored as it is small compared to the distance of the source. The (u, v) complex numbers are called visibilities. A single interferometer observation gives the FT of the source brightness distribution for a particular value of the spatial coordinates of the baseline vector at a given time and frequency, projected onto the (u, v) -plane. The Earth’s rotation varies the projected baseline in time, providing new visibilities during an observation. Figure 3.8 shows the (u, v) -plane for a source with declination $\text{Dec} = +90^\circ$ (upper left panel), $\text{Dec} = +45^\circ$ (upper right panel) and $\text{Dec} = 0^\circ$ (lower panel) for a full-track observation of the European VLBI network and the e -MERLIN. The projected baselines trace perfect circles if the source is at the north (or south) pole, while for an equatorial source the resulting visibilities belong to straight lines. In the intermediate case, the visibilities form an ellipse. Additionally, radio telescopes observe in certain band of frequency $\Delta\nu$, centred at ν . The band width is organised in sub-bands, known as spectral windows, which are further sliced into channels. Therefore, the total number of visibilities N_{vis} computed by an interferometer with N antennas during an observation with a total duration T_{tot} , integration time T_{int} , number of spectral windows and

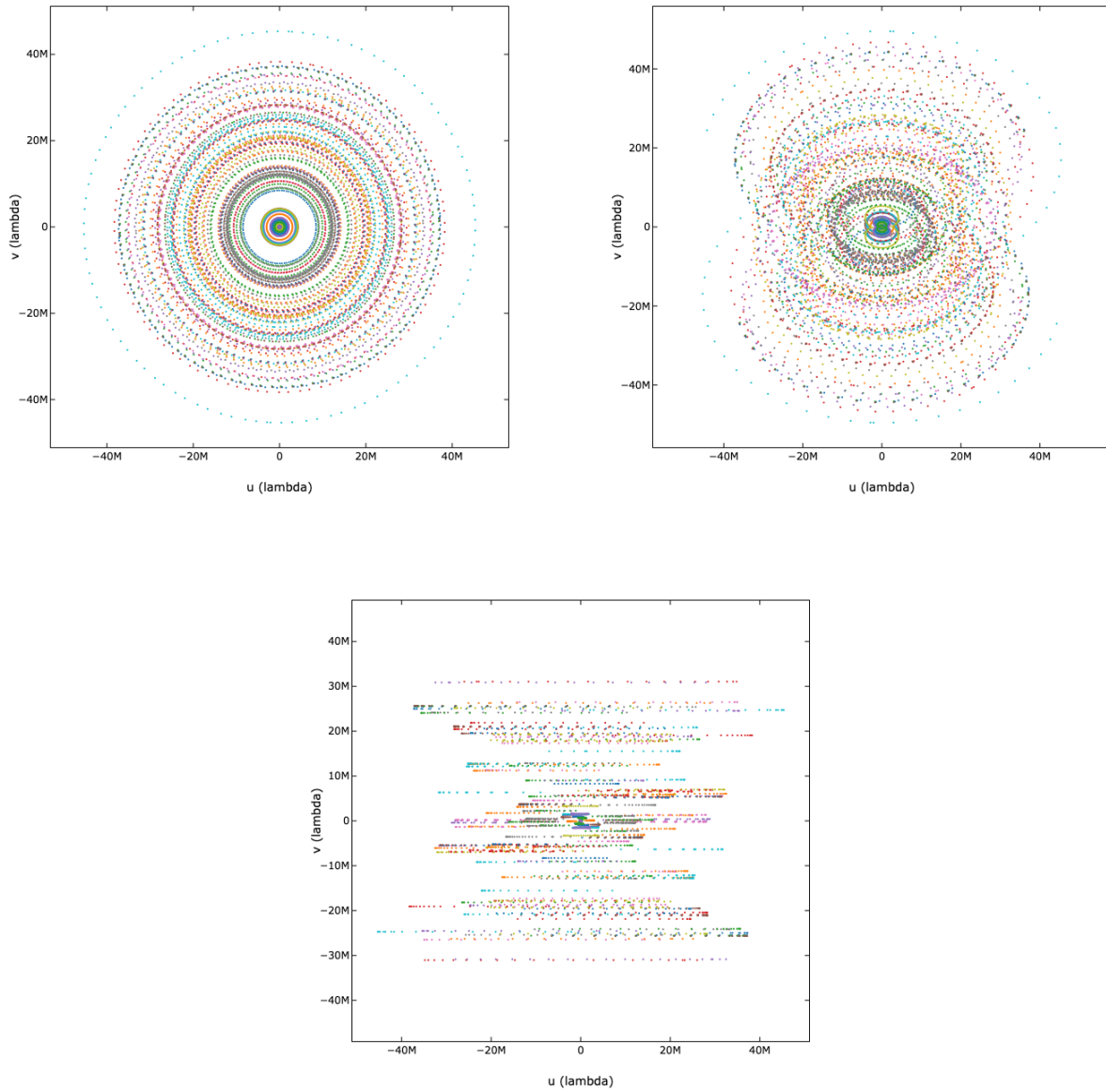


Figure 3.8: Examples of measured visibilities in the (u, v) -plane for a full-track observation with the European VLBI Network and the *e*-MERLIN of a source with $\text{Dec} = +90^\circ$ (upper left panel), $\text{Dec} = +45^\circ$ (upper right panel) and $\text{Dec} = 0^\circ$ (lower panel) at 6 GHz. Figures produced with the European VLBI Network observation planner (<https://planobs.jive.eu/>).

channels N_{spw} and N_{chan} , respectively, is:

$$N_{vis} = \frac{N(N-1)}{2} \times 4 \times N_{spw} \times N_{chan} \times \frac{T_{tot}}{T_{int}} \quad (3.16)$$

where the factor 4 is given by the four polarisations (for instance, RR, LL, RL and LR). Examples of the (u, v) -plane for different configuration of the interferometer are given in Figure 3.5. If the observation covers most of the FT of the source brightness distribution \mathcal{V} , the latter can be inverted to yield the brightness distribution $I_\nu(l, m)$. Nevertheless, to fill the entire (u, v) -plane an infinite number of baselines and/or an infinitely large band width are required. Since this is clearly impossible, the (u, v) -plane is sampled according to the available asset. This means that an observer has access to a quantity $S(u, v)\mathcal{V}(u, v)$, where $S(u, v)$ is the sampling function, which is simply taken as 1 if that particular (u, v) value is sampled, 0 otherwise. The sampling function represents the (u, v) -plane coverage available for that particular observation. The source brightness distribution can be derived by calculating the inverse FT as follows [171]:

$$\text{FT}^{-1}[S(u, v)\mathcal{V}(u, v)] = \text{FT}^{-1}[S(u, v)] * \text{FT}^{-1}[\mathcal{V}(u, v)] = I_\nu(l, m) * B(l, m) \quad (3.17)$$

where $B(l, m)$ is the dirty beam, which is the inverse FT of the sampling function $S(u, v)$. In the first equivalence in eq. (3.17), I used the FT property for the convolution $\text{FT}[f * g] = \text{FT}[f]\text{FT}[g]$ for two generic functions f, g . The convolution $I_\nu(l, m) * B(l, m)$ is called dirty map. An observation provides an observer with the quantities $S(u, v)$, and $S(u, v)\mathcal{V}(u, v)$. Applying the inverse FT to $S(u, v)$ and $S(u, v)\mathcal{V}(u, v)$ gives the dirty beam $B(l, m)$ and the dirty map $I_\nu(l, m) * B(l, m)$, respectively. The source brightness distribution is derived through the deconvolution of the dirty map with the dirty beam. More intuitively, this means that an observer measures the FT of the convolution of the true source brightness distribution with the dirty beam, i.e. the response of the interferometer. Figure 3.9 summarises the aforementioned steps. Finally, since the main contributors to the (u, v) -plane coverage are the number of antennas, the total time on source T_{tot} and the band width $\Delta\nu$, the r.m.s. noise level for the final map of a point-like source as seen by an interferometer array with N antennas is [170]:

$$\sigma \propto [N(N-1)\Delta\nu T_{tot}]^{-1/2} \quad (3.18)$$

The most sensitive arrays employ large frequency ranges to minimise the time required on the source for achieving high sensitivity (around $10 \mu\text{Jy}/\text{beam}$). Currently, the Very Large Array, detailed below, is the most sensitive array at centimetre wavelengths.

3.2 Calibration

The quantity that is actually measured by an interferometer is the result of many physical effects that corrupt the ideal sampled visibilities. Incoming light travels through the ionosphere and the troposphere, whose complicated and highly variable structure alters the phase of the radio wave. Additionally, instrumentation is not flawless: the response of the antenna is affected by the system temperature, the electronic gains, the frequency dependence, etc., which impact on the amplitudes and the phases. Therefore, for each pair of antennas i, j , an observer has access to the quantity $\mathcal{V}_{ij}^{\text{obs}}$, which is related to the unperturbed visibility $\mathcal{V}_{ij}^{\text{true}}$ through the following equation [171]:

$$\mathcal{V}_{ij}^{\text{obs}} = G_{ij} \mathcal{V}_{ij}^{\text{true}} \quad (3.19)$$

where G_{ij} , known as Jones' matrix, encompasses all the perturbation effects. Eq. (3.19) is known as the radio interferometry measurement equation. Jones' matrix can be expressed through its most relevant components as (see, e.g., [172, 173]):

$$G_{ij} = K_{ij} B_{ij} J_{ij} D_{ij} E_{ij} P_{ij} T_{ij} F_{ij} \quad (3.20)$$

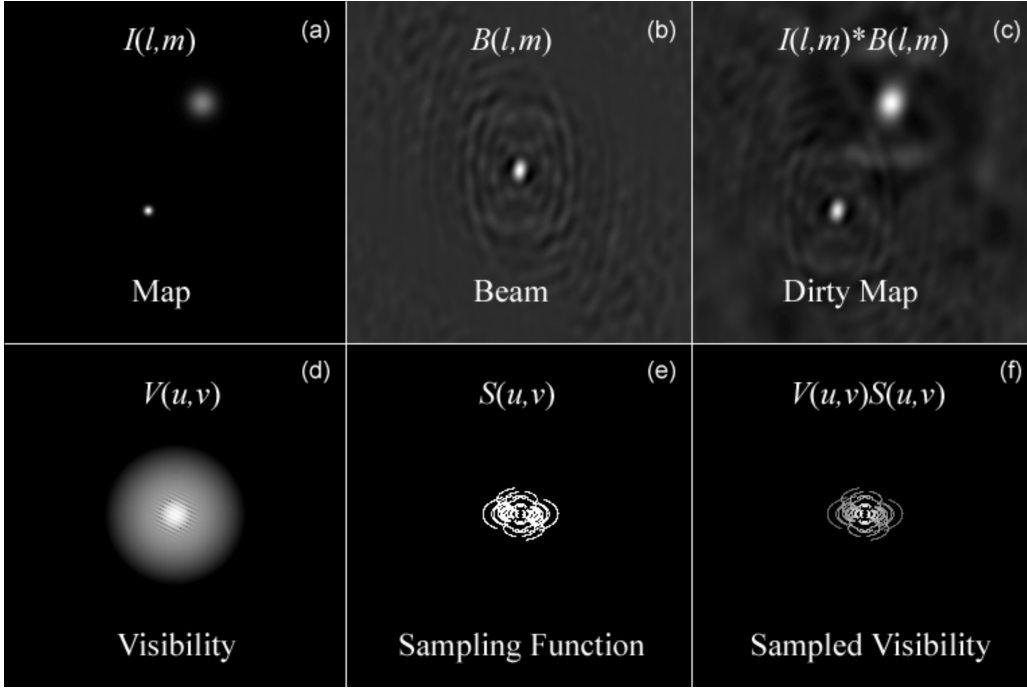


Figure 3.9: Relation between the observed visibilities and the true brightness distribution of a source: (a) example of sky brightness distribution; (d) corresponding visibilities, namely $\text{FT}[I(l, m)]$; (b) synthesised beam, or dirty beam, of a model antenna array; (e) sampling function $S(u, v)$, i.e. $\text{FT}[B(l, m)]$; (c) dirty map, i.e. the convolution $I_\nu(l, m) * B(l, m)$; (f) sampled visibilities, namely $\text{FT}[I_\nu(l, m) * B(l, m)] = S(u, v)\mathcal{V}(u, v)$. The sampled visibilities are the actual measurements of the array. Credits: D. E. Gary.

where K_{ij} refers to the geometric compensation, non-closing errors, B_{ij} is the bandpass response, J_{ij} represent the electronic amplitude and phase gains, D_{ij} takes into account the effects of the instrumental polarisation, also known as polarisation leakages, E_{ij} is the antenna voltage pattern, P_{ij} is caused by the change in the parallactic angle, T_{ij} and F_{ij} trace the effects of the troposphere and ionosphere, respectively.

The calibration is the process to determine the complex gains G_{ij} , in order to invert eq. (3.19) and derive the true sampled visibilities $\mathcal{V}_{ij}^{\text{true}}$. To accomplish this, it is generally assumed that

- most of the aforementioned effects are antenna-based, hence the cross-correlation between antennas i and j can be safely ignored, i.e. $G_{ij} = G_i G_j^*$;
- temporal and frequency dependence are only slightly coupled, thus their variations can be determined independently, namely $B_i(\nu, t) = B_i(\nu)$ and $J_i(\nu, t) = J_i(t)$.

As shown in eq. (3.14), visibilities are complex numbers characterised by an amplitude A and a phase ϕ . For an array featuring N antennas, eq. (3.19) yields $N(N - 1)/2$ equations, which means that the system is solvable. Closing the phases requires three antennas, while amplitudes are completely determined with at least four antennas. In practice, the conventional approach to solve the system of equations involves the observation of bright sources, termed calibrators, whose true visibilities have been previously modelled. In fact, for these standard calibrators [171]:

$$\mathcal{V}_{ij}^{\text{obs}} = G_{ij} \mathcal{V}_{ij}^{\text{model}} \quad (3.21)$$

where $\mathcal{V}_{ij}^{\text{model}}$ are the model visibilities for the calibrator. Since $\mathcal{V}_{ij}^{\text{obs}}$ and $\mathcal{V}_{ij}^{\text{model}}$ are known, eq. (3.21) can be inverted to derive G_{ij} . In a standard, continuum experiment that does not involve polarisation measurements, the important factors in eq. (3.20) are the bandpass B_{ij} , the electronic gains J_{ij} and the atmospheric effects T_{ij} and F_{ij} . The term B_{ij} arises from the

frequency-dependent response of the receiver. As the edge channels of the band exhibit a lower response, the source’s amplitude decreases at the band’s beginning and end. This effect is corrected by observing a bright source, ensuring a high signal-to-noise ratio for modelling the receiver’s response. Atmospheric effects on phases are typically modelled by observing a bright source in close proximity to the target source of the experiment, both before and after the scan on the target. This source is referred to as the phase calibrator. This procedure is based on the assumption that the atmosphere equally affects the phase calibrator and the target, given that the two sources are close in the sky plane. The phase calibrator – target – phase calibrator cycle should not exceed the coherence time of the atmosphere, ensuring that atmospheric effects remain constant throughout the cycle. The phases of the target are corrected by interpolating the phase solutions of the phase calibrator at the time of the scan on the target. The entire procedure is known as phase-referencing. Finally, the receiver records a temperature in Kelvin. A bright, non-variable source, with a known total flux, is used to define a Jy/K scale, which enables the conversion to Janskys, the conventional unit for the radio flux density ($1 \text{ Jy} = 10^{-26} \text{ W m}^{-2} \text{ Hz}^{-1} = 10^{-23} \text{ erg s}^{-1} \text{ cm}^{-2} \text{ Hz}^{-1}$). This source is named amplitude calibrator. However, for sufficiently small angular scales, such as for VLBI experiments, amplitude calibrators may not be available. In this case, the flux calibration is determined with coefficients calculated *a priori* (Section 3.4).

3.3 Compact Arrays

In this section I will briefly present the connected interferometers I employed during my Ph.D course.

3.3.1 The Karl G. Jansky Very Large Array

The Very Large Array (VLA) is a connected interferometer composed of 27 dishes in The Plains of San Agustin, New Mexico (Figure 3.10). The first VLA dates back to the 1970s and 1980s [174]. In 2012, the Expanded VLA, a project to modernise the electronics of the VLA, was completed [175]. All the goals of the upgrade were met: a complete frequency coverage from 1 to 50 GHz; a continuum sensitivity improvement by up to an order of magnitude; the implementation of a new correlator. The array was subsequently dedicated to the father of radio astronomy, Karl Guthe Jansky.

The dishes, which have a diameter of 25 m each, are disposed in a Y-shape and they can be placed at different relative distances, enabling four different configurations. Presently, the most compact configuration (D) provides baselines between 0.035 and 1.03 km. The most extended configuration (A) provides baselines between 0.068 and 36.4 km. The frequency bands of the VLA ranges from 74 MHz (4-band) to 45 GHz (Q-band). The width of the resulting synthesised beam ranges between 0.043 (A-configuration, Q-band) and 850 arcseconds (D-configuration, Band 4)².

Data from the VLA were used for the campaign presented in Chapters 4. Data are generally reduced using the VLA pipeline available in CASA³. After applying some deterministic flags, such as data affected by antenna shadowing, the pipeline derives the antenna position corrections, the gain curves, the atmospheric opacity corrections and the requantiser gains. Subsequently, the pipeline iteratively determines the initial delay and bandpass calibrations. Afterwards, the initial gain calibration is calculated. Lastly, the final delay, bandpass, and gain/phase calibrations are derived and applied to the data. Each of the main step is followed by a thorough flagging of bad data. For our purposes, the imaging was also performed in CASA, using the task `tclean`.

²Information on the configuration properties of the VLA can be found at: <https://science.nrao.edu/facilities/vla/docs/manuals/oss/performance/resolution>

³<https://science.nrao.edu/facilities/vla/data-processing/pipeline>



Figure 3.10: The Very Large Array dishes in D-configuration. Credits: NRAO/AUI/NSF.

Besides the statistical noise of the image, a 5% of the source flux density is usually added in quadrature, in order to account for the calibration uncertainty.

In the 2030s, after 60 years of honourable service and ground-breaking discoveries, the VLA will be replaced by the ngVLA. This interferometric array, which will be placed in the United States, Mexico and Canada, is designed to improve by more than an order of magnitude the sensitivity and spatial resolution of the VLA at the same wavelengths. The ngVLA will be composed by a core of 214 antennas of 18 m each, a short baseline array of 19 antennas of 6 m each and a long baseline array of 30 antennas of 18 m each. The ngVLA will operate at frequencies of 1.2 GHz to 116 GHz.

3.3.2 MeerKAT

The Meer Karoo Array Telescope (MeerKAT) consists of 64 dishes with a diameter of 13.5 m, located in the Karoo Desert, South Africa [176]. The majority of the antennas are concentrated in a central cluster, enabling sensitivity to diffuse structures, complemented by longer baselines extending out to 7.7 km (Figure 3.11). The frequency coverage ranges from 0.580 (UHF-band) to 3.5 GHz (S-band), resulting in a synthesised beam size between ~ 4 (S-band) and ~ 7 arcseconds (UHF-band), respectively [177]. Data may be reduced using `oxkat2`, a set of python scripts used for semi-automatic processing [178]. Firstly, the calibrator fields are flagged for radio frequency interference (RFI) as well as the first and last 100 spectral channels. A spectral model from the primary calibrator is applied to the secondary. Delay, bandpass and complex gain calibration is performed on the primary and secondary calibrators and applied to the target field. The target field is subsequently flagged using `tricolour3`. The data are imaged with `WSCLEAN` using a Briggs weighting with robust parameter of -0.7 [179]. A model is then derived from the image and used to re-image after a round of phase-only self calibration. Usually, the expected uncertainties on the measured flux density include a 10% calibration error, besides statistical uncertainties.

At the time of writing, MeerKAT is being upgraded with the addition of 20 more dishes that will increase the maximum baseline from 7.7 to ~ 17 km, improving both the sensitivity and the angular resolution. This initiative, now known as MeerKAT+, is financially supported by the



Figure 3.11: The MeerKAT radio telescope. Credits: University of Manchester.

South African Radio Astronomy Observatory (SARAO), the Max Planck Gesellschaft (MPG) and the Istituto Nazionale di Astrofisica (INAF). Lastly, in the 2030s MeerKAT+ will eventually be integrated into SKA1-Mid, the first phase of the SKA telescope, which will encompass a total of 197 dishes working between 0.350 and 15.4 GHz.

3.4 Very Long Baseline Interferometry

Increasing the separation between two antennas improves the resolution, as previously mentioned in eq. (3.11). To simulate a dish as large as the entire surface of the Earth, astronomers employ antennas spaced all over the world. This technique is known as VLBI and it provides an angular resolution of approximately 0.1 to ~ 10 mas.

In VLBI, each telescope independently records data, which is then transmitted to a single station for correlation. Calibration of VLBI data differs from the conventional procedure applied for connected interferometers. First, amplitude scaling using a compact, bright source is not viable, as sources compact at the mas level are highly variable, making their total flux density difficult to model accurately. Instead, the amplitude is calibrated using measurements of the antenna temperature taken every few seconds, i.e. the receiver noise, combined with gain curves, representing the antenna's response as a function of the elevation of the observed source. Since this *a priori* procedure is less accurate than using an amplitude calibrator, a systematic 10% uncertainty is generally considered in the final r.m.s. noise level.

Regarding phases, while connected interferometers can interpolate phase solutions from a calibrator and apply them to the target, this is unfeasible for VLBI experiments due to rapidly changing phases over long baselines. Phases $\phi(t, \nu)$ can be expressed using a Taylor expansion of the form:

$$\phi(t, \nu) \simeq \phi_0 + \frac{\delta\phi}{\delta\nu}\Delta\nu + \frac{\delta\phi}{\delta t}\Delta t \quad (3.22)$$

where ϕ_0 is the phase error at the reference time and frequency, $\frac{\delta\phi}{\delta\nu}$ and $\frac{\delta\phi}{\delta t}$ are the delay and rate terms. Instead of solving for the phases, solutions for delays and rates are obtained through a process called fringe fit. During a fringe fit, the difference between model phases of the phase calibrator and measured phases is minimised. The initial fringe fit on a bright calibrator solves for station-based instrumental phase offsets and slopes as a function of frequency, which arise

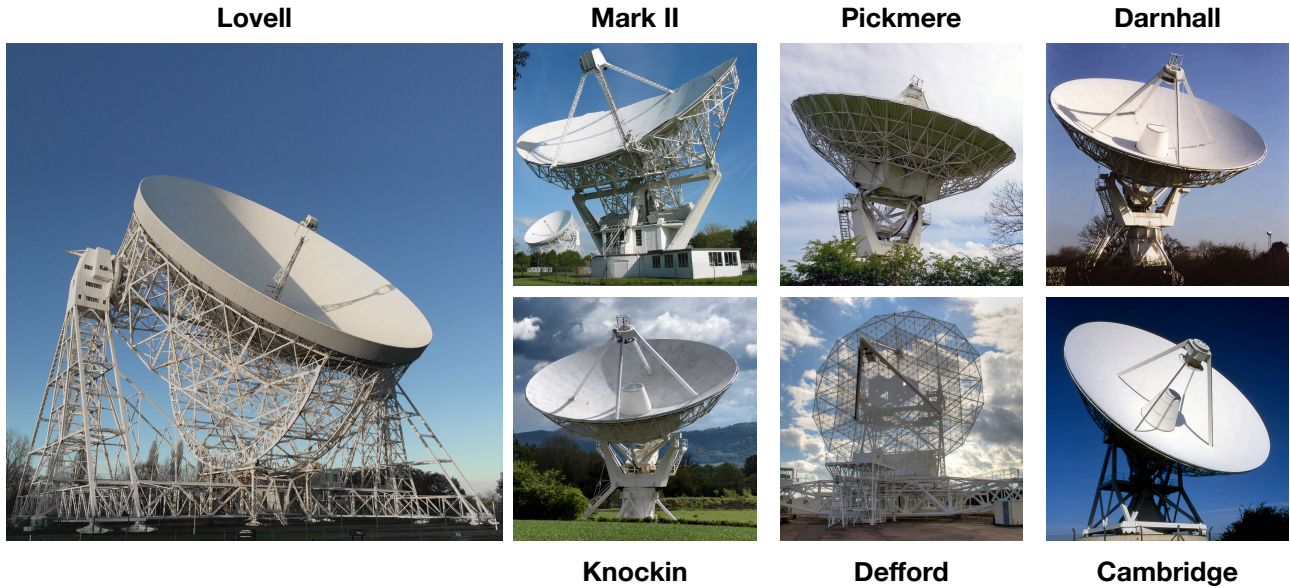


Figure 3.12: The *e*-MERLIN array.

from the different path travelled by the light in the station cables. This step, termed single band delay, is independent on time, hence the fringe fit can be computed on a single scan for the entire observation. The calibrator, which often coincides with the bandpass calibrator, is termed fringe finder. Subsequently, time- and frequency-dependent effects are computed with a fringe fit on the phase calibrator. This step, called global fringe fit, solves for the rates and delays in eq. (3.22). Once the solutions are determined, they are interpolated and applied to the target.

During my Ph.D course I made extensive use of VLBI data. In Chapter 4, 5 and 6 I show the results of dedicated VLBI campaigns. The VLBI arrays employed are briefly presented in the following sections.

3.4.1 The enhanced Multi-Element Remotely Linked Interferometer Network

The enhanced Multi-Element Radio Linked Interferometer Network (*e*-MERLIN) is an array of seven radio telescopes across Great Britain (Figure 3.12): Lovell (76 m), Mark II (25 × 38 m), Pickmere, Darnhall, Knockin, Defford (25 m), Cambridge (32 m). Three observing bands are available: L-band (1.23 – 1.74 GHz), C-band (4.3 – 7.5 GHz), and K-band (19 – 25 GHz). The longest baselines is 217 km, which provides a resolution between 20 mas (K-band) and 200 mas (L-band). Data from *e*-MERLIN were used for the analysis of GRB 201015A in Chapter 4. Since its baselines can be considered as intermediate between the short baselines of a compact array and the long baselines of a VLBI network, *e*-MERLIN serves as a fundamental ‘core’ for the European VLBI Network (see below). Combined European VLBI Network + *e*-MERLIN data were used to study the candidate host galaxy of GRB 200716C (see Chapter 6).

e-MERLIN data are generally calibrated with the custom *CASA* pipeline⁴. The pipeline flags the data for RFI, the edges of each spectral channels and adds observatory flags. Bandpass and phase calibration are performed and applied to the target, followed by flux scaling. Finally, images of the target field are made. For our purposes, the imaging was also performed in *CASA*,

⁴https://github.com/e-merlin/eMERLIN_CASA_pipeline

using the task `tclean`. Besides the statistical noise of the image, a 10% of the source flux density is usually added in quadrature, in order to account for the calibration uncertainty.

3.4.2 The European VLBI Network

The European VLBI Network (EVN) is a network of radio telescopes operated by the Joint Institute of VLBI ERIC (JIVE) and located primarily in Europe and Asia (Figure 3.13): Badary (32 m, Russia), Effelsberg (100 m, Germany), Hartebeesthoek (26 m, South Africa), Irbene (32 m, Latvia), Kunming (40 m, China), Lovell (76 m, England), Medicina (32 m, Italy), Metsähovi (14 m, Finland), Noto (32 m, Italy), Onsala (O8: 25 m, O6: 20 m, Sweden), Sardinia (64 m, Italy), Sheshan (25 m, China), Svetloe (32 m, Russia), Tianma (65 m, China), Torun (32 m, Poland), Urumqi (25 m, China), Westerbork (25 m, The Netherlands), Yebes (40 m, Spain), Zelenchukskaya (32 m, Russia). The frequency coverage ranges from 0.3 to 49 GHz, even though not all the antennas are available at each frequency. The maximum baseline is 9833 km (Badary–Hartebeesthoek). The synthesised beam size is between 24 mas (0.3 GHz) and 0.19 mas (43 GHz). The lack of short baselines which samples the diffuse emission can be partially solved by including the *e*-MERLIN in the EVN observation. Before its collapse, the Arecibo radio telescope (305 m, Puerto Rico) was part of the EVN.

Even if in standard VLBI the data are recorded on disks at the stations and then shipped to the a central correlator for processing, EVN is capable of real-time observations with the *e*-VLBI technique, which uses fibre optic networks to connect EVN telescopes to the JIVE data processor that correlates the data in real-time. Presently, the EVN is the most sensitive VLBI array and the only one capable of real-time observations.

The EVN can perform joint observations with the Very Long Baseline Array, detailed below, the phased-array VLA and the Green Bank Telescope (100 m, United States of America). The array formed by the EVN and the VLBA is named global-VLBI array. Finally, at frequencies above 22 GHz, joint EVN+Korean VLBI Network (KVN) observations can be requested. The KVN consists of three 21 m millimeter telescopes (Tamna, Ulsan, Yonsei). EVN data are calibrated with the procedure mentioned at the beginning of this section. Results obtained from EVN data are presented in Chapter 4, 5 and 6.

3.4.3 The Very Long Baseline Array

The Very Long Baseline Array (VLBA) is a network of ten identical 25 m dishes located across the United States of America and operated by the National Radio Astronomy Observatory (Figure 3.14): St. Croix (U.S. Virgin Islands), Hancock (New Hampshire), North Liberty (Iowa), Fort Davis (Texas), Los Alamos (New Mexico), Pie Town (New Mexico), Kitt Peak (Arizona), Owens Valley (California), Brewster (Washington) and Mauna Kea (Hawaii). The frequency range covers from 0.3 GHz to 96 GHz. The longest baseline is 8611 km (Mauna Kea – St.Croix), resulting in a synthesised beam size of 22 mas (0.3 GHz) to 0.17 mas (96 GHz). The VLBA represents the largest array specifically assembled for VLBI observations, and it operates on a regular basis all day every day. VLBA data are calibrated following the procedure mentioned at the beginning of this section. Results obtained from VLBA data are presented in Chapter 5.

3.4.4 The Long Baseline Array

The Long Baseline Array (LBA) consists of five telescopes located in Australia (Figure 3.15): Parkes (64 m), the Australia Telescope Compact Array (ATCA, six 22 m antennas), Mopra (22 m), Hobart (12 m) and Ceduna (30 m). Joint observation with the Warkworth (12 m and 30 m, New Zealand), Hartebeesthoek (26 m, South Africa), Katherine (12 m) and Tidbinbilla

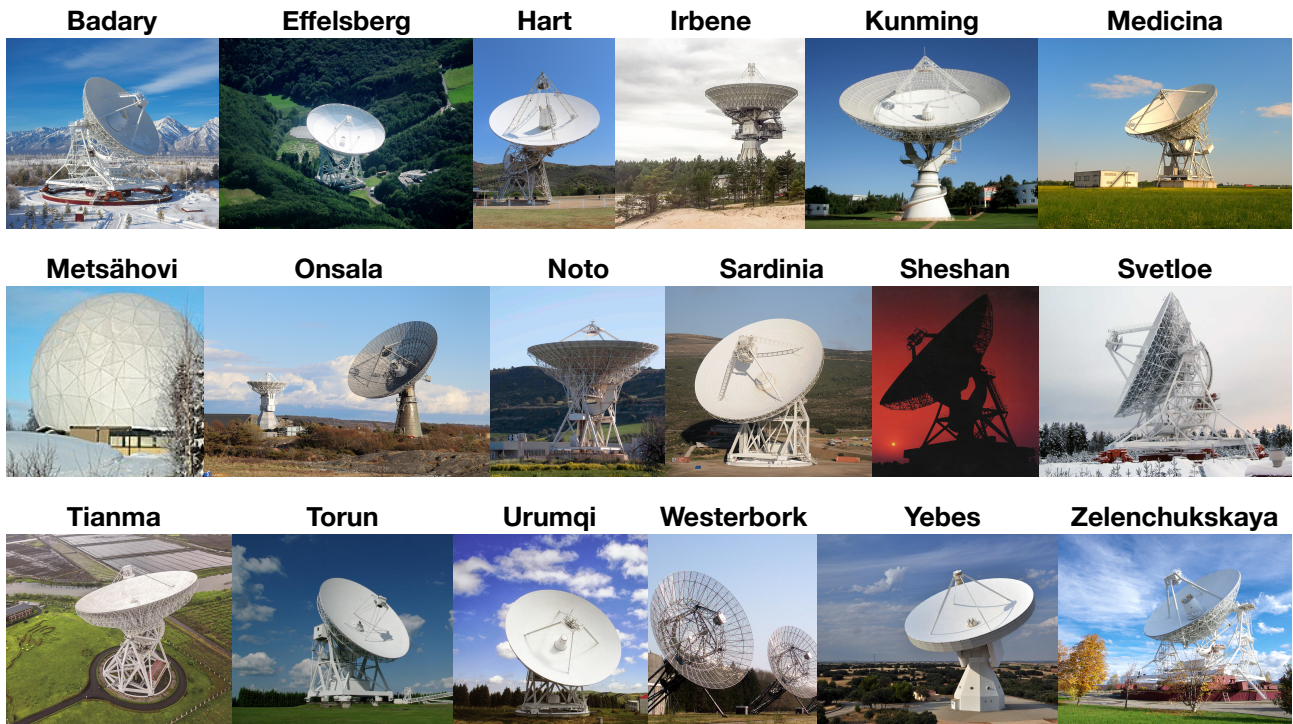


Figure 3.13: Main telescopes of the European VLBI Network.

(70 m) telescopes can be requested. The frequency range covers between 1.4 GHz to 22 GHz, but not all antennas can observe at all available frequencies. The longest baseline is 1702 km (Hobart – Ceduna), resulting in a synthesised beam size between 20 mas (1.4 GHz) and 2 mas (22 GHz). LBA data are calibrated following the procedure mentioned at the beginning of this section.

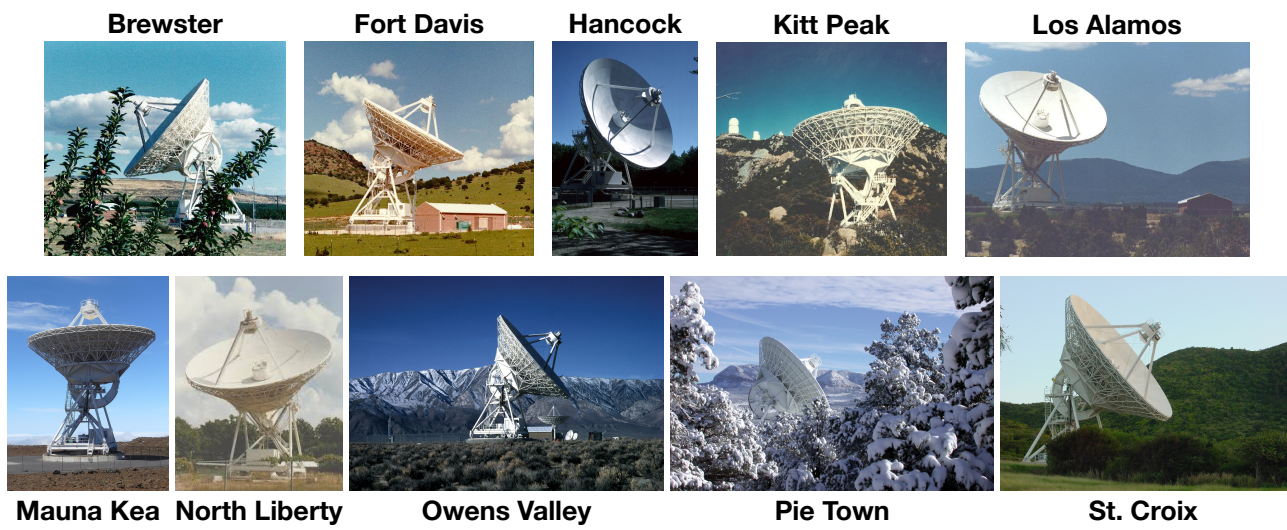


Figure 3.14: The Very Long Baseline Array.

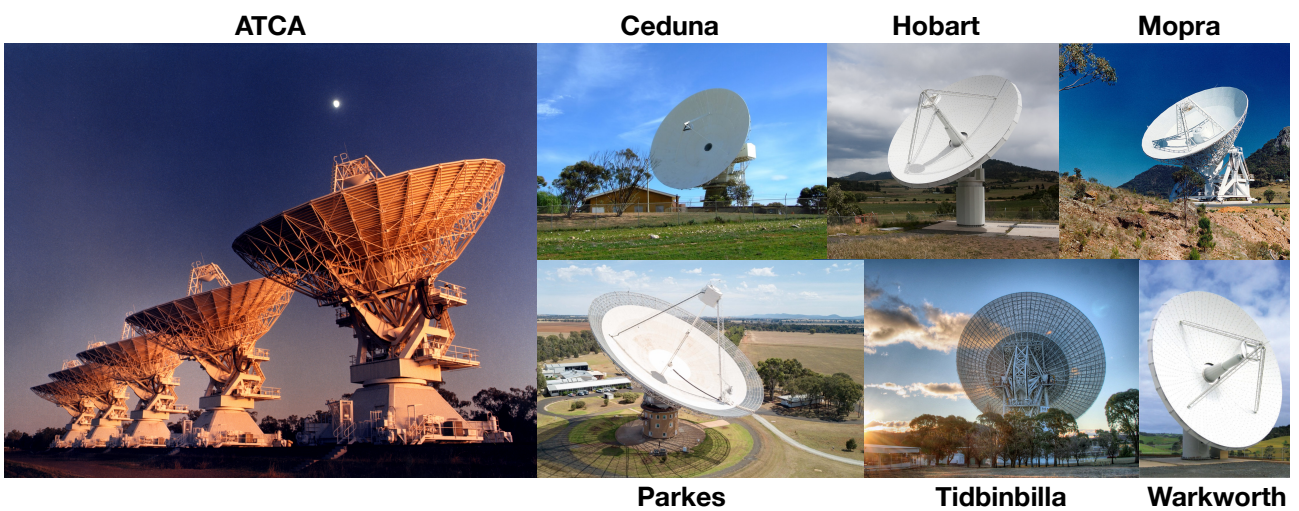


Figure 3.15: The Long Baseline Array.

Chapter 4

GRB 201015A

In this chapter I present the multi-wavelength analysis we performed for GRB 201015A. The following work was published in *Astronomy & Astrophysics* with the title “*VLBI observations of GRB 201015A, a relatively faint GRB with a hint of very high-energy gamma-ray emission*”.

4.1 Introduction

Only four GRBs have a bona fide detection in the VHE range at either early epochs (e.g. GRB 190114C, 300 GeV–1 TeV [61] and GRB 201216C [180]) or at later times deep in the afterglow phase (e.g. GRB 180720B, 100–400 GeV [60] and GRB 190829A, 180 GeV–3.3 TeV [181]). Studying this emission component allows the physical properties of the emitting region and/or of the shocked accelerated particles to be constrained, and the most natural interpretation for this VHE emission is the SSC emission. Based on the very few events detected so far, it seems that the VHE emission characterises both very energetic events, such as GRB 180720B and GRB 190114C, and low-energy events, such as 190829A, but any possible peculiarities of VHE detected bursts will become clearer as the sample of events increases. However, multi-wavelength follow-up of these events has proved a fundamental tool to test the afterglow emission model; for example, for GRB 190829A the VHE emission detected by the H.E.S.S. telescopes was first interpreted as synchrotron emission [181], while multi-wavelength follow-up studies agree on an SSC emission origin [137–139].

GRB 201015A was discovered on 2020 October 15 at 22:50:13 UT as a multi-peaked 10s GRB by *Swift*–BAT [182]. Subsequent observations reported the presence of an associated transient in the optical [183–198], X-rays [199–202], UV [203], and radio [204–206] bands. Remarkably, GRB 201015A was observed by the MAGIC telescopes about 40s after the *Swift* trigger, and a hint of a VHE counterpart with a significance $\geq 3.5\sigma$ was reported from preliminary analyses [207, 208]. With the *Fermi*–GBM spectrum, [209] suggested that this burst is consistent with the $E_{\text{peak}} - E_{\text{iso}}$ Amati relation [38] for long-duration GRBs, with an isotropic equivalent energy of $E_{\text{iso}} \simeq (1.1 \pm 0.2) \times 10^{50}$ erg. If confirmed, this would be the fifth and least luminous GRB ever detected in this band.

Optical spectroscopy in the 3700–7800 Å range revealed a redshift for the source of ~ 0.426 [188, 210]. To date, all the GRBs that have been detected at VHE have relatively low redshifts: 0.654, 0.425, 0.0785, and 1.1 for GRB 180720B, GRB 190114C, GRB 190829A, and GRB 201216C, respectively [211–214]; their isotropic equivalent energies span three orders of magnitude [215]. Throughout the chapter we assume a standard Λ -CDM cosmology with $H_0 = 69.32 \text{ km Mpc}^{-1} \text{ s}^{-1}$, $\Omega_m = 0.286$, and $\Omega_\Lambda = 0.714$ [216]. With this cosmology, 1'' corresponds to roughly 5.6 kpc at $z = 0.426$.

4.2 Observations

4.2.1 VLA Observations at 6 GHz

Observations with the VLA were performed 1.41 days post-burst (PI: Fong; project code: 19B-217) at a central frequency of 5.7 GHz with a bandwidth of 1.6 GHz (C-band). The target and the phase calibrator J2355+4950 were observed in eight-minute cycles, with seven minutes on the former and one minute on the latter. The distance between the target and the phase calibrator is about 4.5° . Finally, 3C147 was used as bandpass and flux calibrator. The data were calibrated using the *CASA* pipeline, and they were subsequently imaged with the *tclean* task in *CASA* (Version 5.1.1., [217]).

4.2.2 *e*-MERLIN observations at 1.5 GHz

We started observing at 1.5 GHz with *e*-MERLIN 20 days post-burst (2020 November 4; PI: Rhodes, project code: DD10003) with two further observations 23 (2020 November 7) and 101 (2021 January 24) days post-burst. The observations were made at a central frequency of 1.51 GHz with a bandwidth of 512 MHz (L-band). For each epoch the target and phase calibrator, J2353+5518, were observed in ten-minute cycles, with seven minutes on the former and three on the latter. The distance between the phase calibrator and the target is about 3° . Each observation ended with scans of the flux (J1331+3030) and bandpass calibrators (J1407+2827). The data were reduced using the custom *e*-MERLIN pipeline¹. The calibrated measurement sets were imaged in *CASA* (Version 4.7).

4.2.3 *e*-MERLIN observations at 5 GHz

Observations at 5 GHz with *e*-MERLIN were performed 21 (2020 November 5), 24 (November 8), 60 (December 14), 85 (2021 January 8), and 100 (January 23) days post-burst (PI: Giroletti; project code: DD10004). All epochs but December 14 were centred at 4.50–5.01 GHz (C-band) with a bandwidth of 512 MHz divided into four spectral windows of 128 MHz each. For December 14 the frequency range was within 6.55–7.06 GHz (C-band). The data were first pre-processed with the *CASA e*-MERLIN pipeline using J1407+2827 as bandpass calibrator and J1331+3030 as flux calibrator. Two phase calibrators were used: J2353+5518, a fainter one on a rapid cycle, and J2322+5057, a brighter one used less frequently (once per hour) to correct for both short- and long-term atmospheric effects. All epochs were observed in eight-minute cycles, with six minutes on the target and two minutes on J2353+5518.

On November 5 an electronic problem occurred and the Defford antenna missed the bandpass and flux calibrators; consequently, the pipeline automatically flagged out this antenna, and there was a considerable data loss. To recover it we performed a further calibration of this epoch. We built a model for J0319+4130 using the pipeline results first, and we subsequently calibrated the data manually using the J0319+4130 model as bandpass and flux calibrator, improving the final image output. After the calibration, we cleaned the dirty image with the *tclean* task in *CASA* (Version 5.1.1.).

On November 8 the Knockin antenna lost one polarisation channel, and an improved image was achieved using only J2322+5057 for the phase calibration, which is about 3.3° from the target source.

¹https://github.com/e-MERLIN/eMERLIN_CASA_pipeline

4.2.4 EVN observations at 5 GHz

Observations at 5 GHz with EVN were performed 25 (2020 November 9), 47 (December 1), and 117 (2021 February 9) days post-burst (PI: Marcote; project code: RM016). The first epoch (2020 November 9) was conducted at a maximum bitrate of 4 Gbps per station, dividing the full band upon correlation into 16 spectral windows of 32 MHz and 64 frequency channels each, covering the frequency range of 4.57–5.11 GHz (C-band). The other two following epochs were conducted at a lower rate of 2 Gbps, resulting in eight spectral windows of 32 MHz and 64 frequency channels each, covering the frequency range of 4.77–5.05 GHz. All observations were correlated in real time (*e*-EVN operational mode) at JIVE (the Netherlands) using the SFXC software correlator [218].

The following sources were used as fringe finders and/or bandpass calibrators among the different epochs: BL LAC, J0854+2006, 3C 84, J0555+3948, and J0102+5824. The same phase calibrator as in the *e*-MERLIN observations was used: J2353+5518, in a phase-referencing cycle of 4.5 minutes on the target source and 1.5 minutes on the phase calibrator. The source J2347+5142 was observed as a check source to account for possible phase-referencing losses.

The EVN data were reduced using AIPS² [219] and Difmap [220] following standard procedures. An *a priori* amplitude calibration method was performed using the known gain curves and system temperature measurements recorded individually on each station during the observation. We manually flagged data affected by RFI and then we fringe-fitted and bandpass-calibrated the data using the fringe finders and the phase calibrator. We imaged and self-calibrated the phase calibrator in Difmap to improve the final calibration of the data. We used the same model of the phase calibrator, obtained from the 2020 December 1 epoch, to improve the calibration of all epochs. We note that we chose this epoch because it produced the most reliable image of J2353+5518 in terms of amplitude scales at all baseline lengths (including the short spacing given by the *e*-MERLIN stations). No apparent changes in the calibrator were observed among these three observations. The obtained solutions were then transferred to the target scans, which were subsequently imaged for each epoch. The check source J2347+5142 was also imaged and self-calibrated, confirming that no significant losses ($\lesssim 10$ –20%) were present in the obtained amplitudes due to the phase-referencing technique. We note that the Shanghai 65 m Radio Telescope (Tianma) and the Nanshan 25 m Radio Telescope (Urumqi) only participated in the first observation, and since they provided the longest baselines the resolution for the other two epochs decreases significantly (see Table 4.1).

4.2.5 Optical observations and public data

At 1.4, 2.2, and 4.3 days post-burst, we observed the position of the afterglow in the *i* and *z* bands with the Binospec instrument mounted on the 6.5m MMT (PI: Fong; project code: 2020c-UAO-G204-20B). We reduced our images using a custom Python pipeline³ and registered the images to the USNO-B1 catalogue [221] using standard IRAF tasks [222]. In the first two epochs we clearly detected an uncatalogued source in both bands that did not appear in our deep image at 4.3 days post-burst. To remove any contamination from the nearby galaxy, we performed image subtractions between the first two epochs and the final epoch using HOTPANTS [223]. We then calibrated the images to the PanSTARRS Data Release 2 catalogue [224] and performed aperture photometry on the image subtractions with the IRAF/phot task.

We gathered additional optical information from the public GCN Circulars Archive, and the detected emission was de-absorbed with the `dust_extinction` Python package⁴, using a

²The Astronomical Image Processing System (AIPS) is a software package produced and maintained by the National Radio Astronomy Observatory (NRAO).

³https://github.com/CIERA-Transients/Imaging_pipelines/

⁴<https://dust-extinction.readthedocs.io/en/stable/>

Galactic extinction $A_v = 0.93$ [225].

4.2.6 X-ray observations and public data

We obtained the *Swift*-XRT unabsorbed flux light curve integrated in the 0.3–10 keV energy range from the SWIFT BURST ANALYZER⁵ provided by the UK *Swift* Science Data Centre at the University of Leicester (UKSSDC, [226, 227]). Moreover, we obtained two epochs of *Chandra* observations with the Advanced CCD Imaging Spectrometer (ACIS) in very faint mode (PI: Gompertz; project code: 22400511). Exposures were centred around 8.4 and 13.6 days after trigger, with exposure times of 30 ks and 45 ks, respectively. The data were analysed using CIAO v4.14 and XSPEC v12.11.1, following the *Chandra* X-ray Observatory science threads⁶.

4.3 Results

4.3.1 Radio

A point-like source was clearly visible with the VLA 1.4 days post-burst with a peak brightness of $132 \pm 8 \mu\text{Jy beam}^{-1}$, where the uncertainty includes the r.m.s. noise and a 5% calibration error added in quadrature. The r.m.s. noise uncertainty is $5 \mu\text{Jy beam}^{-1}$, and therefore the detection has a significance of 26σ confidence. The source was found at a position (J2000) $\alpha = 23^{\text{h}}37^{\text{m}}16.403^{\text{s}}$, $\delta = 53^{\circ}24'56.39''$, with an uncertainty of $0.14''$ (1/10 of the beam size, [171]). The wide bandwidth and high signal-to-noise ratio allowed us to split the data in four spectral windows in order to estimate the spectral index β , where the flux density is $F \propto \nu^\beta$. We found $\beta \simeq 2.5$. To further improve this estimate, we produced a spectral map with the `tclean` task in `CASA` by setting `nterms=2` and `deconvolver='mtmfs'`. We found $\beta = 2.3 \pm 0.1$ at the peak of the target emission. We attribute the emission to the afterglow of GRB 201015A. Finally, we divided the one-hour observation into two intervals of equal duration and determined the peak brightness in each one, which turned out to be $126 \pm 9 \mu\text{Jy beam}^{-1}$ and $144 \pm 10 \mu\text{Jy beam}^{-1}$ (see Figure 4.2, blue stars).

The resulting images from the first and second *e*-MERLIN epoch at 1.5 GHz showed a point source with a peak brightness of $213 \pm 40 \mu\text{Jy beam}^{-1}$ and $261 \pm 48 \mu\text{Jy beam}^{-1}$, where the quoted uncertainty includes the r.m.s. noise and a 10% calibration error added in quadrature, at the position (J2000) $\alpha = 23^{\text{h}}37^{\text{m}}16.423^{\text{s}}$, $\delta = +53^{\circ}24'56.43''$. The r.m.s. noise uncertainties are $34 \mu\text{Jy beam}^{-1}$ and $40 \mu\text{Jy beam}^{-1}$, hence the detections have a significance of 6.2 and 6.5σ confidence, respectively. The uncertainty on the position, which was computed as the ratio between the beam size and the signal-to-noise ratio [171], is $0.03''$. Unfortunately, the observation at 101 days was heavily affected by RFI and as a result we obtained a 5σ upper limit of $285 \mu\text{Jy beam}^{-1}$. The data are shown in Figure 4.2 as gold squares.

At 5 GHz a point-like transient was clearly detected with *e*-MERLIN on November 5 (Figure 4.1) at the position (J2000) of $\alpha = 23^{\text{h}}37^{\text{m}}16.422^{\text{s}}$, $\delta = 53^{\circ}24'56.44''$. The uncertainty on the position is $0.01''$. The point-like source was also detected on November 8 at the position (J2000) $\alpha = 23^{\text{h}}37^{\text{m}}16.419^{\text{s}}$, $\delta = 53^{\circ}24'56.33''$. The uncertainty on the position is $0.02''$. Although both positions are in agreement with the coordinates provided by the VLA, we note that they are not consistent with each other at 3σ confidence level. We ascribe the offset in the position to the phase calibration of the second epoch: if the phase calibrator is observed less frequently (i.e. once per hour), it may not be able to trace perfectly the short-term atmospheric effects, and therefore correct for them. Nevertheless, we were not able to improve the phase calibration further. The measured peak brightness is $107 \pm 20 \mu\text{Jy beam}^{-1}$ and $116 \pm 28 \mu\text{Jy beam}^{-1}$ for November 5 and

⁵https://www.swift.ac.uk/burst_analyser/01000452/

⁶<https://cxc.harvard.edu/ciao/>

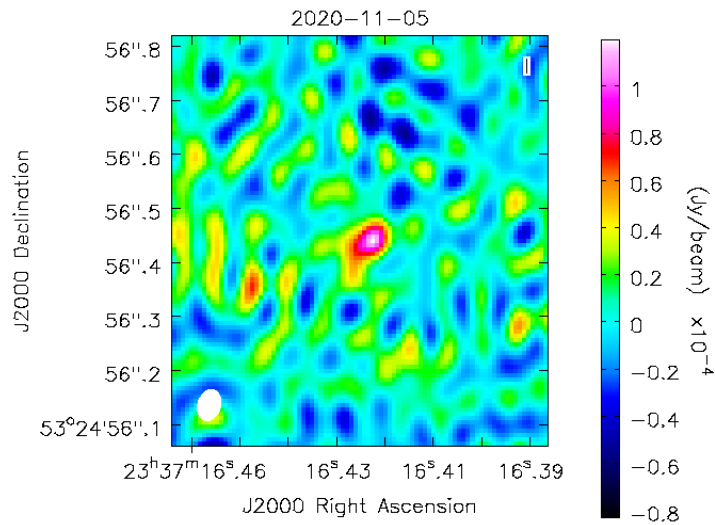


Figure 4.1: *e*-MERLIN detection on 2020 November 5. The synthesised beam is shown in the lower left corner.

8, respectively, where the quoted uncertainty includes the r.m.s. noise uncertainty and a 10% calibration error added in quadrature. The r.m.s. noise uncertainties are $17 \mu\text{Jy beam}^{-1}$ and $26 \mu\text{Jy beam}^{-1}$, hence the detections have a significance of 6.3 and 4.5σ confidence, respectively. On December 14, January 8, and January 23 no source was detected; the r.m.s. noise is 43 , 19 , and $16 \mu\text{Jy beam}^{-1}$, respectively. The data are shown in Figure 4.2 as blue dots.

GRB 201015A was detected as a point-like source also in the first two epochs with EVN at 5 GHz (25 and 47 days after the burst) at a consistent (J2000) position of $\alpha = 23^{\text{h}}37^{\text{m}}16.42232^{\text{s}} \pm 0.2 \text{ mas}$, $\delta = 53^{\circ}24'56.4392'' \pm 0.3 \text{ mas}$. The quoted uncertainties include the statistical uncertainties (0.05 and 0.12 mas for α and δ , respectively), the uncertainties in the absolute International Celestial Reference Frame position of the phase calibrator (0.11 mas), and check source (0.15 mas; [228, 229]), and the estimated uncertainties from the phase-referencing technique (0.13 and 0.2 mas; [230]) added in quadrature.

The derived peak brightness measurements are $85 \pm 13 \mu\text{Jy beam}^{-1}$ and $73 \pm 12 \mu\text{Jy beam}^{-1}$, respectively, where the errors comprise both the r.m.s. noise uncertainty and a 10% calibration error, added in quadrature. The r.m.s. noise uncertainties are $9 \mu\text{Jy beam}^{-1}$ and $10 \mu\text{Jy beam}^{-1}$, hence the detections have a significance of 9.4 and 7.3σ confidence, respectively. No significant emission above the 3σ r.m.s. level ($\sigma = 13 \mu\text{Jy beam}^{-1}$) was reported in the third epoch. The data are shown in Figure 4.2 as blue squares. The upper limits for the flux densities in the radio band were taken with 3σ confidence level. The full list of radio observations is given in Table 4.1.

4.3.2 Optical

At 1.4 and 2.2 days post-burst, we clearly detected the optical afterglow in both *i* and *z* bands at $\alpha = 23^{\text{h}}37^{\text{m}}16.43^{\text{s}}$, $\delta = +53^{\circ}24'56.6''$ (J2000; uncertainty = $0.2''$). In addition, we detected the host galaxy at $\alpha = 23^{\text{h}}37^{\text{m}}16.48^{\text{s}}$, $\delta = +53^{\circ}24'54.6''$ (J2000; uncertainty = $0.2''$).

The optical light curve is shown in Figure 4.2: *g*-band data from [192] (green hexagons), [193]

Date	UTC [hh:mm]	T-T ₀ [days]	T _s [hour]	ν [GHz]	Peak Brightness [μ Jy/beam]	r.m.s. [μ Jy/beam]	Array	Beam size
2020/10/17	8:58 – 9:38	1.4	0.7	4.23 – 7.10	132	5	VLA	1.70" \times 1.14"
2020/11/04	21:25 – 06:30	20	9.2	1.25 – 1.76	213	34	<i>e</i> -MERLIN	0.18" \times 0.12"
2020/11/05	20:35 – 14:00	21	6.1	4.50 – 5.01	107	17	<i>e</i> -MERLIN	0.06" \times 0.04"
2020/11/07	22:00 – 11:40	23	14	1.25 – 1.76	261	40	<i>e</i> -MERLIN	0.19" \times 0.12"
2020/11/08	23:30 – 08:30	24	3.9	4.50 – 5.01	116	26	<i>e</i> -MERLIN	0.06" \times 0.04"
2020/11/09	13:00 – 23:00	25	4.2	4.57 – 5.11	85	9	EVN	1.8 mas \times 0.9 mas
2020/12/01	13:00 – 23:00	47	4.4	4.77 – 5.05	73	10	EVN	3.4 mas \times 2.8 mas
2020/12/14	09:18 – 12:43	60	1.4	6.55 – 7.06	-	43	<i>e</i> -MERLIN	0.12" \times 0.07"
2021/01/08	12:34 – 03:10	85	6.9	4.50 – 5.01	-	19	<i>e</i> -MERLIN	0.04" \times 0.04"
2021/01/23	17:35 – 08:55	100	8.9	4.50 – 5.01	-	16	<i>e</i> -MERLIN	0.07" \times 0.03"
2021/01/24	11:00 – 01:20	101	14	1.25 – 1.76	-	57	<i>e</i> -MERLIN	0.17" \times 0.14"
2021/02/09	13:00 – 18:00 & 06:00 – 11:00	117	5.0	4.77 – 5.05	-	13	EVN	3.1 mas \times 3.6 mas

Table 4.1: Radio observations performed with the VLA, *e*-MERLIN, and EVN in the L- and C-bands. T-T₀ is the total time from the GRB trigger to half of the observation, while T_s is the total time on source. The 1 σ r.m.s. noise shown does not include the systematic flux density uncertainty (which we consider as 5% for the VLA and 10% for *e*-MERLIN and EVN throughout the work).

(green dots) and [186] (green circles); *r*-band data from [190] (red pentagons), [192] (red stars), [189, 195] (red hexagons), [197] (red diamonds), [193] (thin red diamonds), [231] (red plus), [198] (red circles); *i*-band data from [193] (purple squares) and our MMT/Binospec observations (purple circles); our *z*-band MMT/Binospec observations (brown circles).

The emission peaked between 200–300 s after the GRB trigger, reaching a maximum of $R \sim 16.5$ mag ([191]; [189]). Between 0.1 and 3 days our light curve follows a power law $F(t) \propto t^{-0.84 \pm 0.06}$, which is consistent with previous results in the GCNs [198]. Remarkably, a type Ic-BL supernova (SN) contribution can be seen between 3 and 20 days after the burst [198, 232], which corroborates the long-duration nature of this burst.

4.3.3 X-rays

The *Swift*-XRT light curve was further analysed by splitting the last two observations in four time intervals. We retrieved the XRT spectral files from the online archive⁷ and analyse them with the public software XSPEC v12.10.1F, assuming a simple power-law model. The `tbabs` model for the Galactic absorption and the `ztbabs` model for the host galaxy absorption, adopting the source redshift $z = 0.426$, are used in the fitting procedure. The absorption parameters are fixed to the values reported by the *Swift* website for this burst, namely $N_{\text{H,gal}} = 3.6 \times 10^{21}$ atoms cm^{-2} [233, 234] and $N_{\text{H,intr}} = 5 \times 10^{21}$ atoms cm^{-2} . Leaving the normalisation and the photon index of the power-law free to vary, we find integrated fluxes consistent with those reported on the *Swift* website.

From our two epochs of *Chandra* observations we find 0.5 – 7 keV source count rates of $(4.07 \pm 0.38) \times 10^{-3}$ cts/s and $(3.11 \pm 0.29) \times 10^{-3}$ cts/s. In a combined spectral fit of both *Chandra* epochs and the late XRT observations (> 10 days), the data are well modelled (cstat/dof = 600/1808) by an absorbed power law of the form `POWERLAW*TBABS*ZTBABS` [235] with a photon index of $\Gamma = 2.10 \pm 0.13$. The intrinsic absorption column is fixed to $N_{\text{H,intr}} = 5 \times 10^{21}$ atoms cm^{-2} at $z = 0.426$ over the Galactic value of $N_{\text{H,gal}} = 3.6 \times 10^{21}$ atoms cm^{-2} [233, 234] to match those reported on the UKSSDC. From this we derived unabsorbed 0.3–10 keV fluxes of $(1.26 \pm 0.05) \times 10^{-13}$ erg $\text{cm}^{-2} \text{s}^{-1}$ at 8.4 days and $(1.10 \pm 0.04) \times 10^{-13}$ erg $\text{cm}^{-2} \text{s}^{-1}$ at 13.6 days.

The X-ray light curve is shown in Figure 4.2 for the *Swift*-XRT public data (dark blue circles) and our *Chandra* observations (dark blue squares). For the *Swift*-XRT light curve we included the results from the SWIFT BURST ANALYZER up to ~ 0.12 days, and from that epoch

⁷https://www.swift.ac.uk/xrt_spectra

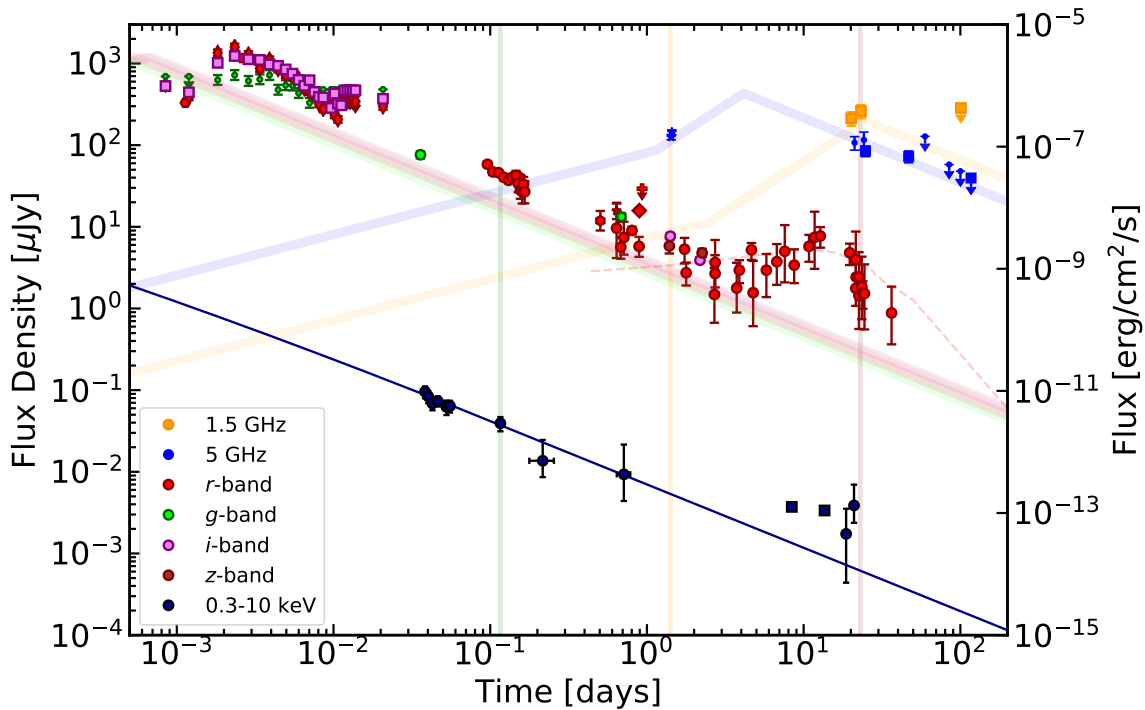


Figure 4.2: Multi-wavelength afterglow light curves (see Section 4.3). For each band the light curves predicted by the standard model with $\nu_a = 13$ GHz, $\nu_i = 6$ GHz, $\nu_c = 2 \times 10^7$ GHz, $F_p = 800 \mu\text{Jy}$, and $p = 2.05$ at 1 day for a homogeneous surrounding medium are shown: 1.5 GHz (orange); 5 GHz (blue); r , g , i , and z bands (red, lime, violet, and brown, respectively); integrated X-ray light curve (dark blue). The green, orange, and brown vertical lines pinpoint the epochs of the spectra at 0.12, 1.41, and 23 days, respectively (see also Figure 4.3). The dashed line shows a simple model for the SN contribution in the r band (see Section 4.5.1).

on we used our re-analysis of the last two observations. Our XRT analysis suggests that the light curve can be fitted with a power law with index $F^{-1.1 \pm 0.3}$ between 0.04 and 0.71 days post-burst, which is shallower but still consistent with the previous analysis from [236]. However, the subsequent detections at 8.4 and 13.6 days with *Chandra* show a respective flux ~ 6 and 8 times higher than expected from extrapolating the earlier XRT light curve, and the increased flux is further confirmed by the late time (~ 20 days after the burst) *Swift*-XRT follow-up [202].

4.4 Broadband modelling

As shown in Chapter 2, the multi-wavelength afterglow synchrotron emission of a GRB seen on-axis can be studied through a standard model. First, assuming that the flux density can be parametrised as $F \propto \nu^\beta t^\alpha$, the spectrum can be fitted with several power law segments, which join at specific break frequencies: (i) the self-absorption frequency ν_a , (ii) the maximum frequency ν_i , and (iii) the cooling frequency ν_c . The other parameters needed to build the spectrum are (iv) the maximum flux density F_p and (v) the electron distribution index p . Once we have determined these quantities and their temporal evolution, the multi-wavelength light curves are constrained. In this chapter we use the relations provided by [150], and throughout the work we consider two possible density profiles for the circum-burst medium: a wind-like profile $n = Ar^{-2}$, which is naturally expected if the progenitor is a massive star collapsing into a BH or a NS, and a homogeneous surrounding medium $n = \text{const}$, which can be ascribed either to the canonical ISM or to a wind bubble shocked against the ISM [237]. Hereafter we use the

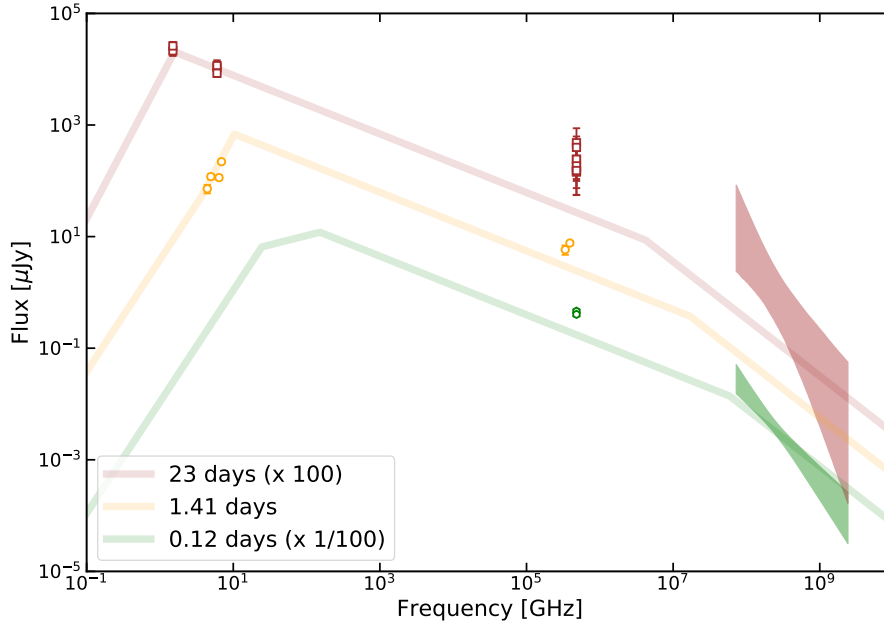


Figure 4.3: Spectra at 0.12 (green), 1.41 (orange), and 23 (brown) days after the GRB onset for a homogeneous surrounding medium with $\nu_a = 13$ GHz, $\nu_i = 6$ GHz, $\nu_c = 2 \times 10^7$ GHz, $F_p = 800 \mu\text{Jy}$, and $p = 2.05$ at 1 day. *Spectrum at 0.12 days*: Optical observations from [198] and XRT butterfly plot. *Spectrum at 1.41 days*: Our VLA and MMT detections. *Spectrum at 23 days*: Our 1.5 and 5 GHz observations, optical data from [198] and the XRT butterfly plot; the optical emission is dominated by the SN component.

term ISM for a homogeneous profile indiscriminately.

We note that in our modelling we do not include the description of the coasting phase, the contribution from the RS, or the late time SN emission. A more sophisticated modelling that comprises the RS contribution would introduce more parameters; if frequent observations are available around the epoch at which the RS is supposed to prevail (at about 1 day in the radio band; see e.g. [215]) these parameters can be constrained. With only one detection in the C-band before 20 days post-burst, we could not constrain the parameters. In the optical, the emission before 0.01 days shows a bump that could be due to a possible RS contribution, while after 3 days the SN emission becomes dominant [198, 232], hence the prediction of the modelling should be considered only from about 0.01 to 3 days post-burst in this band.

To derive the modelling light curves, we performed a comparison of the simplified afterglow prescription with the available data, changing the above-mentioned parameters to get as close as possible to the observed multi-wavelength light curves and to reproduce the afterglow spectrum at three sampling epochs, namely 0.12, 1.41, and 23 days after the GRB trigger (see Figure 4.3).

4.4.1 ISM profile

For the ISM profile we built the spectrum at 0.12 days, with the optical r band from [198] and the XRT detections at 1.41 days with the VLA detection (see Section 4.3) and our optical i - and z -band observations, and the spectrum at 23 days with our radio detection at 1.5 and 5 GHz, the optical r band from [198], and the last XRT detection (Figure 4.3). From the spectra and the multi-wavelength light curves we constrain the parameter space as follows. First, from the spectral index $\beta = 2.3 \pm 0.1$ derived with the VLA data we cannot discern whether the emission at 6 GHz lies in the ν^2 or $\nu^{5/2}$ portion of the spectrum at 1.41 days, and therefore we consider three different cases. At this epoch it could be that (i) $6 \text{ GHz} < \nu_a < \nu_i$, (ii) $\nu_i < 6 \text{ GHz} < \nu_a$, or (iii) $6 \text{ GHz} < \nu_i \leq \nu_a$. Moreover, at 23 days the spectral slope between 1.5 GHz and

5 GHz is reversed, meaning that the flux density is decreasing with the frequency, and hence we expect that $\nu_i < \nu_a < 1.5$ GHz. Finally, at 23 days the optical emission is dominated by the SN, hence we consider the optical detections as upper limits. To build the modelling light curves and spectra we derive the break frequencies, the p value, and the maximum flux density F_p at 1 day, in order to simplify the equations from [150].

(i) If $6 \text{ GHz} < \nu_a < \nu_i$, since $\nu_i > 6 \text{ GHz}$ at 1.41 days, $\nu_i \propto t^{-3/2}$ and ν_a is constant in time, to avoid ν_i crossing ν_a before 1.41 days we impose $\nu_i > 15 \text{ GHz}$ and $\nu_a > 9 \text{ GHz}$ at 1 day. However, once ν_i crosses ν_a , $\nu_a \propto t^{-(3p+2)/(2(p+4))}$. Therefore at 1 day $\nu_a < 13 \text{ GHz}$, otherwise at 23 days $\nu_a > 1.5 \text{ GHz}$, and consequently $\nu_i < 24 \text{ GHz}$ (otherwise it does not cross ν_a before 23 days). At 1 day the flux density at ν_i is found to be $500 \mu\text{Jy} < F_p < 600 \mu\text{Jy}$. With a lower F_p we underestimate the emission at 5 GHz observed with EVN, while with a higher flux we overestimate the e -MERLIN detections at the same frequency. With the slope of the optical light curve we can constrain the p value: since the light curve shows a clear slope that can be described by a single power law between 0.01 and 3 days, $\nu_i < \text{optical} < \nu_c$ and $F \propto t^{3(1-p)/4}$ in this regime. Finally, the X-ray integrated light curve allows us to further constrain p and determine ν_c : for $\nu < \nu_c$ we have $F \propto t^{3(1-p)/4}$, while for $\nu > \nu_c$ we have $F \propto t^{(2-3p)/4}$; hence, the sooner ν_c crosses the X-ray band, the fainter the detected emission will be. In summary, to reproduce both the spectra and the light curves we find that $9 \text{ GHz} < \nu_a < 13 \text{ GHz}$, $15 \text{ GHz} < \nu_i < 24 \text{ GHz}$, $5 \times 10^6 \text{ GHz} < \nu_c < 10^8 \text{ GHz}$, $500 \mu\text{Jy} < F_p < 600 \mu\text{Jy}$ and $2.01 < p < 2.10$ at 1 day.

(ii) If $\nu_i < 6 \text{ GHz} < \nu_a$ at 1.41 days, since $\nu_a \propto t^{-(3p+2)/(2(p+4))}$, we impose that $\nu_a > 10 \text{ GHz}$ at 1 day; moreover, $\nu_a < 18 \text{ GHz}$ at 1 day, otherwise at 23 days $\nu_a > 2 \text{ GHz}$ and our detections at 1.5 GHz would lie in the $\nu^{5/2}$ portion of the spectrum and the emission at 5 GHz would be overestimated. To reproduce the spectra and the light curves we find that the range for ν_a is further constrained to $13 \text{ GHz} < \nu_a < 16 \text{ GHz}$. Since at 1.41 days $\nu_i \leq 4 \text{ GHz}$ (otherwise the lowest end of the bandwidth of the VLA detection would be underestimated), at 1 day $\nu_i \leq 7 \text{ GHz}$. Finally, with the same argument presented in case (i), we find that at 1 day $6 \times 10^6 \text{ GHz} < \nu_c < 10^8 \text{ GHz}$, $800 \mu\text{Jy} < F_p < 1 \text{ mJy}$ and $2.01 < p < 2.20$. We note that in this case F_p refers to the flux density at ν_a .

(iii) If $6 \text{ GHz} < \nu_i \leq \nu_a$ at 1.41 days, we can have both $6 \text{ GHz} < \nu_i < \nu_a$ and $6 \text{ GHz} < \nu_a < \nu_i$ at 1 day. Considering both these sub-cases, since $\nu_i \propto t^{-3/2}$, at 1 day $\nu_i > 13 \text{ GHz}$, otherwise at 1.41 days $\nu_i < 8 \text{ GHz}$ and it would lie too close to the highest end of the bandwidth of the VLA detection to reproduce the spectrum; conversely, if at 1 day $\nu_i > 18 \text{ GHz}$, we cannot reproduce the light curve in the C-band because the detections at 6 GHz with the VLA are underestimated, while e -MERLIN and EVN observations are overestimated. Since at 1.41 days $\nu_a \geq \nu_i$, we find that $13 \text{ GHz} < \nu_a < 18 \text{ GHz}$ (for larger values we cannot reproduce the C-band light curve). Once again, with the same argument presented in case (i), we derived $5 \times 10^6 \text{ GHz} < \nu_c < 2 \times 10^8 \text{ GHz}$, $630 \mu\text{Jy} < F_p < 1 \text{ mJy}$ and $2.01 < p < 2.20$ at 1 day. In this case F_p refers to the flux density of ν_a or ν_i for the two sub-cases. We note that these ranges for the parameters are the superposition of the ranges derived for the two sub-cases.

In Table 4.2 we report our results for the parameter space at 1 day. The model light curves for the ISM profile are shown in Figure 4.2 for $\nu_a = 13 \text{ GHz}$, $\nu_i = 6 \text{ GHz}$, $\nu_c = 2 \times 10^7 \text{ GHz}$, $F_p = 800 \mu\text{Jy}$ at 1 day, and an electron distribution index $p = 2.05$. The 1.5 GHz and the 5 GHz light curve are displayed in orange and blue, respectively; the r , g , i , and z bands are in red, lime, violet, and brown, respectively; the X-ray light curve is displayed in dark blue. Although this modelling provides a satisfactory description of the multi-wavelength light curves, the optical light curve contains the already discussed features in addition to the forward shock emission: before 0.01 days there is a bump which could be due to a possible RS contribution, while after three days the SN emission becomes dominant [198, 232].

Parameter	Range
ν_a	9 – 18 GHz
ν_i	≤ 7 GHz \cup 13 – 24 GHz
ν_c	5×10^6 – 2×10^8 GHz
F_p	0.5–1 mJy
p	2.01 – 2.20

Table 4.2: Constraints on the model parameters at 1 day for a homogeneous circumburst medium.

4.4.2 Wind-like profile

For the wind-like profile we first tried to reproduce the optical and X-ray data, finding that $\nu_a = 1$ GHz, $\nu_i = 30$ GHz, $\nu_c = 2 \times 10^7$ GHz, $F_p = 200$ μ Jy at 1 day, and the electron distribution index $p = 2.01$. Since this model conspicuously failed to reproduce the radio detections and the optical slope, we tried to reproduce the radio light curve at 5 GHz first, and we found that $\nu_a = 4$ GHz, $\nu_i = 10^3$ GHz, $\nu_c = 2 \times 10^7$ GHz, $F_p = 600$ μ Jy at 1 day, and the electron distribution index $p = 2.01$. Neither of these models reproduces the optical slope, and the second model fails to reproduce the X-ray emission. Different choices of the parameters in the wind-like scenario provide even poorer fits. We can therefore conclude that the modelling provided by the ISM provides the best agreement with the data, and we consider it hereafter. We note that this further corroborates the need of X-ray, optical, and radio observations in order to break the degeneracy in the afterglow modelling, as with only two of them data can be misinterpreted.

4.4.3 Intrinsic host galaxy extinction

As pointed out by [238], the intrinsic host galaxy extinction can be relevant in the optical/NIR. By changing the model parameters, we tried overestimating the optical emission and, from the discrepancy between the observed and the modelled optical flux densities, the contribution due to the intrinsic host galaxy absorption can be estimated. However, our modelling light curves and spectra cannot predict values for the flux density that are larger than those observed in the optical data. Moreover, by changing the maximum flux density and the p -value, we cannot reproduce the observed light curves in the radio band. As our modelling light curve already underestimates the afterglow optical emission (see Figure 4.3), by adding the intrinsic host galaxy extinction the discrepancy would increase. Therefore the only constraint we can put on the intrinsic host galaxy absorption is that it is negligible, if we assume that the model is correct. Although more sophisticated models could take into account this further correction, this is beyond the goals of this work.

4.5 Discussion

Once the free parameters ν_a , ν_i , ν_c , F_p , and p are constrained, we can exploit the relations provided by [150] to derive the global and microphysical parameters of the jet: the isotropic kinetic energy E , the density of the medium that surrounds the progenitor n , the fraction of internal energy retained by the magnetic field ϵ_B , and the fraction of internal energy retained by the electrons ϵ_e . From the conservation of energy we know that $\epsilon_e \leq 1$, $\epsilon_B \leq 1$, and $\epsilon_e + \epsilon_B \leq 1$. A further constraint is given by the VHE emission; if we consider the sub-TeV emission to be due to the SSC from the relativistic electrons, then $\epsilon_e \geq \epsilon_B$ [134, 239]. If we try to solve the equations from [150], the inferred parameters violate the conservation of energy (i.e. $\epsilon_e + \epsilon_B \geq 1$); however, these values are determined under the implicit assumption that all the electrons that

Parameter	Value	Median	
		ISM Sample	RS Sample
E_{52}/erg	$0.03 - 10^3$	12	20
ϵ_e	$10^{-4} - 0.99$	0.32	0.104
ϵ_B	$8 \times 10^{-7} - 0.05$	2.7×10^{-2}	1.4×10^{-4}
n/cm^{-3}	$0.4 - 2 \times 10^4$	1.5	2.15
f	$0.01 - 1.00$		

Table 4.3: Global and microphysical parameters for GRB 201015A in the ISM scenario. The parameter name and the inferred value are listed in the first and second column, respectively. The median of the sample by [237] for those bursts that can be reproduced with an ISM profile is reported in the third column (ISM Sample), while the median for the sample of bursts with a claimed RS component is reported in the fourth column (RS Sample).

Parameter	Value	Median	
		ISM Sample	RS Sample
E_{52}/erg	$0.03 - 14$	12	20
ϵ_e	$0.05 - 0.15$	0.32	0.104
ϵ_B	$1.5 \times 10^{-6} - 0.05$	2.7×10^{-2}	1.4×10^{-4}
n/cm^{-3}	$0.4 - 10^4$	1.5	2.15
f	$0.02 - 1.00$		

Table 4.4: Global and microphysical parameters for GRB 201015A in the ISM scenario if $0.05 \leq \epsilon_e \leq 0.15$. The parameter name and the inferred value are listed in the first and second column, respectively. The median of the sample by [237] for those bursts that can be reproduced with an ISM profile is reported in the third column (ISM Sample), while the median for the sample of bursts with a claimed RS component is reported in the fourth column (RS Sample).

are swept up by the forward shocks are accelerated, while this is expected to be true only for a fraction f of them. As shown by [240], if $m_e/m_p \leq f \leq 1$ the observed emission does not change when scaling the parameters as follows: $E \rightarrow E/f$, $\epsilon_e \rightarrow \epsilon_e f$, $\epsilon_B \rightarrow \epsilon_B f$, $n \rightarrow n/f$ [55]. In order to find the solutions, we make E and ϵ_e vary within physically reasonable ranges (i.e. $10^{50} \text{ erg} \leq E \leq 10^{55} \text{ erg}$ and $10^{-4} \leq \epsilon_e \leq 1$), and we subsequently calculate ϵ_B and n using the inferred break frequencies, F_p and p . Finally, we apply the constraints given by the conservation of energy and the sub-TeV emission. The final solutions are listed in the second column of Table 4.3.

Furthermore, since we expect ϵ_e to be of the order of 0.1 from numerical simulations [241], we provide the full set of inferred values for the $0.05 \leq \epsilon_e \leq 0.15$ case in the second column of Table 4.4. We find that the isotropic kinetic energy goes from 3×10^{50} to 10^{55} erg. If we consider the isotropic-equivalent energy derived by [209] from the prompt emission, we can roughly estimate the efficiency of the prompt emission as $\eta = E_{iso}/(E + E_{iso})$. We estimate that $\eta \simeq 10^{-3}$ –27%.

To discuss these values in a broader context we consider a recent work by [237], who examined 26 GRBs with well-sampled broadband data sets. The authors found that ϵ_B ranges from $\approx 2.6 \times 10^{-6}$ (GRB 030329) to ≈ 0.91 (GRB 130907A) for those GRBs that can be described with an ISM profile (hereafter ISM Sample), and 3 out of 13 GRBs have $\epsilon_B \geq 0.5$; for ϵ_e they found a range between ≈ 0.14 (GRB 090328) and ≈ 0.89 (GRB 010222); finally, n goes from $\approx 5 \times 10^{-3}$ (GRB 010222) to $\approx 390 \text{ cm}^{-3}$ (GRB 030329).

We then consider long GRBs with a claimed RS detection (in X-rays, optical, and/or radio)

whose multi-wavelength light curves can be aptly described with an ISM profile (hereafter RS Sample): GRB 990123, 021004, 021211, 060908, 061126, 080319B, 090102, and 090424 [154]; GRB 130427A [58]; GRB 160509A [242]; GRB 160625B [56]; GRB 161219B [159]; GRB 180720B [243]; GRB 190829A [215]. The circumburst density for the GRBs of the RS Sample goes from $\approx 5 \times 10^{-5} \text{ cm}^{-3}$ for GRB 160625B to $\approx 360 \text{ cm}^{-3}$ for GRB 090201, while ϵ_e ranges from $\approx 4 \times 10^{-4}$ for GRB 090102 to ≈ 0.93 for 161219B and ϵ_B goes from $\approx 2 \times 10^{-5}$ for GRB 090102 to ≈ 0.11 for GRB 160509A. The values we infer for GRB 201015A are therefore consistent with those found in the ISM and RS samples, even though the surrounding density is generally higher.

Finally, we consider three GRBs that have been detected at VHE: GRB 180720B, GRB 190114C, and GRB 190829A. For these bursts ϵ_e goes from 0.02 (GRB 190114C; [244]) to 0.1 (GRB 180720B; [243]); ϵ_B goes from 4.7×10^{-5} (GRB 190114C; [244]) to 10^{-4} (GRB 180720B; [243]); and the surrounding medium density n goes from 0.1 (GRB 180720B; [243]) to 23 (GRB 190114C; [244]). These values are consistent with those we derive for GRB 201015A in this work.

From the maximum flux density F_p at 8.5 GHz we calculate the luminosity L of the afterglow with $L = F_p 4\pi d_l^2 (1+z)^{\beta-\alpha-1}$ [44], where d_l is the luminosity distance in cm, F_p is expressed in $\text{erg s}^{-1} \text{ cm}^{-2} \text{ Hz}^{-1}$, z is the redshift, and $\alpha = \beta = 0$ since the peak in the light curve is also a peak in the spectrum. We find that $L \simeq 3.5 \times 10^{30} \text{ erg s}^{-1} \text{ Hz}^{-1}$ at 1.9 days, which is slightly below the average value for radio-detected GRB afterglows [44]. Finally, the maximum luminosity $L \simeq 5.4 \times 10^{30} \text{ erg s}^{-1} \text{ Hz}^{-1}$ at 15.7 GHz at 0.8 days is consistent with the radio luminosity previously found for the other GRBs detected at VHE [215].

We note that the allowed ranges inferred for the microphysical and global parameters of GRB 201015A are too large to pinpoint any possible deviation of this burst from the samples we used, and hence to derive important information on the production of VHE photons in GRBs. Moreover, a population study is still hindered by the paucity of GRBs detected at VHE and their proximity ($z < 1.1$), which could lead to a strong bias. A larger and more complete sample is therefore needed. On the other hand, the fact that we cannot flag any possible deviation from the mentioned samples could be consistent with the VHE GRBs being drawn from the same parent population as the other radio-detected long GRBs [215].

4.5.1 Additional emission components

It is worth noting that a refined model could possibly be obtained by including the RS component, whose prescription could explain the bump and the observed excess in the optical emission before 0.01 days. All the GRBs with a confirmed VHE emission were in fact successfully modelled once a RS component was included: GRB 180720B [243, 245], GRB 190114C [246], GRB 190829A [215].

Concerning the SN emission, if we take the emission of SN1998bw in the r band [105], de-absorb the flux density using $A_V = 0.2$ [105], and move the SN to $z = 0.426$ and seven days earlier, we find that its light curve is consistent with that observed for GRB 201015A after three days from the burst (see Figure 4.2, dashed line). This further strengthens the SN origin of the bump observed around ten days post-burst.

Finally, we suggest that a transition between the wind-like profile and the ISM profile at around 0.1 – 0.2 days could possibly explain the change in slope observed in the X-ray light curve after ~ 0.2 days (see e.g. [247, 248]). The optical slope between 0.03 and 0.2 days follows a power law $F \propto t^{-1.1 \pm 0.2}$, which is consistent with the prediction from a model with a wind-like profile, namely $F \propto t^{-1.3}$, if the optical lies between ν_m and ν_c . The prediction for the fireball model with a homogeneous circumburst medium is $F \propto t^{-0.8}$, which is still consistent but shallower.

4.5.2 High-resolution observations

To measure the expansion or the proper motion of the outflow, a high signal-to-noise ratio is required as it allows both a follow-up of the afterglow up to later times and a smaller uncertainty on the position of the detected source [171]. While we achieved a milliarcsecond angular resolution with EVN, we could not pinpoint any displacement of the centroid (off-axis GRB, [100, 101]) nor an expansion of the source (on-axis GRB, [249]).

The position of the afterglow in the two detections with EVN is consistent within the uncertainties (i.e. $\Delta\alpha = 0.2 \text{ mas}$ and $\Delta\delta = 0.3 \text{ mas}$). At $z = 0.426$, the centroid displacement before 47 days post-burst is therefore smaller than 1.1 pc in right ascension and 1.7 pc in declination; assuming that the burst is observed at the viewing angle θ that maximises the apparent velocity $\beta_{app} = \Gamma$ (i.e. $\theta \sim \beta_{app}^{-1}$), we derive a Lorentz factor upper limit of $\Gamma_\alpha \leq 40$ in right ascension and $\Gamma_\delta \leq 61$ in declination. Considering the previous outstanding burst for which a proper motion was observed (i.e. GRB 170817A at $z = 0.0093$), a displacement of the same magnitude as that of GRB 170817A would have been seen as 0.08 mas at $z = 0.426$ after ~ 207 days post-burst.

On the other hand, if the GRB is seen on-axis, by taking the minor axis of the beam we constrain the size of the afterglow to be $\leq 5 \text{ pc}$ and $\leq 16 \text{ pc}$ at 25 and 47 days, respectively. Considering the only case for which the expansion was confirmed (i.e. GRB 030329 at $z = 0.1685$), an expansion of the same magnitude as that of GRB 030329 would have been seen as 0.09 mas at $z = 0.426$ after ~ 80 days post-burst.

Since our best resolution with EVN is $1.8 \text{ mas} \times 0.9 \text{ mas}$, we would have detected such an expansion or displacement if (i) the size of the beam had not changed in later observations; (ii) the afterglow had been observable and detectable with a signal-to-noise ratio higher than 10 for about 200 days and 80 days in the case of displacement and expansion, respectively; and (iii) the displacement or expansion had occurred along the coordinate corresponding to the minor axis of the beam.

Conversely, considering the worst resolution reached with our VLBI observations, $3.1 \text{ mas} \times 3.6 \text{ mas}$, we would have pinpointed these effects if the afterglow had been detectable for about 800 days or 320 days in the case of proper motion and expansion, respectively, so that the measurements to be performed would have been of the order of 0.3 mas.

4.5.3 Host galaxy

The host galaxy was first pinpointed by [190] and subsequently confirmed by [194] and [232], who found a magnitude $r = 22.9 \pm 0.2$. With the MMT observations, we derive the position of the host of $\alpha = 23^{\text{h}}37^{\text{m}}16.4757^{\text{s}}$, $\delta = +53^{\circ}24'54.626''$ (J2000; uncertainty = 0.235 arcsec); this is found to be $1.86''$ from the source observed at 1.5 GHz, which corresponds to roughly 10 kpc at $z = 0.426$. The uncertainty in the radio position at 1.5 GHz is $0.03''$, which is $\sim 170 \text{ pc}$, and therefore we can state that the emission observed at 1.5 GHz is consistent with being generated by the afterglow. Moreover, as the beam size at 1.5 GHz is roughly $0.18'' \times 0.12''$, the emitting region should be of the order of $1 \text{ kpc} \times 0.7 \text{ kpc}$; if the detected emission were caused by a very active star-forming region, we would have observed a stable emission in the optical at the same position instead of a transient event.

A safe discrimination between the galactic contamination and the proper afterglow emission at 1.5 GHz could also be achieved with a higher resolution and an improved sensitivity in late epochs in order to obtain better constraints on the light curve. While the former requirement is provided by VLBI observations, the latter is reached with the Pathfinders of the SKA: MeerKAT and the Australian Square Kilometre Array Pathfinder (ASKAP). Moreover, a better sensitivity allows the detection of possible late time jet breaks, and therefore the measurement of the jet opening angle.

4.6 Conclusions

GRB 201015A was a nearby ($z = 0.426$; [188, 210]) long-duration GRB discovered on 2020 October 15 by *Swift*-BAT [182]. Its long-lasting afterglow emission has been observed from γ rays down to radio bands; it is claimed to be the fifth GRB ever detected at VHE energies [207, 208].

We performed a radio follow-up with the VLA, *e*-MERLIN, and EVN at 1.5 and 5 GHz over 12 epochs from 1.4 to 117 days after the GRB onset. At 5 GHz we detected a point-like source consistent with the afterglow position on 2020 October 17; 2020 November 5, 8, and 9; and 2020 December 1; conversely, on 2020 December 14, 2021 January 8 and 23, and 2021 February 9 no source was detected. At 1.5 GHz we detected a point-like source on 2020 November 4 and 7, while on 2021 January 24 no source was detected.

We observed and detected the afterglow of GRB 201015A also in X-rays with *Chandra* (8.4 and 13.6 days post-burst) and in the optical with MMT (1.4 and 2.2 days post-burst). Finally, we collected public X-ray data from *Swift*-XRT and optical data from the GCN Circulars Archive. We built multi-wavelength light curves and three spectra at 0.12, 1.41, and 23 days post-burst, and we exploited the standard model provided by [150] for a sharp-edged jet seen on-axis to constrain the global and microphysical parameters of the outflow. We find that the observed light curves can be reproduced with a homogeneous circumburst medium profile, and that the parameters we derived for GRB 201015A are consistent with those previously found in the literature for other GRBs, even though we caution that a fully reliable modelling will require a proper characterisation of the VHE detection, which was unavailable at the time of writing.

Despite the high angular resolution we achieved with the EVN observations, we could not pinpoint any change in the afterglow position. If the GRB is seen slightly off-axis, we constrain the proper motion of the outflow to be smaller than 1.1 pc in right ascension and 1.7 pc in declination before 47 days post-burst. This proper motion corresponds to a Lorentz factor upper limit of $\Gamma_\alpha \leq 40$ in right ascension and $\Gamma_\delta \leq 61$ in declination, if we assume that the GRB is seen at the viewing angle θ which maximises the apparent velocity β_{app} (i.e. $\theta \sim \beta_{app}^{-1}$). Conversely, if the GRB is seen on-axis, we find that the size of the afterglow is ≤ 5 pc and ≤ 16 pc at 25 and 47 days, respectively.

We note that the bump before 0.01 days post-burst in the optical light curve could be explained by an RS component. On the other hand, we find that the *Chandra* and the last *Swift*-XRT detections are brighter than expected from the model and from the extrapolation of the previous data points. Even though further observations are needed, a late time central engine activity or a transition from a wind-like profile to a homogeneous surrounding medium at early times could possibly explain the change in the slope of the X-ray light curve.

Chapter 5

GRB 221009A

In this chapter I present the VLBI campaign we carried out to pinpoint the expansion of GRB 221009A. The following work is currently under review by *Astronomy & Astrophysics* with the title “*The expansion of the GRB 221009A afterglow*”.

5.1 Introduction

On the 9th October 2022, all satellites equipped for transient detection were triggered by the extraordinary GRB 221009A [250–263]. At a redshift of $z = 0.151$ [264, 265], GRB 221009A holds the record of the highest ever measured isotropic equivalent energy, $E_{\gamma,\text{iso}} \gtrsim 10^{55}$ erg [266]. Relative to other GRBs observed in the past half century, it is the brightest of all time and it is estimated to have a 1 in ~ 10000 -year occurrence based on the observed flux distribution of other known long GRBs [265, 267, 268]. Such a unique event initiated an unprecedented follow-up campaign, characterised by extensive temporal and spectral coverage. At the highest energies, the LHAASO Collaboration reported the detection of sustained emission well above 1 TeV [63, 269]. At the lower end of the electromagnetic spectrum, radio observations of GRB 221009A commenced just three hours post-burst and detected the brightest ever radio counterpart, reaching a flux density of 60 mJy [270]. Initial attempts to model the multi-wavelength afterglow emission considered contributions from both the RS and the FS resulting from the deceleration of the ultra-relativistic jet by the surrounding material [267, 271–274]. However, uncertainties persist in the final interpretation of the data, despite incorporating most of the presently known physical ingredients governing the dynamics and emission of GRB jets.

Unique measurements able to independently constrain the afterglow evolution can be obtained with milliarcsecond resolution observations. VLBI allows for direct measurements of the size of the emission region, together with high-precision astrometry. As a result, proper motion and source expansion can be measured [100, 101, 249]. If the viewing angle θ_v between the observer line of sight and the GRB jet axis is smaller than the jet half-opening angle θ_j (‘on-axis’ GRB), the projected image during the afterglow is expected to expand, but not to show appreciable proper motion. Conversely, if the outflow is observed ‘off-axis’ ($\theta_v > \theta_j$), an apparent superluminal motion is expected. To date, measurements of the size and expansion of the emitting region have only been possible for GRB 030329 [249, 275], providing the first direct evidence of the relativistic expansion of GRB outflows. Over the last two decades, numerous campaigns were aimed to repeat the success of GRB 030329 [137, 276, 277]. However, no event shone brightly and long enough to provide an expansion measurement. On the other hand, for the multi-messenger event GW 170817 [90, 91, 96], VLBI observations were fundamental to measure the apparent superluminal motion and to constrain the size of the emitting region of the non-thermal electromagnetic counterpart [100, 101], proving, for the first time ever, that the mergers of two neutron stars are able to successfully launch ultra-relativistic jets.

In this chapter, I present our VLBI follow-up campaign of GRB 221009A. The method implemented to measure the source properties from radio observations is described in Sec. 5.3. In Sec. 5.4 I present the results of our campaign and discuss the physical implications in Sec. 5.5. Throughout the work, we assume [278] cosmological parameters. With these parameters, the angular diameter distance at $z = 0.151$ is $d_A = 560.3$ Mpc. Therefore, 1 mas separation corresponds to roughly 2.72 pc in projection at such a distance.

5.2 VLBI observations and data reduction

5.2.1 European VLBI Network

We observed the field of GRB 221009A with the EVN from 40 to 261 days post-burst (PI: Giarratana, project code: RG013). Given the target-of-opportunity nature of the proposal, not all antennas were available at all epochs. Table 5.2 in Appendix 5.7.1 lists the antennas joining each epoch. Table 5.1 presents a summary of the properties of the observations. The observations were performed in two different bands centred at 4.9 and 8.3 GHz, respectively. The data were recorded at 4 Gbits s⁻¹ and correlated at the JIVE (Dwingeloo, Netherlands) using the SFXC software correlator, [218] into sixteen sub-bands with 32 MHz bandwidth and 64 channels each, through two polarisations (RR, LL). For the last epoch, RG013 F, the data were correlated into eight sub-bands with 32 MHz bandwidth and 64 channels each. A first, EVN epoch (RG013 A), carried out 6 days post burst at a central frequency of 22.2 GHz, was not usable due to unfavourable observing conditions.

The observations consisted of phase-referencing cycles with 4.5 and 2.5 minutes on the target at 4.9 and 8.3 GHz, respectively, and 1.5 minutes on the phase calibrator. Further scans every approximately 30 minutes on some ‘check’ sources were also included. Throughout the observations, some scans on a fringe finder were performed. The radio source J1905+1943 and the VLASS compact radio source J191142+1952 were used as phase calibrators in the first two (RG013 B and C) and in the last three observations (RG013 D, E and F), respectively.

The calibration was performed using AIPS [219], following the standard procedure for EVN phase-referenced observations. The amplitude calibration, which accounts for the bandpass response, the antenna gain curves and the system temperatures, was performed using the results from the EVN pipeline. We performed a correction for the dispersive delay, we calculated a manual single band delay on the fringe finder and we carried out the global fringe fitting on the phase calibrator using a model of the source derived by a concatenation (in CASA, [217]) and self-calibration (in Difmap, [220]) of all the visibilities on the source obtained across the various epochs. Solutions were interpolated and applied to the phase calibrator itself, the target and some check sources (see Appendix 5.7.1). For the last three epochs, we corrected the visibilities of J191142+1952 by fixing the phase centre in CASA, as the position of this phase calibrator was not constrained with a sub-mas resolution.

Images of the sources were produced using Difmap. For the analysis presented in this manuscript, we selected the image with the best signal-to-noise ratio among the two images produced before and after the self-calibration of the phase calibrator, respectively. Further information on the structure and the data reduction process can be found in Appendix 5.7.1.

5.2.2 Very Long Baseline Array

The VLBA data were acquired between 44 and 262 days post-burst (PI: Atri, project code: BA160). The central frequency was 15.2 GHz, with a total bandwidth of 512 MHz, divided in 4 spectral windows of 128 MHz and 256 channels each, in dual polarisation. The number of participating stations contributing useful data was 7, 8, 10 and 10 in experiments BA160 B, C, C1

Table 5.1: Log table of our VLBI campaign and summary results of circular Gaussian fits to source visibilities.

Code	Date	Time [hh:mm UT]	$t_{\text{obs}} - t_0$ [days]	Array	ν_{obs} [GHz]	b_{maj}^{\dagger} [mas]	b_{min}^{\dagger} [mas]	$b_{\text{p.a.}}^{\dagger}$ [deg]	Phase Calibrator	r.m.s. [†] [$\mu\text{Jy}/\text{b}$]	F_{ν}^* [mJy]	FWHM* [mas]	$\langle\beta_{\text{app}}\rangle^*$ c
RG013 B	2022-11-18	09:30 – 13:30	40	EVN	8.1 – 8.6	1.4	0.45	11	J1905+1943	67	$0.99_{-0.06}^{+0.04}$	$0.14_{-0.05}^{+0.07}$	$5.7_{-2.5}^{+3.2}$
RG013 C	2022-11-21	09:30 – 13:30	43	EVN	4.6 – 5.1	4.3	0.75	11	J1905+1943	64	$1.29_{-0.01}^{+0.01}$	< 0.045	< 1.9
BA160 B	2022-11-22, 23	19:58 – 00:58	44	VLBA	14.9 – 15.3	1.4	0.40	–9	J1905+1943	130	$0.90_{-0.09}^{+0.08}$	$0.28_{-0.06}^{+0.08}$	$12_{-2.7}^{+3.1}$
BA160 C	2023-01-31	15:15 – 20:14	114	VLBA	14.9 – 15.3	1.4	0.58	3.5	J1905+1943	66	$0.27_{-0.08}^{+0.07}$	$0.56_{-0.33}^{+0.25}$	$8.7_{-4.9}^{+4.6}$
RG013 D	2023-02-03	05:30 – 11:30	117	EVN	4.6 – 5.1	7.1	0.9	7.8	J191142+1952	10	$0.44_{-0.02}^{+0.01}$	$0.14_{-0.13}^{+0.06}$	$2.1_{-2.0}^{+1.0}$
RG013 E	2023-02-04	05:30 – 11:30	118	EVN	8.1 – 8.6	1.4	0.59	10	J191142+1952	21	$0.49_{-0.05}^{+0.05}$	$0.29_{-0.08}^{+0.11}$	$4.8_{-1.5}^{+1.6}$
BA160 C1	2023-05-02	10:17 – 15:16	205	VLBA	14.9 – 15.3	1.5	0.51	–10	J1905+1943	35	$0.33_{-0.12}^{+0.14}$	$1.6_{-0.8}^{+0.6}$	$14.8_{-7.5}^{+5.2}$
RG013 F	2023-06-27, 28	19:30 – 02:36	261	EVN	4.8 – 5.1	1.8	1.5	62	J191142+1952	10	$0.15_{-0.02}^{+0.01}$	$0.51_{-0.19}^{+0.19}$	$3.6_{-1.4}^{+1.4}$
BA160 D	2023-06-28	04:08 – 09:19	262	VLBA	14.9 – 15.3	1.7	0.57	–3	J1905+1943	37	$0.31_{-0.27}^{+0.18}$	$4.0_{-2.8}^{+2.6}$	28_{-20}^{+18}

[†]Beam major axis, minor axis, position angle, r.m.s. noise level with natural weights.

*Median and 68% confidence interval of the flux density F_{ν} and full width at half maximum FWHM from fitting a circular Gaussian to the source visibilities; and of the average apparent expansion speed $\langle\beta_{\text{app}}\rangle$, assuming zero size at t_0 . If the lower extremum of the 68% credible interval is 0, we report the 95% upper limit instead.

and D respectively (see Table 5.2 in Appendix 5.7.1). Each observation includes approximately 30-minute-long geodetic-style blocks at the beginning and at the end of the observation, used to determine troposphere modelling errors. The inner 3 hours of observations included scans on fringe finder bright calibrators and repetitions of the J1905+1943 – J1925+2106 – GRB 221009A sequence, with respective duration of 30s – 30s – 80s.

The data were correlated at the NRAO in Socorro using the Distributed FX software correlator (DiFX; [279]). The data reduction was carried out in AIPS, following standard procedures for continuum phase-referencing experiments. Procedures `vlbaeops`, `vlbaccor`, `vlbampc1`, `vlbabpss`, `vlbaamp` were carried out in this order for the initial bandpass and amplitude calibration. The following step consisted in the calibration of the troposphere modeling errors by running the task `fring` on the geodetic blocks, followed by `mbdly` and `delzn`. The final phase, rate, and delay fringe-fitting was carried out separately on J1905+1943 and J1925+2106, yielding high signal-to-noise ratio and well-behaved solutions for both sources. The solutions from the closer phase calibrator, J1905+1943, were applied to the target field. After preparing a model of the phase calibrator using `Difmap`, a cycle of amplitude and phase solutions were determined for the calibrator itself and applied to the target to further refine the calibration. Finally, we produced single-source frequency-averaged datasets for the target, which were imaged in AIPS with a natural weighting scheme.

Our VLBA campaign included one more epoch, BA160 A, at approximately 14 days post-burst. However, as the antennas were pointed at an incorrect position in the sky, the GRB fell outside the primary beam of the VLBA, which is approximately 3 arcmin at 15 GHz. While the reduced sensitivity (approximately 25%) still allows for the detection of the burst, a satisfactory calibration of the complex visibilities was hampered. Therefore, we did not include this experiment in our analysis.

5.3 Methods

5.3.1 Source flux density, size and average apparent expansion velocity estimate

In order to extract information about the total flux density, size and position of the source from each of our epochs, we fitted a circular Gaussian source model to the calibrated visibility data adopting a Markov Chain Monte Carlo (MCMC) approach, closely following [137]. We describe the method in detail in Appendix 5.7.2. Once the source size (which we identify with the full width at half maximum – FWHM – of the circular Gaussian model) is measured, the

average apparent expansion velocity can be calculated (assuming the size to be zero at the time t_0 of the explosion) as

$$\langle \beta_{\text{app}} \rangle = \frac{(1+z)d_A s}{2(t_{\text{obs}} - t_0)c}, \quad (5.1)$$

where s is the FWHM, t_{obs} is the time of the observation, and c is the speed of light.

Table 5.1 summarises the result of the circular Gaussian fitting, along with the derived average apparent expansion velocity. In Appendix 5.7.2 we provide more detailed information in the form of corner plots that visualise the posterior probability density on the flux density and source size from the circular Gaussian fitting. Figure 5.1 additionally shows ‘violin plots’ that visualise a kernel density estimate of the posterior probability density on the FWHM for each epoch.

5.3.2 Source size evolution model fitting

In order to fit a size evolution model $s_m(t_{\text{obs}}, \vec{\theta})$ to the observations, where $\vec{\theta}$ is a vector of free parameters, we adopted a Bayesian approach. By Bayes’ theorem, and given the fact that the size estimates from different observations are independent, the posterior probability on $\vec{\theta}$ is proportional to the prior $\pi(\vec{\theta})$ times the product of the likelihoods. This can be written as

$$P(\vec{\theta} | \{\vec{d}_i\}_{i=1}^M) \propto \pi(\vec{\theta}) \prod_{i=1}^M \frac{P(s_m(t_{\text{obs},i}) | \vec{d}_i)}{\pi(s)}, \quad (5.2)$$

where M is the number of epochs included in the fit, \vec{d}_i is the data (i.e. the visibilities) of the i -th epoch, $t_{\text{obs},i}$ is the time of the i -th observation, $\pi(s) = \Theta(s)$ (where Θ is the Heaviside step function) is the prior on the size adopted in the circular Gaussian fits, $P(s | \vec{d}_i)$ is the posterior from such fits (eq. 5.5 in Appendix 5.7.2) marginalized on all parameters except s . In order to evaluate eq. (5.2), we approximated the marginalized posterior on the size $P(s | \vec{d}_i)$ with a Gaussian kernel density estimate based on the posterior samples derived from the MCMC described in Sect. 5.3.1. This allowed us to sample the posterior on $\vec{\theta}$ again through an MCMC approach.

5.3.3 FS and RS size evolution and proper motion model

In order to interpret our observations in the context of the standard afterglow scenario, we derived a simple physical model of the size evolution and, in the case of a misaligned viewing angle, the proper motion of the source expected if the emission is dominated by either the FS or the RS produced as a relativistic jet expands into an external medium with a power law number density profile $n(R) = A(R/R_\star)^{-k}$, where R is the distance from the explosion site (i.e. the progenitor vestige) and $R_\star = 5.5 \times 10^{17}$ cm is a reference radius¹. We assumed a uniform jet angular energy profile for simplicity, with an isotropic-equivalent kinetic energy E , a half-opening angle θ_j , an initial Lorentz factor Γ_0 and a duration T (which sets the jet radial width $\Delta R \sim cT$). The viewing angle is assumed to be either $\theta_v = 0$ (on-axis, for the calculation of the projected size) or $\theta_v > \theta_j$ (off-axis, for the calculation of the apparent proper motion). The model is based on the standard relativistic-hydrodynamical theory of a relativistic, homogeneous shell expanding into a static, cold external medium [280–285] and is described in detail in Appendix 5.7.4.

¹With this definition, A has the same meaning as the usual $A_\star = 1 (\dot{M}_w/10^{-5} M_\odot \text{ yr}^{-1})(v_w/1000 \text{ km s}^{-1}) \text{ cm}^{-3}$ parameter in the wind-like external medium case ($k = 2$), where \dot{M}_w and v_w are the mass loss rate and the velocity of the progenitor wind, assumed constant [143]. In the $k = 0$ case, it is simply equal to the homogeneous external number density, $A = n$.

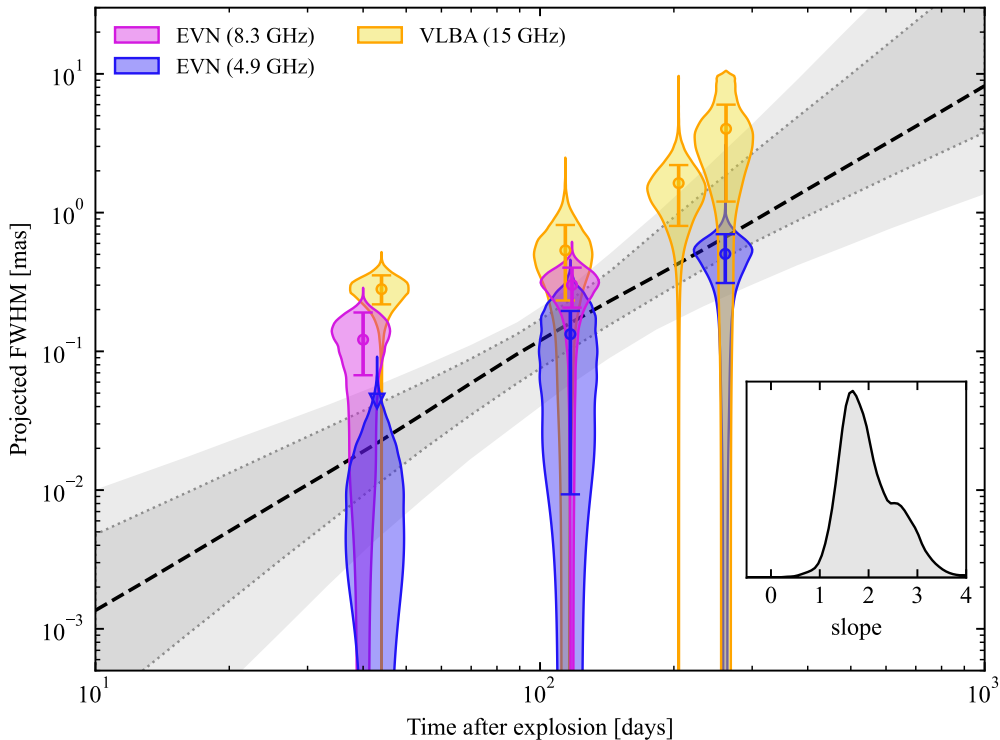


Figure 5.1: Source size as a function of time. The source size constraints obtained as described in Section 5.3.1 are shown in the form of violin plots of different colours, centred at the observing time of each epoch and of proportional width to the posterior probability density on the FWHM. In addition, we show the median and 68% credible interval with an error bar of the same color, or the 95% credible upper limit with a triangle if the former interval extends to 0. The black dashed line and the two grey shaded areas show respectively the median, 68% credible interval and 95% credible interval of the posterior predictive distribution of the source size evolution obtained from fitting a power law model $s \propto t_{\text{obs}}^a$ to the sizes from all the epochs. The inset shows the posterior probability density on the slope a from such fit.

The free parameters of the model are the energy-to-density ratio E/A , the duration T , the initial Lorentz factor Γ_0 , the jet half-opening angle θ_j , the external medium density profile slope k , the viewing angle θ_v and the slope g of the reverse-shocked material Lorentz factor deceleration with radius, $\Gamma \propto R^{-g}$, after it ‘detaches’ from the forward-shocked shell. Hereafter we fix $T \approx T_{90}/(1+z) = 521 \text{ s}$ and $\Gamma_0 = 10^{2.5} \approx 316$ [266], and we consider two values of the external medium density profile, that is, $k = 0$ (homogeneous external medium) and $k = 2$ (wind-like external medium).

5.4 Results

5.4.1 Source size expansion

Figure 5.1 shows the source size constraints from Table 5.1 in the form of a ‘violin plot’ whose width is proportional to the posterior probability density on the FWHM, horizontally centred at the time of the observation. Additionally, we show the median and 68% symmetric credible interval on the FWHM by means of an error bar for each observation. In order to quantify the source size evolution from these observations, we fit a simple phenomenological power law evolution model, $s_m(t_{\text{obs}}) \propto t_{\text{obs}}^a$, to these size measurements, through the method outlined in Sect. 5.3.2. The resulting posterior probability density on the power law slope is shown in the

inset of Figure 5.1. The median and symmetric 68% credible interval is $a = 1.9_{-0.6}^{+0.7}$. We found that 99.966% of the posterior probability (3.6σ -equivalent) is located at $a > 0$. Therefore, our observations strongly support the expansion of the source. In the main panel of Figure 5.1, we show with a black dashed line the median of the posterior predictive distribution, that is, the probability distribution of $s_m(t_{\text{obs}})$ at each fixed t_{obs} , as derived from the fit. The dotted lines encompass the 68% symmetric credible interval of the same distribution, filled with a grey shade. A lighter grey shading shows the 95% symmetric credible interval. The steep slope is mainly driven by our EVN 4.9 GHz observation at 43 days post-burst, which provides an upper limit of 0.045 mas, which cannot be explained by simple calibration errors. Conversely, our first 15 GHz VLBA epoch at 44 days is in mild tension with such an evolution, with a measured size $s(44 \text{ d}) = 0.28_{-0.06}^{+0.08}$ mas. This might be ascribed to coherence loss at the longest baselines, which is more severe at these high frequencies [286]. On the other hand, it could reflect a frequency-dependent source size. To explore that possibility, we repeated the power law size evolution model fit considering only observations at a single frequency. Figure 5.2 shows the resulting size evolution for observations at 4.9 GHz (upper panel), 8.3 GHz (middle panel) and 15 GHz (lower panel). The plots are similar to Figure 5.1, except that the epochs not considered in the fit are shown with a light grey shading. The constraint on a from these fits is somewhat looser, with the medians and symmetric credible intervals being $a = 2.1_{-0.8}^{+1.0}$ (4.9 GHz), $a = 1.7_{-1.9}^{+2.0}$ (8.3 GHz) and $a = 1.1_{-0.3}^{+0.4}$ (15 GHz). While these slopes are formally all compatible with each other, the normalisations of the 4.9 GHz and 15 GHz power laws differ with a $> 3\sigma$ significance, as can be evinced from the posterior predictive distributions shown in grey in the panels, suggesting a dependence of the evolution on frequency.

In order to exclude the possibility that our results with the EVN are driven by systematic effects, we carried out a series of tests including the check source J1905+1943. We present the results of our tests in Appendix 5.7.3. The results of these tests indicate that the observed evolution is not driven by systematic errors in the calibrations.

5.4.2 Apparent proper motion

VLBI observations can constrain the apparent proper motion of the centroid of the emission and, therefore, the jet viewing angle. The source position at each VLBA epoch is displayed in Figure 5.3: our results do not show any significant apparent proper motion between 44 and 262 days post-burst, but our errors can accommodate a displacement of up to about 0.6 mas (at the 1σ level) over that period. As shown in Appendix 5.7.4, such an upper limit does not constrain strongly θ_v , which can still be several degrees off the edge of the jet, unless the energy-to-density ratio of the explosion is very large. Still, a number of studies including [269] and [267] have used their data to justify a very small θ_v for GRB 221009A, indicating that we are viewing the jet close to on-axis. The lack of significant proper motion observed during our VLBI campaign is fully consistent with such on-axis scenario.

We note that the EVN campaign is not used for such study because of the change in phase reference source between the second and third epoch. While this change was motivated by the discovery of a closer phase calibrator (and hence a more efficient observing strategy), the different systematics and the lack of a reliable *a priori* position of the new calibrator prevent a reliable astrometric characterisation.

5.5 Discussion

The size evolution power law slope $a = 1.9_{-0.6}^{+0.7}$ we derived is only marginally compatible (at the 3σ level) with the expected slopes for a [148] blast wave expanding into a homogeneous medium, $\alpha = 5/8 = 0.625$, or a wind-like medium, $\alpha = 3/4 = 0.75$. However, the preferred value

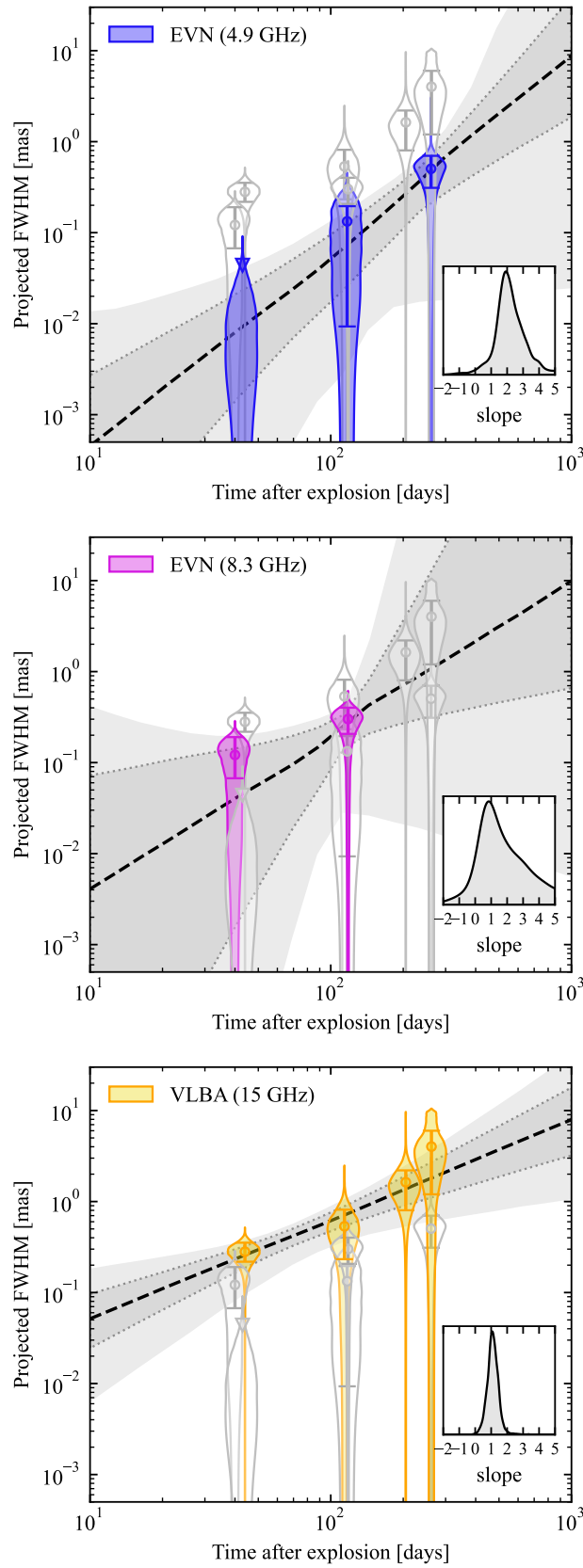


Figure 5.2: Size evolution considering only observations at a single frequency (upper panel: 4.9 GHz; middle panel: 8.3 GHz; lower panel: 15 GHz). Each panel is similar to Figure 5.1, except that the epochs not considered in the fit are shown with light grey shading for clarity.

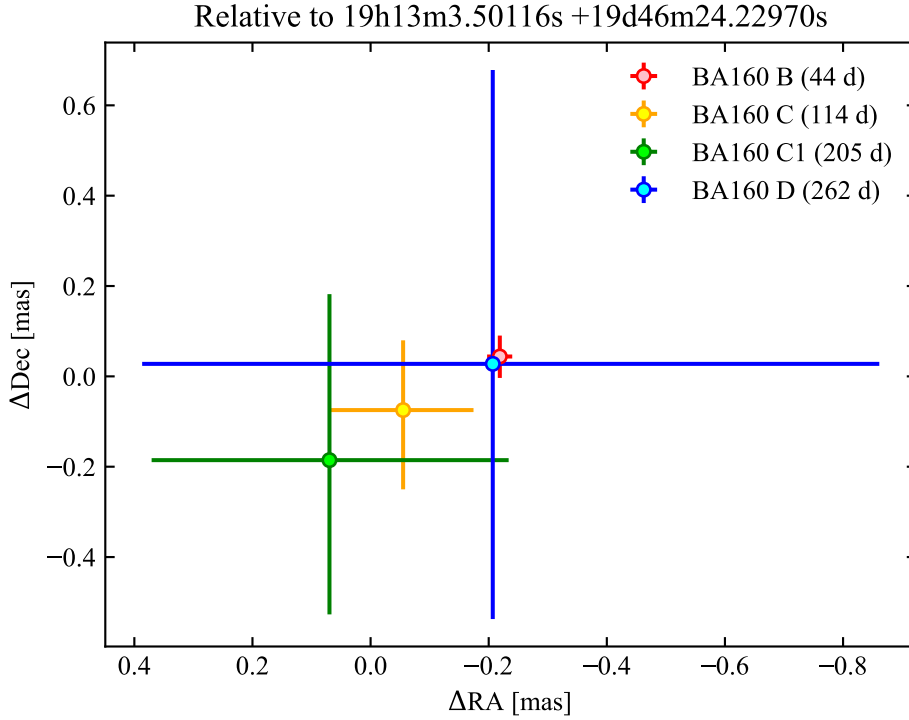


Figure 5.3: Source position in our VLBA observations. For each epoch, we show an error bar centered on the median position from the circular Gaussian source fit, with bars spanning the symmetric 68% credible interval on the source position in each direction.

for the slope is substantially higher and it even allows for an accelerating ($a > 1$) expansion. Moreover, when compared to GRB 030329, the only other burst to date with a measured expansion rate [249], our a value reveals an unprecedented size evolution (Figure 5.5). It is possible that the apparent rapid expansion favoured by our observations is a result of observing different emission regions at different frequencies.

Many efforts aimed at modelling the multi-wavelength evolution of the GRB 221009A afterglow indicate that the radio wavelengths are likely dominated by a RS component at $t_{\text{obs}} \lesssim 100$ d, possibly transitioning to a FS dominated regime at later times. Indeed, the radio afterglow of this GRB cannot be explained by a simple FS propagating either in a wind-like or a homogeneous environment [271, 272, 288]. Using a data set encompassing observations from the GeV to the radio domain, [273] showed that the standard afterglow model struggles at explaining the radio emission both with a FS and a RS of a conical jet propagating through a wind-like environment, leading them to invoke an additional component whose temporal evolution does not follow the standard prescriptions. A somewhat improved description could be obtained by including a jet with an angular structure [267, 274], but it is unclear whether this scenario favours a wind-like or a homogeneous surrounding medium.

Inspired by these results, together with our finding that the size evolution may be frequency-dependent, we explored a scenario where the emission we observed is a superposition of a FS and a RS, leveraging on the model described in Sect. 5.3.3, with $\vec{\theta} = (E/A, \theta_j, g)$ as our free parameter vector. The external medium power law index was fixed to $k = 0$ or $k = 2$. Based on the apparent frequency-dependent behaviour, we assumed the higher-frequency observations (15 GHz) to be dominated by the FS, while the lower-frequency ones (4.9 – 8.3 GHz) to be dominated by the RS. For each external density profile, the posterior probability density on $\vec{\theta}$ was derived through the Bayesian approach described in Sect. 5.3.2, with a uniform-in-log prior on E/A in the range $[10^{50}, 10^{60}]$ erg cm³, a uniform prior on g in the range $[(3 - k)/2, 6]$ and a

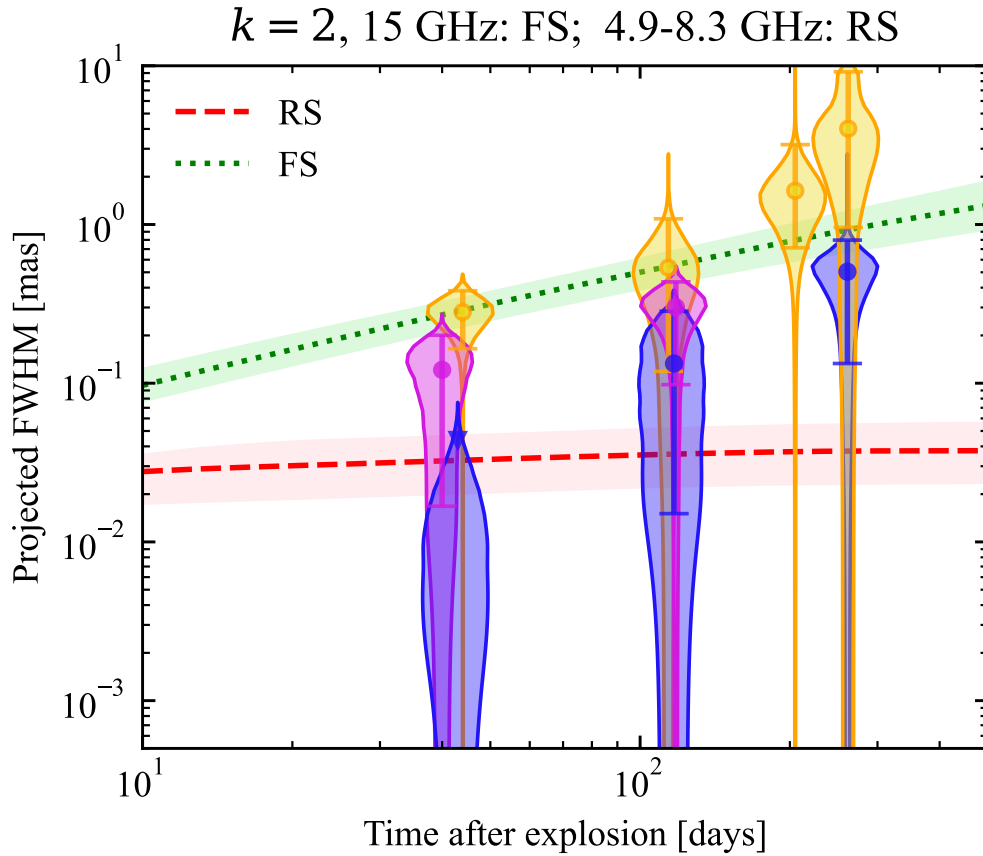


Figure 5.4: Model size evolution in a FS plus RS scenario. The violins and the error bars show the source size evolution as inferred by our observations, in the same way as in Figure 5.1. The green dotted line and red dashed lines show the medians of the posterior predictive distributions of the FS and RS size, respectively, as obtained by fitting the physical model described in Appendix 5.7.4 to the sizes shown in the figure, assuming a wind-like external medium, and assuming the FS to dominate at 15 GHz and the RS to dominate at 4.9 and 8.3 GHz. The shaded bands around these lines show the 68% credible interval of the posterior predictive distribution.

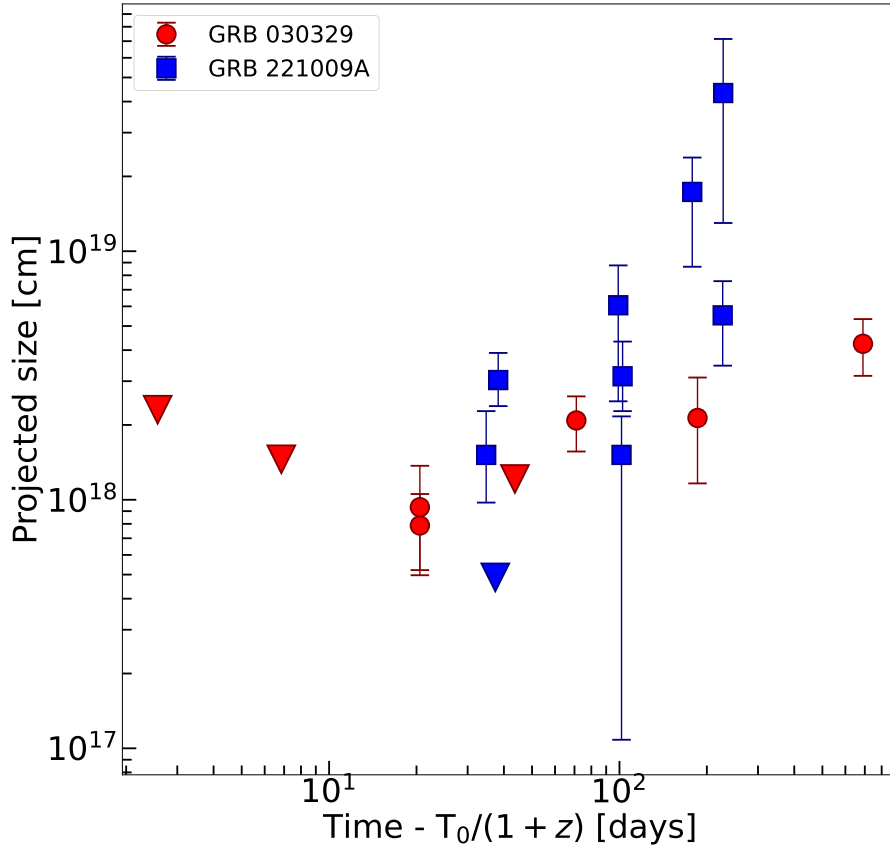


Figure 5.5: Comparison of size measurements from VLBI observations of GRB 030329 (red circles; [249, 287]) and GRB 221009A (dark blue squares, this work). Triangles represent upper limits.

uniform prior on θ_j in the range $[0.5, 30]$ deg.

In the homogeneous external medium ($k = 0$) case, our model predicts too small a difference between the projected size of the FS and that of the RS, which is insufficient to explain the apparent frequency-dependent size and its evolution. In the case of a wind external medium ($k = 2$), on the other hand, the scenario provides a good agreement with the data, as shown in Figure 5.4. The evolution predicted by the model additionally suggests that the 4.9 GHz observations may transition from being RS-dominated at $t \lesssim 100$ d to being FS-dominated at later times, consistently with the multi-wavelength predictions of [267] and [274]. The marginalised posterior on E/A shows a clear peak (see Figure 5.6), with a median and 68% symmetric credible interval $\log(E/A) = 54.3^{+0.4}_{-0.5}$ (expressed in erg cm^3). Within this scenario, this indicates a high prompt emission efficiency (so that $E < 10^{55}$ erg) in combination with a relatively high wind density $A > 1 \text{ cm}^{-3}$, even though a lower efficiency and wind density can be accommodated if a more stringent prior on the half-opening angle is adopted, as explained below. We also caution here that we have assumed the measured FWHM to correspond to the source diameter as calculated by our model, but this is correct only up to a constant $\xi \sim 1$, which depends on the detailed surface brightness distribution of the source [137, 249, 287]. Since E/A is proportional to the fourth power of the FWHM in the $k = 2$ case [e.g. 289], this introduces a possible systematic error of up to a factor of $\xi^4 \sim 1.4^4 \approx 4$ on E/A (taking a reference value $\xi = 1.4$ as in [287]), or equivalently an offset of 0.6 in $\log(E/A)$. The posterior probability density on g is not very informative, but it indicates that $g > 2.1$ (95% credible lower limit), which implies a quite fast deceleration of the RS after it detaches from the FS (hence, in this model, the reverse-shocked material essentially reaches the end of its expansion at around 200 d, as shown in Figure 5.4). The jet half-opening angle θ_j is not well constrained ($\theta_j < 21$ deg at 1σ), but there is a clear correlation between E/A and θ_j , with larger values of

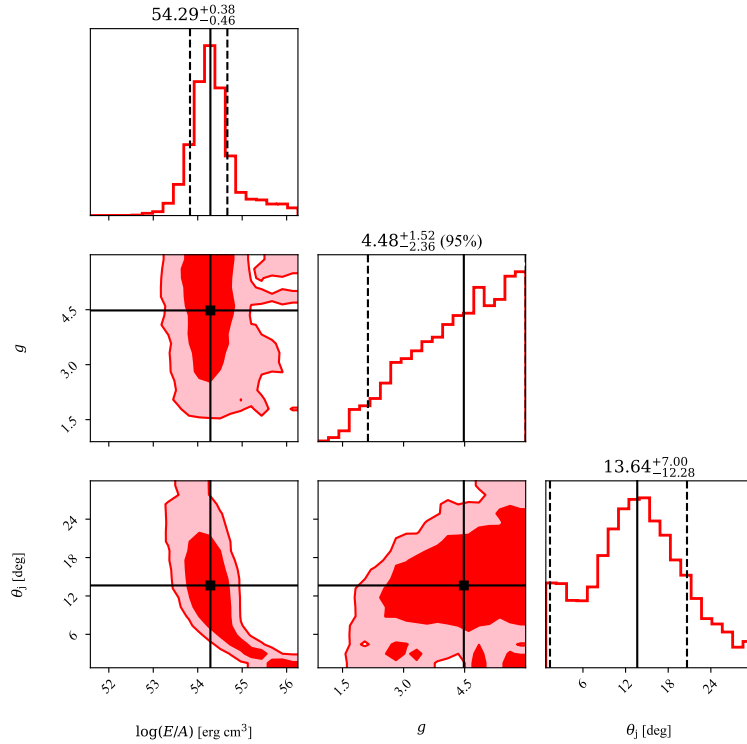


Figure 5.6: Corner plot of the posterior probability density on the physical model parameters in the wind-like external medium case and assuming the FS to dominate at 15 GHz and the RS to dominate at 4.9–8.3 GHz. The red histograms in the panels on the diagonal show the marginalized posterior probability densities, with black solid vertical lines showing the median and dashed lines showing the 68% credible interval or, if the latter extends to the lower (upper) extremum of the prior range, the 95% upper (lower) limit (values reported on top of the panels). The remaining panels show the smallest contours containing 68% and 95% of the two-dimensional marginalised posterior probabilities on parameter pairs, with the black squares showing the position of the median.

$E/A \gtrsim 10^{55}$ erg being compatible with smaller half-opening angles $\theta_j \lesssim 5$ deg. The inspection of the two-dimensional $(E/A, \theta_j)$ posterior (lower left panel of Figure 5.6) shows that for $\theta_j \lesssim 3$ deg, the preferred $\log(E/A)$ increases up to 55–56.

5.6 Conclusions

In this chapter, I presented VLBI observations of the brightest γ -ray burst ever observed, GRB 221009A. The high angular resolution provided by the EVN and the VLBA allowed us to constrain the size and the expansion of the blast wave produced by the GRB ejecta for the second time ever. Although still consistent with the standard expansion expected for a [148] blast wave propagating into a circumburst medium (i.e., an ultra-relativistic FS), the derived expansion rate tends to prefer higher values. We suggest that the unusual expansion may be due to our observations transitioning from being dominated by the RS emission to being dominated by the FS emission, in agreement with interpretations that stem from the modelling of the multi-wavelength emission [267, 274]. For our interpretation to hold, the external medium must be wind-like. Our work highlights the crucial role played by multi-wavelength VLBI monitoring of transient events both at early and late times, in order to provide a vital insight into the physics of these sources.

5.7 Appendices

5.7.1 EVN observation strategy and data reduction

In this Appendix I provide detailed information on the observation strategy and the data reduction of the EVN observations. As explained in Section 5.2, the structure of the observations followed a typical phase-referencing experiment. Three compact, extragalactic radio sources J1800+3848, J1925+2106 and J0121+0422 were used as fringe finders and bandpass calibrators throughout the campaign. The target scans, lasting approximately 4.5 and 2.5 minutes at 5 and 8 GHz, respectively, were interleaved with 1.5 minute scans of the phase calibrator. In the first two observations, namely 40 and 43 days post-burst (RG013 B and C), the radio source J905+1943 was used as a phase calibrator and the Very Large Array Sky Survey (VLASS) compact radio source J191142+1952 was included for testing its suitability as a closer phase reference source ($d = 0.33^\circ$ from the GRB position). Given the success of such test, J191142+1952 was then adopted as phase calibrator in the last three epochs, i.e. from 117 to 261 days post-burst (RG013 D, E and F). In order to inspect the consistency of the calibration procedure, one or multiple compact radio sources were observed approximately every 30 minutes. The phase and amplitude solutions derived from the calibrators were applied to these check sources to verify the quality of the calibration.

The calibration was performed using AIPS [219], following the standard procedure for EVN phase-referenced observations. The amplitude calibration, which accounts for the bandpass response, the antenna gain curves and the system temperatures, was performed using the results from the EVN pipeline. Procedures `vlbatecr` and `vlbampcl` were used to correct for the dispersive delay and to calculate the manual single band delay on the fringe finder, respectively. Subsequently, we carried out the global fringe fitting on the phase calibrator with the task `fring`. Solutions were interpolated and applied to the phase calibrator itself, the check sources and the target with the task `clcal`. At this point, the calibration procedure differs according to the epoch.

For the first two epochs (RG013 B and C), we carried out the fringe fitting on J1905+1943 using a model of the source derived by a concatenation (in CASA, [217]) and self-calibration (in

Difmap) of all the visibilities on the source obtained across the various epochs. This approach is warranted by the stability of the structure of extragalactic sources on the duration of the campaign, and improves the phase, delay, and rate calibration by accounting for the possible structure of the phase-reference source. We then interpolated the solutions and applied the results to J1905+1943 itself, the check source (J1923+2010) and GRB 221009A. Lastly, we perform two rounds of self-calibration on J1905+1943, first in phase-only, with a solution interval of 2 minutes, and then in amplitude and phase with a solution interval of 60 minutes in AIPS. We interpolated the solutions and applied the results to the phase calibrator itself, the check sources and the target.

In the last three epochs, we employed a different phase calibrator, J191142+1952, motivated by the significantly smaller separation from the source (0.33° vs 1.75°). If the phase calibrator is closer to the target, any possible decorrelation of the phase solutions is significantly reduced. However, the position of J191142+1952 was constrained with a precision of the order of an arcsecond: for VLBI observations, this means that the coordinates of the centre of the source were not aligned with the phase centre of the observation. If one does not correct for the uncertainty in the position, the phase solutions of the global fringe fitting on the phase calibrator will contain a systematic error and the apparent coordinates of the centre of the sources to which these solutions are applied will be incorrect. To avoid this, we started from the fourth epoch, made at 8 GHz, which provides higher angular resolution and therefore a more precise position of the calibrator. We applied the solutions of the first global fringe fitting on J191142+1952 to the check sources, J1905+1943 and J1923+2010, we produced an image of each of them and we compared the apparent coordinates of each source with the actual position, known with an uncertainty of the order of \sim mas. Since J1905+1943 and J1923+2010 appear to be aligned in the sky, with J191142+1952 placed in between, we derived the real coordinates with a 1D interpolation at the position of J191142+1952 of the offset observed for the check sources. We then re-calculated the visibilities of J191142+1952 by fixing the phase centre with the `fixvis` task in `CASA`, inserting the new coordinates. We then repeated the entire calibration process iteratively, until the apparent and the real sky coordinates of the check sources were consistent within the resolution of the observation. We corrected the third and fifth epoch using the position derived at 8.3 GHz.

Subsequently, we produced a model of J191142+1952 in `Difmap` and we used the model as input to perform the global fringe fitting of the phase calibrator in `AIPS`, in order to take into account any possible structure of J191142+1952 and correct for it. We interpolated the solutions and we applied them to J191142+1952, J1905+1943, J1923+2010 and GRB 221009A. Lastly, we performed a round of amplitude and phase self-calibration of J191142+1952 in `AIPS`, using a solution interval of 2 minutes and we applied the interpolated solutions to J191142+1952, J1905+1943, J1923+2010 and GRB 221009A. After each of the aforementioned steps of the procedure, the derived solutions were inspected and bad data were properly flagged.

Images of the target and the check sources were produced using `Difmap`. Unfortunately, due to the sparse (u, v) -plane coverage and the distance from the phase calibrator, J1923+2010 was not usable to check the consistency of the calibration process.

5.7.2 Circular Gaussian fits to source visibilities

In this appendix we provide more detailed information about our circular Gaussian fits to source visibilities from our VLBI observations. We assumed a chi-squared log-likelihood for the visibilities, namely

$$\ln \mathcal{L} (\{\mathcal{V}_i\}_{i=1}^N | \vec{x}) = -\frac{1}{2} \sum_{i=0}^N w_i \{ [\mathcal{V}_{R,m}(u_i, v_i, \vec{x}) - \mathcal{V}_{R,i}]^2 + [\mathcal{V}_{I,m}(u_i, v_i, \vec{x}) - \mathcal{V}_{I,i}]^2 \} \quad (5.3)$$

Table 5.2: List of antennas that join each observing run.

Code	$t_{\text{obs}} - t_0$ [days]	Array	Antennas
RG013 B	40	EVN	Wb, Ef, Nt, O6, Ur, Tm, Ys, Tr, Hh, Mh
RG013 C	43	EVN	Jb, Wb, Ef, Mc, O8, Ur, Tm, Ys, Tr, Hh
BA160 B	44	VLBA	Fd, Hn, Mk, Nl, Ov, Pt, Sc
BA160 C	114	VLBA	Br, Fd, La, Mk, Nl, Ov, Pt, Sc
RG013 D	117	EVN	Jb, Wb, Ef, Mc, O8, Ur, Tm, Ys, Tr
RG013 E	118	EVN	Wb, Ef, Mc, Nt, O6, Ur, Tm, Ys, Tr, Hh, Mh
BA160 C1	205	VLBA	Br, Fd, Hn, Kp, La, Mk, Nl, Ov, Pt, Sc
RG013 F	261	EVN	Jb, Ef, Mc, Nt, O8, Tm, Ys, Tr, Hh, Ir
BA160 D	262	VLBA	Br, Fd, Hn, Kp, La, Mk, Nl, Ov, Pt, Sc

Wb: Westerbork, 25m; Ef: Effelsberg, 100m; Nt: Noto, 32m; O6: Onsala, 20m; Ur: Ürumqi; Tm: Tianma, 65m; Ys: Yebes, 40m; Tr: Torun, 32m; Hh: Hartebeesthoek, 25m; Mh: Metsähovi, 14m; Jb: Jodrell bank (Lovell), 76m; Mc: Medicina, 32m; O8: Onsala, 25m; Ir: Irbene; Br: Brewster, 25m; Fd: Fort Davis, 25m; Hn: Hancock, 25m; Kp: Kitt Peak, 25m; La: Los Alamos, 25m; Mk: Mauna Kea, 25m; Nl: North Liberty, 25m; Ov: Owen Valley, 25m; Pt: Pie Town, 25m; Sc: Saint Croix, 25m.

where $\mathcal{V}_{R,i}$ and $\mathcal{V}_{I,i}$ are the real and imaginary part, respectively, of the i -th visibility measurement \mathcal{V}_i , corresponding to position (u_i, v_i) on the (u, v) -plane, and w_i is its data weight as determined by our calibration procedure. By definition $w_i = \sigma_i^{-2}$, where σ_i is the uncertainty in the visibility measurement. Our source model is represented by $\mathcal{V}_{R,m}(u, v, \vec{x})$ and $\mathcal{V}_{I,m}(u, v, \vec{x})$, which are the real and imaginary parts of a circular Gaussian source model defined by

$$\mathcal{V}_m(\vec{x}) = F_\nu e^{-2\pi^2 \left(\frac{s}{\sqrt{8 \ln 2}}\right)^2 (u^2 + v^2) - 2\pi j(u\rho + v\delta)}, \quad (5.4)$$

where $j = \sqrt{-1}$, F_ν is the total flux density, s the full width at half maximum (FWHM), and ρ and δ the spherical offsets of the source with respect to the phase centre. These parameters collectively constitute the components of the parameter vector $\vec{x} = (F_\nu, s, \rho, \delta)$. By Bayes' theorem, we defined the posterior probability on \vec{x} , given our data $\{\mathcal{V}_i\}_{i=1}^N$, as

$$P(\vec{x} | \{\mathcal{V}_i\}_{i=1}^N) \propto \pi(\vec{x}) \mathcal{L}(\{\mathcal{V}_i\}_{i=1}^N | \vec{x}), \quad (5.5)$$

where $\pi(\vec{x})$ is the prior probability on the parameters. For the latter, we adopted simple independent uniform priors on each parameter, with the due bounds $F_\nu > 0$ and $s > 0$. Where necessary, in order to prevent the fitting procedure from picking up some noise peak instead of the actual source, we restricted the position (ρ, δ) to within a small angular distance $\Delta_{\text{pos}} \sim 1$ mas from the peak (ρ_0, δ_0) of the dirty map constructed with AIPS. Therefore, our prior took the form

$$\begin{aligned} \pi(\vec{x}) \propto & \Theta(F_\nu) \Theta(s) \Theta(\rho - \rho_0 + \Delta_{\text{pos}}) \Theta(\rho_0 + \Delta_{\text{pos}} - \rho) \times \\ & \times \Theta(\delta - \delta_0 + \Delta_{\text{pos}}) \Theta(\delta_0 + \Delta_{\text{pos}} - \delta), \end{aligned} \quad (5.6)$$

where Θ is the Heaviside step function. Only for the VLBA D epoch, we added the constraint $s < 10$ mas (i.e. we added a factor $\Theta(10 \text{ mas} - s)$ to the prior) to remove a secondary peak of the posterior at $s \sim 30$ mas, which we consider as spurious. For each epoch, we sampled the posterior probability using the EMCEE [290] python package. We initialised EMCEE with the initial guess $\vec{x} = (I_{\nu, \text{pk}}, 10^{-4} \text{ mas}, \rho_0, \delta_0)$, where $I_{\nu, \text{pk}}$ is the peak surface brightness (expressed in Jy/beam) in the dirty map, corresponding to an unresolved circular Gaussian source at the

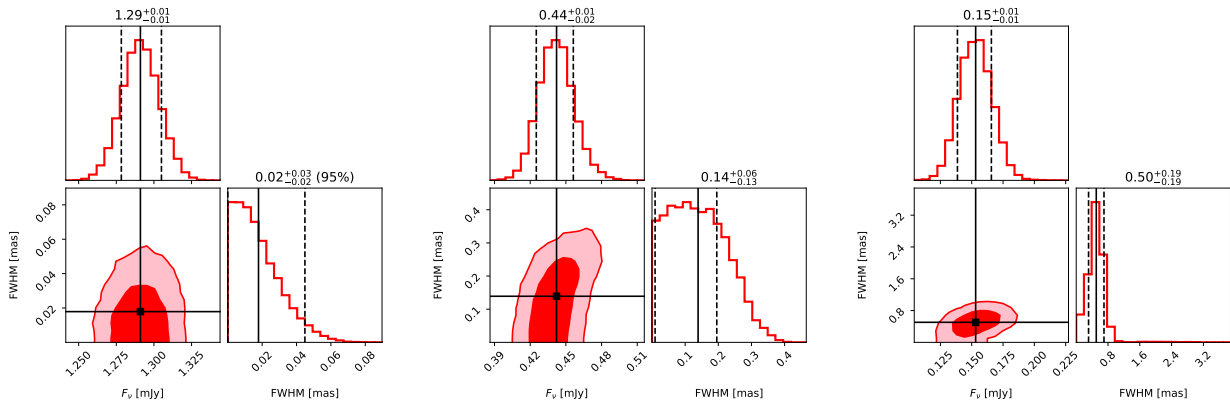


Figure 5.7: Posterior probability distribution on the source size and flux density in our EVN 4.9 GHz epochs at $T - T_0 = 43$ (RG1013 C, left), 117 (RG013 D, center) and 261 (RG013 F, right) days. In each corner plot, the top-left and bottom-right sub-panels show histograms of the posterior samples of F_ν and FWHM, with the vertical solid lines showing the median and the vertical dashed lines bracketing the 68% credible interval or, if the latter extends to 0, the 95% credible upper limit. The bottom-left sub-panel of each corner plot shows the smallest contours containing 68% and 95% of the posterior probability.

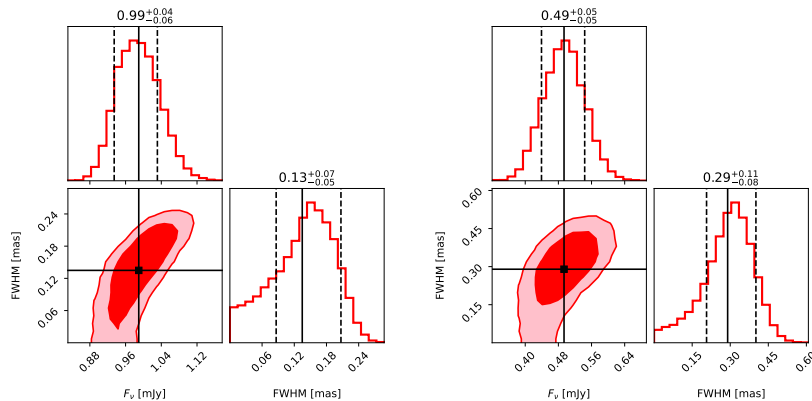


Figure 5.8: Similar to Figure 5.7, but for our EVN 8.3 GHz epochs at $T - T_0 = 40$ (EVN B, left) and 118 (EVN E, right) days.

position of the peak of the dirty map and with a flux density that yields the observed peak surface brightness. We then ran 3000 iterations of the MCMC with 32 walkers, for a total of 96000 samples of the posterior probability density for each epoch. The results were constructed after discarding the initial 30% of these samples as burn-in.

Figure 5.7 shows corner plots that visualize the properties of the posterior probability density on (F_ν, FWHM) for our EVN 4.9 GHz epochs. Figures 5.8 and 5.9 show the corresponding corner plots for our EVN 8.3 GHz epochs and for our VLBA 15 GHz epochs, respectively.

5.7.3 Tests on the evolution of the flux density and the size

In this Appendix we present tests on the EVN observational results that we carried out in order to exclude the possibility that the measured evolution of the GRB size is a result of systematic effects. These tests include the check source J1905+1943. Unfortunately, due to the sparse (u, v) -plane coverage and the large separation, J1923+2010 could not be used to get meaningful constraints. First, the measured GRB afterglow size as a function of the equivalent radius (left panel) and area (right panel) of the synthesised beam are presented in Fig.

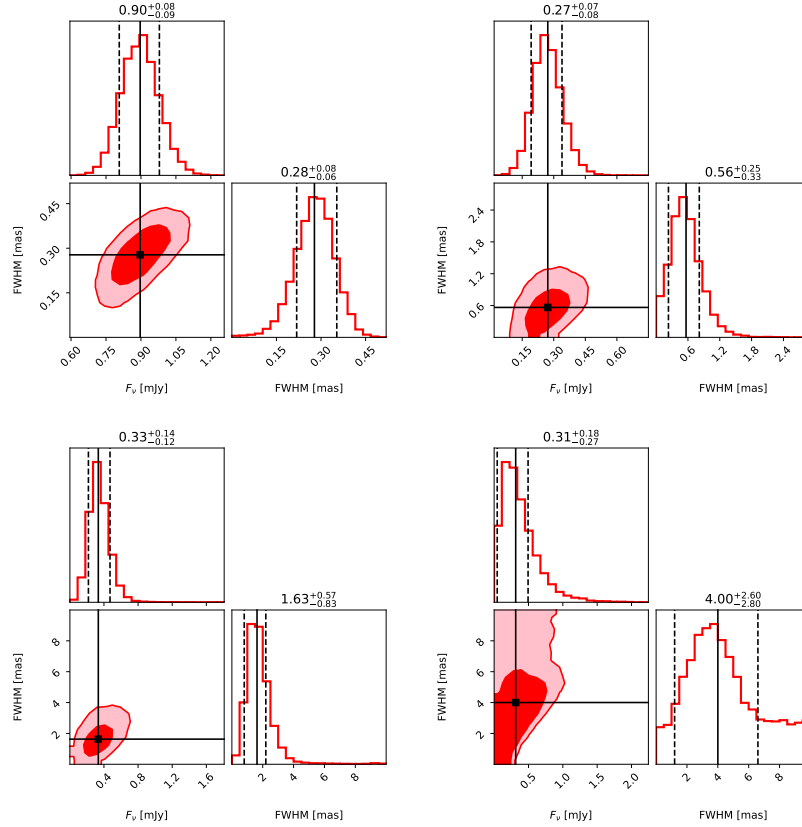


Figure 5.9: Similar to Figure 5.7, but for our VLBA 15 GHz epochs at $T - T_0 = 44$ (VLBA B, upper left), 114 (VLBA C, upper right), 205 (VLBA C1, lower left) and 262 (VLBA D, lower right) days.

5.10. These quantities are clearly not correlated, hence we can exclude the possibility that the observed expansion of the GRB is driven by a systematic change in the width of the synthesised beam. In Fig. 5.11, the flux density (left panel) and the size (right panel) of GRB 221009A and the check source J1905+1943 are compared. The decrease in the GRB 221009A flux density is not accompanied by a variation of the J1905+1943 flux density, as expected. In the 8.3 GHz observations, the size of J1905+1943 is constant, as expected, while that of the GRB afterglow shows a mild evidence for an increase across the two observations. At 4.9 GHz, the size we measure for J1905+1943 differs by approximately a factor of 2 between the first two epochs (C and D, where it is approximately 188 μ as) and the last epoch (F, where it is 402 μ as). On the other hand, across the same observations, the FWHM of the GRB afterglow varies by almost an order of magnitude. Therefore, the variation in the observed size of the GRB afterglow cannot be ascribed to a systematic effect due to an imprecise calibration. Concerning the VLBA, no test was performed because of the lack of close enough check sources.

5.7.4 Projected size and proper motion model of the FS and RS

Dynamics and size evolution

In the following, we describe an approximate analytical model of the dynamics of the FS and RS, based on similar calculations as [283–285]. The aim is to extend approaches such as those described in [291] and [289] by including the RS, which was not considered there. We assume a cold external medium with a power law density profile $\rho = Am_p(R/R_\star)^{-k}$, where R is the radial distance from the progenitor, m_p is the proton mass and A is the number density at a reference radius $R_\star = 5.5 \times 10^{17}$ cm. With this definition, A plays the role of either the ISM number density, $A \equiv n$ if $k = 0$, or that of the wind density parameter, $A \equiv A^\star$ if

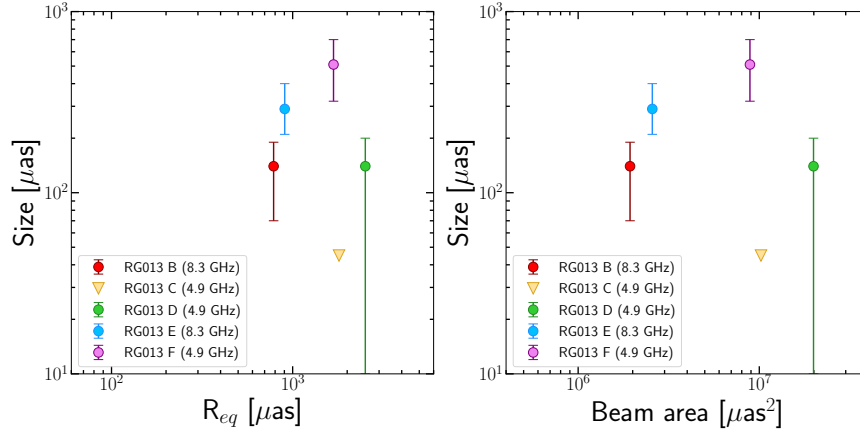


Figure 5.10: Estimates of the FWHM of the GRB as a function of the equivalent radius (left panel) and the total area (right panel) of the synthesised beam for the EVN observations.

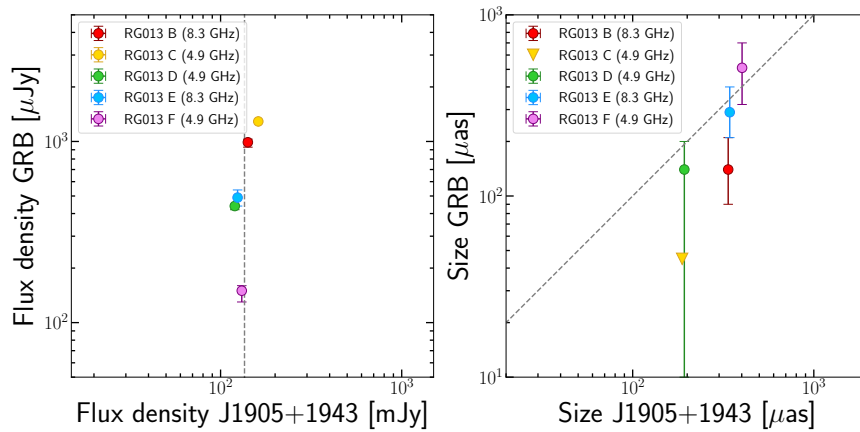


Figure 5.11: Flux density (left panel) and size (right panel) of GRB 221009A and J1905+1943 in the EVN observations. The average flux density of J1905+1943 (left panel) and the 1:1 correlation (right panel) are shown as grey dashed lines for the sake of comparison.

$k = 2$. We assume a simplified description of the jet as a cold, kinetic-energy-dominated shell with uniform initial bulk Lorentz factor $\Gamma_0 \approx 316 \Gamma_{0,2.5} \gg 1$ and constant isotropic-equivalent kinetic luminosity $L = E/T$, where $E = 10^{55} E_{55}$ erg is the isotropic-equivalent jet energy and $T \sim T_{90}/(1+z) \approx 500 T_{2.7}$ s is the lifetime of the central engine. The Sedov length associated with this shell is $\ell_S = [(3-k)E/(4\pi AR_*^k m_p c^2)]^{1/(3-k)}$. As this shell expands into the external medium at relativistic speed, a FS arises, which sweeps the external medium moving with a Lorentz factor $\Gamma_{\text{FS},0} \sim \sqrt{2}\Gamma_0$. The shocked external medium resides in the region contained between the FS and the contact discontinuity (CD) that separates it from the jet material. Since this implies some deceleration of the jet material behind the CD as well, as soon as the ram pressure of such material overcomes the pressure in the jet (formally already at $R=0$ given our assumption of a cold jet), a RS also arises, which separates shocked from cold unperturbed jet material. Let us indicate with numbers from 1 to 4 the unperturbed external medium, shocked external medium, shocked jet and unperturbed jet respectively, as usual. The RS is initially non-relativistic (i.e. the relative speed of regions 3 and 4 is $\beta_{34} \ll 1$), but it can become relativistic before the RS crosses the whole jet if the condition [149, 165, 282–285]

$$\frac{E}{A} < \frac{4\pi m_p c^2 R_*^k}{3-k} (cT)^{3-k} \Gamma_0^{2(4-k)} \approx \begin{cases} 2.1 \times 10^{57} \Gamma_{0,2.5}^8 T_{2.7}^3 \text{ erg cm}^3 & k=0 \\ 8.6 \times 10^{56} \Gamma_{0,2.5}^3 T_{2.7}^3 \text{ erg cm}^3 & k=2 \end{cases} \quad (5.7)$$

is satisfied, in which case the jet deceleration is said to be in the ‘thick shell regime’. In the following we describe the dynamics in such regime, and we defer to later the treatment of the opposite, ‘thin shell’ regime. For the homogeneous ISM case, $k=0$, the RS transitions from Newtonian to relativistic at a radius $R_N \sim \ell_S^{3/2} [(12cT)^{1/2} \Gamma_0^2]^{-1} \sim 3 \times 10^{16} E_{55}^{1/2} A_0^{-1/2} \Gamma_{0,2.5}^{-2} T_{2.7}^{-1/2}$ cm, while in the wind case, $k=2$, the RS is always relativistic as long as condition 5.7 holds. As regions 2 and 3 decelerate due to the increasing amount of swept external medium mass, at some point the RS crosses the whole jet, at a radius

$$R_\otimes = (4(3-k)cT)^{1/(4-k)} \ell_S^{(3-k)/(4-k)}. \quad (5.8)$$

Before R_\otimes , regions 2 and 3 effectively expand at the same Lorentz factor Γ , whose evolution can be described approximately as

$$\Gamma(R) \sim \begin{cases} \Gamma_0 & R \leq R_N \\ \frac{\ell_S^{(3-k)/4}}{[4(3-k)cT]^{1/4}} R^{-(2-k)/4} & R_N < R \leq R_\otimes \end{cases}. \quad (5.9)$$

The Lorentz factor of region 3 at the end of the RS crossing is therefore

$$\Gamma_\otimes = [\ell_S / (4(3-k)cT)]^{(3-k)/[2(4-k)]}$$

At radii larger than R_\otimes , the Lorentz factor of region 2 follows the [148] relativistic blast wave evolution, $\Gamma_2 \sim (R/\ell_S)^{-(3-k)/2}$. This holds as long as the lateral expansion of the shocked material in region 2 is negligible: numerical simulations and analytical arguments [292–296] show that such expansion has a very limited impact on the dynamics until region 2 becomes mildly relativistic, which justifies such assumption. In the homogeneous ISM case, $k=0$, the subsequent evolution of Γ_3 has been historically described phenomenologically [297] as $\Gamma_3 = \Gamma_\otimes (R/R_\otimes)^{-g}$, with g being typically fixed at around $g \sim 2$ in the case of a non-relativistic RS, or at $g = 1.5$ (i.e. the same evolution as the FS) in the case of a relativistic RS (when condition 5.7 holds), based on insights from the numerical simulations described in [283] and [297]. Physically, the different evolution is likely related to the conversion of internal to kinetic energy in region 3 as it expands, which allows it to remain ‘attached’ to region 2 as long as its temperature is relativistic. For historical reasons, in the case of a wind environment, $k=2$, the evolution in this phase has been always assumed to track that of the FS (i.e. $g = 0.5$),

despite the lack of numerical simulations to compare to. We argue here that generally, as the internal energy conversion terminates, region 3 must eventually ‘detach’ and expand backwards (as seen from the CD) into a rarefaction wave, and thus the evolution of Γ_3 with radius must steepen. In order to estimate the radius R_{det} at which regions 2 and 3 detach, we need to know the evolution of the internal energy in region 3, $E_{\text{int},3}$ (as measured in the comoving frame of region 3). From the first equation of thermodynamics, $d \ln E_{\text{int},3} = (1 - \hat{\gamma}) d \ln V'_3$, where $\hat{\gamma}$ is the adiabatic index and V'_3 is the comoving volume of region 3. We assume $V'_3 \propto R^3/\Gamma_3$. Right after the shock crossing regions 2 and 3 still move together, hence we can assume $\Gamma_3 \propto R^{-(3-k)/2}$, which leads to $E_{\text{int},3} = E_{\text{int},3,\otimes} (R/R_\otimes)^{(1-\hat{\gamma})(9-k)/2}$. Taking the internal energy at the end of RS crossing to be $E_{\text{int},3,\otimes} \sim (\Gamma_{34,\otimes} - 1)m_3c^2 \sim (\Gamma_\otimes/\Gamma_0 + \Gamma_0/\Gamma_\otimes)m_3c^2/2$ (where $\Gamma_{34,\otimes}$ is the relative Lorentz factor of regions 3 and 4 at the RS crossing radius, and m_3 is the jet rest mass), we finally conclude that the effective dimensionless temperature in region 3 evolves as

$$\Theta_3 \equiv E_{\text{int},3}/m_3c^2 \sim \left[\frac{1}{2} \left(\frac{\Gamma_\otimes}{\Gamma_0} + \frac{\Gamma_0}{\Gamma_\otimes} \right) - 1 \right] (R/R_\otimes)^{(1-\hat{\gamma})(9-k)/2}. \quad (5.10)$$

Assuming $\hat{\gamma} = 4/3$ since the RS is relativistic, we finally obtain the detachment radius from the condition $\Theta_3(R_{\text{det}}) = 1$, which yields

$$R_{\text{det}} = \max \left\{ \left[\frac{1}{2} \left(\frac{\Gamma_\otimes}{\Gamma_0} + \frac{\Gamma_0}{\Gamma_\otimes} \right) - 1 \right]^{6/(9-k)}, 1 \right\} R_\otimes, \quad (5.11)$$

where the maximum function is introduced to account for cases where $\Theta_3 < 1$ at R_\otimes , in which case $R_{\text{det}} = R_\otimes$.

Based on these considerations, we model the evolution of Γ_3 after RS crossing as

$$\Gamma_3(R) = \begin{cases} \Gamma_\otimes \left(\frac{R}{R_\otimes} \right)^{-(3-k)/2} & R_\otimes \leq R < R_{\text{det}} \\ \Gamma_\otimes \left(\frac{R_{\text{det}}}{R_\otimes} \right)^{-(3-k)/2} \left(\frac{R}{R_{\text{det}}} \right)^{-g} & R_{\text{det}} \leq R \end{cases}. \quad (5.12)$$

The above relations completely specify the evolution of Γ_2 and Γ_3 with radius as a function of the Sedov length ℓ_S , initial Lorentz factor Γ_0 and jet duration T for a given choice of k and g in the thick shell regime. The thin shell regime is obtained [283] by setting all transition radii equal to the ‘deceleration’ radius, $R_N = R_\otimes = R_{\text{det}} = \ell_S/\Gamma_0^{2/(3-k)}$. The relation between the radius R and the observer time for region $i \in \{2, 3\}$ can be obtained by noting that most of the emission that the observer receives comes from material moving at an angle $\sim \Gamma_i^{-1}$ from the line of sight, for which the arrival time is $t_{\text{obs}}/(1+z) = t(R) - R\beta_i(R)/c$, where $\beta_i = \sqrt{1 - \Gamma_i^{-2}}$. The progenitor-frame time t as a function of the radius can be obtained by integrating $t(R) = \int_0^R dR/(\beta_i c)$. By numerically inverting the resulting relation between t_{obs} and R , we finally obtain $R_i(t_{\text{obs}})$, and thus $\Gamma_2(t_{\text{obs}})$ and $\Gamma_3(t_{\text{obs}})$. The projected angular diameter of region $i = 2, 3$ is then approximately [291]

$$s_{\text{m},i}(t_{\text{obs}}) \sim 2 \frac{R_i(t_{\text{obs}})}{d_A} \times \begin{cases} \Gamma_i^{-1}(t_{\text{obs}}) & \Gamma_i(t_{\text{obs}}) \geq 1/\theta_j \\ \theta_j & \Gamma_i(t_{\text{obs}}) < 1/\theta_j \end{cases}, \quad (5.13)$$

where θ_j is the jet half-opening angle. We find that the predicted size of the FS from this model matches that of the more refined model of [289] within 10% for $k \in \{0, 2\}$ in the self-similar deceleration stage.

Proper motion

If the jet is observed at a viewing angle $\theta_v > \theta_j$, an apparent displacement of the projected image is expected. As long as $\Gamma^{-1} < (\theta_v - \theta_j)$, the observed emission is dominated by the border

of the shock closest to the observer. Its apparent displacement Δ can be modelled effectively as that of a point source moving at $\sim c$ at an angle $\theta_v - \theta_j$ away from the line of sight, so that the displacement increases linearly in time, $\Delta \propto t_{\text{obs}}$. For $(\theta_v - \theta_j) < \Gamma^{-1} < (\theta_v + \theta_j)$, the emission is dominated by material moving at $\sim 1/\Gamma$ from the line of sight, hence the displacement evolves as $\Delta(t_{\text{obs}}) \sim R(t_{\text{obs}})/\Gamma(t_{\text{obs}})d_A$, with $R(t_{\text{obs}})$ being the same as in the on-axis case. Eventually, for $\Gamma^{-1} > (\theta_v + \theta_j)$, the emission is dominated by the material at the shock border farthest from the observer, and the displacement is therefore $\Delta(t_{\text{obs}}) \sim R(t_{\text{obs}})\sin(\theta_v + \theta_j)/d_A$. The transition times $t_{j,\text{obs},\pm}$ that separate the three regimes described above can be obtained by setting $\Gamma(t_{\text{obs}}) = (\theta_v \pm \theta_j)^{-1}$ in the on-axis case, which we do numerically.

The model described here neglects the effects of lateral expansion of the shock and of a non-trivial jet structure outside the ‘core’ of half-opening angle θ_j . The former would generally slow down the evolution, so that the displacement predicted by this model can be considered as an upper limit. The latter would change (generally steepen) the slope of the evolution before the time $t_{j,\text{obs},-}$ at which the jet core starts coming into sight, but not thereafter. For the most likely parameters, our observations are at $t_{\text{obs}} > t_{j,\text{obs},-}$, so that the effects of a jet structure are unimportant for this particular source.

Figure 5.12 shows the displacement predicted by such a model between 44 d and 262 d, assuming the emission to be dominated by the FS (which produces the largest displacement, and dominates the VLBA data according to our interpretation) for different assumptions on θ_j (varying across columns) and on the external medium power law index (top row: $k = 2$; bottom row: $k = 0$), as a function of the off-edge viewing angle $\theta_v - \theta_j$ and of the energy to density ratio E/A . These predictions show that our upper limit on the observed displacement only excludes off-edge viewing angles between a few degrees and around 11 deg, combined with large energy to density ratios $E/A \gtrsim 10^{55} \text{ erg cm}^3$ for $k = 2$, or rather extreme $E/A \gtrsim 10^{58} \text{ erg cm}^3$ for $k = 0$. Viewing angles larger than $\theta_v - \theta_j \sim 11 \text{ deg}$ cannot be constrained because in that case the shock is in the ‘point-source at the jet edge’ regime all the way to 262 d, with a rather small apparent transverse velocity. On the other hand, such a large viewing angle would be very unlikely given the huge γ -ray isotropic-equivalent energy of this source.

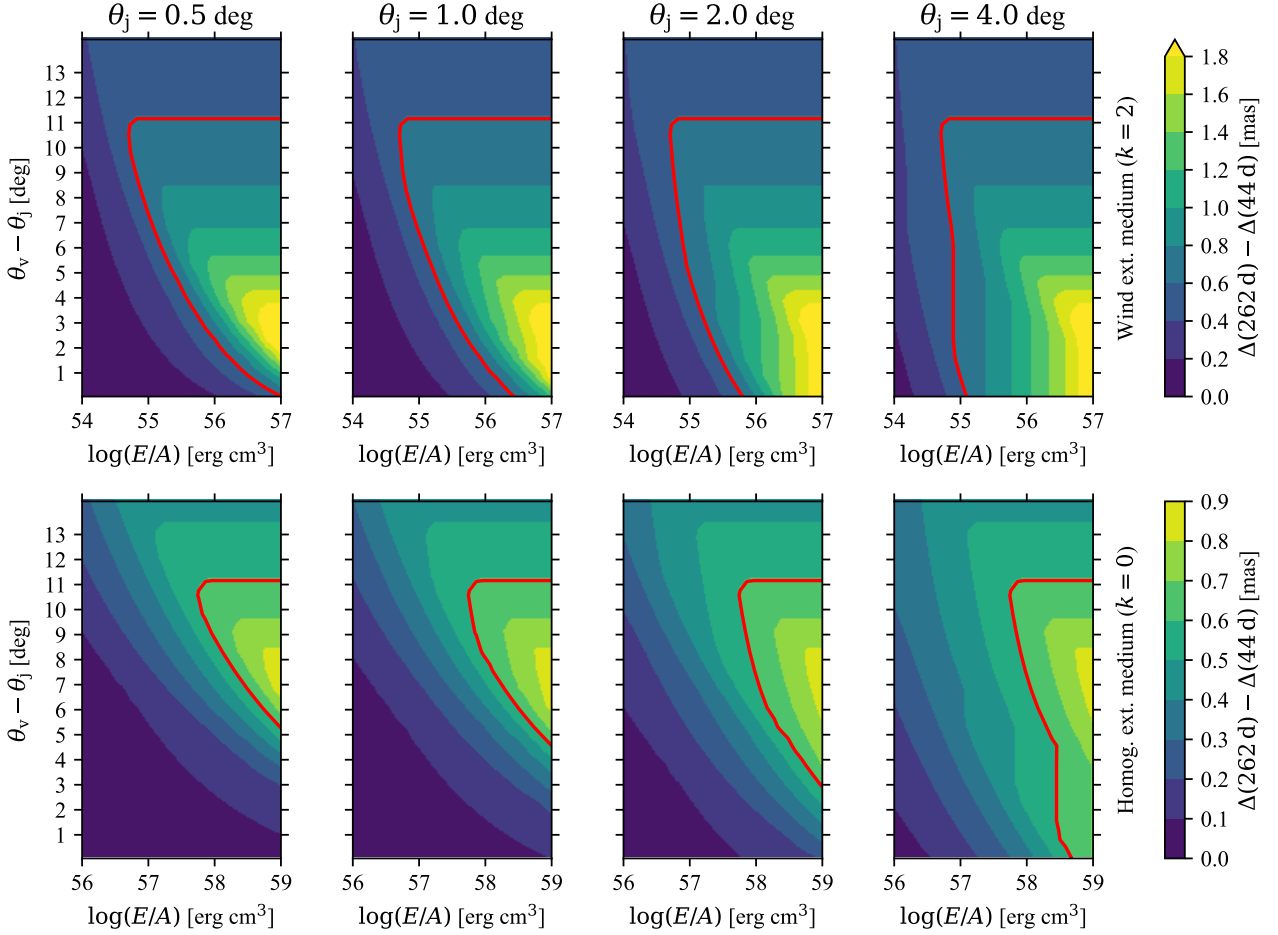


Figure 5.12: Constraint on the viewing angle from the absence of an observed source apparent displacement in our VLBA observations. In each panel, filled contours show the source centroid displacement expected between 44 d and 262 d, color coded as shown in the colorbar on the right, as a function of the E/A ratio and of the off-edge viewing angle $\theta_v - \theta_j$. The red contour shows $\Delta(262 \text{ d}) - \Delta(44 \text{ d}) = 0.6 \text{ mas}$, which represents the largest displacement compatible at 1σ with our observations. The red contour hence contains the excluded parameter region. The upper panel row refers to a wind-like external medium, while the lower row refers to a homogeneous external medium. Each column assumes a different jet half-opening angle, as reported on top of the column.

Chapter 6

The candidate host galaxy of GRB 200716C

In this chapter I present the analysis of the candidate host galaxy of GRB 200716C. The following work was published in *Astronomy & Astrophysics* with the title “*Multi-scale VLBI observations of the candidate host galaxy of GRB 200716C*”.

6.1 Introduction

Studying GRB host galaxies is crucial for directly investigating the nature of the progenitor, its formation channel, and the circumburst medium. In particular, radio and submillimeter observations can be useful for determining the level of obscured star formation and the overall properties of highly star-forming galaxies at high redshifts, such as metallicity and SFR [71], or the interaction between the host galaxy and the surrounding intergalactic medium [116, 117]. The first study of the radio properties of GRB host galaxies was performed by [118]: the authors studied 20 sources and found that the SFR inferred from the radio measurements exceeds the values determined from the optical by an order of magnitude, suggesting significant dust obscuration. Conversely, [119] observed a sample of five galaxies and found a radio-derived $\text{SFR} < 15 M_{\odot} \text{yr}^{-1}$, in agreement with the values inferred from optical estimators, suggesting little dust obscuration. Other studies tackled this problem [71, 116–118, 120–125] and, although they generally agree with the hypothesis of little dust obscuration, a conclusive result is still missing due to the dearth of detected sources: among the approximately 87 host galaxies that have been observed in the radio, only 20 have a confirmed detection, corresponding to a $\sim 23\%$ detection rate. As a consequence, outstanding questions remain unanswered, such as whether or not long GRBs are unbiased tracers of the cosmic star formation history, or whether or not they provide clues as to a particular formation channel of young massive stars [71, 127], .

A complementary approach is based on the use of ongoing radio sky surveys provided by the SKA precursors and pathfinders, such as the Rapid Australian SKA Pathfinder Continuum Survey (RACS; [298]), the VLASS [299], and the LOw-Frequency ARray (LOFAR) Two-metre Sky Survey (LoTSS; [300]). The rms noise levels of these surveys are seldom deep enough to reveal faint radio emission from GRB hosts; however, they provide a handy resource with which to carry out a systematic search, which is ideal for singling out the most extreme objects for subsequent follow up with dedicated observations. In this work, we follow this approach and present a detailed radio study of the candidate host galaxy of GRB 200716C based on public survey data and new, dedicated, deep and high angular resolution radio observations.

GRB 200716C triggered the *Fermi*–GBM at 22:57:41 UT on 2020 July 16, which classified it as a long-duration GRB [301, 302]. The prompt emission was subsequently detected by *Swift*-BAT and XRT ([303]), *AGILE* Mini-CALorimeter [304], *CALET* Gamma-Ray Burst

Monitor [305], Insight-HXMT/HE [306], and Konus–Wind [307]. An extended source was detected in the Sloan Digital Sky Survey (SDSS) within ~ 1 arcsec from the location of the optical afterglow of GRB 200716C [308], and a photometric redshift of $z = 0.348 \pm 0.053$ for SDSS J130402.36+293840.6 (J1304+2938 hereafter) was estimated. Other optical detections of this galaxy were subsequently reported [309–311].

On the other hand, based on the analysis of its prompt emission light curve, it was recently proposed that GRB 200716C might not be a long-duration GRB, but a short-duration GRB that is lensed by an intermediate-mass black hole (IMBH; $M_{\text{IMBH}} \sim 10^5 M_{\odot}$; [312, 313]). According to this scenario, the optical source J1304+2938 could be a foreground galaxy hosting the IMBH that gravitationally deforms the emission from GRB 200716C (hence, a background source).

The structure of the chapter is the following. The observations and their analysis are reported in Section 6.2. We present and discuss our results in Section 6.3 and 6.4, respectively. In Section 6.5 we conclude with a brief summary. Throughout the work we assume a standard Λ -CDM cosmology with $H_0 = 69.32 \text{ km s}^{-1} \text{ Mpc}^{-1}$, $\Omega_m = 0.286$ and $\Omega_{\Lambda} = 0.714$ [216]. At $z = 0.341$ (Section 6.3), 1 arcsec corresponds to roughly 4.9 kpc.

6.2 Observations

6.2.1 Multi-wavelength archival data

We searched for J1304+2938 in publicly available data and surveys. Its coordinates are (J2000) $\alpha = 13^{\text{h}}04^{\text{m}}02.371^{\text{s}}$, $\delta = +29^{\circ}38'40.66''$ [314]. This galaxy is present in catalogues produced with LOFAR at 130–170 MHz (LOFAR J130402.62+293839.8, [315]), the Wide-field Infrared Survey Explorer (WISE; [316]) at 3.4, 4.6, 12, and 22 μm (WISEA J130402.47+293839.3) and the SDSS [314] in the optical z , i , r , g , and u filters (SDSS J130402.37+293840.6, [308]). For these three surveys, we obtained the flux densities directly from the above references.

We also investigated the RACS at 0.89 GHz, the Faint Images of the Radio Sky at Twenty-centimeters (FIRST; [317]), the NRAO Very Large Array Sky Survey (NVSS, [318]), and the APERTure Tile In Focus array (Apertif, [319]) imaging survey at 1.4 GHz, and the VLASS at 3 GHz. The angular resolution and the epoch of each observation are provided in Table 6.2 in Appendix 6.6.1. At the radio wavelengths, the public observations with the highest angular resolution are those from the VLASS, with the beam size being $2.5''$. We downloaded the FITS images from The Canadian Initiative for Radio Astronomy Data Analysis (CIRADA¹) for the NRAO surveys, from the CSIRO ASKAP Science Data Archive (CASDA²) for the RACS, and from the Apertif DR1 documentation website³ for the Apertif imaging survey, and we subsequently performed Gaussian fits with the JMFIT task in AIPS [219]. We show the radio measurements in Figure 6.1, while a full spectrum from 0.1 to 10^6 GHz is provided in Figure 6.4 in Appendix 6.6.1.

6.2.2 European VLBI Network and e -MERLIN follow up

We also carried out dedicated VLBI observations of J1304+2938. On 2021 October 23, we observed at 5 GHz with the EVN for a total time of 6 h (PI: Giarratana; project: EG118A). These data were recorded at $2048 \text{ Mbits s}^{-1}$ and correlated at the JIVE into eight sub-bands (IFs) with 32 MHz bandwidth and 64 channels each, through two polarisations (RR, LL). On 2021 October 30, we performed a sensitive 12 h observation with the EVN including the e -MERLIN at 1.6 GHz (PI: Giarratana; project: EG118B). The data were recorded at $1024 \text{ Mbits s}^{-1}$ and

¹<http://cutouts.cirada.ca>

²<https://data.csiro.au/domain/casdaObservation>

³<https://www.astron.nl/telescopes/wsrt-apertif/apertif-dr1-documentation/>

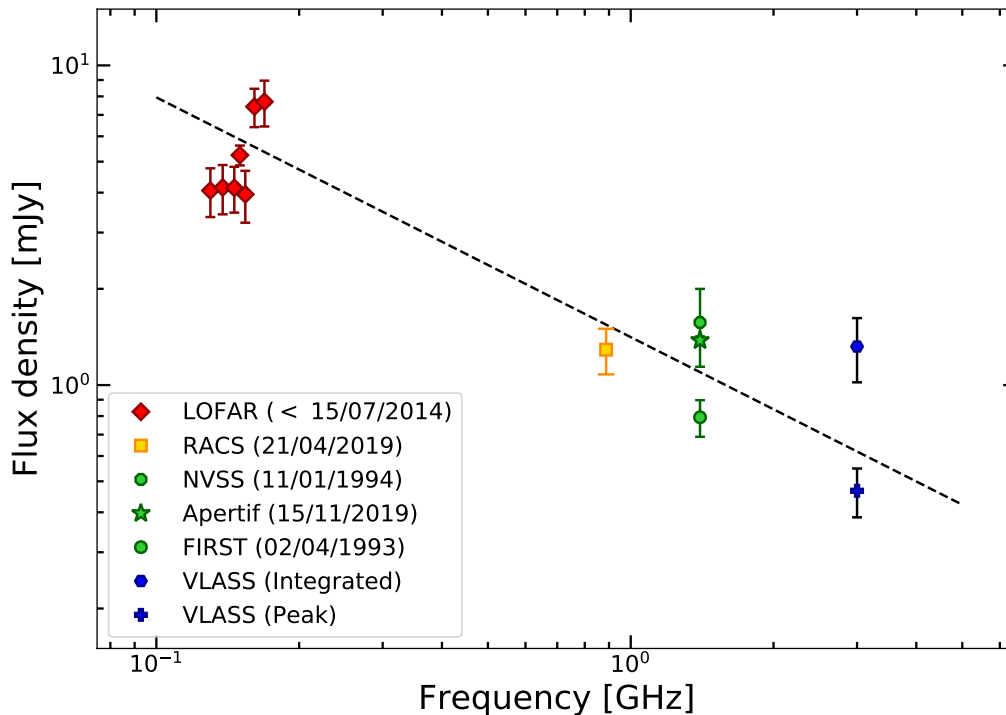


Figure 6.1: Flux-density measurements (mJy) as a function of frequency (GHz) for J1304+2938 in the radio band. Data were taken at different epochs (see Table 6.2 in Appendix 6.6.1). The dashed black line corresponds to a power law $F \propto \nu^\alpha$ with spectral index $\alpha = -0.75$.

correlated at JIVE into eight sub-bands (IFs) with 16 MHz bandwidth and 32 channels each, through two polarisations (RR, LL). The averaging time for the visibilities was of 2 s. The structure of the observations followed a typical phase-referencing experiment, with scans of ~ 3 min on the target followed by scans of ~ 1.5 min on two phase reference sources (J1310+3220 and J1300+2830). 3C345 was the fringe finder and bandpass calibrator for both the 1.6 and 5 GHz observations.

The calibration and imaging were performed using AIPS following the standard procedure for EVN phase referenced observations, except that for the global fringe fitting, for which we used both the phase calibrators in the following way. We first derived the solutions for J1300+2830, which we applied to the target and the other calibrators. We then derived the residual solutions using a model of the other calibrator J1310+3220, and applied these final solutions to J1310+3220 and the target.

The time- and bandwidth-limited field of view of these observations was of about ~ 5 arcsec, but the source is well localised in the observations with an angular resolution of 2.5 arcsec. Therefore, we searched for the radio emission of the putative host galaxy in an area of 2.5 arcsec in diameter, which corresponds to ~ 12 kpc at $z = 0.341$ (see also Section 6.3). We adopted a natural weighting scheme to maximise the sensitivity to detect any potential extended structure. We obtained dirty images with an rms of $8 \mu\text{Jy beam}^{-1}$ at 1.6 GHz, and $9.6 \mu\text{Jy beam}^{-1}$ at 5 GHz (Table 6.1). At 1.6 GHz, the largest angular scale detectable ϑ_{LAS} is of about 2 arcsec, which corresponds to roughly 10 kpc at $z = 0.341$, while at 5 GHz it is $\vartheta_{\text{LAS}} \sim 50$ mas, which amounts to 245 pc.

6.2.3 Spectroscopy from the Telescopio Nazionale Galileo

We performed a dedicated spectroscopic follow up of J1304+2938 with the Device Optimized for LOw RESolution (DOLORES) installed at the Telescopio Nazionale Galileo (TNG), with

Table 6.1: VLBI observations of J1304+2938.

Array	Central frequency (GHz)	T-T ₀ (days)	Angular resolution (arcsec)	Flux density (μ Jy)
EVN+e-MERLIN	1.6	379	0.010	< 24
EVN	5.0	372	0.005	< 29

Column 1: Array; *Column 2:* observing frequency (GHz); *Column 3:* T-T₀ (days), which is the total time from the burst; *Column 4:* angular resolution (arcsec); *Column 5:* Upper limits (3σ) for the flux density (μ Jy).

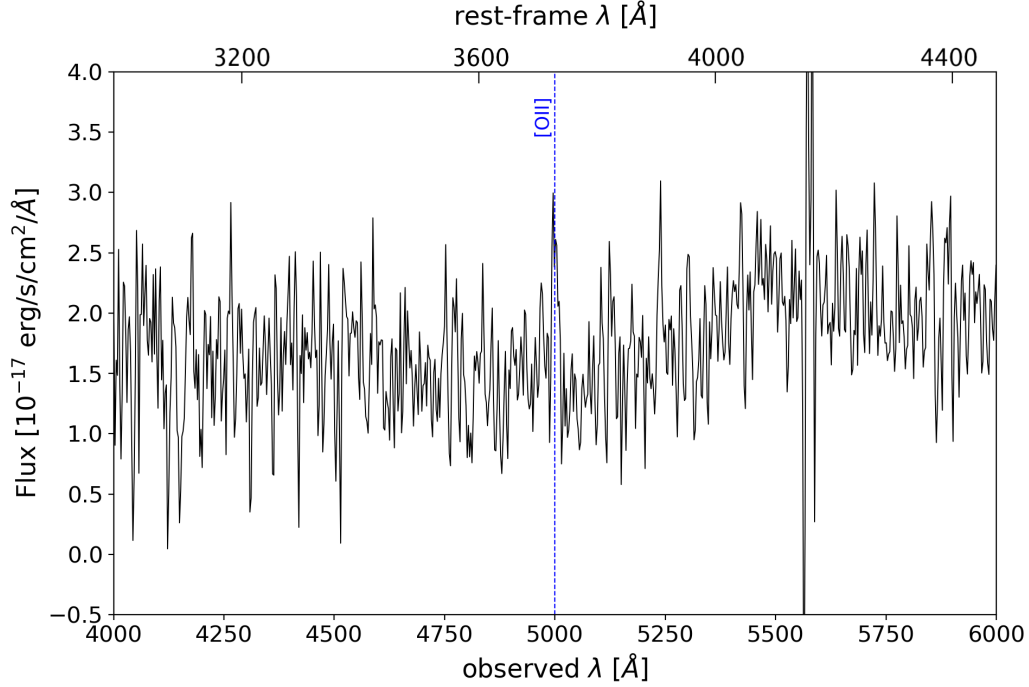


Figure 6.2: TNG DOLORES observed spectrum of the galaxy J1034+2938. The [OII] λ 3727 Å line is marked. At \sim 5600 Å a residual sky line remains after the data reduction. The rest frame wavelengths are shown on the upper x-axis.

the aim of confirming its photometric redshift of $z = 0.348 \pm 0.053$ as reported by the SDSS [308]. We took a single 30 min observation on the night of 2022 March 5 with the LR-B grism and a long-slit of $1.0''$ width. The mean air mass during the observation was 1.05.

An exposure of a He+Ne+Hg lamp was done to ensure the wavelength calibration and the flux calibration was obtained by observing the Feige 67 ($\alpha = 12^{\text{h}}41^{\text{m}}51.80^{\text{s}}$, $\delta = +17^{\circ}31'21.0''$) spectro-photometric standard star of the catalogs of [320]. The data reduction was performed using standard IRAF procedures [222]. The DOLORES spectrum is shown in Figure 6.2. We then smoothed the spectrum with a three-pixel boxcar to reduce the noise. Starting from the photometric redshift, we were able to identify one single emission line, corresponding to OII λ 3727 Å, with a signal-to-noise ratio of 10.5. The continuum is detected with a signal-to-noise ratio of 3.2. We measured the object redshift by fitting the line with a single Gaussian profile using the IRAF task `splot`. Although H β (\sim 6524 Å) and OIII λ 5007 Å (\sim 6720 Å) emission lines fall in the wavelength range covered by the DOLORES spectrum, we did not detect them. This could suggest that the emission of the two lines is very weak and drowned in the spectrum noise. A further observation is necessary to place any constraints on the H β and OIII λ 5007 Å emission.

6.3 Results

Based on our TNG spectroscopic observations, we determine a redshift of $z = 0.341 \pm 0.004$. This value confirms and refines the already-known photometric redshift of the galaxy [308]. At $z = 0.341$, the luminosity distance is 1825 Mpc, which gives a scale of $4.9 \text{ kpc arcsec}^{-1}$.

Inspection of the radio surveys, together with measurements available in the literature, reveals unresolved radio emission at the location of the optical galaxy at a significance of between $\sim 3\sigma$ and $\sim 34\sigma$ in all the datasets. The resulting flux densities are reported in Table 6.2 in Appendix 6.6.1 and shown in the spectrum of Figure 6.1, with error bars reporting the 1σ nominal uncertainties from the fitting procedure.

The source is brightest at the lowest frequency, where the LOFAR flux densities range between 4.0 and 7.7 mJy. The spectrum is rather puzzling in this region, with a flat trend between 130 and 150 MHz and a rise between 150 and 200 MHz (Figure 6.1). In the ~ 1 GHz region, the source is somewhat fainter; the most significant detection is achieved with the most sensitive Apertif data (1.38 ± 0.04 mJy); the NVSS data indicate slightly larger values, while the highest resolution FIRST data show a slightly lower value, perhaps suggestive of the presence of some extended emission (see Figure 6.5 in Appendix 6.6.1); however, the signal-to-noise ratios of the NVSS and the FIRST are lower and the results could be considered overall consistent with Apertif. At 3 GHz, the VLASS data are the only ones in which the fitting result suggests that the source is resolved, providing a significantly larger value for the integrated flux density than the brightness surface peak. However, J1304+2938 is located exactly on a side lobe of the relatively bright ($S_{3 \text{ GHz}} = 6.0 \pm 0.4$ mJy) and clearly extended radio source FIRST J130353.7+293734 (coincident with SDSS J130353.70+293733.1); considering this fact, the low signal-to-noise ratio, and the ‘‘quick look’’ nature of the VLASS data, we cannot conclusively determine the nature of the detected source and consider the values for both components in our analysis. The nominal deconvolved size of the major axis of the component would be $5.6''$, corresponding to ~ 27 kpc at $z = 0.341$.

We further point out that the VLASS data were taken in two separate epochs, one before and one (85 d) after the occurrence of the GRB. Nevertheless, the two measurements are in agreement with each other within the uncertainties, and so we cannot claim any contribution from the afterglow, whose flux density is constrained to be no higher than $180 \mu\text{Jy}$. As a matter of fact, under the reasonable assumption that the afterglow does not contribute to the second epoch emission, we also combined the two epochs in a single image, which allows us to obtain a better constrained fit, which is also reported in Table 6.2 in Appendix 6.6.1.

On milliarcsecond scales, our deep VLBI observations did not detect any source at 1.6 and 5 GHz. We can put stringent 3σ upper limits on the peak surface brightness of about $30 \mu\text{Jy beam}^{-1}$ at both frequencies, which corresponds to $\sim 9 \times 10^{28} \text{ erg s}^{-1} \text{ Hz}^{-1}$ if we use our spectroscopic redshift and adopt a reference spectral index of $\alpha = 0.0$ (typical of compact components). On the larger scales, the moderate signal-to-noise ratio, the difference in angular resolution and observing epochs, and the still preliminary nature of the data from the latest surveys do not allow an accurate modeling of the spectrum, which will be the subject of a future study. However, the overall trend of optically thin emission, perhaps with a hint of self-absorption at low frequency, indicates the nonthermal nature of the emission in the observed frequency range. As a reference, in Figure 6.1 we overlay a $F_\nu \propto \nu^{-0.75}$ power law on the observed data. Using this reference value for the extended emission, and the measurement with the highest signal-to-noise ratio (from the Apertif imaging survey), we derive a luminosity at 1.4 GHz of $L \simeq (5.1 \pm 0.2) \times 10^{30} \text{ erg s}^{-1} \text{ Hz}^{-1}$.

In order to discuss our results within a broader context, we carried out an extensive search for long-duration GRB host galaxies in the literature, looking in particular for previous observations in the radio band [71, 116–118, 120–125]. We ended up with 87 galaxies: among these, only

20 are detected in the radio. Table 6.3 in Appendix 6.6.2 presents the redshift, the radio (monochromatic) luminosity, the frequency, and SFR for the GRB host galaxies detected in radio. The SFR was calculated from the observed flux density at a frequency ν according to the following formula [125]:

$$\left(\frac{\text{SFR}}{\text{M}_{\odot}/\text{yr}}\right) = 0.059 \left(\frac{F_{\nu}}{\mu\text{Jy}}\right) (1+z)^{-(\alpha+1)} \left(\frac{D_L}{\text{Gpc}}\right)^2 \left(\frac{\nu}{\text{GHz}}\right)^{-\alpha}, \quad (6.1)$$

where F_{ν} is the flux at the frequency ν , z is the redshift, D_L is the luminosity distance, and α is the spectral index, which we assume to be -0.75 . In addition to the sources reported in Table 6.3 in Appendix 6.6.2, we collected 67 non-detections from the literature, resulting in upper limits on the SFRs down to $<0.02 \text{ M}_{\odot} \text{ yr}^{-1}$ (GRB 060218, [125]). The measured flux density of J1304+2938 is well above the upper limits found in the literature, making it the third-most luminous GRB host galaxy ever discovered. More generally, a radio emission above $10^{30} \text{ erg s}^{-1} \text{ Hz}^{-1}$ turned out to be rare (see Table 6.3 in Appendix 6.6.2).

6.4 Discussion

Having multi-frequency and multi-resolution data is an element of novelty in the study of GRB host galaxies, although it leads to a relatively complex picture. The spectrum in Figure 6.1 shows a scattered trend between 1 and 3 GHz: the poor signal-to-noise ratio of most detections in the surveys explains most of this scatter, although additional factors at work could be external, such as scintillation; physical, such as a variable AGN; or instrumental, in the case of diffuse regions, due to the different angular resolutions of the surveys. As our VLBI observations do not reveal any compact emitters, we can rule out the scintillation scenario. In the following sections, we discuss the origin of the radio emission in the framework of the other two extreme cases: a radio-loud AGN versus emission from a diffuse star-forming region.

6.4.1 The radio-loud AGN

The radio-to-optical luminosity ratio $R = F_{\text{radio}}/F_{\text{opt}}$ is a classical tool for characterising the radio loudness of an active galaxy [321]. Considering the nearest available bands to those traditionally used to calculate R , we obtain for J1304+2938 a value of $R = 53$, which is well into the radio-loud domain. The 1.4 GHz radio luminosity from the Apertif imaging survey is (5.1×10^{23} , in units of W Hz^{-1}) and the steep spectral index in the radio band would place J1304+2938 in the Fanaroff-Riley I (FRI) class [322]. However, the available data do not allow direct confirmation of the expected morphology for an FRI radio galaxy, with a compact core and twin jets ending in diffuse, edge-dimmed lobes or plumes. The survey data are overall compatible with the presence of some diffuse emission on scales of a few tens of kiloparsecs (kpc), as indicated by the apparently resolved nature of the VLASS image and the increase in total flux density when decreasing the resolution in the 1.4 GHz data (from FIRST, to Apertif, and NVSS). If the total extension of the radio emission were confined within a few kpc, the source could be classified as FR0 [323] or a low-power compact source (LPC, [324]), which indeed represent a substantial fraction of the radio-loud population at lower redshift [325].

However, in spite of all the circumstantial support from the radio surveys, the AGN scenario lacks the ultimate signature, that is, the presence of an active compact core, either from high-energy data or from VLBI observations. In this sense, the stringent upper limits provided by our deep images argue against the presence of a compact core down to rather low luminosities. Therefore, our result disfavours the radio-loud AGN scenario, leaving only the less likely

possibility of a strongly debeamed core (if the axis of the jets of the radio galaxy are seen under a large viewing angle) or of a recently switched-off nuclear activity [326].

At high energy, before the GRB detection by *Swift*, in X-rays only the ROSAT satellite pointed towards this region of the sky between July and December 1990. No source is visible in the 0.1–2.4 keV image of the ROSAT All-Sky Survey (RASS; [327]). With PIMMS, assuming a power-law model with a photon index of 1.7, we could set only loose upper limits on the flux ($\sim 1 \times 10^{-13}$ erg cm $^{-2}$ s $^{-1}$ in the 0.2–10 keV band) and luminosity ($\lesssim 4 \times 10^{43}$ s $^{-1}$), which are not sufficient to conclude on the presence of AGN-related X-ray emission.

Future experiments able to test the debeamed AGN scenario would be a detection at high energy or a successful imaging of a radio-galaxy structure based on deeper radio data at intermediate angular resolution. In this case, and if GRB 200716C belongs to J1304+2938, this would be the third GRB found within a galaxy with an AGN, after GRB 170817A, which occurred in NGC 4993 [93, 328–331], and GRB 150101B, which belonged to WISEA J123204.97-105600.6 [332]. NGC 4993 is a low-luminosity, radio-loud galaxy [331], while WISEA J123204.97-105600.6 (2MASX J12320498-1056010) is an X-ray bright, radio-loud galaxy [332].

6.4.2 The extreme star formation

An immediate implication of the non-detection with the EVN is that the radio emission detected by lower angular resolution surveys is consistent with being extended on scales that are larger than the largest detectable angular scale ϑ_{LAS} , which is of 2 arcsec at 1.6 GHz (hence smaller than the angular scales sampled by the VLASS). Moreover, the lack of a compact component disfavours variability as the most viable explanation for the discrepancy between low angular resolution measurements. On the other hand, the trend of increasing total flux density when considering lower resolutions in the survey data at 1.4 GHz corroborates the hypothesis of the presence of diffuse emission on galactic scales. Moreover, considering the FIRST and the Apertif imaging surveys, the beam area is roughly 23 and 309 arcsec 2 (Figure 6.5 in Appendix 6.6.1), respectively, while the flux density is (790 ± 100) and (1380 ± 40) μJy , respectively. Thus, in the FIRST survey we would have a contribution from the galaxy of (590 ± 108) μJy spread over 39 beams, and hence an average of (15 ± 3) $\mu\text{Jy beam}^{-1}$, which is under its rms noise level. This is a rather simplified approach, assuming uniform brightness distribution over the entire Apertif beam area, but it is generally in agreement with the presence of more intense star formation in the central regions (within the ~ 25 kpc beam of the FIRST) and lower, yet significant additional regions falling in the 140 kpc \times 54 kpc beam of Apertif.

We further note the presence of a second emitting component in the FIRST and Apertif imaging surveys (Figure 6.5 in Appendix 6.6.1): this contaminating source is found at a distance of ~ 40 arcsec, which is 200 kpc at $z = 0.341$, and is therefore likely unrelated to J1304+2938. However, in the NVSS, J1304+2938 and the contaminating source are not well separated, possibly explaining the observed discrepancy in the total flux density between the Apertif imaging survey and the NVSS.

Possible mechanisms for a diffuse radio emission unrelated to nuclear activity are the free-free emission from the ionised gas surrounding a population of bright OB stars, which would lead to a thermal spectrum, and/or the SN contribution from young stars, which is characterised by a steep non-thermal spectrum. As our data are clearly suggestive of a steep spectral index, we can assume the latter to be the predominant emission mechanism in the portion of the spectrum we are interested in. Considering the high luminosity we find, this leads to a high SFR 4 . As the SFR can be inferred from the radio luminosity with different formulas, from the flux density at 1.4 GHz with the FIRST, the Apertif imaging survey, and the NVSS, we estimate that SFR = (186 ± 42) $M_{\odot} \text{ yr}^{-1}$, (324 ± 61) $M_{\odot} \text{ yr}^{-1}$, and (376 ± 117) $M_{\odot} \text{ yr}^{-1}$, using the

⁴we consider a galaxy as highly star forming if SFR $\geq 15 M_{\odot} \text{ yr}^{-1}$ [125]

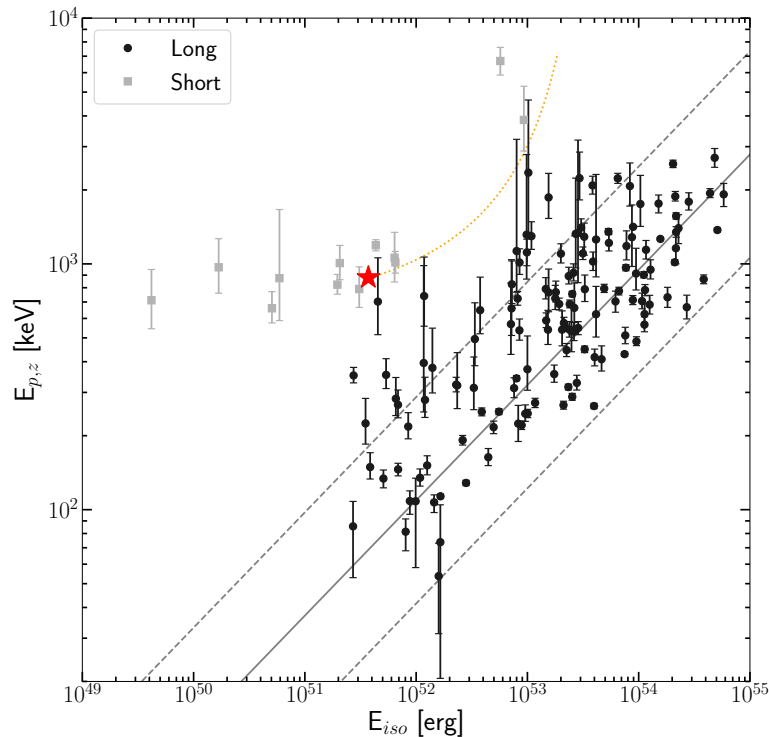


Figure 6.3: Location of GRB 200716 (red star) in the rest-frame $(E_{iso}, E_{p,z})$ plane for the short-duration GRBs (grey squares) and the long-duration GRBs (black circles) of [335]. The grey solid line indicates the Amati relation estimated using the long-duration GRBs of [335], while the grey dashed lines indicate its 3σ uncertainty. The orange dotted line shows the position of the burst for $0.341 \leq z \leq 10$.

conversion from [125], respectively. Even taking the more conservative SFR derived with the FIRST, J1304+2938 would be among the ten most-star-forming GRB host galaxies discovered so far.

As the SFR derived from the radio is not affected by dust extinction, by comparing it with the value provided by optical estimators, it is possible to determine the amount of dust within the host galaxy, which is important for characterising the environment that leads to a burst [71, 118]. To obtain meaningful constraints on the SFR, [120] used a complete sample of 30 hosts with $z < 1$, including those from the The Optically Unbiased Gamma-Ray Burst Host (TOUGH) sample [110] and sources compiled from the literature. The authors found that at least $\sim 63\%$ of GRB hosts have $\text{SFR} < 100 M_{\odot} \text{yr}^{-1}$ and at most $\sim 8\%$ can have $\text{SFR} > 500 M_{\odot} \text{yr}^{-1}$. Surprisingly, $\gtrsim 88\%$ of the $z \lesssim 1$ GRB hosts have UV dust attenuation $A_{UV} < 6.7 \text{ mag}$ and $A_V < 3 \text{ mag}$, suggesting that the majority of GRB host galaxies are not heavily obscured by dust. The latter result is further strengthened by subsequent studies on samples of GRB hosts (see, e.g., [121–123, 125]). To determine the level of dust obscuration, a reliable estimate of the SFR from optical estimators is needed, such as the $\text{H}\alpha$, $\text{H}\beta$, or NII emission lines, which could also provide further confirmation of the photometric redshift. Above all, such optical estimators would allow a detailed study of the chemical composition of the galaxy. Among these, the $\text{H}\beta$ emission line falls in the wavelength range covered; nevertheless, our spectral observation does not allow us to calculate the SFR from the latter emission lines, possibly due to the fact that they are too weak. A preliminary estimate of the flux expected from the $\text{H}\beta$ emission line can be provided by taking the relation between OII , $\text{H}\alpha$, and $\text{H}\beta$ from [333], and assuming the ratio $\text{OII}/\text{H}\alpha = 1.26$ for star-forming galaxies in the local Universe provided by [334]; for a signal-to-noise ratio of 10.5 for the OII detection, we get a flux three times smaller for the $\text{H}\beta$ emission line, which would be too weak to be detected above the continuum emission. Further, deeper spectroscopic follow up is therefore needed.

6.4.3 J1304+2938 and GRB 200716C

The overall radio properties of J1304+2938 seem to favour a highly star-forming galaxy, which is the natural environment expected for explosive transient events generated during the collapse of young massive stars, such as long-duration GRBs. Therefore, the radio properties of J1304+2938 are in agreement with the long-duration nature of GRB 200716C. Nevertheless, there are still some caveats that are relevant to the interpretation of this burst. First of all, the spectrum of the galaxy in the radio band shows some peculiarities that could be due to the low signal-to-noise ratio, the different angular resolutions, and/or the epochs of the surveys. To solve the conundrum, deep observations with arcsecond resolution and a broad bandwidth are required, such those provided by the VLA, for example. Second, taking the isotropic equivalent energy E_{iso} and the time-integrated peak energy E_p for 150 long- and short-duration Konus–Wind GRBs [335], with $E_{iso} = 3.7 \times 10^{51}$ erg and $E_{p,z} = 880$ keV, GRB 200716C is a clear outlier of the Amati relation, where $E_{p,z} = E_p(1+z)$ (see Figure 6.3) and E_{iso} was rescaled to $z = 0.341$. This holds true even in the case where J1304+2938 is a foreground galaxy and GRB 200716C is at a higher redshift (Figure 6.3, orange dotted line). To be consistent with the 3σ uncertainty of the Amati relation, the uncertainty on the peak energy should be at least ~ 230 keV (1σ). Finally, we note that GRB 200716C is located close to another well-known and still puzzling outlier of the E_{iso} - $E_{p,z}$ relation, namely GRB 061021 [336]. Nevertheless, the GRB 061021 host galaxy was not detected up to $6 \mu\text{Jy beam}^{-1}$ at 6 GHz [337], suggesting different properties with respect to J1304+2938.

The position of GRB 200716C on the E_{iso} - $E_{p,z}$ plane, together with the fact that its prompt emission light curve shows two prominent peaks, followed by an extended emission up to $T_{90} \sim 90$ s [302, 305, 306, 338], led some authors to question the long-duration nature of this burst. An alternative explanation could be that GRB 200716C is a short-duration GRB gravitationally lensed by an IMBH, which is probably hosted by J1304+2938 [312, 313]. We highlight the fact that, because of their high luminosities (up to 10^{53-54} erg s $^{-1}$; [22, 339]), GRBs can be detected up to the highest redshifts (the farthest GRB currently known is GRB 090429B at a photometric redshift of $z = 9.4$; [340]) and therefore they can be used as probes of the early Universe [341]. As they could be cosmologically distant events, some GRBs might be gravitationally lensed (e.g. [342] and references therein). Because of the strong lensing effect, photons coming from a distant source travel different geometric paths as they approach the foreground lensing object and form multiple magnified images of the same background source [343]. As a consequence, we observe variations in the lensed images with a time delay that depends on the gravitational potential of the lens. In the case of GRBs, if gravitationally lensed, we expect to measure a bright γ -ray pulse followed by a dimmer duplicate. To date only a few GRBs have been suggested as candidate lensed events, namely GRB 950830 [342], GRB 210812A [344], GRB 081126A, and GRB 090717A [345], based on the analysis of their light curves.

If J1304+2938 hosts the gravitational lens of GRB 200716C, VLBI observations could potentially detect a compact emission from a radio-loud IMBH acting as a (milli-)lens [346]. Possible radio emission from an IMBH would greatly help our understanding of the localisation of these objects in galaxies, which is highly unconstrained from an observational perspective [347]. Ultra-luminous X-ray sources (ULXs) have been suggested as possible IMBHs [348, 349] and they are variable objects on different timescales (from months to years; see e.g. [350–352]). However, not even our sensitive VLBI follow up can shed light on this hypothesis as the radio emission from accreting IMBH can only be detected in local galaxies [353, 354].

To date, only a few (macro-)lensing galaxies showing radio/mm emission [355–357] have been found, making ‘radio-emitting’ lenses extremely rare objects⁵. In general, VLBI is the only method that allows us to pinpoint the multiple images produced by a gravitational lens with

⁵These radio-loud lenses are at higher redshifts than J1304+2938 ($z \sim 0.65 - 0.8$).

mass $< 10^{5-6} M_{\odot}$, which are expected to be separated by a few mas [358, 359]. Nevertheless, in order to detect the putative radio-lensed images of GRB 200716C, the VLBI observations would have had to be carried out within a few hours or days of the detection of the burst at γ -rays.

6.5 Conclusions

In this chapter, I presented the analysis of dedicated VLBI observations together with IR and optical public data of the putative host galaxy J1304+2938 of GRB 200716C at $z = 0.341$. We set stringent upper limits (sensitivity of $< 10 \mu\text{Jy beam}^{-1}$) on the presence of compact radio emission, namely < 50 mas at 5 GHz, within a field of view of 2.5 arcsec at 1.6 and 5 GHz. Moreover, by performing a dedicated spectroscopic follow up with the TNG, we corroborated the previous redshift estimate of the galaxy [308].

The non-detection with EVN and EVN+*e*-MERLIN suggests that the radio emission detected at low angular resolution by the RACS, FIRST, the Apertif imaging survey, and the NVSS and VLASS surveys might be diffuse and therefore completely resolved out by our VLBI observations. Moreover, the observed scatter in the publicly available flux density measurements at low frequencies cannot be explained by a variable, compact source, further corroborating the hypothesis of diffuse emission from highly star-forming regions. We derived a 1.4 GHz luminosity greater than $10^{30} \text{ erg s}^{-1} \text{ Hz}^{-1}$, which implies a SFR $\sim 300 M_{\odot} \text{ yr}^{-1}$. This high SFR is consistent with the most extreme environments for long-duration GRBs. That being the case, J1304+2938 would be among the most radio-bright long-GRB host galaxies discovered so far. Nevertheless, the temporal and spectral properties of the prompt emission of GRB 200716C, together with the offset with respect to the Amati relation for long-duration GRBs, mean that the nature of this burst remains puzzling.

6.6 Appendices

6.6.1 Photometric data

Table 6.2 presents the various measurements for J1304+2938 available from the literature and/or our analysis of survey data. Figure 6.4 presents the flux density measurements (mJy) as a function of frequency (GHz), from 0.1 to 10^6 GHz. Figure 6.5 shows the radio detection of J1304+2938 in the FIRST (colours) and Apertif imaging survey (surface brightness contours, in white).

Table 6.2: Publicly available data for J1304+2938 from different surveys.

Survey / Instrument	Central frequency (GHz)	Date	Angular resolution (arcsec)	Flux density (mJy)	Ref.
LOFAR	0.130	<15/07/2014	6×10	4.1±0.7	[315]
LOFAR	0.138	<15/07/2014	6×10	4.2±0.7	[315]
LOFAR	0.146	<15/07/2014	6×10	4.1±0.7	[315]
LOFAR	0.150	<15/07/2014	6×10	5.2±0.4	[315]
LOFAR	0.154	<15/07/2014	6×10	4.0±0.7	[315]
LOFAR	0.161	<15/07/2014	6×10	7.4±1.0	[315]
LOFAR	0.169	<15/07/2014	6×10	7.7±1.3	[315]
RACS	0.89	21/04/2019	26×11	1.3±0.2	This work
FIRST	1.4	02/04/1993	5.4	0.79±0.10	This work
Apertif imaging survey	1.4	15/11/2019	28.6×11.1	1.38±0.04	This work
NVSS	1.4	11/01/1994	45	1.6±0.4	This work
VLASS1 ^a	3	25/11/2017	3.0×2.3	0.38±0.10	This work
VLASS1 ^b	3	25/11/2017	3.0×2.3	1.4±0.5	This work
VLASS2 ^a	3	9/10/2020	2.7×2.4	0.56±0.12	This work
VLASS2 ^b	3	9/10/2020	2.7×2.4	1.3±0.3	This work
VLASS-combined ^a	3		3.0×2.3	0.47±0.08	This work
VLASS-combined ^b	3		3.0×2.3	1.3±0.3	This work
WISE	1.36×10 ⁴	<06/08/2010	12	< 1.6	[316]
WISE	1.36×10 ⁴	<06/08/2010	12	< 3.7	[316]
WISE	1.36×10 ⁴	<06/08/2010	12	< 4.6	[316]
WISE	2.59×10 ⁴	<06/08/2010	6.5	< 0.5	[316]
WISE	2.59×10 ⁴	<06/08/2010	6.5	< 0.7	[316]
WISE	2.59×10 ⁴	<06/08/2010	6.5	0.4±0.2	[316]
WISE	6.51×10 ⁴	<06/08/2010	6.4	0.158±0.011	[316]
WISE	6.51×10 ⁴	<06/08/2010	6.4	0.19±0.02	[316]
WISE	6.51×10 ⁴	<06/08/2010	6.4	0.24±0.03	[316]
WISE	8.94×10 ⁴	<06/08/2010	6.1	0.252±0.008	[316]
WISE	8.94×10 ⁴	<06/08/2010	6.1	0.309±0.012	[316]
WISE	8.94×10 ⁴	<06/08/2010	6.1	0.35±0.03	[316]
SDSS (<i>z</i>)	3.36×10 ⁵	23/05/2004		0.141±0.012	[360]
SDSS (<i>i</i>)	4.01×10 ⁵	23/05/2004		0.104±0.003	[360]
SDSS (<i>r</i>)	4.86×10 ⁵	23/05/2004		0.072±0.002	[360]
SDSS (<i>g</i>)	6.40×10 ⁵	23/05/2004		0.024±0.001	[360]
SDSS (<i>u</i>)	8.45×10 ⁵	23/05/2004		0.010±0.003	[360]

Column 1: survey or instrument. *Column 2:* observing frequency (GHz). *Column 3:* Date of the observation. *Column 4:* angular resolution (arcsec). *Column 5:* Flux density (mJy). The upper limits for the flux density are given with a 1 σ confidence. *Column 6:* References.

^a From JMFIT peak intensity.

^b From JMFIT integral intensity.

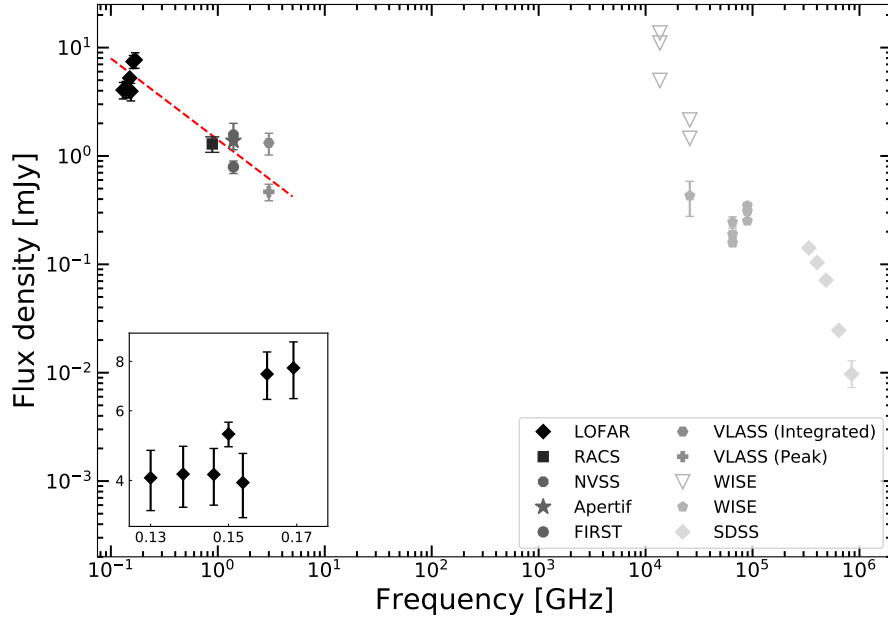


Figure 6.4: Flux-density measurements (mJy) as a function of frequency (GHz) for J1304+2938 from 0.1 to 10^6 GHz. The inset shows the LOFAR data, while the arrows indicate the 3σ upper limits. Data are taken at different epochs (see Table 6.2). The dashed red line corresponds to a power law $F \propto \nu^\alpha$ with spectral index $\alpha = -0.75$.

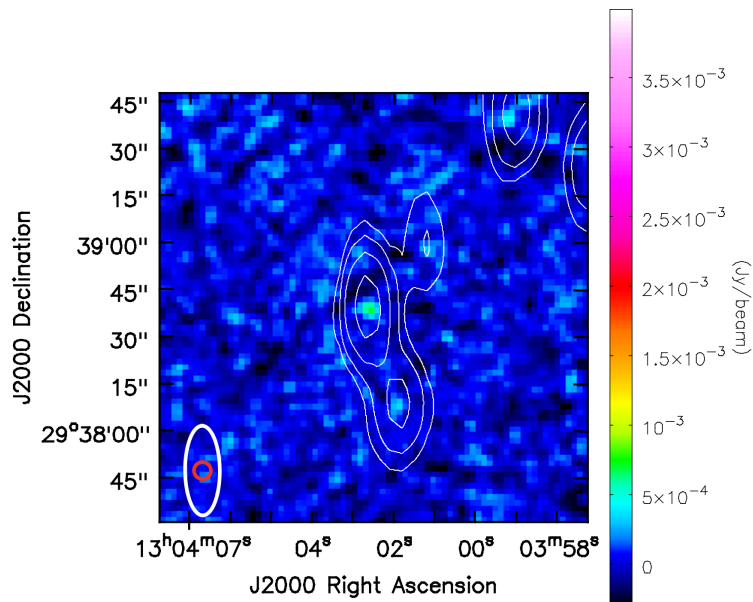


Figure 6.5: Radio detection of J1304+2938 in the FIRST survey at 1.4 GHz, shown by the coloured map and the associated colour bar. The surface brightness contours at levels of 3, 6, 12, 24, and 48σ from the Apertif imaging survey are superimposed in white, where the rms noise level of the Apertif imaging survey is $\sigma = 40 \mu\text{Jy beam}^{-1}$. On the lower left, the restoring beams are shown as a red and a white ellipse for the FIRST and the Apertif imaging survey, respectively. A second, resolved source at roughly 40 arcsec is found to the south.

6.6.2 Luminosities of the GRB host galaxies

Table 6.3 presents the redshift, the radio (monochromatic) luminosity, the frequency, and SFR for the GRB host galaxies detected in radio. The SFR was calculated from the observed flux density at a frequency ν according to the following formula [125]:

$$\left(\frac{\text{SFR}}{M_{\odot}/\text{yr}}\right) = 0.059 \left(\frac{F_{\nu}}{\mu\text{Jy}}\right) (1+z)^{-(\alpha+1)} \left(\frac{D_L}{\text{Gpc}}\right)^2 \left(\frac{\nu}{\text{GHz}}\right)^{-\alpha}, \quad (6.2)$$

where F_{ν} is the flux at the frequency ν , z is the redshift, D_L is the luminosity distance, and α is the spectral index, which we assume to be -0.75. In addition to the sources reported in Table 6.3, we collected 67 non-detections from the literature, resulting in upper limits on the SFRs down to $<0.02 M_{\odot} \text{ yr}^{-1}$ (GRB 060218, [125]).

Table 6.3: Long-duration GRB host galaxies detected in radio so far.

GRB	z	ν (GHz)	F_{ν} ($\mu\text{Jy beam}^{-1}$)	L_{ν} ($\text{erg s}^{-1} \text{ Hz}^{-1}$)	SFR $M_{\odot} \text{ yr}^{-1}$	Ref.
980425	0.0085	1.38	840 ± 160	$(1.4 \pm 0.3) \times 10^{27}$	0.08 ± 0.02	[120]
980703	0.967	1.43	76 ± 10	$(3.2 \pm 0.4) \times 10^{30}$	206 ± 27	[71]
000418	1.119	1.43	69 ± 15	$(4.1 \pm 0.9) \times 10^{30}$	264 ± 57	[118]
020819B	0.41	3.0	31 ± 8	$(1.7 \pm 0.4) \times 10^{29}$	20 ± 5	[125]
021211	1.006	1.43	330 ± 31	$(1.5 \pm 0.1) \times 10^{31}$	982 ± 82	[120]
031203 ^a	0.105	1.39	254 ± 46	$(7 \pm 1) \times 10^{28}$	4.5 ± 0.8	[120]
050223	0.591	5.5	90 ± 30	$(1.2 \pm 0.4) \times 10^{30}$	210 ± 70	[123]
051006	1.059	3.0	9 ± 3	$(5 \pm 2) \times 10^{29}$	53 ± 18	[124]
051022	0.809	5.23	13 ± 4	$(4 \pm 1) \times 10^{29}$	61 ± 19	[122]
060505	0.089	1.38	76 ± 35	$1.5 \pm 0.7 \times 10^{28}$	0.9 ± 0.4	[117]
060729 ^b	0.54	5.5	65 ± 28	$(7 \pm 3) \times 10^{29}$	123 ± 53	[123]
060814	1.92	3.0	11 ± 3	$(2.3 \pm 0.6) \times 10^{30}$	258 ± 70	[124]
061121	1.314	3.0	17 ± 5	$(1.5 \pm 0.4) \times 10^{30}$	165 ± 48	[124]
070306	1.496	3.0	11 ± 3	$(1.3 \pm 0.4) \times 10^{30}$	145 ± 39	[124]
080207	2.086	5.23	17 ± 2	$(4.3 \pm 0.5) \times 10^{30}$	731 ± 86	[122]
080517	0.089	4.5	220 ± 40	$(4.4 \pm 0.8) \times 10^{28}$	7 ± 1	[116]
090404 ^d	3.0	5.23	11 ± 3	$(6 \pm 2) \times 10^{30}$	1074 ± 293	[122]
100316D	0.059	1.38	657 ± 21	$(5.5 \pm 0.2) \times 10^{28}$	3.5 ± 0.1	[117]
100621A ^c	0.542	5.5	120 ± 32	$(1.3 \pm 0.3) \times 10^{30}$	229 ± 61	[123]
111005A	0.013	1.38	245 ± 30	$(9 \pm 1) \times 10^{26}$	0.06 ± 0.01	[117]
200716C	0.341	1.4	1380 ± 40	$(5.1 \pm 0.2) \times 10^{30}$	324 ± 61	This work

Column 1: GRB name. *Column 2:* redshift. *Column 3:* observing frequency (GHz). *Column 4:* Flux density ($\mu\text{Jy beam}^{-1}$) referred to the observing frequency. *Column 5:* monochromatic luminosity ($\text{erg s}^{-1} \text{ Hz}^{-1}$). *Column 6:* SFR calculated with the formula provided by [125]. *Column 7:* References. The uncertainties on the monochromatic luminosity and the SFR are derived with the standard formula for the propagation of errors.

^a We used the flux density measurement at 1.39 GHz from [120], while the SFR from [125] is derived from the flux density at 5.5 GHz.

^b We used the flux density value from [123] at 5.5 GHz, while [125] derived an upper limit for the SFR using the upper limit for the flux density at 1.39 GHz from [120].

^c We used the flux density at 5.5 GHz from [123], while [125] used an upper limit for the flux density at 2.1 GHz.

^d Even though the host galaxy of GRB 090404 was detected by [122], the authors stated that an afterglow origin for the observed detection could not be ruled out.

Chapter 7

Radio afterglows of *Swift* Gamma-Ray Bursts

The radio emission during the afterglow phase, stemming from the interaction between the GRB outflow and the surrounding material, provides crucial insights into the progenitor's environment. Since different progenitors are expected to inhabit different environments, a detailed study of the radio emission offers a window into the nature of the central engine propelling the GRB. In particular, it was recently posited that two sub-populations of GRBs may exist based on radio emission. Radio-bright (or radio-loud) GRBs, whose afterglow is detected at centimetre wavelengths, and radio-dark (or radio-quiet) GRBs, lacking radio detection, may point to different progenitors. Confirming or rejecting this hypothesis typically involves statistical analyses on GRB afterglow samples. However, such studies face sensitivity limitations, potentially introducing biases into the inferred outcomes. In this chapter I present the preliminary analysis we carried out on a well-selected sample of *Swift* GRBs observed in radio. The ongoing work will be incorporated in a forthcoming manuscript.

7.1 Introduction

The first, extensive study on radio emission from GRBs was conducted by [44]. The authors compiled a catalogue of 304 afterglows observed primarily at 8.5 GHz with the VLA. Spanning observations from 1997 to 2011, the data set encompassed 2995 flux density measurements, including upper limits. The authors reported a detection rate of 31%, notably lower than the X-ray (95%) and optical (70%) detection rates following the launch of the *Swift* satellite [45]. The narrow flux density range between the brightest and faintest detected cosmological bursts ($z \geq 0.4$) further implies that the detectability of radio afterglows is limited by instrument sensitivity rather than intrinsic properties.

They noted that radio-detected GRBs exhibited larger isotropic equivalent energies and brighter counterparts at other wavelengths, reinforcing the association between radio afterglow detectability and burst energetics. In fact, the energetics of the prompt emission serves a proxy for the kinetic energy of the GRB outflow. Consequently, the larger this value is, the higher the radio luminosity is for the same microphysical conditions of the external shock. Therefore, a higher isotropic equivalent energy is naturally linked to a higher radio luminosity and, hence, to the detectability of the radio afterglow.

To quantify these relationships, the sample was divided into two sub-groups: radio-detected and radio-undetected GRBs. Conducting a K-S test between the isotropic equivalent energy distributions of the two sub-groups revealed that they are inconsistent with being drawn from the same parent distribution. The latter result suggested that γ -ray energetics serves as a reliable indicator of radio detectability. However, no direct correlation between E_{iso} and the

peak radio flux density was identified. Finally, the study explored potential correlations between the peak radio flux density and γ -ray fluence, optical flux density and X-ray flux density. The only significant correlation discovered was between the peak radio flux density and the optical flux density at 11 hr post-burst.

Similar results were obtained from a comprehensive analysis of the bright *Swift* GRB sample known as BAT6 [361]. Within the BAT6 sub-sample of GRBs with at least one radio observation (approximately 68% of the BAT6 sample), a detection rate of around 50% was reported [362]. The authors acknowledged that the relatively higher detection rate, compared to the study by [44], is partly attributed to the BAT6 sample's selection criteria, which focuses on bright *Swift* GRBs. They pointed out that this detection rate is essentially a lower limit, given the follow-up strategy employed. Notably, a non-detection at early times often precludes subsequent follow-up observations. However, considering that the radio afterglow emission might be self-absorbed at early times, the radio light curve is expected to peak at later stages (typically between 1 and 10 d post-burst), when the emission transitions from an optically thick to an optically thin regime at radio frequencies. Consequently, many bursts peaking at later times might be overlooked.

To test the potential influence of sensitivity limits on the non-detections, the authors developed a code named PSYCHE. This code integrates a Population Synthesis Code [363] with a Hydrodynamical Emission model for the afterglow [364]. With PSYCHE, they successfully reproduced the radio flux distribution of the BAT6 sub-sample, providing compelling evidence that the observed rate is constrained by sensitivity limits.

The latter conclusion was corroborated by the Arcminute Microkelvin Imager Large Array (AMI-LA) catalogue comprising 139 GRBs [365]. Utilising the fully automated rapid-response mode of AMI-LA, the authors compiled the first sample of GRB radio afterglows unbiased by multi-wavelength selection criteria. They reported a potential detection rate ranging between 44% and 56%. This rate was attributed to the feasibility of observing the GRB afterglow at very early times (within 1 d post-burst), during which the radio emission is dominated by the RS component.

Nonetheless, an alternative explanation was proposed already in 2013 by [45]. The authors employed 737 observations of 178 GRBs observed with the VLA by [44]. Combining the visibilities of each epoch with the visibility stacking technique, they produced integrated, deeper radio images with lower r.m.s. noise levels. Given that the more sensitive images did not reveal any new afterglows, the authors compared the derived upper limits with the predictions generated from a model. The lack of detection, well below the anticipated radio emission from the model, was clearly inconsistent with the idea that GRBs that are not detected in radio (referred to as radio-dark or radio-quiet GRBs) are simply a fainter tail of the radio-detected GRB population (termed radio-bright or radio-loud GRBs). Moreover, the authors noted that the radio-bright GRBs exhibit higher gamma-ray fluence, isotropic energies, X-ray fluxes, and optical fluxes than the radio-dark GRBs. The authors ascribed these differences to the existence of two physically distinct sub-populations, possibly associated with different prompt emission mechanisms or attributed to different central engines.

Following this interpretation, many authors tackled the problem. When considering GRBs from [44] with an isotropic equivalent energy $E_{iso} > 10^{52}$ erg, a study found that the distributions of the duration of the prompt γ -ray emission $T_{int} = T_{90}/(1+z)$ and the isotropic equivalent energy differ between the sub-samples of radio-bright and radio-dark GRBs [366]. Specifically, radio-dark GRBs exhibited a significantly shorter T_{int} value. The lack of a difference in the redshift distribution between the two populations led the authors to suggest that the absence of radio afterglow might be attributed to physical phenomena related to the circum-burst density profile, rather than being a consequence of the energetics of the GRBs. Furthermore, no convincing correlation between E_{iso} and the radio peak flux density, computed from [150], was identified.

These results were supported when considering larger samples of bursts [367], even extending the analysis to the entire range of E_{iso} values [368]. The key results include:

- radio-bright GRBs being significantly longer than radio-dark GRBs;
- radio-bright GRBs exhibiting higher E_{iso} values;
- a significant anti-correlation between T_{int} and z ;
- a significant anti-correlation between the jet opening angle and z ;
- a significant correlation between T_{int} and E_{iso} ;
- the VHE emission being found predominantly in the radio-bright sample;
- No apparent difference in jet opening angle, presence (or absence) of X-ray plateaus, and redshift between the radio-bright and the radio-quiet samples;
- No evidence of a correlation between E_{iso} and the radio peak flux density computed from [150].

The authors proposed that the observed dichotomy might be attributed to different progenitor systems. Specifically, they explored the possibility that radio-bright GRBs result from the collapse of massive stars in interacting binary systems, while radio-dark GRBs are produced by the collapse of isolated massive stars [47]. Consistent conclusions were drawn from another group, which found a dichotomy also in the distribution of circum-burst density, the spectral radio peak luminosity and flux densities of GRB host galaxies [369].

Nevertheless, concerns were raised regarding potential biases in the aforementioned studies. Previous research highlighted a robust positive correlation between the γ -ray energetics of long GRBs and their intrinsic duration [370, 371]. Using this relation, it was demonstrated that much of the evidence supporting the dichotomy could be explained by selection effects and sample incompleteness [372].

It is evident that the scientific community has not reached a consensus yet. Whether the lack of afterglow detections is due to the limited sensitivity of current radio facilities and selection biases in GRB samples, or if it is the result of a profound difference in the production channel of GRBs is still debated. Therefore, the selection of well-defined GRB samples devoid of systematic biases becomes crucial. In this study, we employ a sample of radio afterglows from all *Swift* GRBs up to 2022 to explore potential biases in the search for GRB sub-populations. I present the sample and the statistical analysis in Section 7.2 and 7.3, respectively. Lastly, I summarise and discuss the preliminary results in Section 7.4.

7.2 The *Swift* GRB sample

We gathered all *Swift* GRBs that had at least one radio observation of the afterglow at centimetre wavelengths. From this sample, we selected those bursts with a spectroscopic redshift estimate and a value for the energy at which the prompt emission spectrum peaks, E_p . The selection criteria are motivated by the desire to keep biases from high-energy instrumentation under control. Choosing bursts discovered by the same facility ensures that we are not introducing different sensitivity thresholds into our sample. Even if we acknowledge that requiring a redshift estimate limits the study to the most energetic bursts that have a bright optical afterglow [372], knowing z and E_p is crucial to calculate the isotropic equivalent energy E_{iso} , which will be the fundamental parameter in the statistical analysis. The final sample comprises 151 GRBs. We refer to GRBs with detected radio afterglows as radio-bright GRBs, while those without detected

radio afterglows are termed radio-dark GRBs. The final sample consists of 71 radio-bright (47%) and 80 radio-dark (53%) GRBs. The detection rate we derived is consistent with previous studies [362, 365]. Table 7.1 and 7.2 list the selected radio-bright and radio-dark GRBs, respectively.

Table 7.1: Radio-bright GRBs from our *Swift* sample. First column: GRB name. Second Column: total intrinsic duration T_{int} . Third column: redshift z . Fourth column: peak photon flux at 1 s (15 – 150 keV). Fifth column: energy E_p at which the spectrum of the prompt emission peaks. Sixth column: isotropic equivalent energy E_{iso} . Seventh column: satellite whose prompt emission data have been used to measure E_p and calculate E_{iso} .

GRB	T_{int} [s]	z	Peak Photon Flux [ph cm ⁻² s ⁻¹]	$\log E_p$ [keV]	$\log E_{iso}$ [erg]	Prompt
050315	32.418	1.949	1.9 ± 0.2	$2.14^{+0.04}_{-0.05}$	$52.94^{+0.03}_{-0.03}$	Konus–Wind
050401	8.538	2.9	10.7 ± 0.9	$2.70^{+0.10}_{-0.10}$	$53.61^{+0.08}_{-0.08}$	<i>Fermi</i>
050416A	1.512	0.6535	4.9 ± 0.5	$1.46^{+0.13}_{-0.13}$	$50.92^{+0.15}_{-0.15}$	<i>Swift</i>
050525A	5.479	0.606	41.7 ± 0.9	$2.11^{+0.01}_{-0.01}$	$52.45^{+0.01}_{-0.01}$	Konus–Wind
050730	31.502	3.968	0.6 ± 0.1	$3.40^{+2.41}_{-0.25}$	$53.84^{+0.20}_{-0.16}$	Konus–Wind
050820A	7.193	2.6147	2.4 ± 0.2	$3.24^{+0.13}_{-0.08}$	$54.02^{+0.02}_{-0.02}$	Konus–Wind
050904	24.535	6.1	0.6 ± 0.2	$3.46^{+0.12}_{-0.09}$	$54.17^{+0.06}_{-0.06}$	Konus–Wind
050922C	1.407	2.198	7.3 ± 0.3	$3.37^{+0.42}_{-0.19}$	$53.01^{+0.10}_{-0.10}$	Konus–Wind
051109A	11.118	2.346	3.9 ± 0.7	$2.76^{+0.20}_{-0.11}$	$52.85^{+0.05}_{-0.05}$	Konus–Wind
051111	18.086	1.549	2.7 ± 0.2	$2.82^{+0.08}_{-0.06}$	$52.90^{+0.04}_{-0.04}$	Konus–Wind
060218	2032.717	0.0331	0.2 ± 0.1	$0.69^{+0.03}_{-0.03}$	$49.89^{+0.08}_{-0.08}$	<i>Swift</i>
060418	41.406	1.49	6.5 ± 0.4	$2.73^{+0.06}_{-0.05}$	$53.17^{+0.03}_{-0.02}$	Konus–Wind
061121	35.134	1.314	21.1 ± 0.5	$3.15^{+0.04}_{-0.03}$	$53.48^{+0.02}_{-0.02}$	Konus–Wind
061222A	23.122	2.088	8.5 ± 0.3	$2.96^{+0.04}_{-0.03}$	$53.41^{+0.01}_{-0.01}$	Konus–Wind
070612A	228.077	0.617	1.5 ± 0.4	$2.37^{+0.08}_{-0.06}$	$52.43^{+0.04}_{-0.04}$	Konus–Wind
071003	71.428	1.1	6.3 ± 0.4	$3.32^{+0.04}_{-0.03}$	$53.58^{+0.02}_{-0.02}$	Konus–Wind
071020	1.337	2.142	8.4 ± 0.3	$3.01^{+0.06}_{-0.05}$	$52.93^{+0.04}_{-0.04}$	Konus–Wind
071021	65.180	2.452	0.7 ± 0.1	$3.03^{+1.05}_{-0.20}$	$52.83^{+0.16}_{-0.12}$	Konus–Wind
080810	24.368	3.35	2.0 ± 0.2	$3.35^{+0.14}_{-0.09}$	$53.74^{+0.05}_{-0.05}$	Konus–Wind
081007	6.538	0.5295	2.6 ± 0.4	$1.78^{+0.11}_{-0.11}$	$51.23^{+0.03}_{-0.03}$	<i>Fermi</i>
081221	10.429	2.26	18.2 ± 0.5	$2.42^{+0.01}_{-0.01}$	$53.60^{+0.01}_{-0.01}$	Konus–Wind
090418A	21.472	1.608	1.9 ± 0.3	$3.09^{+0.10}_{-0.07}$	$53.15^{+0.04}_{-0.04}$	Konus–Wind
090423	1.112	8.26	1.7 ± 0.2	$2.88^{+0.08}_{-0.08}$	$53.02^{+0.13}_{-0.13}$	<i>Fermi</i>
090424	31.088	0.544	71.0 ± 2.0	$2.44^{+0.01}_{-0.01}$	$52.66^{+0.01}_{-0.01}$	<i>Fermi</i>
090618	73.506	0.54	38.9 ± 0.8	$2.38^{+0.03}_{-0.03}$	$53.40^{+0.04}_{-0.04}$	<i>Fermi</i>
090715B	66.500	3	3.8 ± 0.2	$2.73^{+0.13}_{-0.13}$	$53.33^{+0.04}_{-0.04}$	<i>Fermi</i>
091020	12.768	1.71	4.2 ± 0.3	$2.79^{+0.09}_{-0.09}$	$52.87^{+0.04}_{-0.04}$	<i>Fermi</i>
100621A	41.245	0.542	12.8 ± 0.3	$2.21^{+0.04}_{-0.03}$	$52.65^{+0.02}_{-0.02}$	Konus–Wind
100814A	71.516	1.44	2.5 ± 0.2	$2.49^{+0.04}_{-0.04}$	$52.88^{+0.03}_{-0.03}$	Konus–Wind
100901A	182.309	1.408	0.8 ± 0.2	$2.75^{+0.23}_{-0.12}$	$52.58^{+0.15}_{-0.11}$	Konus–Wind
100906A	41.951	1.727	10.1 ± 0.4	$2.73^{+0.13}_{-0.08}$	$53.40^{+0.05}_{-0.05}$	Konus–Wind
101219B	21.909	0.5519	0.6 ± 0.3	$2.04^{+0.05}_{-0.05}$	$51.60^{+0.05}_{-0.05}$	<i>Fermi</i>
110205A	79.814	2.22	3.6 ± 0.2	$2.85^{+0.10}_{-0.07}$	$53.80^{+0.03}_{-0.03}$	Konus–Wind
110503A	3.827	1.613	1.4 ± 0.1	$2.76^{+0.02}_{-0.02}$	$53.33^{+0.02}_{-0.02}$	Konus–Wind
110715A	7.143	0.82	53.9 ± 1.1	$2.34^{+0.02}_{-0.02}$	$52.70^{+0.03}_{-0.03}$	Konus–Wind
111008A	10.595	4.9898	6.4 ± 0.7	$2.80^{+0.13}_{-0.08}$	$53.62^{+0.07}_{-0.07}$	Konus–Wind
120326A	24.875	1.798	4.6 ± 0.2	$2.06^{+0.06}_{-0.07}$	$52.81^{+0.05}_{-0.05}$	Konus–Wind
120404A	9.984	2.876	1.2 ± 0.2	$2.43^{+0.13}_{-0.08}$	$53.01^{+0.08}_{-0.06}$	Konus–Wind

Table 7.1: *continued*

GRB	T_{int} [s]	z	Peak Photon Flux [ph cm ⁻² s ⁻¹]	$\log E_p$ [keV]	$\log E_{iso}$ [erg]	Prompt
120521C	3.814	6	1.9 ± 0.2	$3.12^{+0.38}_{-0.14}$	$53.29^{+0.11}_{-0.08}$	Konus–Wind
121024A	20.922	2.298	1.3 ± 0.2	$3.28^{+0.29}_{-0.14}$	$52.70^{+0.09}_{-0.09}$	Konus–Wind
130215A	41.140	0.597	2.5 ± 0.7	$2.39^{+0.18}_{-0.18}$	$52.40^{+0.04}_{-0.04}$	<i>Fermi</i>
130427A	118.854	0.37	331.0 ± 4.6	$3.139^{+0.003}_{-0.003}$	$53.91^{+0.04}_{-0.04}$	<i>Fermi</i>
130606A	40.026	5.91	2.6 ± 0.2	$3.16^{+0.36}_{-0.37}$	$53.93^{+0.10}_{-0.11}$	Konus–Wind
140304A	2.483	5.283	1.7 ± 0.2	$3.06^{+0.08}_{-0.08}$	$53.20^{+0.04}_{-0.04}$	<i>Fermi</i>
140311A	11.992	4.954	1.3 ± 0.5	$2.76^{+0.26}_{-0.11}$	$53.41^{+0.13}_{-0.09}$	Konus–Wind
140419A	19.108	3.956	4.9 ± 0.2	$3.16^{+0.12}_{-0.12}$	$54.16^{+0.15}_{-0.15}$	<i>Fermi</i>
140515A	3.197	6.32	0.9 ± 0.1	$2.57^{+0.12}_{-0.12}$	$52.98^{+0.17}_{-0.17}$	<i>Swift</i>
140703A	16.208	3.14	2.8 ± 0.6	$2.86^{+0.03}_{-0.03}$	$52.22^{+0.02}_{-0.02}$	<i>Fermi</i>
141109A	50.088	2.993	2.5 ± 0.2	$2.81^{+0.07}_{-0.06}$	$53.60^{+0.04}_{-0.04}$	Konus–Wind
150314A	5.362	1.758	38.5 ± 0.9	$2.93^{+0.01}_{-0.01}$	$54.26^{+0.05}_{-0.05}$	<i>Fermi</i>
150413A	63.687	3.139	1.6 ± 0.3	$2.66^{+0.32}_{-0.10}$	$53.61^{+0.08}_{-0.08}$	Konus–Wind
150910A	47.562	1.359	1.1 ± 0.4	$2.73^{+0.09}_{-0.07}$	$52.72^{+0.06}_{-0.06}$	Konus–Wind
151027A	71.652	0.81	6.8 ± 0.6	$2.50^{+0.15}_{-0.08}$	$52.52^{+0.05}_{-0.05}$	Konus–Wind
160131A	164.807	0.972	6.4 ± 0.3	$3.11^{+0.15}_{-0.10}$	$53.94^{+0.03}_{-0.03}$	Konus–Wind
160804A	83.064	0.736	2.9 ± 0.3	$2.11^{+0.02}_{-0.02}$	$52.39^{+0.09}_{-0.09}$	<i>Fermi</i>
161017A	71.796	2.0127	2.8 ± 0.2	$2.95^{+0.07}_{-0.07}$	$52.87^{+0.03}_{-0.03}$	<i>Fermi</i>
161219B	6.048	0.1475	5.3 ± 0.4	$2.03^{+0.09}_{-0.06}$	$50.30^{+0.04}_{-0.04}$	Konus–Wind
171205A	182.677	0.0368	1.0 ± 0.3	$2.06^{+0.09}_{-0.06}$	$49.48^{+0.35}_{-0.0}$	Konus–Wind
190114C	253.684	0.425	101.0 ± 1.5	$3.15^{+0.01}_{-0.01}$	$53.50^{+0.04}_{-0.04}$	<i>Fermi</i>
190829A	53.964	0.0785	18.0 ± 2.7	$1.13^{+0.06}_{-0.06}$	$50.30^{+0.04}_{-0.04}$	<i>Fermi</i>
191221B	22.346	1.148	4.8 ± 0.7	$2.91^{+0.03}_{-0.03}$	$53.56^{+0.05}_{-0.05}$	Konus–Wind
201216C	22.857	1.1	18.0 ± 1.1	$2.84^{+0.04}_{-0.04}$	$53.79^{+0.04}_{-0.04}$	Konus–Wind
210610B	32.573	1.13	13.5 ± 0.7	$2.74^{+0.02}_{-0.02}$	$53.66^{+0.0}_{-0.0}$	Konus–Wind
210619B	20.735	1.937	115.0 ± 2.2	$2.88^{+0.04}_{-0.02}$	$54.64^{+0.01}_{-0.01}$	Konus–Wind
210702A	63.981	1.16	0.0 ± 0.0	$2.91^{+0.07}_{-0.07}$	$53.97^{+0.0}_{-0.0}$	Konus–Wind
210731A	9.993	1.2525	1.6 ± 0.3	$2.60^{+0.03}_{-0.03}$	$52.30^{+0.02}_{-0.02}$	<i>Fermi</i>
210822A	66.082	1.736	27.7 ± 0.7	$3.04^{+0.03}_{-0.03}$	$53.98^{+0.04}_{-0.04}$	Konus–Wind
220101A	30.858	4.618	7.3 ± 0.3	$3.27^{+0.02}_{-0.02}$	$54.62^{+0.01}_{-0.01}$	<i>Fermi</i>
220521A	2.053	5.6	4.7 ± 0.4	$2.39^{+0.08}_{-0.08}$	$52.63^{+0.03}_{-0.03}$	<i>Fermi</i>

Table 7.2: Radio-dark GRBs from our *Swift* sample. First column: GRB name. Second Column: total intrinsic duration T_{int} . Third column: redshift z . Fourth column: peak photon flux at 1 s (15 – 150 keV). Fifth column: energy E_p at which the spectrum of the prompt emission peaks. Sixth column: isotropic equivalent energy E_{iso} . Seventh column: satellite whose prompt emission data have been used to measure E_p and calculate E_{iso} .

GRB	T_{int} [s]	z	Peak Photon Flux [ph cm ⁻² s ⁻¹]	$\log E_p$ [keV]	$\log E_{iso}$ [erg]	Prompt
050126	10.830	1.29	0.7 ± 0.2	$2.56^{+0.22}_{-0.11}$	$52.09^{+0.14}_{-0.09}$	Konus–Wind
050803	61.814	0.422	1.0 ± 0.1	$2.47^{+0.14}_{-0.16}$	$51.74^{+0.11}_{-0.08}$	Konus–Wind
050814	23.952	5.3	0.7 ± 0.2	$2.53^{+0.10}_{-0.06}$	$53.09^{+0.14}_{-0.13}$	Konus–Wind
051006	16.901	1.059	1.6 ± 0.3	$2.87^{+0.23}_{-0.12}$	$52.27^{+0.10}_{-0.08}$	Konus–Wind
060124	227.273	2.3	0.9 ± 0.2	$2.90^{+0.06}_{-0.05}$	$53.52^{+0.02}_{-0.02}$	Konus–Wind

Table 7.2: *continued*

GRB	T_{int} [s]	z	Peak Photon Flux [ph cm ⁻² s ⁻¹]	$\log E_p$ [keV]	$\log E_{iso}$ [erg]	Prompt
060206	1.506	4.045	2.8 ± 0.2	$2.58^{+0.11}_{-0.11}$	$52.67^{+0.07}_{-0.07}$	<i>Fermi</i>
060210	51.935	3.91	2.7 ± 0.3	$2.76^{+0.14}_{-0.14}$	$53.62^{+0.06}_{-0.06}$	<i>Fermi</i>
060614	96.195	0.13	11.5 ± 0.7	$1.74^{+0.36}_{-0.36}$	$51.40^{+0.17}_{-0.17}$	<i>Swift</i>
060707	14.944	3.43	1.0 ± 0.2	$2.48^{+0.06}_{-0.06}$	$52.82^{+0.09}_{-0.09}$	<i>Fermi</i>
060908	6.693	1.8836	3.0 ± 0.2	$2.60^{+0.05}_{-0.04}$	$52.77^{+0.04}_{-0.03}$	Konus–Wind
060912A	2.581	0.937	8.6 ± 0.4	$2.60^{+0.65}_{-0.16}$	$52.07^{+0.12}_{-0.12}$	Konus–Wind
061007	33.289	1.262	14.6 ± 0.4	$2.96^{+0.01}_{-0.01}$	$54.04^{+0.02}_{-0.02}$	Konus–Wind
070721B	73.498	3.626	1.5 ± 0.3	$3.26^{+0.61}_{-0.19}$	$53.43^{+0.19}_{-0.13}$	Konus–Wind
071112C	8.228	0.823	8.0 ± 1.0	$2.87^{+0.19}_{-0.11}$	$52.07^{+0.07}_{-0.07}$	Konus–Wind
080129	8.974	4.349	0.2 ± 0.1	$2.90^{+0.20}_{-0.10}$	$52.93^{+0.13}_{-0.10}$	Konus–Wind
080210	12.359	2.641	1.6 ± 0.2	$2.60^{+0.16}_{-0.11}$	$52.84^{+0.16}_{-0.08}$	Konus–Wind
080411	27.586	1.03	43.2 ± 0.9	$2.73^{+0.03}_{-0.03}$	$53.38^{+0.01}_{-0.01}$	Konus–Wind
080413A	13.399	2.433	5.6 ± 0.2	$2.77^{+0.15}_{-0.15}$	$52.93^{+0.05}_{-0.05}$	<i>Fermi</i>
080413B	3.810	1.1	18.7 ± 0.8	$2.19^{+0.09}_{-0.09}$	$52.30^{+0.08}_{-0.08}$	Suzaku
080430	9.257	0.75	2.6 ± 0.2	$2.50^{+0.32}_{-0.13}$	$51.81^{+0.08}_{-0.06}$	Konus–Wind
080516	1.381	3.2	1.8 ± 0.3	$2.39^{+0.16}_{-0.13}$	$52.30^{+0.18}_{-0.12}$	Konus–Wind
080603B	16.260	2.69	3.5 ± 0.2	$2.58^{+0.09}_{-0.09}$	$53.04^{+0.06}_{-0.06}$	<i>Fermi</i>
080604	33.940	1.416	0.4 ± 0.1	$2.17^{+0.11}_{-0.06}$	$52.11^{+0.09}_{-0.07}$	Konus–Wind
080721	4.498	2.602	20.9 ± 1.8	$3.24^{+0.06}_{-0.06}$	$54.08^{+0.04}_{-0.04}$	<i>Fermi</i>
080804	10.610	2.2045	3.1 ± 0.4	$2.91^{+0.02}_{-0.02}$	$53.06^{+0.08}_{-0.08}$	<i>Fermi</i>
080913	1.039	6.7	1.4 ± 0.2	$2.95^{+0.13}_{-0.07}$	$52.78^{+0.10}_{-0.07}$	Konus–Wind
081008	62.489	1.9685	1.3 ± 0.1	$2.96^{+0.34}_{-0.15}$	$53.16^{+0.09}_{-0.08}$	Konus–Wind
081029	55.694	3.8479	0.5 ± 0.2	$2.95^{+0.39}_{-0.14}$	$53.31^{+0.18}_{-0.11}$	Konus–Wind
081109A	96.023	0.9787	1.1 ± 0.0	$2.68^{+0.11}_{-0.11}$	$52.26^{+0.03}_{-0.03}$	<i>Fermi</i>
081121	3.986	2.512	4.4 ± 1.0	$2.94^{+0.06}_{-0.06}$	$53.50^{+0.07}_{-0.07}$	<i>Fermi</i>
081203A	94.839	2.1	2.9 ± 0.2	$3.13^{+0.60}_{-0.16}$	$53.45^{+0.15}_{-0.15}$	Konus–Wind
081222	6.366	2.77	7.7 ± 0.2	$2.69^{+0.10}_{-0.10}$	$53.40^{+0.04}_{-0.04}$	<i>Fermi</i>
090102	10.601	1.547	5.5 ± 0.8	$3.04^{+0.04}_{-0.04}$	$53.30^{+0.02}_{-0.02}$	Konus–Wind
090201	26.774	2.1	14.7 ± 1.0	$2.68^{+0.02}_{-0.02}$	$53.98^{+0.01}_{-0.01}$	Konus–Wind
090429B	0.539	9.2	1.6 ± 0.2	$2.63^{+0.12}_{-0.10}$	$53.01^{+0.11}_{-0.10}$	Konus–Wind
090709A	31.786	1.8	7.8 ± 0.3	$2.89^{+0.02}_{-0.02}$	$53.82^{+0.01}_{-0.01}$	Konus–Wind
091127	4.764	0.49034	46.5 ± 2.7	$1.71^{+0.01}_{-0.01}$	$52.21^{+0.0}_{-0.0}$	<i>Fermi</i>
110106B	15.328	0.618	2.1 ± 0.3	$2.23^{+0.14}_{-0.08}$	$51.68^{+0.07}_{-0.05}$	Konus–Wind
110731A	10.130	2.83	11.0 ± 0.3	$3.08^{+0.01}_{-0.01}$	$53.61^{+0.01}_{-0.01}$	<i>Fermi</i>
111107A	6.833	2.893	1.2 ± 0.2	$2.62^{+0.13}_{-0.13}$	$52.48^{+0.07}_{-0.07}$	<i>Fermi</i>
120119A	93.035	1.728	10.3 ± 0.3	$2.62^{+0.03}_{-0.03}$	$53.60^{+0.03}_{-0.03}$	Konus–Wind
120327A	16.496	2.813	3.9 ± 0.2	$2.72^{+0.07}_{-0.05}$	$53.28^{+0.04}_{-0.04}$	Konus–Wind
120722A	21.648	0.9586	1.0 ± 0.3	$1.80^{+0.27}_{-0.43}$	$52.01^{+0.11}_{-0.08}$	Konus–Wind
120724A	29.355	1.48	0.6 ± 0.2	$1.84^{+0.12}_{-0.12}$	$51.76^{+0.04}_{-0.04}$	<i>Swift</i>
120802A	10.425	3.796	3.0 ± 0.2	$2.44^{+0.15}_{-0.15}$	$52.93^{+0.10}_{-0.10}$	<i>Fermi</i>
120811C	7.300	2.671	4.1 ± 0.2	$2.30^{+0.02}_{-0.02}$	$52.73^{+0.02}_{-0.02}$	<i>Fermi</i>
120907A	8.579	0.97	2.9 ± 0.4	$2.48^{+0.09}_{-0.09}$	$51.30^{+0.06}_{-0.06}$	<i>Fermi</i>
120923A	3.090	7.8	0.6 ± 0.1	$2.59^{+0.10}_{-0.10}$	$53.12^{+0.18}_{-0.18}$	<i>Swift</i>
121128A	7.281	2.2	12.9 ± 0.4	$2.30^{+0.03}_{-0.03}$	$53.15^{+0.02}_{-0.02}$	<i>Fermi</i>
121211A	89.965	1.023	1.0 ± 0.3	$2.28^{+0.15}_{-0.09}$	$51.41^{+0.10}_{-0.08}$	Konus–Wind
130131B	1.215	2.539	1.0 ± 0.2	$2.90^{+0.24}_{-0.13}$	$52.13^{+0.14}_{-0.11}$	Konus–Wind

Table 7.2: *continued*

GRB	T_{int} [s]	z	Peak Photon Flux [ph cm ⁻² s ⁻¹]	log E_p [keV]	log E_{iso} [erg]	Prompt
130420A	53.766	1.297	3.4 ± 0.2	$2.11^{+0.02}_{-0.02}$	$52.86^{+0.04}_{-0.04}$	<i>Fermi</i>
130505A	26.911	2.27	30.0 ± 3.1	$3.29^{+0.02}_{-0.02}$	$54.64^{+0.01}_{-0.01}$	Konus–Wind
130511A	2.357	1.3033	1.3 ± 0.2	$2.29^{+0.26}_{-0.11}$	$51.14^{+0.17}_{-0.12}$	Konus–Wind
130514A	44.348	3.6	2.8 ± 0.3	$2.78^{+0.09}_{-0.06}$	$53.79^{+0.04}_{-0.04}$	Konus–Wind
130604A	18.301	1.06	0.8 ± 0.2	$2.75^{+0.12}_{-0.08}$	$52.14^{+0.07}_{-0.06}$	Konus–Wind
130610A	15.006	2.092	1.7 ± 0.2	$2.96^{+0.06}_{-0.06}$	$52.83^{+0.03}_{-0.03}$	<i>Fermi</i>
130612A	1.331	2.006	1.7 ± 0.3	$2.27^{+0.08}_{-0.08}$	$51.86^{+0.07}_{-0.07}$	<i>Fermi</i>
130701A	2.032	1.155	17.1 ± 0.7	$2.28^{+0.02}_{-0.02}$	$52.42^{+0.02}_{-0.02}$	Konus–Wind
130831A	21.973	0.4791	13.6 ± 0.6	$1.91^{+0.03}_{-0.03}$	$51.88^{+0.03}_{-0.03}$	<i>Fermi</i>
131030A	17.924	1.293	28.1 ± 0.7	$2.65^{+0.01}_{-0.01}$	$53.51^{+0.02}_{-0.02}$	Konus–Wind
140114A	34.925	3	0.9 ± 0.1	$2.19^{+0.03}_{-0.03}$	$53.20^{+0.07}_{-0.06}$	Konus–Wind
140206A	25.027	2.74	19.4 ± 0.5	$3.04^{+0.01}_{-0.01}$	$54.34^{+0.01}_{-0.01}$	<i>Fermi</i>
140423A	31.455	3.26	2.1 ± 0.2	$2.73^{+0.03}_{-0.03}$	$53.75^{+0.02}_{-0.02}$	<i>Fermi</i>
140518A	10.601	4.707	1.0 ± 0.1	$2.46^{+0.07}_{-0.07}$	$52.96^{+0.15}_{-0.08}$	Konus–Wind
140710A	2.259	0.558	1.9 ± 0.3	$1.84^{+0.15}_{-0.18}$	$50.69^{+0.23}_{-0.13}$	Konus–Wind
140907A	35.837	1.21	2.5 ± 0.2	$2.40^{+0.03}_{-0.03}$	$52.35^{+0.02}_{-0.02}$	<i>Fermi</i>
141220A	3.108	1.3195	8.9 ± 0.7	$2.51^{+0.03}_{-0.03}$	$52.36^{+0.02}_{-0.02}$	Konus–Wind
141225A	21.013	0.915	1.3 ± 0.4	$2.71^{+0.09}_{-0.07}$	$52.31^{+0.06}_{-0.06}$	Konus–Wind
150323A	93.911	0.593	5.4 ± 0.3	$2.18^{+0.04}_{-0.04}$	$52.10^{+0.02}_{-0.02}$	Konus–Wind
160327A	4.670	4.99	1.8 ± 0.2	$2.82^{+0.35}_{-0.18}$	$53.32^{+0.10}_{-0.10}$	Konus–Wind
161014A	4.787	2.823	2.9 ± 0.6	$2.80^{+0.04}_{-0.04}$	$52.99^{+0.02}_{-0.02}$	<i>Fermi</i>
161108A	48.680	1.159	0.6 ± 0.1	$2.22^{+0.68}_{-0.11}$	$51.82^{+0.23}_{-0.09}$	Konus–Wind
161129A	21.599	0.645	3.4 ± 0.2	$2.51^{+0.05}_{-0.05}$	$51.99^{+0.02}_{-0.02}$	<i>Fermi</i>
170202A	9.946	3.645	4.7 ± 0.3	$3.06^{+0.22}_{-0.22}$	$53.24^{+0.10}_{-0.10}$	<i>Fermi</i>
170607A	25.690	0.557	0.0 ± 0.0	$2.38^{+0.04}_{-0.04}$	$51.95^{+0.01}_{-0.01}$	<i>Fermi</i>
190719C	53.531	2.469	5.5 ± 0.3	$2.45^{+0.05}_{-0.05}$	$52.26^{+0.03}_{-0.03}$	<i>Fermi</i>
191004B	8.372	3.503	5.0 ± 0.2	$2.89^{+0.06}_{-0.06}$	$53.04^{+0.04}_{-0.04}$	<i>Fermi</i>
200716C	64.131	0.341	10.7 ± 0.5	$2.98^{+0.06}_{-0.06}$	$51.57^{+0.03}_{-0.03}$	<i>Fermi</i>
210610A	3.000	3.54	2.4 ± 0.4	$2.83^{+0.26}_{-0.18}$	$52.54^{+0.0}_{-0.0}$	Konus–Wind

7.3 Results

Following the statistical analyses conducted in previous works appeared in the literature, we employed a Kolmogorov – Smirnov (KS) test on the distributions of isotropic equivalent energy (E_{iso}), intrinsic duration (T_{int}) and redshift (z) for the radio-dark and radio-bright GRBs. The null hypothesis posited for the KS test assumes that the two distributions are drawn from the same parent population. Results are illustrated in Figure 7.1, 7.2 and 7.3. The hatch-filled blue and red histograms refer to radio-dark and radio-bright GRBs, respectively. The dashed black line represents the overall observed sample, the combined set of radio-bright and radio-dark GRBs. In each figure, the upper panel presents the distributions for the entire sample, while the lower panel shows the distributions for bursts with a peak photon flux at 1 s larger than $2.6 \text{ ph cm}^2 \text{ s}^{-1}$ (15 – 150 keV). The p-value for the KS test on each pair of populations is indicated within the respective panel. It was pointed out by [361] that a peak photon flux at 1 s above $2.6 \text{ ph cm}^2 \text{ s}^{-1}$ corresponds to approximately 6 times the minimum flux threshold *Swift* can reveal. Therefore, the selection of bursts with peak photon flux at 1 s above this threshold

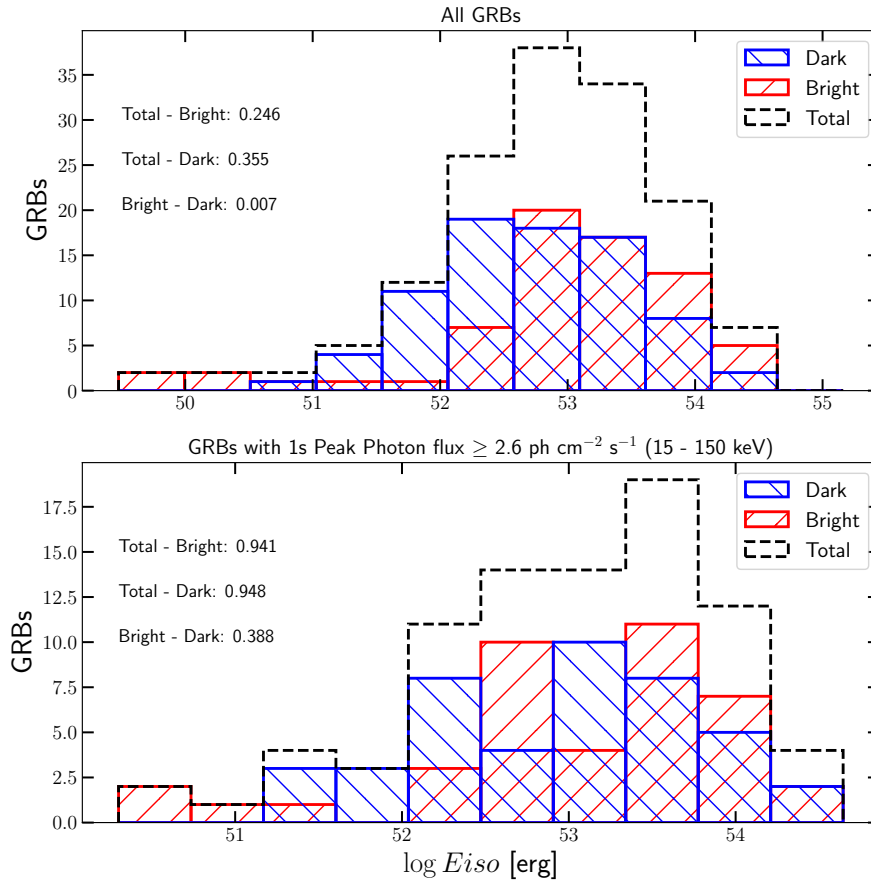


Figure 7.1: Distributions of isotropic equivalent energies E_{iso} for the complete sample (dashed black line), the radio-dark (hatch-filled blue histogram) and radio-bright (hatch-filled red histogram). The upper panel shows the distributions when considering all the GRBs in the sample, while the lower panel limits the analysis to those bursts with a peak photon flux at 1 s larger than $2.6 \text{ ph cm}^{-2} \text{ s}^{-1}$ (15 – 150 keV). The p-value for the KS test on each pair of populations is indicated within the panel.

provides the basis for unbiased statistical studies of the properties of GRBs.

7.4 Discussion and conclusions

The null hypothesis can be rejected at a confidence level exceeding 3σ if the p-value is lower than 0.003. Considering the distribution of isotropic equivalent energy, E_{iso} , for the whole sample (Figure 7.1, upper panel), the p-value for the KS test between radio-dark and radio-bright GRBs is 0.007, which corresponds to a 2.7σ significance that the two distributions are drawn from different parent populations. Regarding the distribution of intrinsic duration, T_{int} , for the entire population (Figure 7.2, upper panel), the p-value for the KS test between radio-dark and radio-bright GRBs is > 0.005 , which corresponds to a $< 2\sigma$ significance. In all other cases, the p-value is larger by an order of magnitude. Consequently, our preliminary results did not reveal compelling evidence ($\geq 3\sigma$ confidence level) for different GRB populations based on the prompt emission energy, the intrinsic duration or the redshift.

To investigate the reasons behind our contrasting results compared with previous findings, we studied the entire GRB sample from [368], which is the most recent data set providing

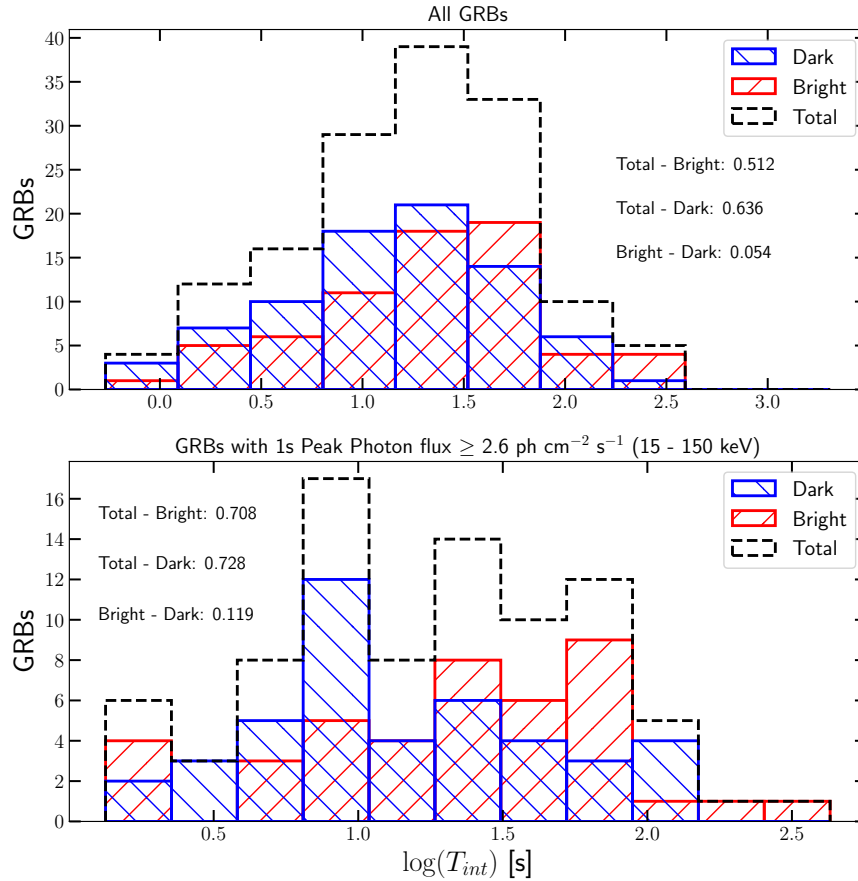


Figure 7.2: Distributions of intrinsic duration T_{int} for the complete sample (dashed black line), the radio-dark (hatch-filled blue histogram) and radio-bright (hatch-filled red histogram). The upper panel shows the distributions when considering all the GRBs in the sample, while the lower panel limits the analysis to those bursts with a peak photon flux at 1 s larger than $2.6 \text{ ph cm}^{-2} \text{ s}^{-1}$ (15 – 150 keV). The p-value for the KS test on each pair of populations is indicated within the panel.

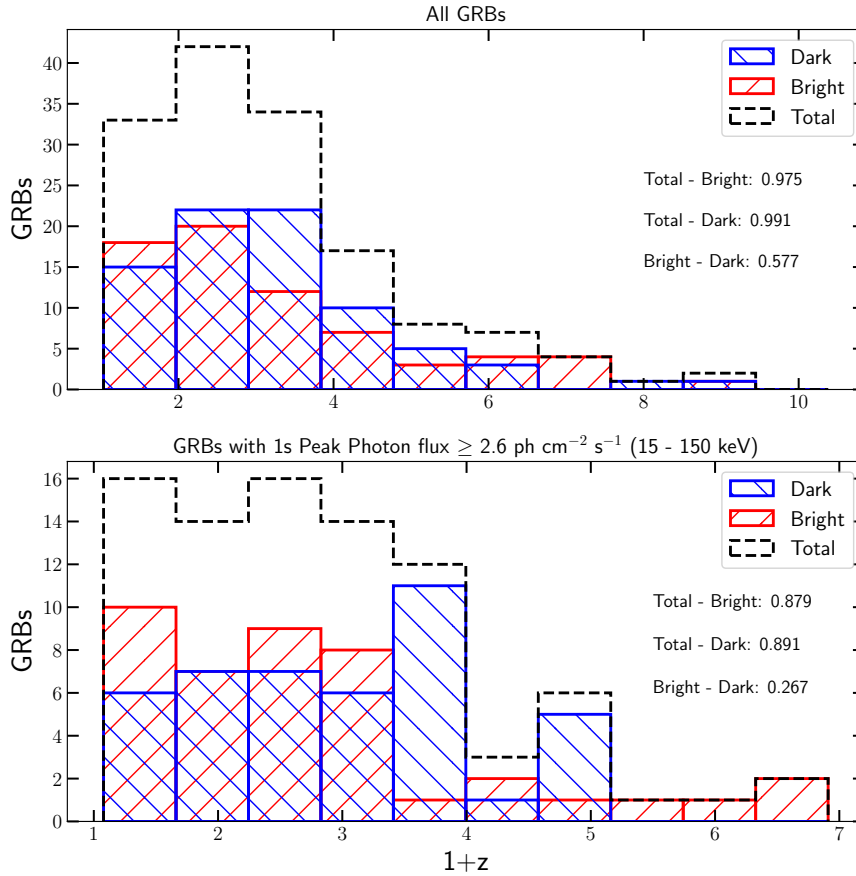


Figure 7.3: Distributions of redshift z for the complete sample (dashed black line), the radio-dark (hatch-filled blue histogram) and radio-bright (hatch-filled red histogram). The upper panel shows the distributions when considering all the GRBs in the sample, while the lower panel limits the analysis to those bursts with a peak photon flux at 1 s larger than $2.6 \text{ ph cm}^2 \text{ s}^{-1}$ (15 – 150 keV). The p-value for the KS test on each pair of populations is indicated within the panel.

significant evidence for the dichotomy. The sample was sliced based on different threshold values for the peak photon flux at 1 s (15 – 150 keV). In Figure 7.4 we present the distribution of redshift as a function of isotropic equivalent energy. Each panel shows the distribution of radio-bright (green dots) and radio-dark (orange squares) GRBs, categorised by a peak photon flux at 1 s exceeding a specified threshold denoted in the panel title. In each panel, GRBs also included in prior panels are depicted by grey dots (radio-bright) and grey squares (radio-dark). For instance, in the second panel from the upper left, including bursts with a peak photon flux at 1 s exceeding $2.0 \text{ ph cm}^2 \text{ s}^{-1}$, those from the first panel on the upper left (peak photon flux at 1 s above $2.6 \text{ ph cm}^2 \text{ s}^{-1}$) are shown in grey. The last two panels on the lower right displays the GRBs without a known peak photon flux at 1 s and the entire sample from [368], respectively. The p-value for the KS test on the distribution of E_{iso} for the two populations is provided in the panel title. Figure 7.4 reveals that the p-value decreases as we include bursts with lower values for the peak photon flux at 1 s. Notably, the dichotomy in the E_{iso} distribution becomes significant when a threshold of $0.5 \text{ ph cm}^2 \text{ s}^{-1}$ is applied. As previously emphasised, a threshold of $2.6 \text{ ph cm}^2 \text{ s}^{-1}$ ensures completeness in flux for the sample. Consequently, the sensitivity limit of *Swift*, where not all bursts are detected, is rapidly approached by lowering the threshold for the peak photon flux at 1 s, resulting in a less complete sample. The sample incompleteness, which cannot be accounted for by statistical tools, is the first driving factor for the discrepancy between our results and those from previous studies.

Although no correlation between the radio peak flux and E_{iso} was reported by [44], a link between the two quantities is *somehow* expected. It is therefore realistic to expect that more energetic GRBs have, in general, higher flux densities in radio. The latter hypothesis is consistent with the conclusions drawn by [44]. As the threshold for the peak photon flux at 1 s is reduced, leading to increased sample incompleteness, more faint bursts are included in the data set. These dimmer bursts have a higher probability of exhibiting lower radio flux densities, potentially falling below the sensitivity limits of radio facilities.

Furthermore, Figure 7.4 underscores that the dichotomy becomes especially significant when considering bursts for which the peak photon flux at 1 s is unknown (second-to-last panel from the lower left). The p-value indicated in this panel refers to the KS test on the distributions of radio-dark and radio-bright GRBs without a known peak photon flux at 1 s. These bursts are primarily detected by satellites other than *Swift*. Among these 60 bursts, 43 exploded before the launch of *Swift*. Of the remaining 17 bursts, *Swift* discovered 3 GRBs (GRB 151027B, GRB 210702A and GRB 210905A), while the rest were observed by *Swift*-XRT a few ks after the discovery, generally performed by other satellites (mostly HETE and *Fermi*).

The average E_{iso} for radio-dark and radio-bright GRBs with a known peak photon flux at 1 s from [368] is 2.11×10^{53} and 2.75×10^{53} , respectively. In contrast, the same quantity for radio-dark and radio-bright GRBs without a known peak photon flux at 1 s is 6.15×10^{52} and 5.08×10^{53} , respectively. This aligns with the hypothesis that instrumental factors can contribute to misleading results. In fact, combining bursts with and without a known peak photon flux at 1 s, which should not be physically different as this classification is purely determined by an instrumental effect, is equivalent to include different “observed” populations. As a result, multiple sub-populations of GRBs are observed. Therefore, rather than an intrinsic phenomenon, the increased significance of the dichotomy obtained by [368] seems to be driven by instrumental factors.

Altogether, our preliminary analysis supports the idea that the observed dichotomy between radio-bright and radio-dark GRBs may arise from sample incompleteness and the sensitivity limits of current γ -ray and radio facilities. This is in agreement with the findings of [362] and [372]. However, to confirm or reject the apparent dichotomy, a comprehensive comparison between the observed upper limits for radio-dark GRBs and the predictions from state-of-the-art afterglow models based on hydrodynamical simulations is essential.

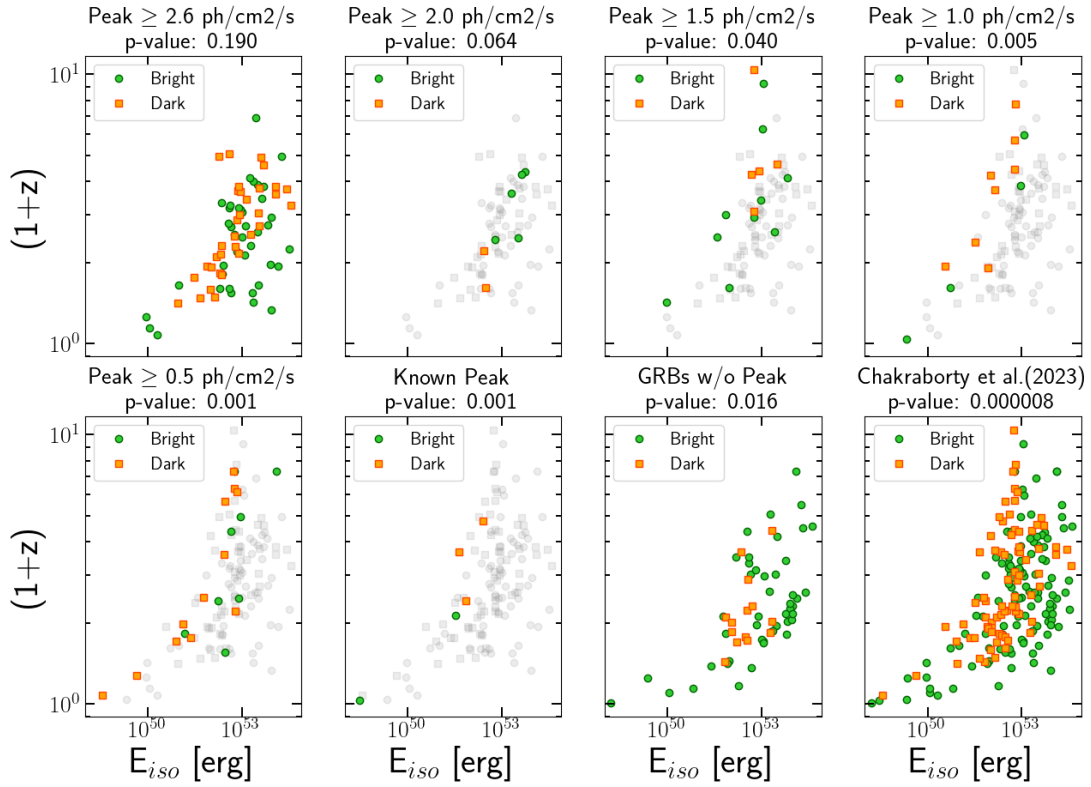


Figure 7.4: Redshift distribution as a function of the isotropic equivalent energy E_{iso} for the GRB sample from [368]. Each panel displays the distribution of radio-bright (green dots) and radio-dark (orange squares) GRBs categorised by a peak photon flux at 1 s above a specified threshold indicated in the panel title. The detailed explanation of this figure is provided in the main text.

Moreover, it's crucial to acknowledge the need for a complete sample devoid of biases or, at the very least, with known and consistent biases. Achieving this is challenging: spectroscopic measurements of GRB redshift, crucial for calculating E_{iso} , are typically limited to bursts with a bright optical afterglow. Future γ -ray satellites like the Transient High Energy Sky and Early Universe Surveyor (THESEUS)¹ will be able to provide real-time localisation ($\sim 1\text{--}2$ arcmin within a few seconds; ~ 1 arcsec within a few minutes), enabling multi-wavelength follow-up with ground-based telescopes, and rapid redshift measurements for the bulk of the GRB population [373]. On the other end of the electromagnetic spectrum, next generation radio facilities such as the SKA and the ngVLA will push sensitivity limits at these wavelengths to unprecedented levels, facilitating the detection of less luminous GRB afterglows.

¹<https://www.isdc.unige.ch/theseus/>

Chapter 8

Conclusions and prospects

The unique feature of GRB afterglows lies in the fact that they show the complete synchrotron spectrum, spanning all the break frequencies expected from theoretical arguments, and evolving over timescales that are within the reach of human observation. Given that synchrotron emission from relativistic ejecta is ubiquitous in the Universe and since expanding jets are associated to a vast plethora of other transient and/or variable objects, GRBs provide us with an invaluable astrophysical laboratory to investigate this fundamental emission mechanism and the dynamics of material ejected and accelerated up to relativistic energies. However, even the most sophisticated, state-of-the-art models employed to characterise the complex emission processes within GRBs suffer from degeneracies in the multi-dimensional parameter space. Complementary information provided by multi-wavelength, multi-scale and multi-messenger observations is crucial to alleviate, or even break, this degeneracy. In this Thesis, I demonstrated the fundamental role played by radio interferometry in providing critical constraints on the properties of GRBs and their progenitors.

Regarding radio and VLBI studies of single GRBs, in Chapter 4 I presented the multi-wavelength analysis of GRB 201015A, a remarkable GRB with a hint of VHE emission. Together with publicly available optical and X-ray data, our radio observations with the VLA, EVN and *e*-MERLIN were fundamental to model the GRB emission, deriving the microphysical and global parameters. In particular, the combination of the three bands allowed us to unambiguously characterise the surrounding density profile as that of a homogeneous medium. However, the limited sensitivity of current radio facilities, together with the relatively faint brightness of the GRB afterglow, prevented us from measuring the expansion of the GRB outflow, despite its proximity ($z \simeq 0.426$). As γ -ray data were not publicly available at the time of our analysis, we could not test the origin of the VHE emission, i.e. whether it stemmed from SSC, synchrotron or EIC processes. The advent of next-generation facilities operating at the extremes of the electromagnetic spectrum promises to extend such studies to a broader spectrum of nearby GRBs. The enhanced sensitivity of the Cherenkov Telescope Array Observatory (CTAO) in γ -rays, the Square Kilometre Array Observatory (SKAO) and the next generation Very Large Array in radio will empower the detection of faint afterglows, shedding light on the mechanisms occurring within GRBs. Additionally, combining the sensitivity of the latter radio facilities with the high angular resolution provided by the current VLBI networks will enable precise constraints on the expansion dynamics and geometry of nearby GRB outflows.

In Chapter 5, I presented our VLBI observations of GRB 221009A, the brightest GRB ever recorded. Our comprehensive VLBI campaign, comprising five EVN and four VLBA epochs ranging from 40 to 262 days post-burst, provided robust support ($> 3\sigma$ -equivalent significance) for the expansion of the relativistic shock, marking the second instance of such evidence after almost twenty years from the first. Furthermore, the observations confirmed the relativistic nature, revealing an apparent superluminal expansion rate. Applying a power law expansion

model, $s(t) \propto t^a$, to the observed size evolution $s(t)$, we derived a slope $a = 1.9_{-0.6}^{+0.7}$. This value, steeper than expected from either a FS or RS model, implies an apparent acceleration of the expansion. Fitting the data at each frequency separately, we found different expansion rates, pointing to a frequency-dependent behaviour. We showed that the observed size evolution can be reconciled with a RS plus FS in the case of a wind-like circum-burst medium, provided that the two shocks dominate the emission at different frequencies and at different times.

Despite reporting the second-ever instance of the apparent superluminal expansion of a GRB outflow, such studies remain confined to extraordinary bursts. The complexity of measuring sizes smaller than the instrumental beam, particularly through super-resolution techniques, poses challenges even for exceptionally bright GRBs. The dearth of close, luminous, and long-lived afterglows, coupled with the current limitations in radio telescope sensitivity, further restricts the potential targets. As previously pointed out, the enhanced sensitivity of future radio facilities will raise the number of GRB candidates for which such analysis can be performed, by both increasing the significance of the detections and facilitating the early and late time follow-up of fainter bursts.

In addition to the study of single events, exploring the properties of GRB host galaxies provides a valuable asset for understanding the environment that gives rise to GRB progenitors. This is particularly important for assessing the extent of obscured star formation, where radio observations play a crucial role. In Chapter 6 I reported the analysis of J1304+2938, initially identified as the candidate host galaxy of the long GRB 200716C. On the other hand, based on the analysis of its prompt emission light curve, GRB 200716C was proposed to be a short GRB lensed by an IMBH located in J1304+2938. In this scenario, the latter would act as a foreground lens. In order to test this hypothesis, we performed dedicated observations with the EVN and EVN+*e*-MERLIN. The non-detection with VLBI arrays suggests that the radio emission detected at lower angular resolution by the RACS, FIRST, the Apertif imaging survey, the NVSS and VLASS surveys might be diffuse and therefore completely resolved out by our VLBI observations. We ascribed this emission to highly star-forming regions within the galaxy and we derived a SFR of approximately $\sim 300 M_{\odot} \text{ yr}^{-1}$. This high SFR is consistent with the most extreme environments for long-duration GRBs, further corroborating the hypothesis of GRB 200716 being a long-duration GRB located in J1304+2938. In this case, the latter would be among the most radio-luminous long-GRB host galaxies discovered so far. Although our VLBI observations did not pinpoint a compact emitting region, we cannot exclude the presence of an isolated IMBH. In fact, radio emission from these sources is expected to be fainter than the upper limits currently achievable. Future radio observatories will push these limits, and we may possibly be able to either confirm or rule out their existence.

Hitherto, only 21 long-GRB host galaxies have been detected in radio. In principle, surveys represent a handy resource to discover these object. However, they are seldom deep enough. With its superior surveying capabilities, the SKAO will be able to reveal many more host galaxies and to characterise the progenitor's environment without the contamination effect of dust extinction affecting optical observations. With the SKAO, it will be possible to follow the approach we proposed for the candidate host galaxy of GRB 200716C.

Additionally, this Thesis underscores the important role radio observations can play in the characterisation of the astrophysical sources responsible for producing GRBs. It was recently proposed that two sub-populations within long GRBs may exist based on their radio emission. Those GRBs with a detected afterglow in radio are termed radio-bright, or radio-loud GRBs. Conversely, those bursts without a detected radio afterglow are classified as radio-dark, or radio-quiet. This dichotomy has been linked to different progenitors: in this scenario, radio-bright GRBs result from the collapse of massive stars in interacting binary systems, while radio-dark GRBs are produced by the collapse of isolated massive stars. However, the completeness of the sample used in these studies may be affected by instrumental biases. In Chapter 7, our

analysis focused on a sample of radio-bright and radio-dark *Swift* GRBs. The selection of a sample with uniform biases supports the hypothesis that the aforementioned dichotomy is primarily driven by instrumental factors, particularly the limited sensitivity of both γ -ray and radio facilities. Nevertheless, to firmly confirm or reject the potential dichotomy, a sample of GRB radio afterglows devoid of biases is required. Achieving this goal is challenging. While future facilities will allow the follow-up of fainter bursts, the measurement of GRB redshift, crucial for estimating prompt emission quantities in statistical analyses, is only feasible for bursts with a bright optical counterpart. Additionally, verifying whether non-detections are due to sensitivity limits or if the GRB is genuinely radio-dark requires comparing derived upper limits with predictions from sophisticated afterglow models. Two approaches are proposed to reach the purpose: conducting multi-wavelength afterglow modeling and/or calculating the radio emission expected from a realistic, synthesised population of GRBs.

To conclude, the advent of future radio facilities will undoubtedly play a pivotal role in advancing our understanding of GRBs. The enhanced sensitivity reached by these facilities will offer several key benefits. First, next generation radio telescopes will strengthen the study of individual events by mitigating the degeneracy in afterglow modeling. When complemented by next-generation ground-based VHE detectors like CTAO, they will enable detailed analysis of the different emission mechanisms, such as SSC and EIC. Furthermore, the enhanced sensitivity will allow the detailed characterisation of the geometry and structure of GRB outflows for the nearest bursts, providing valuable insights into their intricate dynamics. Moreover, it will facilitate the detection and characterisation of GRB host galaxies, shedding light on the environments that give rise to these powerful cosmic events. Future radio observatories will contribute to verify the existence of multiple channels in long-GRB production by confirming or rejecting the proposed dichotomy in the radio afterglow population, especially when combined with new γ -ray satellites like THESEUS. The surveying capabilities of future facilities will ease the search for late-time radio emission from orphan afterglows, i.e., off-axis GRBs for which the prompt emission cannot be observed, as the jet is not pointing towards the observer. The quest for these objects is fundamental to estimate the GRB production rate and gaining further insight into their progenitor. Finally, stellar models postulate that extremely energetic ($E_{iso} \simeq 10^{56}$ erg) bursts may be produced by the collapse of Pop-III stars during the epoch of reionisation ($z \geq 6$; [374]). While X-ray and optical data cannot discern between a high-redshift, pop-II and a Pop-III GRB, radio observations represent an invaluable asset, as the radio light curve from Pop-III stars is expected to peak at later times [375]. The golden era of radio interferometry studies of GRBs has just started, promising unprecedented discoveries and deeper insights into these extraordinary phenomena.

Bibliography

- [1] R. W. Klebesadel, I. B. Strong, and R. A. Olson. “Observations of Gamma-Ray Bursts of Cosmic Origin”. In: *ApJ* 182 (June 1973), p. L85. DOI: [10.1086/181225](https://doi.org/10.1086/181225).
- [2] D. Q. Lamb. “The Distance Scale to Gamma-Ray Bursts”. In: *PASP* 107 (Dec. 1995), p. 1152. DOI: [10.1086/133673](https://doi.org/10.1086/133673).
- [3] B. Paczynski. “Gamma-ray bursters at cosmological distances”. In: *ApJ* 308 (Sept. 1986), pp. L43–L46. DOI: [10.1086/184740](https://doi.org/10.1086/184740).
- [4] B. Paczynski. “How Far Away Are Gamma-Ray Bursters?” In: *PASP* 107 (Dec. 1995), p. 1167. DOI: [10.1086/133674](https://doi.org/10.1086/133674). arXiv: [astro-ph/9505096](https://arxiv.org/abs/astro-ph/9505096) [[astro-ph](#)].
- [5] C. A. Meegan et al. “Spatial distribution of γ -ray bursts observed by BATSE”. In: *Nature* 355.6356 (Jan. 1992), pp. 143–145. DOI: [10.1038/355143a0](https://doi.org/10.1038/355143a0).
- [6] E. Costa et al. “Discovery of an X-ray afterglow associated with the γ -ray burst of 28 February 1997”. In: *Nature* 387.6635 (June 1997), pp. 783–785. DOI: [10.1038/42885](https://doi.org/10.1038/42885). arXiv: [astro-ph/9706065](https://arxiv.org/abs/astro-ph/9706065) [[astro-ph](#)].
- [7] J. van Paradijs et al. “Transient optical emission from the error box of the γ -ray burst of 28 February 1997”. In: *Nature* 386.6626 (Apr. 1997), pp. 686–689. DOI: [10.1038/386686a0](https://doi.org/10.1038/386686a0).
- [8] D. A. Frail et al. “The radio afterglow from the γ -ray burst of 8 May 1997”. In: *Nature* 389.6648 (Sept. 1997), pp. 261–263. DOI: [10.1038/38451](https://doi.org/10.1038/38451).
- [9] M. R. Metzger et al. “Spectral constraints on the redshift of the optical counterpart to the γ -ray burst of 8 May 1997”. In: *Nature* 387.6636 (June 1997), pp. 878–880. DOI: [10.1038/43132](https://doi.org/10.1038/43132).
- [10] E. P. Mazets et al. “Catalog of cosmic gamma-ray bursts from the KONUS experiment data”. In: *Ap&SS* 80.1 (Nov. 1981), pp. 119–143. DOI: [10.1007/BF00649142](https://doi.org/10.1007/BF00649142).
- [11] J. P. Norris et al. “Frequency of fast, narrow γ -ray bursts”. In: *Nature* 308.5958 (Mar. 1984), pp. 434–435. DOI: [10.1038/308434a0](https://doi.org/10.1038/308434a0).
- [12] C. Kouveliotou et al. “Identification of Two Classes of Gamma-Ray Bursts”. In: *ApJ* 413 (Aug. 1993), p. L101. DOI: [10.1086/186969](https://doi.org/10.1086/186969).
- [13] E. Nakar. “Short-hard gamma-ray bursts”. In: *Phys. Rep.* 442.1-6 (Apr. 2007), pp. 166–236. DOI: [10.1016/j.physrep.2007.02.005](https://doi.org/10.1016/j.physrep.2007.02.005). arXiv: [astro-ph/0701748](https://arxiv.org/abs/astro-ph/0701748) [[astro-ph](#)].
- [14] E. Berger. “The Host Galaxies of Short-Duration Gamma-Ray Bursts: Luminosities, Metallicities, and Star-Formation Rates”. In: *ApJ* 690.1 (Jan. 2009), pp. 231–237. DOI: [10.1088/0004-637X/690/1/231](https://doi.org/10.1088/0004-637X/690/1/231). arXiv: [0805.0306](https://arxiv.org/abs/0805.0306) [[astro-ph](#)].
- [15] W. Fong and E. Berger. “The Locations of Short Gamma-Ray Bursts as Evidence for Compact Object Binary Progenitors”. In: *ApJ* 776.1, 18 (Oct. 2013), p. 18. DOI: [10.1088/0004-637X/776/1/18](https://doi.org/10.1088/0004-637X/776/1/18). arXiv: [1307.0819](https://arxiv.org/abs/1307.0819) [[astro-ph.HE](#)].
- [16] E. Berger. “Short-Duration Gamma-Ray Bursts”. In: *ARA&A* 52 (Aug. 2014), pp. 43–105. DOI: [10.1146/annurev-astro-081913-035926](https://doi.org/10.1146/annurev-astro-081913-035926). arXiv: [1311.2603](https://arxiv.org/abs/1311.2603) [[astro-ph.HE](#)].

- [17] A. E. Nugent et al. “Short GRB Host Galaxies. II. A Legacy Sample of Redshifts, Stellar Population Properties, and Implications for Their Neutron Star Merger Origins”. In: *ApJ* 940.1, 57 (Nov. 2022), p. 57. DOI: [10.3847/1538-4357/ac91d1](https://doi.org/10.3847/1538-4357/ac91d1). arXiv: [2206.01764](https://arxiv.org/abs/2206.01764) [[astro-ph.GA](#)].
- [18] W. Fong et al. “Short GRB Host Galaxies. I. Photometric and Spectroscopic Catalogs, Host Associations, and Galactocentric Offsets”. In: *ApJ* 940.1, 56 (Nov. 2022), p. 56. DOI: [10.3847/1538-4357/ac91d0](https://doi.org/10.3847/1538-4357/ac91d0). arXiv: [2206.01763](https://arxiv.org/abs/2206.01763) [[astro-ph.GA](#)].
- [19] T. Piran. “Gamma-ray bursts and the fireball model”. In: *Phys. Rep.* 314.6 (June 1999), pp. 575–667. DOI: [10.1016/S0370-1573\(98\)00127-6](https://doi.org/10.1016/S0370-1573(98)00127-6). arXiv: [astro-ph/9810256](https://arxiv.org/abs/astro-ph/9810256) [[astro-ph](#)].
- [20] P. Mészáros. “Theories of Gamma-Ray Bursts”. In: *ARA&A* 40 (Jan. 2002), pp. 137–169. DOI: [10.1146/annurev.astro.40.060401.093821](https://doi.org/10.1146/annurev.astro.40.060401.093821). arXiv: [astro-ph/0111170](https://arxiv.org/abs/astro-ph/0111170) [[astro-ph](#)].
- [21] E. Waxman. “Gamma-Ray Bursts: The Underlying Model”. In: *Supernovae and Gamma-Ray Bursters*. Ed. by K. Weiler. Vol. 598. 2003, pp. 393–418. DOI: [10.1007/3-540-45863-8_19](https://doi.org/10.1007/3-540-45863-8_19).
- [22] T. Piran. “The physics of gamma-ray bursts”. In: *Reviews of Modern Physics* 76.4 (Oct. 2004), pp. 1143–1210. DOI: [10.1103/RevModPhys.76.1143](https://doi.org/10.1103/RevModPhys.76.1143). arXiv: [astro-ph/0405503](https://arxiv.org/abs/astro-ph/0405503) [[astro-ph](#)].
- [23] B. Zhang and P. Mészáros. “Gamma-Ray Bursts: progress, problems & prospects”. In: *International Journal of Modern Physics A* 19.15 (Jan. 2004), pp. 2385–2472. DOI: [10.1142/S0217751X0401746X](https://doi.org/10.1142/S0217751X0401746X). arXiv: [astro-ph/0311321](https://arxiv.org/abs/astro-ph/0311321) [[astro-ph](#)].
- [24] G. Vedrenne and J.-L. Atteia. *Gamma-Ray Bursts*. 2009. DOI: [10.1007/978-3-540-39088-6](https://doi.org/10.1007/978-3-540-39088-6).
- [25] C. Kouveliotou, R. A. M. J. Wijers, and S. Woosley. *Gamma-ray Bursts*. 2012.
- [26] T. Ahumada et al. “Discovery and confirmation of the shortest gamma-ray burst from a collapsar”. In: *Nature Astronomy* 5 (July 2021), pp. 917–927. DOI: [10.1038/s41550-021-01428-7](https://doi.org/10.1038/s41550-021-01428-7). arXiv: [2105.05067](https://arxiv.org/abs/2105.05067) [[astro-ph.HE](#)].
- [27] J. C. Rastinejad et al. “A kilonova following a long-duration gamma-ray burst at 350 Mpc”. In: *Nature* 612.7939 (Dec. 2022), pp. 223–227. DOI: [10.1038/s41586-022-05390-w](https://doi.org/10.1038/s41586-022-05390-w). arXiv: [2204.10864](https://arxiv.org/abs/2204.10864) [[astro-ph.HE](#)].
- [28] A. Mei et al. “Gigaelectronvolt emission from a compact binary merger”. In: *Nature* 612.7939 (Dec. 2022), pp. 236–239. DOI: [10.1038/s41586-022-05404-7](https://doi.org/10.1038/s41586-022-05404-7). arXiv: [2205.08566](https://arxiv.org/abs/2205.08566) [[astro-ph.HE](#)].
- [29] B. Gendre et al. “The Ultra-long Gamma-Ray Burst 111209A: The Collapse of a Blue Supergiant?” In: *ApJ* 766.1, 30 (Mar. 2013), p. 30. DOI: [10.1088/0004-637X/766/1/30](https://doi.org/10.1088/0004-637X/766/1/30). arXiv: [1212.2392](https://arxiv.org/abs/1212.2392) [[astro-ph.HE](#)].
- [30] A. J. Levan et al. “A New Population of Ultra-long Duration Gamma-Ray Bursts”. In: *ApJ* 781.1, 13 (Jan. 2014), p. 13. DOI: [10.1088/0004-637X/781/1/13](https://doi.org/10.1088/0004-637X/781/1/13). arXiv: [1302.2352](https://arxiv.org/abs/1302.2352) [[astro-ph.HE](#)].
- [31] D. Band et al. “BATSE Observations of Gamma-Ray Burst Spectra. I. Spectral Diversity”. In: *ApJ* 413 (Aug. 1993), p. 281. DOI: [10.1086/172995](https://doi.org/10.1086/172995).
- [32] M. S. Briggs et al. “Observations of GRB 990123 by the Compton Gamma Ray Observatory”. In: *ApJ* 524.1 (Oct. 1999), pp. 82–91. DOI: [10.1086/307808](https://doi.org/10.1086/307808). arXiv: [astro-ph/9903247](https://arxiv.org/abs/astro-ph/9903247) [[astro-ph](#)].
- [33] G. Ghirlanda, A. Celotti, and G. Ghisellini. “Time resolved spectral analysis of bright gamma ray bursts”. In: *A&A* 393 (Oct. 2002), pp. 409–423. DOI: [10.1051/0004-6361:20021038](https://doi.org/10.1051/0004-6361:20021038). arXiv: [astro-ph/0206377](https://arxiv.org/abs/astro-ph/0206377) [[astro-ph](#)].

- [34] G. Oganessian et al. “Detection of Low-energy Breaks in Gamma-Ray Burst Prompt Emission Spectra”. In: *ApJ* 846.2, 137 (Sept. 2017), p. 137. DOI: [10.3847/1538-4357/aa831e](https://doi.org/10.3847/1538-4357/aa831e). arXiv: [1709.04689](https://arxiv.org/abs/1709.04689) [[astro-ph.HE](#)].
- [35] G. Oganessian et al. “Characterization of gamma-ray burst prompt emission spectra down to soft X-rays”. In: *A&A* 616, A138 (Sept. 2018), A138. DOI: [10.1051/0004-6361/201732172](https://doi.org/10.1051/0004-6361/201732172). arXiv: [1710.09383](https://arxiv.org/abs/1710.09383) [[astro-ph.HE](#)].
- [36] M. E. Ravasio et al. “Evidence of two spectral breaks in the prompt emission of gamma-ray bursts”. In: *A&A* 625, A60 (May 2019), A60. DOI: [10.1051/0004-6361/201834987](https://doi.org/10.1051/0004-6361/201834987). arXiv: [1903.02555](https://arxiv.org/abs/1903.02555) [[astro-ph.HE](#)].
- [37] G. Oganessian et al. “Prompt optical emission as a signature of synchrotron radiation in gamma-ray bursts”. In: *A&A* 628, A59 (Aug. 2019), A59. DOI: [10.1051/0004-6361/201935766](https://doi.org/10.1051/0004-6361/201935766). arXiv: [1904.11086](https://arxiv.org/abs/1904.11086) [[astro-ph.HE](#)].
- [38] L. Amati et al. “Intrinsic spectra and energetics of BeppoSAX Gamma-Ray Bursts with known redshifts”. In: *A&A* 390 (July 2002), pp. 81–89. DOI: [10.1051/0004-6361:20020722](https://doi.org/10.1051/0004-6361:20020722). arXiv: [astro-ph/0205230](https://arxiv.org/abs/astro-ph/0205230) [[astro-ph](#)].
- [39] G. Ghirlanda, G. Ghisellini, and C. Firmani. “Gamma-ray bursts as standard candles to constrain the cosmological parameters”. In: *New Journal of Physics* 8.7 (July 2006), p. 123. DOI: [10.1088/1367-2630/8/7/123](https://doi.org/10.1088/1367-2630/8/7/123). arXiv: [astro-ph/0610248](https://arxiv.org/abs/astro-ph/0610248) [[astro-ph](#)].
- [40] G. Ghirlanda, G. Ghisellini, and D. Lazzati. “The Collimation-corrected Gamma-Ray Burst Energies Correlate with the Peak Energy of Their νF_ν Spectrum”. In: *ApJ* 616.1 (Nov. 2004), pp. 331–338. DOI: [10.1086/424913](https://doi.org/10.1086/424913). arXiv: [astro-ph/0405602](https://arxiv.org/abs/astro-ph/0405602) [[astro-ph](#)].
- [41] D. Yonetoku et al. “Gamma-Ray Burst Formation Rate Inferred from the Spectral Peak Energy-Peak Luminosity Relation”. In: *ApJ* 609.2 (July 2004), pp. 935–951. DOI: [10.1086/421285](https://doi.org/10.1086/421285). arXiv: [astro-ph/0309217](https://arxiv.org/abs/astro-ph/0309217) [[astro-ph](#)].
- [42] G. Ghirlanda et al. “Gamma-Ray Bursts: New Rulers to Measure the Universe”. In: *ApJ* 613.1 (Sept. 2004), pp. L13–L16. DOI: [10.1086/424915](https://doi.org/10.1086/424915). arXiv: [astro-ph/0408350](https://arxiv.org/abs/astro-ph/0408350) [[astro-ph](#)].
- [43] L. Amati and M. Della Valle. “Measuring Cosmological Parameters with Gamma Ray Bursts”. In: *International Journal of Modern Physics D* 22.14, 1330028 (Dec. 2013), p. 1330028. DOI: [10.1142/S0218271813300280](https://doi.org/10.1142/S0218271813300280). arXiv: [1310.3141](https://arxiv.org/abs/1310.3141) [[astro-ph.CO](#)].
- [44] P. Chandra and D. A. Frail. “A Radio-selected Sample of Gamma-Ray Burst Afterglows”. In: *ApJ* 746.2, 156 (Feb. 2012), p. 156. DOI: [10.1088/0004-637X/746/2/156](https://doi.org/10.1088/0004-637X/746/2/156). arXiv: [1110.4124](https://arxiv.org/abs/1110.4124) [[astro-ph.CO](#)].
- [45] P. J. Hancock, B. M. Gaensler, and T. Murphy. “Two Populations of Gamma-Ray Burst Radio Afterglows”. In: *ApJ* 776.2, 106 (Oct. 2013), p. 106. DOI: [10.1088/0004-637X/776/2/106](https://doi.org/10.1088/0004-637X/776/2/106). arXiv: [1308.4766](https://arxiv.org/abs/1308.4766) [[astro-ph.HE](#)].
- [46] G. Schroeder et al. “A Radio Flare in the Long-Lived Afterglow of the Distant Short GRB 210726A: Energy Injection or a Reverse Shock from Shell Collisions?” In: *arXiv e-prints*, arXiv:2308.10936 (Aug. 2023), arXiv:2308.10936. DOI: [10.48550/arXiv.2308.10936](https://doi.org/10.48550/arXiv.2308.10936). arXiv: [2308.10936](https://arxiv.org/abs/2308.10936) [[astro-ph.HE](#)].
- [47] N. Lloyd-Ronning. “Radio-loud versus Radio-quiet Gamma-Ray Bursts: The Role of Binary Progenitors”. In: *ApJ* 928.2, 104 (Apr. 2022), p. 104. DOI: [10.3847/1538-4357/ac54b3](https://doi.org/10.3847/1538-4357/ac54b3). arXiv: [2109.14122](https://arxiv.org/abs/2109.14122) [[astro-ph.HE](#)].

- [48] B. Zhang et al. “Physical Processes Shaping Gamma-Ray Burst X-Ray Afterglow Light Curves: Theoretical Implications from the Swift X-Ray Telescope Observations”. In: *ApJ* 642.1 (May 2006), pp. 354–370. DOI: [10.1086/500723](https://doi.org/10.1086/500723). arXiv: [astro-ph/0508321](https://arxiv.org/abs/astro-ph/0508321) [[astro-ph](#)].
- [49] J. K. Leung et al. “A search for radio afterglows from gamma-ray bursts with the Australian Square Kilometre Array Pathfinder”. In: *MNRAS* 503.2 (May 2021), pp. 1847–1863. DOI: [10.1093/mnras/stab326](https://doi.org/10.1093/mnras/stab326). arXiv: [2102.01948](https://arxiv.org/abs/2102.01948) [[astro-ph.HE](#)].
- [50] B. J. Rickett. “Radio propagation through the turbulent interstellar plasma.” In: *ARA&A* 28 (Jan. 1990), pp. 561–605. DOI: [10.1146/annurev.aa.28.090190.003021](https://doi.org/10.1146/annurev.aa.28.090190.003021).
- [51] J. Goodman. “Radio scintillation of gamma-ray-burst afterglows”. In: *New A* 2.5 (Nov. 1997), pp. 449–460. DOI: [10.1016/S1384-1076\(97\)00031-6](https://doi.org/10.1016/S1384-1076(97)00031-6). arXiv: [astro-ph/9706084](https://arxiv.org/abs/astro-ph/9706084) [[astro-ph](#)].
- [52] M. A. Walker. “Interstellar scintillation of compact extragalactic radio sources”. In: *MNRAS* 294 (Feb. 1998), pp. 307–311. DOI: [10.1046/j.1365-8711.1998.01238.x](https://doi.org/10.1046/j.1365-8711.1998.01238.x).
- [53] D. A. Frail, E. Waxman, and S. R. Kulkarni. “A 450 Day Light Curve of the Radio Afterglow of GRB 970508: Fireball Calorimetry”. In: *ApJ* 537.1 (July 2000), pp. 191–204. DOI: [10.1086/309024](https://doi.org/10.1086/309024). arXiv: [astro-ph/9910319](https://arxiv.org/abs/astro-ph/9910319) [[astro-ph](#)].
- [54] P. Chandra et al. “A Comprehensive Study of GRB 070125, A Most Energetic Gamma-Ray Burst”. In: *ApJ* 683.2 (Aug. 2008), pp. 924–942. DOI: [10.1086/589807](https://doi.org/10.1086/589807). arXiv: [0802.2748](https://arxiv.org/abs/0802.2748) [[astro-ph](#)].
- [55] A. J. van der Horst et al. “A comprehensive radio view of the extremely bright gamma-ray burst 130427A”. In: *MNRAS* 444.4 (Nov. 2014), pp. 3151–3163. DOI: [10.1093/mnras/stu1664](https://doi.org/10.1093/mnras/stu1664). arXiv: [1404.1945](https://arxiv.org/abs/1404.1945) [[astro-ph.HE](#)].
- [56] K. D. Alexander et al. “A Reverse Shock and Unusual Radio Properties in GRB 160625B”. In: *ApJ* 848.1, 69 (Oct. 2017), p. 69. DOI: [10.3847/1538-4357/aa8a76](https://doi.org/10.3847/1538-4357/aa8a76). arXiv: [1705.08455](https://arxiv.org/abs/1705.08455) [[astro-ph.HE](#)].
- [57] K. D. Alexander et al. “An Unexpectedly Small Emission Region Size Inferred from Strong High-frequency Diffractive Scintillation in GRB 161219B”. In: *ApJ* 870.2, 67 (Jan. 2019), p. 67. DOI: [10.3847/1538-4357/aaf19d](https://doi.org/10.3847/1538-4357/aaf19d). arXiv: [1806.08017](https://arxiv.org/abs/1806.08017) [[astro-ph.HE](#)].
- [58] D. A. Perley et al. “The Afterglow of GRB 130427A from 1 to 10^{16} GHz”. In: *ApJ* 781.1, 37 (Jan. 2014), p. 37. DOI: [10.1088/0004-637X/781/1/37](https://doi.org/10.1088/0004-637X/781/1/37). arXiv: [1307.4401](https://arxiv.org/abs/1307.4401) [[astro-ph.HE](#)].
- [59] R. Mirzoyan. “First time detection of a GRB at sub-TeV energies; MAGIC detects the GRB 190114C”. In: *The Astronomer’s Telegram* 12390 (Jan. 2019), p. 1.
- [60] H. Abdalla et al. “A very-high-energy component deep in the γ -ray burst afterglow”. In: *Nature* 575.7783 (Nov. 2019), pp. 464–467. DOI: [10.1038/s41586-019-1743-9](https://doi.org/10.1038/s41586-019-1743-9). arXiv: [1911.08961](https://arxiv.org/abs/1911.08961) [[astro-ph.HE](#)].
- [61] MAGIC Collaboration et al. “Teraelectronvolt emission from the γ -ray burst GRB 190114C”. In: *Nature* 575.7783 (Nov. 2019), pp. 455–458. DOI: [10.1038/s41586-019-1750-x](https://doi.org/10.1038/s41586-019-1750-x). arXiv: [2006.07249](https://arxiv.org/abs/2006.07249) [[astro-ph.HE](#)].
- [62] H. Abe et al. “MAGIC detection of GRB 201216C at $z = 1.1$ ”. In: *MNRAS* 527.3 (Jan. 2024), pp. 5856–5867. DOI: [10.1093/mnras/stad2958](https://doi.org/10.1093/mnras/stad2958). arXiv: [2310.06473](https://arxiv.org/abs/2310.06473) [[astro-ph.HE](#)].
- [63] LHAASO Collaboration et al. “A tera-electron volt afterglow from a narrow jet in an extremely bright gamma-ray burst.” In: *Science* 380.6652 (June 2023), pp. 1390–1396. DOI: [10.1126/science.adg9328](https://doi.org/10.1126/science.adg9328). arXiv: [2306.06372](https://arxiv.org/abs/2306.06372) [[astro-ph.HE](#)].

- [64] H. E. S. S. Collaboration et al. “Revealing x-ray and gamma ray temporal and spectral similarities in the GRB 190829A afterglow”. In: *Science* 372.6546 (June 2021), pp. 1081–1085. DOI: [10.1126/science.abe8560](https://doi.org/10.1126/science.abe8560). arXiv: [2106.02510](https://arxiv.org/abs/2106.02510) [[astro-ph.HE](#)].
- [65] T. Sakamoto et al. “The Second Swift Burst Alert Telescope Gamma-Ray Burst Catalog”. In: *ApJS* 195.1, 2 (July 2011), p. 2. DOI: [10.1088/0067-0049/195/1/2](https://doi.org/10.1088/0067-0049/195/1/2). arXiv: [1104.4689](https://arxiv.org/abs/1104.4689) [[astro-ph.HE](#)].
- [66] E. Berger. “The Prompt Gamma-Ray and Afterglow Energies of Short-Duration Gamma-Ray Bursts”. In: *ApJ* 670.2 (Dec. 2007), pp. 1254–1259. DOI: [10.1086/522195](https://doi.org/10.1086/522195). arXiv: [astro-ph/0702694](https://arxiv.org/abs/astro-ph/0702694) [[astro-ph](#)].
- [67] N. Gehrels et al. “A short γ -ray burst apparently associated with an elliptical galaxy at redshift $z = 0.225$ ”. In: *Nature* 437.7060 (Oct. 2005), pp. 851–854. DOI: [10.1038/nature04142](https://doi.org/10.1038/nature04142). arXiv: [astro-ph/0505630](https://arxiv.org/abs/astro-ph/0505630) [[astro-ph](#)].
- [68] P. D’Avanzo et al. “The optical afterglows and host galaxies of three short/hard gamma-ray bursts”. In: *A&A* 498.3 (May 2009), pp. 711–721. DOI: [10.1051/0004-6361/200811294](https://doi.org/10.1051/0004-6361/200811294). arXiv: [0901.4038](https://arxiv.org/abs/0901.4038) [[astro-ph.CO](#)].
- [69] W. Fong, E. Berger, and D. B. Fox. “Hubble Space Telescope Observations of Short Gamma-Ray Burst Host Galaxies: Morphologies, Offsets, and Local Environments”. In: *ApJ* 708.1 (Jan. 2010), pp. 9–25. DOI: [10.1088/0004-637X/708/1/9](https://doi.org/10.1088/0004-637X/708/1/9). arXiv: [0909.1804](https://arxiv.org/abs/0909.1804) [[astro-ph.HE](#)].
- [70] B. O’Connor et al. “A deep survey of short GRB host galaxies over z 0-2: implications for offsets, redshifts, and environments”. In: *MNRAS* 515.4 (Oct. 2022), pp. 4890–4928. DOI: [10.1093/mnras/stac1982](https://doi.org/10.1093/mnras/stac1982). arXiv: [2204.09059](https://arxiv.org/abs/2204.09059) [[astro-ph.HE](#)].
- [71] E. Berger, S. R. Kulkarni, and D. A. Frail. “The Host Galaxy of GRB 980703 at Radio Wavelengths—a Nuclear Starburst in an Ultraluminous Infrared Galaxy”. In: *ApJ* 560.2 (Oct. 2001), pp. 652–658. DOI: [10.1086/322247](https://doi.org/10.1086/322247). arXiv: [astro-ph/0105081](https://arxiv.org/abs/astro-ph/0105081) [[astro-ph](#)].
- [72] J. M. Lattimer and D. N. Schramm. “Black-Hole-Neutron-Star Collisions”. In: *ApJ* 192 (Sept. 1974), p. L145. DOI: [10.1086/181612](https://doi.org/10.1086/181612).
- [73] S. Rosswog et al. “Mass ejection in neutron star mergers”. In: *A&A* 341 (Jan. 1999), pp. 499–526. DOI: [10.48550/arXiv.astro-ph/9811367](https://doi.org/10.48550/arXiv.astro-ph/9811367). arXiv: [astro-ph/9811367](https://arxiv.org/abs/astro-ph/9811367) [[astro-ph](#)].
- [74] C. Freiburghaus, S. Rosswog, and F. -K. Thielemann. “R-Process in Neutron Star Mergers”. In: *ApJ* 525.2 (Nov. 1999), pp. L121–L124. DOI: [10.1086/312343](https://doi.org/10.1086/312343).
- [75] L.-X. Li and B. Paczyński. “Transient Events from Neutron Star Mergers”. In: *ApJ* 507.1 (Nov. 1998), pp. L59–L62. DOI: [10.1086/311680](https://doi.org/10.1086/311680). arXiv: [astro-ph/9807272](https://arxiv.org/abs/astro-ph/9807272) [[astro-ph](#)].
- [76] B. D. Metzger et al. “Electromagnetic counterparts of compact object mergers powered by the radioactive decay of r-process nuclei”. In: *MNRAS* 406.4 (Aug. 2010), pp. 2650–2662. DOI: [10.1111/j.1365-2966.2010.16864.x](https://doi.org/10.1111/j.1365-2966.2010.16864.x). arXiv: [1001.5029](https://arxiv.org/abs/1001.5029) [[astro-ph.HE](#)].
- [77] N. R. Tanvir et al. “A ‘kilonova’ associated with the short-duration γ -ray burst GRB 130603B”. In: *Nature* 500.7464 (Aug. 2013), pp. 547–549. DOI: [10.1038/nature12505](https://doi.org/10.1038/nature12505). arXiv: [1306.4971](https://arxiv.org/abs/1306.4971) [[astro-ph.HE](#)].
- [78] E. Berger, W. Fong, and R. Chornock. “An r-process Kilonova Associated with the Short-hard GRB 130603B”. In: *ApJ* 774.2, L23 (Sept. 2013), p. L23. DOI: [10.1088/2041-8205/774/2/L23](https://doi.org/10.1088/2041-8205/774/2/L23). arXiv: [1306.3960](https://arxiv.org/abs/1306.3960) [[astro-ph.HE](#)].
- [79] D. Eichler et al. “Nucleosynthesis, neutrino bursts and γ -rays from coalescing neutron stars”. In: *Nature* 340.6229 (July 1989), pp. 126–128. DOI: [10.1038/340126a0](https://doi.org/10.1038/340126a0).

- [80] V. A. Villar et al. “The Combined Ultraviolet, Optical, and Near-infrared Light Curves of the Kilonova Associated with the Binary Neutron Star Merger GW170817: Unified Data Set, Analytic Models, and Physical Implications”. In: *ApJ* 851.1, L21 (Dec. 2017), p. L21. DOI: [10.3847/2041-8213/aa9c84](https://doi.org/10.3847/2041-8213/aa9c84). arXiv: [1710.11576](https://arxiv.org/abs/1710.11576) [[astro-ph.HE](#)].
- [81] E. Pian et al. “Spectroscopic identification of r-process nucleosynthesis in a double neutron-star merger”. In: *Nature* 551.7678 (Nov. 2017), pp. 67–70. DOI: [10.1038/nature24298](https://doi.org/10.1038/nature24298). arXiv: [1710.05858](https://arxiv.org/abs/1710.05858) [[astro-ph.HE](#)].
- [82] D. Kasen, R. Fernández, and B. D. Metzger. “Kilonova light curves from the disc wind outflows of compact object mergers”. In: *MNRAS* 450.2 (June 2015), pp. 1777–1786. DOI: [10.1093/mnras/stv721](https://doi.org/10.1093/mnras/stv721). arXiv: [1411.3726](https://arxiv.org/abs/1411.3726) [[astro-ph.HE](#)].
- [83] M. Tanaka et al. “Kilonova from post-merger ejecta as an optical and near-Infrared counterpart of GW170817”. In: *PASJ* 69.6, 102 (Dec. 2017), p. 102. DOI: [10.1093/pasj/psx121](https://doi.org/10.1093/pasj/psx121). arXiv: [1710.05850](https://arxiv.org/abs/1710.05850) [[astro-ph.HE](#)].
- [84] E. Nakar and T. Piran. “Detectable radio flares following gravitational waves from mergers of binary neutron stars”. In: *Nature* 478.7367 (Oct. 2011), pp. 82–84. DOI: [10.1038/nature10365](https://doi.org/10.1038/nature10365). arXiv: [1102.1020](https://arxiv.org/abs/1102.1020) [[astro-ph.HE](#)].
- [85] A. Kathirgamaraju, D. Giannios, and P. Beniamini. “Observable features of GW170817 kilonova afterglow”. In: *MNRAS* 487.3 (Aug. 2019), pp. 3914–3921. DOI: [10.1093/mnras/stz1564](https://doi.org/10.1093/mnras/stz1564). arXiv: [1901.00868](https://arxiv.org/abs/1901.00868) [[astro-ph.HE](#)].
- [86] A. Hajela et al. “Two Years of Nonthermal Emission from the Binary Neutron Star Merger GW170817: Rapid Fading of the Jet Afterglow and First Constraints on the Kilonova Fastest Ejecta”. In: *ApJ* 886.1, L17 (Nov. 2019), p. L17. DOI: [10.3847/2041-8213/ab5226](https://doi.org/10.3847/2041-8213/ab5226). arXiv: [1909.06393](https://arxiv.org/abs/1909.06393) [[astro-ph.HE](#)].
- [87] E. Troja et al. “A thousand days after the merger: Continued X-ray emission from GW170817”. In: *MNRAS* 498.4 (Nov. 2020), pp. 5643–5651. DOI: [10.1093/mnras/staa2626](https://doi.org/10.1093/mnras/staa2626). arXiv: [2006.01150](https://arxiv.org/abs/2006.01150) [[astro-ph.HE](#)].
- [88] B. P. Abbott et al. “GW151226: Observation of Gravitational Waves from a 22-Solar-Mass Binary Black Hole Coalescence”. In: *Phys. Rev. Lett.* 116.24, 241103 (June 2016), p. 241103. DOI: [10.1103/PhysRevLett.116.241103](https://doi.org/10.1103/PhysRevLett.116.241103). arXiv: [1606.04855](https://arxiv.org/abs/1606.04855) [[gr-qc](#)].
- [89] B. P. Abbott et al. “GW170814: A Three-Detector Observation of Gravitational Waves from a Binary Black Hole Coalescence”. In: *Phys. Rev. Lett.* 119.14, 141101 (Oct. 2017), p. 141101. DOI: [10.1103/PhysRevLett.119.141101](https://doi.org/10.1103/PhysRevLett.119.141101). arXiv: [1709.09660](https://arxiv.org/abs/1709.09660) [[gr-qc](#)].
- [90] B. P. Abbott et al. “GW170817: Observation of Gravitational Waves from a Binary Neutron Star Inspiral”. In: *Phys. Rev. Lett.* 119.16, 161101 (Oct. 2017), p. 161101. DOI: [10.1103/PhysRevLett.119.161101](https://doi.org/10.1103/PhysRevLett.119.161101). arXiv: [1710.05832](https://arxiv.org/abs/1710.05832) [[gr-qc](#)].
- [91] B. P. Abbott et al. “Gravitational Waves and Gamma-Rays from a Binary Neutron Star Merger: GW170817 and GRB 170817A”. In: *ApJ* 848.2, L13 (Oct. 2017), p. L13. DOI: [10.3847/2041-8213/aa920c](https://doi.org/10.3847/2041-8213/aa920c). arXiv: [1710.05834](https://arxiv.org/abs/1710.05834) [[astro-ph.HE](#)].
- [92] A. Goldstein et al. “An Ordinary Short Gamma-Ray Burst with Extraordinary Implications: Fermi-GBM Detection of GRB 170817A”. In: *ApJ* 848.2, L14 (Oct. 2017), p. L14. DOI: [10.3847/2041-8213/aa8f41](https://doi.org/10.3847/2041-8213/aa8f41). arXiv: [1710.05446](https://arxiv.org/abs/1710.05446) [[astro-ph.HE](#)].
- [93] D. A. Coulter et al. “Swope Supernova Survey 2017a (SSS17a), the optical counterpart to a gravitational wave source”. In: *Science* 358.6370 (Dec. 2017), pp. 1556–1558. DOI: [10.1126/science.aap9811](https://doi.org/10.1126/science.aap9811). arXiv: [1710.05452](https://arxiv.org/abs/1710.05452) [[astro-ph.HE](#)].

- [94] E. Troja et al. “The X-ray counterpart to the gravitational-wave event GW170817”. In: *Nature* 551.7678 (Nov. 2017), pp. 71–74. DOI: [10.1038/nature24290](https://doi.org/10.1038/nature24290). arXiv: [1710.05433](https://arxiv.org/abs/1710.05433) [[astro-ph.HE](#)].
- [95] G. Hallinan et al. “A radio counterpart to a neutron star merger”. In: *Science* 358.6370 (Dec. 2017), pp. 1579–1583. DOI: [10.1126/science.aap9855](https://doi.org/10.1126/science.aap9855). arXiv: [1710.05435](https://arxiv.org/abs/1710.05435) [[astro-ph.HE](#)].
- [96] R. Margutti and R. Chornock. “First Multimessenger Observations of a Neutron Star Merger”. In: *ARA&A* 59 (Sept. 2021), pp. 155–202. DOI: [10.1146/annurev-astro-112420-030742](https://doi.org/10.1146/annurev-astro-112420-030742). arXiv: [2012.04810](https://arxiv.org/abs/2012.04810) [[astro-ph.HE](#)].
- [97] B. P. Abbott et al. “Properties of the Binary Neutron Star Merger GW170817”. In: *Physical Review X* 9.1, 011001 (Jan. 2019), p. 011001. DOI: [10.1103/PhysRevX.9.011001](https://doi.org/10.1103/PhysRevX.9.011001). arXiv: [1805.11579](https://arxiv.org/abs/1805.11579) [[gr-qc](#)].
- [98] K. P. Mooley et al. “A mildly relativistic wide-angle outflow in the neutron-star merger event GW170817”. In: *Nature* 554.7691 (Feb. 2018), pp. 207–210. DOI: [10.1038/nature25452](https://doi.org/10.1038/nature25452). arXiv: [1711.11573](https://arxiv.org/abs/1711.11573) [[astro-ph.HE](#)].
- [99] D. Lazzati et al. “Late Time Afterglow Observations Reveal a Collimated Relativistic Jet in the Ejecta of the Binary Neutron Star Merger GW170817”. In: *Phys. Rev. Lett.* 120.24, 241103 (June 2018), p. 241103. DOI: [10.1103/PhysRevLett.120.241103](https://doi.org/10.1103/PhysRevLett.120.241103). arXiv: [1712.03237](https://arxiv.org/abs/1712.03237) [[astro-ph.HE](#)].
- [100] G. Ghirlanda et al. “Compact radio emission indicates a structured jet was produced by a binary neutron star merger”. In: *Science* 363.6430 (Mar. 2019), pp. 968–971. DOI: [10.1126/science.aau8815](https://doi.org/10.1126/science.aau8815). arXiv: [1808.00469](https://arxiv.org/abs/1808.00469) [[astro-ph.HE](#)].
- [101] K. P. Mooley et al. “Superluminal motion of a relativistic jet in the neutron-star merger GW170817”. In: *Nature* 561.7723 (Sept. 2018), pp. 355–359. DOI: [10.1038/s41586-018-0486-3](https://doi.org/10.1038/s41586-018-0486-3). arXiv: [1806.09693](https://arxiv.org/abs/1806.09693) [[astro-ph.HE](#)].
- [102] J. Hjorth et al. “The Distance to NGC 4993: The Host Galaxy of the Gravitational-wave Event GW170817”. In: *ApJ* 848.2, L31 (Oct. 2017), p. L31. DOI: [10.3847/2041-8213/aa9110](https://doi.org/10.3847/2041-8213/aa9110). arXiv: [1710.05856](https://arxiv.org/abs/1710.05856) [[astro-ph.GA](#)].
- [103] C. Tinney et al. “GRB 980425”. In: *IAU Circ.* 6896 (May 1998), p. 3.
- [104] R. Salvaterra et al. “GRB090423 at a redshift of $z \sim 8.1$ ”. In: *Nature* 461.7268 (Oct. 2009), pp. 1258–1260. DOI: [10.1038/nature08445](https://doi.org/10.1038/nature08445). arXiv: [0906.1578](https://arxiv.org/abs/0906.1578) [[astro-ph.CO](#)].
- [105] T. J. Galama et al. “An unusual supernova in the error box of the γ -ray burst of 25 April 1998”. In: *Nature* 395.6703 (Oct. 1998), pp. 670–672. DOI: [10.1038/27150](https://doi.org/10.1038/27150). arXiv: [astro-ph/9806175](https://arxiv.org/abs/astro-ph/9806175) [[astro-ph](#)].
- [106] S. Savaglio, K. Glazebrook, and D. Le Borgne. “The Galaxy Population Hosting Gamma-Ray Bursts”. In: *ApJ* 691.1 (Jan. 2009), pp. 182–211. DOI: [10.1088/0004-637X/691/1/182](https://doi.org/10.1088/0004-637X/691/1/182). arXiv: [0803.2718](https://arxiv.org/abs/0803.2718) [[astro-ph](#)].
- [107] D. A. Perley et al. “The Swift GRB Host Galaxy Legacy Survey. II. Rest-frame Near-IR Luminosity Distribution and Evidence for a Near-solar Metallicity Threshold”. In: *ApJ* 817.1, 8 (Jan. 2016), p. 8. DOI: [10.3847/0004-637X/817/1/8](https://doi.org/10.3847/0004-637X/817/1/8). arXiv: [1504.02479](https://arxiv.org/abs/1504.02479) [[astro-ph.GA](#)].
- [108] E. M. Levesque et al. “The Host Galaxies of Gamma-Ray Bursts. I. Interstellar Medium Properties of Ten Nearby Long-Duration Gamma-Ray Burst Hosts”. In: *AJ* 139.2 (Feb. 2010), pp. 694–711. DOI: [10.1088/0004-6256/139/2/694](https://doi.org/10.1088/0004-6256/139/2/694). arXiv: [0907.4988](https://arxiv.org/abs/0907.4988) [[astro-ph.GA](#)].

- [109] E. M. Levesque et al. “The Host Galaxies of Gamma-ray Bursts. II. A Mass-metallicity Relation for Long-duration Gamma-ray Burst Host Galaxies”. In: *AJ* 140.5 (Nov. 2010), pp. 1557–1566. DOI: [10.1088/0004-6256/140/5/1557](https://doi.org/10.1088/0004-6256/140/5/1557). arXiv: [1006.3560](https://arxiv.org/abs/1006.3560) [[astro-ph.GA](#)].
- [110] J. Hjorth et al. “The Optically Unbiased Gamma-Ray Burst Host (TOUGH) Survey. I. Survey Design and Catalogs”. In: *ApJ* 756.2, 187 (Sept. 2012), p. 187. DOI: [10.1088/0004-637X/756/2/187](https://doi.org/10.1088/0004-637X/756/2/187). arXiv: [1205.3162](https://arxiv.org/abs/1205.3162) [[astro-ph.CO](#)].
- [111] K. M. Svensson et al. “The host galaxies of core-collapse supernovae and gamma-ray bursts”. In: *MNRAS* 405.1 (June 2010), pp. 57–76. DOI: [10.1111/j.1365-2966.2010.16442.x](https://doi.org/10.1111/j.1365-2966.2010.16442.x). arXiv: [1001.5042](https://arxiv.org/abs/1001.5042) [[astro-ph.HE](#)].
- [112] R. Lunnan et al. “Hydrogen-poor Superluminous Supernovae and Long-duration Gamma-Ray Bursts Have Similar Host Galaxies”. In: *ApJ* 787.2, 138 (June 2014), p. 138. DOI: [10.1088/0004-637X/787/2/138](https://doi.org/10.1088/0004-637X/787/2/138). arXiv: [1311.0026](https://arxiv.org/abs/1311.0026) [[astro-ph.HE](#)].
- [113] S. D. Vergani et al. “Are long gamma-ray bursts biased tracers of star formation? Clues from the host galaxies of the Swift/BAT6 complete sample of LGRBs . I. Stellar mass at $z < 1$ ”. In: *A&A* 581, A102 (Sept. 2015), A102. DOI: [10.1051/0004-6361/201425013](https://doi.org/10.1051/0004-6361/201425013). arXiv: [1409.7064](https://arxiv.org/abs/1409.7064) [[astro-ph.HE](#)].
- [114] J. D. Lyman et al. “The host galaxies and explosion sites of long-duration gamma ray bursts: Hubble Space Telescope near-infrared imaging”. In: *MNRAS* 467.2 (May 2017), pp. 1795–1817. DOI: [10.1093/mnras/stx220](https://doi.org/10.1093/mnras/stx220). arXiv: [1701.05925](https://arxiv.org/abs/1701.05925) [[astro-ph.GA](#)].
- [115] P. K. Blanchard, E. Berger, and W. Fong. “The Offset and Host Light Distributions of Long Gamma-Ray Bursts: A New View From HST Observations of Swift Bursts”. In: *ApJ* 817.2, 144 (Feb. 2016), p. 144. DOI: [10.3847/0004-637X/817/2/144](https://doi.org/10.3847/0004-637X/817/2/144). arXiv: [1509.07866](https://arxiv.org/abs/1509.07866) [[astro-ph.HE](#)].
- [116] E. R. Stanway et al. “GRB 080517: a local, low-luminosity gamma-ray burst in a dusty galaxy at $z = 0.09$ ”. In: *MNRAS* 446.4 (Feb. 2015), pp. 3911–3925. DOI: [10.1093/mnras/stu2286](https://doi.org/10.1093/mnras/stu2286). arXiv: [1409.5791](https://arxiv.org/abs/1409.5791) [[astro-ph.GA](#)].
- [117] M. J. Michałowski et al. “Massive stars formed in atomic hydrogen reservoirs: H I observations of gamma-ray burst host galaxies”. In: *A&A* 582, A78 (Oct. 2015), A78. DOI: [10.1051/0004-6361/201526542](https://doi.org/10.1051/0004-6361/201526542). arXiv: [1508.03094](https://arxiv.org/abs/1508.03094) [[astro-ph.GA](#)].
- [118] E. Berger et al. “A Submillimeter and Radio Survey of Gamma-Ray Burst Host Galaxies: A Glimpse into the Future of Star Formation Studies”. In: *ApJ* 588.1 (May 2003), pp. 99–112. DOI: [10.1086/373991](https://doi.org/10.1086/373991). arXiv: [astro-ph/0210645](https://arxiv.org/abs/astro-ph/0210645) [[astro-ph](#)].
- [119] E. R. Stanway, L. J. M. Davies, and A. J. Levan. “Low radio-derived star formation rates in $z < 0.5$ gamma-ray burst host galaxies”. In: *MNRAS* 409.1 (Nov. 2010), pp. L74–L78. DOI: [10.1111/j.1745-3933.2010.00951.x](https://doi.org/10.1111/j.1745-3933.2010.00951.x).
- [120] M. J. Michałowski et al. “The Optically Unbiased GRB Host (TOUGH) Survey. VI. Radio Observations at $z < \sim 1$ and Consistency with Typical Star-forming Galaxies”. In: *ApJ* 755.2, 85 (Aug. 2012), p. 85. DOI: [10.1088/0004-637X/755/2/85](https://doi.org/10.1088/0004-637X/755/2/85). arXiv: [1205.4239](https://arxiv.org/abs/1205.4239) [[astro-ph.CO](#)].
- [121] B. Hatsukade et al. “Constraints on Obscured Star Formation in Host Galaxies of Gamma-Ray Bursts”. In: *ApJ* 748.2, 108 (Apr. 2012), p. 108. DOI: [10.1088/0004-637X/748/2/108](https://doi.org/10.1088/0004-637X/748/2/108). arXiv: [1201.4947](https://arxiv.org/abs/1201.4947) [[astro-ph.CO](#)].
- [122] D. A. Perley and R. A. Perley. “Radio Constraints on Heavily Obscured Star Formation within Dark Gamma-Ray Burst Host Galaxies”. In: *ApJ* 778.2, 172 (Dec. 2013), p. 172. DOI: [10.1088/0004-637X/778/2/172](https://doi.org/10.1088/0004-637X/778/2/172). arXiv: [1305.2941](https://arxiv.org/abs/1305.2941) [[astro-ph.CO](#)].

- [123] E. R. Stanway, A. J. Levan, and L. J. M. Davies. “Radio observations of GRB host galaxies”. In: *MNRAS* 444.3 (Nov. 2014), pp. 2133–2146. DOI: [10.1093/mnras/stu1551](https://doi.org/10.1093/mnras/stu1551). arXiv: [1407.8180](https://arxiv.org/abs/1407.8180) [[astro-ph.GA](#)].
- [124] D. A. Perley et al. “Connecting GRBs and ULIRGs: A Sensitive, Unbiased Survey for Radio Emission from Gamma-Ray Burst Host Galaxies at $0 < z < 2.5$ ”. In: *ApJ* 801.2, 102 (Mar. 2015), p. 102. DOI: [10.1088/0004-637X/801/2/102](https://doi.org/10.1088/0004-637X/801/2/102). arXiv: [1407.4456](https://arxiv.org/abs/1407.4456) [[astro-ph.HE](#)].
- [125] J. Greiner et al. “Probing dust-obscured star formation in the most massive gamma-ray burst host galaxies”. In: *A&A* 593, A17 (Aug. 2016), A17. DOI: [10.1051/0004-6361/201628861](https://doi.org/10.1051/0004-6361/201628861). arXiv: [1606.08285](https://arxiv.org/abs/1606.08285) [[astro-ph.GA](#)].
- [126] S. Giarratana et al. “Multi-scale VLBI observations of the candidate host galaxy of GRB 200716C”. In: *A&A* 670, A35 (Feb. 2023), A35. DOI: [10.1051/0004-6361/202243829](https://doi.org/10.1051/0004-6361/202243829). arXiv: [2204.10580](https://arxiv.org/abs/2204.10580) [[astro-ph.HE](#)].
- [127] G. Ghirlanda and R. Salvaterra. “The Cosmic History of Long Gamma-Ray Bursts”. In: *ApJ* 932.1, 10 (June 2022), p. 10. DOI: [10.3847/1538-4357/ac6e43](https://doi.org/10.3847/1538-4357/ac6e43).
- [128] J. S. Bloom et al. “The unusual afterglow of the γ -ray burst of 26 March 1998 as evidence for a supernova connection”. In: *Nature* 401.6752 (Sept. 1999), pp. 453–456. DOI: [10.1038/46744](https://doi.org/10.1038/46744). arXiv: [astro-ph/9905301](https://arxiv.org/abs/astro-ph/9905301) [[astro-ph](#)].
- [129] S. E. Woosley. “Gamma-Ray Bursts from Stellar Mass Accretion Disks around Black Holes”. In: *ApJ* 405 (Mar. 1993), p. 273. DOI: [10.1086/172359](https://doi.org/10.1086/172359).
- [130] S. R. Kulkarni et al. “Radio emission from the unusual supernova 1998bw and its association with the γ -ray burst of 25 April 1998”. In: *Nature* 395.6703 (Oct. 1998), pp. 663–669. DOI: [10.1038/27139](https://doi.org/10.1038/27139).
- [131] J. Hjorth et al. “A very energetic supernova associated with the γ -ray burst of 29 March 2003”. In: *Nature* 423.6942 (June 2003), pp. 847–850. DOI: [10.1038/nature01750](https://doi.org/10.1038/nature01750). arXiv: [astro-ph/0306347](https://arxiv.org/abs/astro-ph/0306347) [[astro-ph](#)].
- [132] K. Z. Stanek et al. “Spectroscopic Discovery of the Supernova 2003dh Associated with GRB 030329”. In: *ApJ* 591.1 (July 2003), pp. L17–L20. DOI: [10.1086/376976](https://doi.org/10.1086/376976). arXiv: [astro-ph/0304173](https://arxiv.org/abs/astro-ph/0304173) [[astro-ph](#)].
- [133] P. M. Garnavich et al. “Discovery of the Low-Redshift Optical Afterglow of GRB 011121 and Its Progenitor Supernova SN 2001ke”. In: *ApJ* 582.2 (Jan. 2003), pp. 924–932. DOI: [10.1086/344785](https://doi.org/10.1086/344785). arXiv: [astro-ph/0204234](https://arxiv.org/abs/astro-ph/0204234) [[astro-ph](#)].
- [134] R. Sari and A. A. Esin. “On the Synchrotron Self-Compton Emission from Relativistic Shocks and Its Implications for Gamma-Ray Burst Afterglows”. In: *ApJ* 548.2 (Feb. 2001), pp. 787–799. DOI: [10.1086/319003](https://doi.org/10.1086/319003). arXiv: [astro-ph/0005253](https://arxiv.org/abs/astro-ph/0005253) [[astro-ph](#)].
- [135] M. Ackermann et al. “Fermi-LAT Observations of the Gamma-Ray Burst GRB 130427A”. In: *Science* 343.6166 (Jan. 2014), pp. 42–47. DOI: [10.1126/science.1242353](https://doi.org/10.1126/science.1242353). arXiv: [1311.5623](https://arxiv.org/abs/1311.5623) [[astro-ph.HE](#)].
- [136] V. A. Acciari et al. “VERITAS Observations of Gamma-Ray Bursts Detected by Swift”. In: *ApJ* 743.1, 62 (Dec. 2011), p. 62. DOI: [10.1088/0004-637X/743/1/62](https://doi.org/10.1088/0004-637X/743/1/62). arXiv: [1109.0050](https://arxiv.org/abs/1109.0050) [[astro-ph.HE](#)].
- [137] O. S. Salafia et al. “Multiwavelength View of the Close-by GRB 190829A Sheds Light on Gamma-Ray Burst Physics”. In: *ApJ* 931.2, L19 (June 2022), p. L19. DOI: [10.3847/2041-8213/ac6c28](https://doi.org/10.3847/2041-8213/ac6c28). arXiv: [2106.07169](https://arxiv.org/abs/2106.07169) [[astro-ph.HE](#)].

- [138] L.-L. Zhang et al. “Nearby SN-associated GRB 190829A: Environment, Jet Structure, and VHE Gamma-Ray Afterglows”. In: *ApJ* 917.2, 95 (Aug. 2021), p. 95. DOI: [10.3847/1538-4357/ac0c7f](https://doi.org/10.3847/1538-4357/ac0c7f). arXiv: [2106.03466](https://arxiv.org/abs/2106.03466) [[astro-ph.HE](#)].
- [139] N. Fraija et al. “On the Origin of the Multi-GeV Photons from the Closest Burst with Intermediate Luminosity: GRB 190829A”. In: *ApJ* 918.1, 12 (Sept. 2021), p. 12. DOI: [10.3847/1538-4357/ac0aed](https://doi.org/10.3847/1538-4357/ac0aed). arXiv: [2003.11252](https://arxiv.org/abs/2003.11252) [[astro-ph.HE](#)].
- [140] X.-Y. Wang, Z. Li, and P. Mészáros. “GeV-TeV and X-Ray Flares from Gamma-Ray Bursts”. In: *ApJ* 641.2 (Apr. 2006), pp. L89–L92. DOI: [10.1086/504151](https://doi.org/10.1086/504151). arXiv: [astro-ph/0601229](https://arxiv.org/abs/astro-ph/0601229) [[astro-ph](#)].
- [141] K. Toma, X.-F. Wu, and P. Mészáros. “An Up-Scattered Cocoon Emission Model of Gamma-Ray Burst High-Energy Lags”. In: *ApJ* 707.2 (Dec. 2009), pp. 1404–1416. DOI: [10.1088/0004-637X/707/2/1404](https://doi.org/10.1088/0004-637X/707/2/1404). arXiv: [0905.1697](https://arxiv.org/abs/0905.1697) [[astro-ph.HE](#)].
- [142] R. A. M. J. Wijers and T. J. Galama. “Physical Parameters of GRB 970508 and GRB 971214 from Their Afterglow Synchrotron Emission”. In: *ApJ* 523.1 (Sept. 1999), pp. 177–186. DOI: [10.1086/307705](https://doi.org/10.1086/307705). arXiv: [astro-ph/9805341](https://arxiv.org/abs/astro-ph/9805341) [[astro-ph](#)].
- [143] A. Panaitescu and P. Kumar. “Analytic Light Curves of Gamma-Ray Burst Afterglows: Homogeneous versus Wind External Media”. In: *ApJ* 543.1 (Nov. 2000), pp. 66–76. DOI: [10.1086/317090](https://doi.org/10.1086/317090). arXiv: [astro-ph/0003246](https://arxiv.org/abs/astro-ph/0003246) [[astro-ph](#)].
- [144] P. Mészáros. “Gamma-ray bursts”. In: *Reports on Progress in Physics* 69.8 (Aug. 2006), pp. 2259–2321. DOI: [10.1088/0034-4885/69/8/R01](https://doi.org/10.1088/0034-4885/69/8/R01). arXiv: [astro-ph/0605208](https://arxiv.org/abs/astro-ph/0605208) [[astro-ph](#)].
- [145] G. B. Rybicki and A. P. Lightman. *Radiative processes in astrophysics*. 1979.
- [146] M. S. Longair. *High Energy Astrophysics*. 2011.
- [147] G. Ghisellini. *Radiative Processes in High Energy Astrophysics*. Vol. 873. 2013. DOI: [10.1007/978-3-319-00612-3](https://doi.org/10.1007/978-3-319-00612-3).
- [148] R. D. Blandford and C. F. McKee. “Fluid dynamics of relativistic blast waves”. In: *Physics of Fluids* 19 (Aug. 1976), pp. 1130–1138. DOI: [10.1063/1.861619](https://doi.org/10.1063/1.861619).
- [149] R. A. Chevalier and Z.-Y. Li. “Wind Interaction Models for Gamma-Ray Burst Afterglows: The Case for Two Types of Progenitors”. In: *ApJ* 536.1 (June 2000), pp. 195–212. DOI: [10.1086/308914](https://doi.org/10.1086/308914). arXiv: [astro-ph/9908272](https://arxiv.org/abs/astro-ph/9908272) [[astro-ph](#)].
- [150] J. Granot and R. Sari. “The Shape of Spectral Breaks in Gamma-Ray Burst Afterglows”. In: *ApJ* 568.2 (Apr. 2002), pp. 820–829. DOI: [10.1086/338966](https://doi.org/10.1086/338966). arXiv: [astro-ph/0108027](https://arxiv.org/abs/astro-ph/0108027) [[astro-ph](#)].
- [151] S. Kobayashi and B. Zhang. “GRB 021004: Reverse Shock Emission”. In: *ApJ* 582.2 (Jan. 2003), pp. L75–L78. DOI: [10.1086/367691](https://doi.org/10.1086/367691). arXiv: [astro-ph/0210584](https://arxiv.org/abs/astro-ph/0210584) [[astro-ph](#)].
- [152] D. W. Fox et al. “Discovery of Early Optical Emission from GRB 021211”. In: *ApJ* 586.1 (Mar. 2003), pp. L5–L8. DOI: [10.1086/374683](https://doi.org/10.1086/374683). arXiv: [astro-ph/0301377](https://arxiv.org/abs/astro-ph/0301377) [[astro-ph](#)].
- [153] A. M. Soderberg et al. “The Afterglow, Energetics, and Host Galaxy of the Short-Hard Gamma-Ray Burst 051221a”. In: *ApJ* 650.1 (Oct. 2006), pp. 261–271. DOI: [10.1086/506429](https://doi.org/10.1086/506429). arXiv: [astro-ph/0601455](https://arxiv.org/abs/astro-ph/0601455) [[astro-ph](#)].
- [154] J. Japelj et al. “Phenomenology of Reverse-shock Emission in the Optical Afterglows of Gamma-Ray Bursts”. In: *ApJ* 785.2, 84 (Apr. 2014), p. 84. DOI: [10.1088/0004-637X/785/2/84](https://doi.org/10.1088/0004-637X/785/2/84). arXiv: [1402.3701](https://arxiv.org/abs/1402.3701) [[astro-ph.HE](#)].
- [155] A. Gomboc et al. “Multiwavelength Analysis of the Intriguing GRB 061126: The Reverse Shock Scenario and Magnetization”. In: *ApJ* 687.1 (Nov. 2008), pp. 443–455. DOI: [10.1086/592062](https://doi.org/10.1086/592062). arXiv: [0804.1727](https://arxiv.org/abs/0804.1727) [[astro-ph](#)].

- [156] J. S. Bloom et al. “Observations of the Naked-Eye GRB 080319B: Implications of Nature’s Brightest Explosion”. In: *ApJ* 691.1 (Jan. 2009), pp. 723–737. DOI: [10.1088/0004-637X/691/1/723](https://doi.org/10.1088/0004-637X/691/1/723). arXiv: [0803.3215](https://arxiv.org/abs/0803.3215) [astro-ph].
- [157] Z.-P. Jin et al. “GRB 081007 and GRB 090424: The Surrounding Medium, Outflows, and Supernovae”. In: *ApJ* 774.2, 114 (Sept. 2013), p. 114. DOI: [10.1088/0004-637X/774/2/114](https://doi.org/10.1088/0004-637X/774/2/114). arXiv: [1306.4585](https://arxiv.org/abs/1306.4585) [astro-ph.HE].
- [158] T. Laskar et al. “A Reverse Shock in GRB 130427A”. In: *ApJ* 776.2, 119 (Oct. 2013), p. 119. DOI: [10.1088/0004-637X/776/2/119](https://doi.org/10.1088/0004-637X/776/2/119). arXiv: [1305.2453](https://arxiv.org/abs/1305.2453) [astro-ph.HE].
- [159] T. Laskar et al. “First ALMA Light Curve Constrains Refreshed Reverse Shocks and Jet Magnetization in GRB 161219B”. In: *ApJ* 862.2, 94 (Aug. 2018), p. 94. DOI: [10.3847/1538-4357/aacbcc](https://doi.org/10.3847/1538-4357/aacbcc). arXiv: [1808.09476](https://arxiv.org/abs/1808.09476) [astro-ph.HE].
- [160] T. Laskar et al. “A Reverse Shock in GRB 181201A”. In: *ApJ* 884.2, 121 (Oct. 2019), p. 121. DOI: [10.3847/1538-4357/ab40ce](https://doi.org/10.3847/1538-4357/ab40ce). arXiv: [1907.13128](https://arxiv.org/abs/1907.13128) [astro-ph.HE].
- [161] P. Mészáros and M. J. Rees. “Optical and Long-Wavelength Afterglow from Gamma-Ray Bursts”. In: *ApJ* 476.1 (Feb. 1997), pp. 232–237. DOI: [10.1086/303625](https://doi.org/10.1086/303625). arXiv: [astro-ph/9606043](https://arxiv.org/abs/astro-ph/9606043) [astro-ph].
- [162] R. Sari and T. Piran. “Predictions for the Very Early Afterglow and the Optical Flash”. In: *ApJ* 520.2 (Aug. 1999), pp. 641–649. DOI: [10.1086/307508](https://doi.org/10.1086/307508). arXiv: [astro-ph/9901338](https://arxiv.org/abs/astro-ph/9901338) [astro-ph].
- [163] H. Gao and P. Mészáros. “Reverse Shock Emission in Gamma-Ray Bursts Revisited”. In: *Advances in Astronomy* 2015, 192383 (Jan. 2015), p. 192383. DOI: [10.1155/2015/192383](https://doi.org/10.1155/2015/192383). arXiv: [1507.01984](https://arxiv.org/abs/1507.01984) [astro-ph.HE].
- [164] S. Kobayashi. “Light Curves of Gamma-Ray Burst Optical Flashes”. In: *ApJ* 545.2 (Dec. 2000), pp. 807–812. DOI: [10.1086/317869](https://doi.org/10.1086/317869). arXiv: [astro-ph/0009319](https://arxiv.org/abs/astro-ph/0009319) [astro-ph].
- [165] Y. C. Zou, X. F. Wu, and Z. G. Dai. “Early afterglows in wind environments revisited”. In: *MNRAS* 363.1 (Oct. 2005), pp. 93–106. DOI: [10.1111/j.1365-2966.2005.09411.x](https://doi.org/10.1111/j.1365-2966.2005.09411.x). arXiv: [astro-ph/0508602](https://arxiv.org/abs/astro-ph/0508602) [astro-ph].
- [166] O. S. Salafia and G. Ghirlanda. “The Structure of Gamma Ray Burst Jets”. In: *Galaxies* 10.5 (Aug. 2022), p. 93. DOI: [10.3390/galaxies10050093](https://doi.org/10.3390/galaxies10050093).
- [167] D. A. Frail et al. “Beaming in Gamma-Ray Bursts: Evidence for a Standard Energy Reservoir”. In: *ApJ* 562.1 (Nov. 2001), pp. L55–L58. DOI: [10.1086/338119](https://doi.org/10.1086/338119). arXiv: [astro-ph/0102282](https://arxiv.org/abs/astro-ph/0102282) [astro-ph].
- [168] E. Berger, S. R. Kulkarni, and D. A. Frail. “A Standard Kinetic Energy Reservoir in Gamma-Ray Burst Afterglows”. In: *ApJ* 590.1 (June 2003), pp. 379–385. DOI: [10.1086/374892](https://doi.org/10.1086/374892). arXiv: [astro-ph/0301268](https://arxiv.org/abs/astro-ph/0301268) [astro-ph].
- [169] W. Fong et al. “A Decade of Short-duration Gamma-Ray Burst Broadband Afterglows: Energetics, Circumburst Densities, and Jet Opening Angles”. In: *ApJ* 815.2, 102 (Dec. 2015), p. 102. DOI: [10.1088/0004-637X/815/2/102](https://doi.org/10.1088/0004-637X/815/2/102). arXiv: [1509.02922](https://arxiv.org/abs/1509.02922) [astro-ph.HE].
- [170] J. J. Condon and S. M. Ransom. *Essential Radio Astronomy*. 2016.
- [171] *Synthesis Imaging in Radio Astronomy II*. Vol. 180. Astronomical Society of the Pacific Conference Series. Jan. 1999.
- [172] J. E. Noordam. “The measurement equation of a generic radio telescope, AIPS++ implementation note nr 185”. In: *Tech. Rep.* (1996).
- [173] S. T. Myers, J. Ott, and N. Elias. *CASA Synthesis & Single Dish Reduction Cookbook, Release 3.0.2*. 2010.

- [174] A. R. Thompson et al. “The Very Large Array.” In: *ApJS* 44 (Oct. 1980), pp. 151–167. DOI: [10.1086/190688](https://doi.org/10.1086/190688).
- [175] R. Perley et al. “The Expanded Very Large Array”. In: *IEEE Proceedings* 97.8 (Aug. 2009), pp. 1448–1462. DOI: [10.1109/JPROC.2009.2015470](https://doi.org/10.1109/JPROC.2009.2015470). arXiv: [0909.1585](https://arxiv.org/abs/0909.1585) [[astro-ph.IM](#)].
- [176] J. Jonas and MeerKAT Team. “The MeerKAT Radio Telescope”. In: *MeerKAT Science: On the Pathway to the SKA*. Jan. 2016, 1, p. 1. DOI: [10.22323/1.277.0001](https://doi.org/10.22323/1.277.0001).
- [177] T. Mauch et al. “The 1.28 GHz MeerKAT DEEP2 Image”. In: *ApJ* 888.2, 61 (Jan. 2020), p. 61. DOI: [10.3847/1538-4357/ab5d2d](https://doi.org/10.3847/1538-4357/ab5d2d). arXiv: [1912.06212](https://arxiv.org/abs/1912.06212) [[astro-ph.GA](#)].
- [178] I. Heywood. *oxkat: Semi-automated imaging of MeerKAT observations*. Astrophysics Source Code Library, record ascl:2009.003. Sept. 2020. ascl: [2009.003](https://ascl.net/2009.003).
- [179] A. R. Offringa et al. “WSCLEAN: an implementation of a fast, generic wide-field imager for radio astronomy”. In: *MNRAS* 444.1 (Oct. 2014), pp. 606–619. DOI: [10.1093/mnras/stu1368](https://doi.org/10.1093/mnras/stu1368). arXiv: [1407.1943](https://arxiv.org/abs/1407.1943) [[astro-ph.IM](#)].
- [180] O. Blanch et al. “GRB 201216C: MAGIC detection in very high energy gamma rays”. In: *GRB Coordinates Network* 29075 (Dec. 2020), p. 1.
- [181] H. E. S. S. Collaboration et al. “Revealing x-ray and gamma ray temporal and spectral similarities in the GRB 190829A afterglow”. In: *Science* 372.6546 (June 2021), pp. 1081–1085. DOI: [10.1126/science.abe8560](https://doi.org/10.1126/science.abe8560). arXiv: [2106.02510](https://arxiv.org/abs/2106.02510) [[astro-ph.HE](#)].
- [182] V. D’Elia et al. “GRB 201015A: Swift detection of a burst”. In: *GRB Coordinates Network* 28632 (Oct. 2020), p. 1.
- [183] V. Lipunov et al. “Swift GRB201015.95: Global MASTER-Net OT detection”. In: *GRB Coordinates Network* 28633 (Oct. 2020), p. 1.
- [184] V. Lipunov et al. “Swift GRB 201015A: Global MASTER-Net observations report”. In: *GRB Coordinates Network* 28634 (Oct. 2020), p. 1.
- [185] D. B. Malesani, A. de Ugarte Postigo, and T. Pursimo. “GRB 201015A: NOT optical afterglow confirmation”. In: *GRB Coordinates Network* 28637 (Oct. 2020), p. 1.
- [186] K. Ackley et al. “GRB 201015A: GOTO confirmation of afterglow detection”. In: *GRB Coordinates Network* 28639 (Oct. 2020), p. 1.
- [187] Y.-D. Hu et al. “GRB 201015A: BOOTES-1 early optical afterglow detection”. In: *GRB Coordinates Network* 28645 (Oct. 2020), p. 1.
- [188] A. de Ugarte Postigo et al. “GRB 201015A: Redshift from GTC/OSIRIS”. In: *GRB Coordinates Network* 28649 (Oct. 2020), p. 1.
- [189] Z. P. Zhu et al. “GRB201015A: Nanshan/NEXT early optical observations”. In: *GRB Coordinates Network* 28653 (Oct. 2020), p. 1.
- [190] S. Belkin et al. “GRB 201015A: CrAO/ZTSH optical observations”. In: *GRB Coordinates Network* 28656 (Oct. 2020), p. 1.
- [191] M. Jelinek et al. “GRB 201015A: FRAM-ORM afterglow detection”. In: *GRB Coordinates Network* 28664 (Oct. 2020), p. 1.
- [192] S. Belkin et al. “GRB 201015A: Assy and Mondy optical observations”. In: *GRB Coordinates Network* 28673 (Oct. 2020), p. 1.
- [193] B. Grossan et al. “GRB 201015A NUTTelA-TAO / BSTI Early Measurements (Preliminary)”. In: *GRB Coordinates Network* 28674 (Oct. 2020), p. 1.
- [194] J. Rastinejad et al. “GRB 201015A: MMT afterglow imaging”. In: *GRB Coordinates Network* 28676 (Oct. 2020), p. 1.

- [195] Z. P. Zhu et al. “GRB 201015A: Xinglong-2.16m optical observations”. In: *GRB Coordinates Network* 28677 (Oct. 2020), p. 1.
- [196] H. Kumar et al. “GRB 201015A: HCT optical photometric follow-up”. In: *GRB Coordinates Network* 28680 (Oct. 2020), p. 1.
- [197] A. S. Moskvitin, V. N. Aitov, and GRB follow-up Team. “GRB 201015A: SAO RAS optical observations”. In: *GRB Coordinates Network* 28721 (Oct. 2020), p. 1.
- [198] A. Pozanenko et al. “GRB 201015A: optical observations and supernova identification”. In: *GRB Coordinates Network* 29033 (Dec. 2020), p. 1.
- [199] J. A. Kennea et al. “GRB 201015A: Swift-XRT observations”. In: *GRB Coordinates Network* 28635 (Oct. 2020), p. 1.
- [200] C. Fletcher, P. Veres, and Fermi-GBM Team. “Fermi GBM Sub-Threshold Detection of GRB 201015A”. In: *GRB Coordinates Network* 28663 (Oct. 2020), p. 1.
- [201] B. Gompertz et al. “GRB 201015A: Late X-ray Detections with Chandra”. In: *GRB Coordinates Network* 28822 (Nov. 2020), p. 1.
- [202] V. D’Elia and Swift Team. “GRB 201015A: Swift-XRT late time observations”. In: *GRB Coordinates Network* 28857 (Nov. 2020), p. 1.
- [203] F. E. Marshall, V. D’Elia, and Swift/UVOT Team. “GRB 201015A: Swift/UVOT Detection”. In: *GRB Coordinates Network* 28662 (Oct. 2020), p. 1.
- [204] W. Fong et al. “GRB 201015A: 6 GHz VLA radio afterglow candidate detection”. In: *GRB Coordinates Network* 28688 (Oct. 2020), p. 1.
- [205] S. Giarratana et al. “GRB 201015A radio afterglow with e-MERLIN”. In: *GRB Coordinates Network* 28939 (Nov. 2020), p. 1.
- [206] L. Rhodes et al. “GRB 201015A L-band observations with e-MERLIN”. In: *GRB Coordinates Network* 28945 (Nov. 2020), p. 1.
- [207] O. Blanch et al. “MAGIC observations of GRB 201015A: hint of very high energy gamma-ray signal”. In: *GRB Coordinates Network* 28659 (Oct. 2020), p. 1.
- [208] Y. Suda et al. “Observation of a relatively low luminosity long duration GRB 201015A by the MAGIC telescopes”. In: *37th International Cosmic Ray Conference*. Mar. 2022, 797, p. 797. DOI: [10.22323/1.395.0797](https://doi.org/10.22323/1.395.0797).
- [209] P. Minaev and A. Pozanenko. “GRB 201015A: classification as long GRB”. In: *GRB Coordinates Network* 28668 (Oct. 2020), p. 1.
- [210] L. Izzo et al. “GRB 201015A: redshift confirmation”. In: *GRB Coordinates Network* 28661 (Oct. 2020), p. 1.
- [211] P. M. Vreeswijk et al. “GRB 180720B: VLT/X-shooter redshift.” In: *GRB Coordinates Network* 22996 (Jan. 2018), p. 1.
- [212] J. Selsing et al. “GRB 190114C: NOT optical counterpart and redshift.” In: *GRB Coordinates Network* 23695 (Jan. 2019), p. 1.
- [213] A. F. Valeev et al. “GRB 190829A: 10.4m GTC spectroscopy”. In: *GRB Coordinates Network* 25565 (Aug. 2019), p. 1.
- [214] J.-B. Vielfaure et al. “GRB 201216C: VLT X-shooter spectroscopy and potential high redshift of a VHE-emitting GRB”. In: *GRB Coordinates Network* 29077 (Dec. 2020), p. 1.
- [215] L. Rhodes et al. “Radio afterglows of very high-energy gamma-ray bursts 190829A and 180720B”. In: *MNRAS* 496.3 (Aug. 2020), pp. 3326–3335. DOI: [10.1093/mnras/staa1715](https://doi.org/10.1093/mnras/staa1715). arXiv: [2004.01538](https://arxiv.org/abs/2004.01538) [[astro-ph.HE](https://arxiv.org/abs/2004.01538)].

- [216] G. Hinshaw et al. “Nine-year Wilkinson Microwave Anisotropy Probe (WMAP) Observations: Cosmological Parameter Results”. In: *ApJS* 208.2, 19 (Oct. 2013), p. 19. DOI: [10.1088/0067-0049/208/2/19](https://doi.org/10.1088/0067-0049/208/2/19). arXiv: [1212.5226](https://arxiv.org/abs/1212.5226) [[astro-ph.CO](#)].
- [217] J. P. McMullin et al. “CASA Architecture and Applications”. In: *Astronomical Data Analysis Software and Systems XVI*. Ed. by R. A. Shaw, F. Hill, and D. J. Bell. Vol. 376. Astronomical Society of the Pacific Conference Series. Oct. 2007, p. 127.
- [218] A. Keimpema et al. “The SFXC software correlator for very long baseline interferometry: algorithms and implementation”. In: *Experimental Astronomy* 39.2 (June 2015), pp. 259–279. DOI: [10.1007/s10686-015-9446-1](https://doi.org/10.1007/s10686-015-9446-1). arXiv: [1502.00467](https://arxiv.org/abs/1502.00467) [[astro-ph.IM](#)].
- [219] E. W. Greisen. “AIPS, the VLA, and the VLBA”. In: *Information Handling in Astronomy - Historical Vistas*. Ed. by André Heck. Vol. 285. Astrophysics and Space Science Library. Mar. 2003, p. 109. DOI: [10.1007/0-306-48080-8_7](https://doi.org/10.1007/0-306-48080-8_7).
- [220] M. C. Shepherd, T. J. Pearson, and G. B. Taylor. “DIFMAP: an interactive program for synthesis imaging.” In: *Bulletin of the American Astronomical Society*. Vol. 26. May 1994, pp. 987–989.
- [221] D. G. Monet et al. “The USNO-B Catalog”. In: *AJ* 125.2 (Feb. 2003), pp. 984–993. DOI: [10.1086/345888](https://doi.org/10.1086/345888). arXiv: [astro-ph/0210694](https://arxiv.org/abs/astro-ph/0210694) [[astro-ph](#)].
- [222] D. Tody. “IRAF in the Nineties”. In: *Astronomical Data Analysis Software and Systems II*. Ed. by R. J. Hanisch, R. J. V. Brissenden, and J. Barnes. Vol. 52. Astronomical Society of the Pacific Conference Series. Jan. 1993, p. 173.
- [223] A. Becker. *HOTPANTS: High Order Transform of PSF AND Template Subtraction*. Astrophysics Source Code Library, record ascl:1504.004. Apr. 2015. ascl: [1504.004](https://ascl.net/1504.004).
- [224] K. C. Chambers et al. “The Pan-STARRS1 Surveys”. In: *arXiv e-prints*, arXiv:1612.05560 (Dec. 2016), arXiv:1612.05560. DOI: [10.48550/arXiv.1612.05560](https://doi.org/10.48550/arXiv.1612.05560). arXiv: [1612.05560](https://arxiv.org/abs/1612.05560) [[astro-ph.IM](#)].
- [225] E. F. Schlafly and D. P. Finkbeiner. “Measuring Reddening with Sloan Digital Sky Survey Stellar Spectra and Recalibrating SFD”. In: *ApJ* 737.2, 103 (Aug. 2011), p. 103. DOI: [10.1088/0004-637X/737/2/103](https://doi.org/10.1088/0004-637X/737/2/103). arXiv: [1012.4804](https://arxiv.org/abs/1012.4804) [[astro-ph.GA](#)].
- [226] P. A. Evans et al. “An online repository of Swift/XRT light curves of γ -ray bursts”. In: *A&A* 469.1 (July 2007), pp. 379–385. DOI: [10.1051/0004-6361:20077530](https://doi.org/10.1051/0004-6361:20077530). arXiv: [0704.0128](https://arxiv.org/abs/0704.0128) [[astro-ph](#)].
- [227] P. A. Evans et al. “Methods and results of an automatic analysis of a complete sample of Swift-XRT observations of GRBs”. In: *MNRAS* 397.3 (Aug. 2009), pp. 1177–1201. DOI: [10.1111/j.1365-2966.2009.14913.x](https://doi.org/10.1111/j.1365-2966.2009.14913.x). arXiv: [0812.3662](https://arxiv.org/abs/0812.3662) [[astro-ph](#)].
- [228] A. J. Beasley et al. “The VLBA Calibrator Survey-VCS1”. In: *ApJS* 141.1 (July 2002), pp. 13–21. DOI: [10.1086/339806](https://doi.org/10.1086/339806). arXiv: [astro-ph/0201414](https://arxiv.org/abs/astro-ph/0201414) [[astro-ph](#)].
- [229] D. Gordon et al. “Second Epoch VLBA Calibrator Survey Observations: VCS-II”. In: *AJ* 151.6, 154 (June 2016), p. 154. DOI: [10.3847/0004-6256/151/6/154](https://doi.org/10.3847/0004-6256/151/6/154).
- [230] N. Pradel, P. Charlot, and J. -F. Lestrade. “Astrometric accuracy of phase-referenced observations with the VLBA and EVN”. In: *A&A* 452.3 (June 2006), pp. 1099–1106. DOI: [10.1051/0004-6361:20053021](https://doi.org/10.1051/0004-6361:20053021). arXiv: [astro-ph/0603015](https://arxiv.org/abs/astro-ph/0603015) [[astro-ph](#)].
- [231] H. Kumar et al. “GRB 201015A: GROWTH-India Telescope (GIT) upper limit”. In: *GRB Coordinates Network* 28681 (Oct. 2020), p. 1.
- [232] A. Rossi et al. “GRB 201015A: evidence of supernova in LBT spectra”. In: *GRB Coordinates Network* 29306 (Jan. 2021), p. 1.

- [233] P. M. W. Kalberla et al. “The Leiden/Argentine/Bonn (LAB) Survey of Galactic HI. Final data release of the combined LDS and IAR surveys with improved stray-radiation corrections”. In: *A&A* 440.2 (Sept. 2005), pp. 775–782. DOI: [10.1051/0004-6361:20041864](https://doi.org/10.1051/0004-6361:20041864). arXiv: [astro-ph/0504140](https://arxiv.org/abs/astro-ph/0504140) [[astro-ph](#)].
- [234] R. Willingale et al. “Calibration of X-ray absorption in our Galaxy”. In: *MNRAS* 431.1 (May 2013), pp. 394–404. DOI: [10.1093/mnras/stt175](https://doi.org/10.1093/mnras/stt175). arXiv: [1303.0843](https://arxiv.org/abs/1303.0843) [[astro-ph.HE](#)].
- [235] J. Wilms, A. Allen, and R. McCray. “On the Absorption of X-Rays in the Interstellar Medium”. In: *ApJ* 542.2 (Oct. 2000), pp. 914–924. DOI: [10.1086/317016](https://doi.org/10.1086/317016). arXiv: [astro-ph/0008425](https://arxiv.org/abs/astro-ph/0008425) [[astro-ph](#)].
- [236] A. D’Ai et al. “GRB 201015A: Swift-XRT refined Analysis”. In: *GRB Coordinates Network* 28660 (Oct. 2020), p. 1.
- [237] M. D. Aksulu et al. “Exploring the GRB population: robust afterglow modelling”. In: *MNRAS* 511.2 (Apr. 2022), pp. 2848–2867. DOI: [10.1093/mnras/stac246](https://doi.org/10.1093/mnras/stac246). arXiv: [2106.14921](https://arxiv.org/abs/2106.14921) [[astro-ph.HE](#)].
- [238] D. A. Kann, S. Klose, and A. Zeh. “Signatures of Extragalactic Dust in Pre-Swift GRB Afterglows”. In: *ApJ* 641.2 (Apr. 2006), pp. 993–1009. DOI: [10.1086/500652](https://doi.org/10.1086/500652). arXiv: [astro-ph/0512575](https://arxiv.org/abs/astro-ph/0512575) [[astro-ph](#)].
- [239] B. Zhang and P. Mészáros. “High-Energy Spectral Components in Gamma-Ray Burst Afterglows”. In: *ApJ* 559.1 (Sept. 2001), pp. 110–122. DOI: [10.1086/322400](https://doi.org/10.1086/322400). arXiv: [astro-ph/0103229](https://arxiv.org/abs/astro-ph/0103229) [[astro-ph](#)].
- [240] D. Eichler and E. Waxman. “The Efficiency of Electron Acceleration in Collisionless Shocks and Gamma-Ray Burst Energetics”. In: *ApJ* 627.2 (July 2005), pp. 861–867. DOI: [10.1086/430596](https://doi.org/10.1086/430596). arXiv: [astro-ph/0502070](https://arxiv.org/abs/astro-ph/0502070) [[astro-ph](#)].
- [241] L. Sironi, A. Spitkovsky, and J. Arons. “The Maximum Energy of Accelerated Particles in Relativistic Collisionless Shocks”. In: *ApJ* 771.1, 54 (July 2013), p. 54. DOI: [10.1088/0004-637X/771/1/54](https://doi.org/10.1088/0004-637X/771/1/54). arXiv: [1301.5333](https://arxiv.org/abs/1301.5333) [[astro-ph.HE](#)].
- [242] T. Laskar et al. “A Reverse Shock in GRB 160509A”. In: *ApJ* 833.1, 88 (Dec. 2016), p. 88. DOI: [10.3847/1538-4357/833/1/88](https://doi.org/10.3847/1538-4357/833/1/88). arXiv: [1606.08873](https://arxiv.org/abs/1606.08873) [[astro-ph.HE](#)].
- [243] X.-Y. Wang et al. “Synchrotron Self-Compton Emission from External Shocks as the Origin of the Sub-TeV Emission in GRB 180720B and GRB 190114C”. In: *ApJ* 884.2, 117 (Oct. 2019), p. 117. DOI: [10.3847/1538-4357/ab426c](https://doi.org/10.3847/1538-4357/ab426c). arXiv: [1905.11312](https://arxiv.org/abs/1905.11312) [[astro-ph.HE](#)].
- [244] K. Misra et al. “Low frequency view of GRB 190114C reveals time varying shock microphysics”. In: *MNRAS* 504.4 (July 2021), pp. 5685–5701. DOI: [10.1093/mnras/stab1050](https://doi.org/10.1093/mnras/stab1050). arXiv: [1911.09719](https://arxiv.org/abs/1911.09719) [[astro-ph.HE](#)].
- [245] N. Fraija et al. “Modeling the Observations of GRB 180720B: from Radio to Sub-TeV Gamma-Rays”. In: *ApJ* 885.1, 29 (Nov. 2019), p. 29. DOI: [10.3847/1538-4357/ab3e4b](https://doi.org/10.3847/1538-4357/ab3e4b). arXiv: [1905.13572](https://arxiv.org/abs/1905.13572) [[astro-ph.HE](#)].
- [246] T. Laskar et al. “ALMA Detection of a Linearly Polarized Reverse Shock in GRB 190114C”. In: *ApJ* 878.1, L26 (June 2019), p. L26. DOI: [10.3847/2041-8213/ab2247](https://doi.org/10.3847/2041-8213/ab2247). arXiv: [1904.07261](https://arxiv.org/abs/1904.07261) [[astro-ph.HE](#)].
- [247] A. Kamble, L. Resmi, and K. Misra. “Observations of the Optical Afterglow of GRB 050319: The Wind-to-ISM Transition in View”. In: *ApJ* 664.1 (July 2007), pp. L5–L8. DOI: [10.1086/520533](https://doi.org/10.1086/520533). arXiv: [0709.3561](https://arxiv.org/abs/0709.3561) [[astro-ph](#)].
- [248] P. Veres et al. “Early-time VLA Observations and Broadband Afterglow Analysis of the Fermi/LAT Detected GRB 130907A”. In: *ApJ* 810.1, 31 (Sept. 2015), p. 31. DOI: [10.1088/0004-637X/810/1/31](https://doi.org/10.1088/0004-637X/810/1/31). arXiv: [1411.7368](https://arxiv.org/abs/1411.7368) [[astro-ph.HE](#)].

- [249] G. B. Taylor et al. “The Angular Size and Proper Motion of the Afterglow of GRB 030329”. In: *ApJ* 609.1 (July 2004), pp. L1–L4. DOI: [10.1086/422554](https://doi.org/10.1086/422554). arXiv: [astro-ph/0405300](https://arxiv.org/abs/astro-ph/0405300) [[astro-ph](#)].
- [250] P. Veres et al. “GRB 221009A: Fermi GBM detection of an extraordinarily bright GRB”. In: *GRB Coordinates Network* 32636 (Oct. 2022).
- [251] E. Bissaldi et al. “GRB 221009A or Swift J1913.1+1946: Fermi-LAT detection”. In: *GRB Coordinates Network* 32637 (Oct. 2022), p. 1.
- [252] A. Ursi et al. “GRB 221009A (Swift J1913.1+1946): AGILE/MCAL detection”. In: *GRB Coordinates Network* 32650 (Oct. 2022), p. 1.
- [253] G. Piano et al. “GRB 221009A (Swift J1913.1+1946): AGILE/GRID detection”. In: *GRB Coordinates Network* 32657 (Oct. 2022), p. 1.
- [254] D. Gotz et al. “GRB221009A/Swift J1913.1+1946: INTEGRAL SPI/ACS observations”. In: *GRB Coordinates Network* 32660 (Oct. 2022), p. 1.
- [255] D. Frederiks et al. “Konus-Wind detection of GRB 221009A”. In: *GRB Coordinates Network* 32668 (Oct. 2022).
- [256] W. J. Tan et al. “Insight-HXMT observation of GRB221009A/Swift J1913.1+1946”. In: *The Astronomer’s Telegram* 15660 (Oct. 2022), p. 1.
- [257] L. J. Mitchell, B. F. Philips, and W. N. Johnson. “GRB 221009A: Gamma-ray Detection by SIRI-2”. In: *GRB Coordinates Network* 32746 (Oct. 2022), p. 1.
- [258] J. C. Liu et al. “GRB 221009A: HEBS detection”. In: *GRB Coordinates Network* 32751 (Oct. 2022), p. 1.
- [259] I. Lapshov et al. “GRB221009A/Swift J1913.1+1946: SRG/ART-XC observation”. In: *GRB Coordinates Network* 32663 (Oct. 2022), p. 1.
- [260] H. Xiao, S. Krucker, and R. Daniel. “GRB221009A/Swift J1913.1+1946: Solar Orbiter STIX measurements.” In: *GRB Coordinates Network* 32661 (Jan. 2022), p. 1.
- [261] J. Ripa et al. “GRB 221009A: Detection by GRBAlpha”. In: *GRB Coordinates Network* 32685 (Oct. 2022), p. 1.
- [262] S. Dichiara et al. “Swift J1913.1+1946 a new bright hard X-ray and optical transient”. In: *GRB Coordinates Network* 32632 (Oct. 2022).
- [263] J. A. Kennea, M. Williams, and Swift Team. “GRB 221009A: Swift detected transient may be GRB”. In: *GRB Coordinates Network* 32635 (Oct. 2022), p. 1.
- [264] A. de Ugarte Postigo et al. “GRB 221009A: Redshift from X-shooter/VLT”. In: *GRB Coordinates Network* 32648 (Oct. 2022).
- [265] D. B. Malesani et al. “The brightest GRB ever detected: GRB 221009A as a highly luminous event at $z = 0.151$ ”. In: *arXiv e-prints*, arXiv:2302.07891 (Feb. 2023), arXiv:2302.07891. DOI: [10.48550/arXiv.2302.07891](https://doi.org/10.48550/arXiv.2302.07891). arXiv: [2302.07891](https://arxiv.org/abs/2302.07891) [[astro-ph.HE](#)].
- [266] S. Lesage et al. “Fermi-GBM Discovery of GRB 221009A: An Extraordinarily Bright GRB from Onset to Afterglow”. In: *ApJ* 952.2, L42 (Aug. 2023), p. L42. DOI: [10.3847/2041-8213/ace5b4](https://doi.org/10.3847/2041-8213/ace5b4).
- [267] B. O’Connor et al. “A structured jet explains the extreme GRB 221009A”. In: *Science Advances* 9.23, eadi1405 (June 2023), eadi1405. DOI: [10.1126/sciadv.adi1405](https://doi.org/10.1126/sciadv.adi1405). arXiv: [2302.07906](https://arxiv.org/abs/2302.07906) [[astro-ph.HE](#)].
- [268] E. Burns et al. “GRB 221009A: The Boat”. In: *ApJ* 946.1, L31 (Mar. 2023), p. L31. DOI: [10.3847/2041-8213/acc39c](https://doi.org/10.3847/2041-8213/acc39c).

- [269] LHAASO Collaboration et al. “A tera-electron volt afterglow from a narrow jet in an extremely bright gamma-ray burst.” In: *Science* 380.6652 (June 2023), pp. 1390–1396. DOI: [10.1126/science.adg9328](https://doi.org/10.1126/science.adg9328).
- [270] J. S. Bright et al. “Precise measurements of self-absorbed rising reverse shock emission from gamma-ray burst 221009A”. In: *Nature Astronomy* 7 (Aug. 2023), pp. 986–995. DOI: [10.1038/s41550-023-01997-9](https://doi.org/10.1038/s41550-023-01997-9).
- [271] J. Ren et al. “The Possibility of Modeling the Very High Energy Afterglow of GRB 221009A in a Wind Environment”. In: *ApJ* 947.2, 53 (Apr. 2023), p. 53. DOI: [10.3847/1538-4357/acc57d](https://doi.org/10.3847/1538-4357/acc57d). arXiv: [2210.10673](https://arxiv.org/abs/2210.10673) [[astro-ph.HE](#)].
- [272] Y. Sato et al. “Two-component jet model for multiwavelength afterglow emission of the extremely energetic burst GRB 221009A”. In: *MNRAS* 522.1 (June 2023), pp. L56–L60. DOI: [10.1093/mnras/slاد038](https://doi.org/10.1093/mnras/slاد038). arXiv: [2212.09266](https://arxiv.org/abs/2212.09266) [[astro-ph.HE](#)].
- [273] T. Laskar et al. “The Radio to GeV Afterglow of GRB 221009A”. In: *ApJ* 946.1, L23 (Mar. 2023), p. L23. DOI: [10.3847/2041-8213/acbfad](https://doi.org/10.3847/2041-8213/acbfad). arXiv: [2302.04388](https://arxiv.org/abs/2302.04388) [[astro-ph.HE](#)].
- [274] R. Gill and J. Granot. “GRB 221009A afterglow from a shallow angular structured jet”. In: *MNRAS* 524.1 (Sept. 2023), pp. L78–L83. DOI: [10.1093/mnras/slاد075](https://doi.org/10.1093/mnras/slاد075). arXiv: [2304.14331](https://arxiv.org/abs/2304.14331) [[astro-ph.HE](#)].
- [275] G. B. Taylor et al. “Late-Time Observations of the Afterglow and Environment of GRB 030329”. In: *ApJ* 622.2 (Apr. 2005), pp. 986–990. DOI: [10.1086/428346](https://doi.org/10.1086/428346). arXiv: [astro-ph/0412483](https://arxiv.org/abs/astro-ph/0412483) [[astro-ph](#)].
- [276] F. Nappo et al. “The 999th Swift gamma-ray burst: Some like it thermal. A multiwavelength study of GRB 151027A”. In: *A&A* 598, A23 (Feb. 2017), A23. DOI: [10.1051/0004-6361/201628801](https://doi.org/10.1051/0004-6361/201628801). arXiv: [1604.08204](https://arxiv.org/abs/1604.08204) [[astro-ph.HE](#)].
- [277] S. Giarratana et al. “VLBI observations of GRB 201015A, a relatively faint GRB with a hint of very high-energy gamma-ray emission”. In: *A&A* 664, A36 (Aug. 2022), A36. DOI: [10.1051/0004-6361/202142919](https://doi.org/10.1051/0004-6361/202142919). arXiv: [2205.12750](https://arxiv.org/abs/2205.12750) [[astro-ph.HE](#)].
- [278] Planck Collaboration et al. “Planck 2018 results. VI. Cosmological parameters”. In: *A&A* 641, A6 (Sept. 2020), A6. DOI: [10.1051/0004-6361/201833910](https://doi.org/10.1051/0004-6361/201833910). arXiv: [1807.06209](https://arxiv.org/abs/1807.06209) [[astro-ph.CO](#)].
- [279] A. T. Deller et al. “DiFX-2: A More Flexible, Efficient, Robust, and Powerful Software Correlator”. In: *PASP* 123.901 (Mar. 2011), p. 275. DOI: [10.1086/658907](https://doi.org/10.1086/658907). arXiv: [1101.0885](https://arxiv.org/abs/1101.0885) [[astro-ph.IM](#)].
- [280] P. Meszaros and M. J. Rees. “Relativistic Fireballs and Their Impact on External Matter: Models for Cosmological Gamma-Ray Bursts”. In: *ApJ* 405 (Mar. 1993), p. 278. DOI: [10.1086/172360](https://doi.org/10.1086/172360).
- [281] T. Piran, A. Shemi, and R. Narayan. “Hydrodynamics of Relativistic Fireballs”. In: *MNRAS* 263 (Aug. 1993), p. 861. DOI: [10.1093/mnras/263.4.861](https://doi.org/10.1093/mnras/263.4.861). arXiv: [astro-ph/9301004](https://arxiv.org/abs/astro-ph/9301004) [[astro-ph](#)].
- [282] R. Sari and T. Piran. “Hydrodynamic Timescales and Temporal Structure of Gamma-Ray Bursts”. In: *ApJ* 455 (Dec. 1995), p. L143. DOI: [10.1086/309835](https://doi.org/10.1086/309835). arXiv: [astro-ph/9508081](https://arxiv.org/abs/astro-ph/9508081) [[astro-ph](#)].
- [283] S. Kobayashi, T. Piran, and R. Sari. “Hydrodynamics of a Relativistic Fireball: The Complete Evolution”. In: *ApJ* 513.2 (Mar. 1999), pp. 669–678. DOI: [10.1086/306868](https://doi.org/10.1086/306868). arXiv: [astro-ph/9803217](https://arxiv.org/abs/astro-ph/9803217) [[astro-ph](#)].

- [284] S. Kobayashi and B. Zhang. “Early Optical Afterglows from Wind-Type Gamma-Ray Bursts”. In: *ApJ* 597.1 (Nov. 2003), pp. 455–458. DOI: [10.1086/378283](https://doi.org/10.1086/378283). arXiv: [astro-ph/0304086](https://arxiv.org/abs/astro-ph/0304086) [[astro-ph](#)].
- [285] S.-X. Yi, X.-F. Wu, and Z.-G. Dai. “Early Afterglows of Gamma-Ray Bursts in a Stratified Medium with a Power-law Density Distribution”. In: *ApJ* 776.2, 120 (Oct. 2013), p. 120. DOI: [10.1088/0004-637X/776/2/120](https://doi.org/10.1088/0004-637X/776/2/120). arXiv: [1308.6095](https://arxiv.org/abs/1308.6095) [[astro-ph.HE](#)].
- [286] I. Martí-Vidal et al. “Coherence loss in phase-referenced VLBI observations”. In: *A&A* 515, A53 (June 2010), A53. DOI: [10.1051/0004-6361/201014203](https://doi.org/10.1051/0004-6361/201014203). arXiv: [1003.2368](https://arxiv.org/abs/1003.2368) [[astro-ph.IM](#)].
- [287] Y. M. Pihlström et al. “Stirring the Embers: High-Sensitivity VLBI Observations of GRB 030329”. In: *ApJ* 664.1 (July 2007), pp. 411–415. DOI: [10.1086/518955](https://doi.org/10.1086/518955). arXiv: [0704.2085](https://arxiv.org/abs/0704.2085) [[astro-ph](#)].
- [288] J. Ren, Y. Wang, and Z.-G. Dai. “Jet Structure and Burst Environment of GRB 221009A”. In: *arXiv e-prints*, arXiv:2310.15886 (Oct. 2023), arXiv:2310.15886. DOI: [10.48550/arXiv.2310.15886](https://doi.org/10.48550/arXiv.2310.15886). arXiv: [2310.15886](https://arxiv.org/abs/2310.15886) [[astro-ph.HE](#)].
- [289] J. Granot, E. Ramirez-Ruiz, and A. Loeb. “Implications of the Measured Image Size for the Radio Afterglow of GRB 030329”. In: *ApJ* 618.1 (Jan. 2005), pp. 413–425. DOI: [10.1086/425899](https://doi.org/10.1086/425899). arXiv: [astro-ph/0407182](https://arxiv.org/abs/astro-ph/0407182) [[astro-ph](#)].
- [290] D. Foreman-Mackey et al. “emcee: The MCMC Hammer”. In: *PASP* 125.925 (Mar. 2013), p. 306. DOI: [10.1086/670067](https://doi.org/10.1086/670067). arXiv: [1202.3665](https://arxiv.org/abs/1202.3665) [[astro-ph.IM](#)].
- [291] Y. Oren, E. Nakar, and T. Piran. “The apparent size of gamma-ray burst afterglows as a test of the fireball model”. In: *MNRAS* 353.4 (Oct. 2004), pp. L35–L40. DOI: [10.1111/j.1365-2966.2004.08247.x](https://doi.org/10.1111/j.1365-2966.2004.08247.x). arXiv: [astro-ph/0406277](https://arxiv.org/abs/astro-ph/0406277) [[astro-ph](#)].
- [292] P. Kumar and J. Granot. “The Evolution of a Structured Relativistic Jet and Gamma-Ray Burst Afterglow Light Curves”. In: *ApJ* 591.2 (July 2003), pp. 1075–1085. DOI: [10.1086/375186](https://doi.org/10.1086/375186). arXiv: [astro-ph/0303174](https://arxiv.org/abs/astro-ph/0303174) [[astro-ph](#)].
- [293] H. van Eerten, W. Zhang, and A. MacFadyen. “Off-axis Gamma-ray Burst Afterglow Modeling Based on a Two-dimensional Axisymmetric Hydrodynamics Simulation”. In: *ApJ* 722.1 (Oct. 2010), pp. 235–247. DOI: [10.1088/0004-637X/722/1/235](https://doi.org/10.1088/0004-637X/722/1/235). arXiv: [1006.5125](https://arxiv.org/abs/1006.5125) [[astro-ph.HE](#)].
- [294] F. De Colle et al. “Gamma-Ray Burst Dynamics and Afterglow Radiation from Adaptive Mesh Refinement, Special Relativistic Hydrodynamic Simulations”. In: *ApJ* 746.2, 122 (Feb. 2012), p. 122. DOI: [10.1088/0004-637X/746/2/122](https://doi.org/10.1088/0004-637X/746/2/122). arXiv: [1111.6890](https://arxiv.org/abs/1111.6890) [[astro-ph.HE](#)].
- [295] M. Lyutikov. “On the sideways expansion of relativistic non-spherical shocks and gamma-ray burst afterglows”. In: *MNRAS* 421.1 (Mar. 2012), pp. 522–524. DOI: [10.1111/j.1365-2966.2011.20331.x](https://doi.org/10.1111/j.1365-2966.2011.20331.x). arXiv: [1106.0025](https://arxiv.org/abs/1106.0025) [[astro-ph.HE](#)].
- [296] J. Granot and T. Piran. “On the lateral expansion of gamma-ray burst jets”. In: *MNRAS* 421.1 (Mar. 2012), pp. 570–587. DOI: [10.1111/j.1365-2966.2011.20335.x](https://doi.org/10.1111/j.1365-2966.2011.20335.x). arXiv: [1109.6468](https://arxiv.org/abs/1109.6468) [[astro-ph.HE](#)].
- [297] S. Kobayashi and R. Sari. “Optical Flashes and Radio Flares in Gamma-Ray Burst Afterglow: Numerical Study”. In: *ApJ* 542.2 (Oct. 2000), pp. 819–828. DOI: [10.1086/317021](https://doi.org/10.1086/317021). arXiv: [astro-ph/9910241](https://arxiv.org/abs/astro-ph/9910241) [[astro-ph](#)].
- [298] D. McConnell et al. “The Rapid ASKAP Continuum Survey I: Design and first results”. In: *PASA* 37, e048 (Nov. 2020), e048. DOI: [10.1017/pasa.2020.41](https://doi.org/10.1017/pasa.2020.41). arXiv: [2012.00747](https://arxiv.org/abs/2012.00747) [[astro-ph.IM](#)].

- [299] M. Lacy et al. “The Karl G. Jansky Very Large Array Sky Survey (VLASS). Science Case and Survey Design”. In: *PASP* 132.1009, 035001 (Mar. 2020), p. 035001. DOI: [10.1088/1538-3873/ab63eb](https://doi.org/10.1088/1538-3873/ab63eb). arXiv: [1907.01981](https://arxiv.org/abs/1907.01981) [[astro-ph.IM](#)].
- [300] T. W. Shimwell et al. “The LOFAR Two-metre Sky Survey. I. Survey description and preliminary data release”. In: *A&A* 598, A104 (Feb. 2017), A104. DOI: [10.1051/0004-6361/201629313](https://doi.org/10.1051/0004-6361/201629313). arXiv: [1611.02700](https://arxiv.org/abs/1611.02700) [[astro-ph.IM](#)].
- [301] Fermi GBM Team. “GRB 200716C: Fermi GBM Final Real-time Localization”. In: *GRB Coordinates Network* 28123 (July 2020), p. 1.
- [302] P. Veres, C. Meegan, and Fermi GBM Team. “GRB 200716C: Fermi GBM detection”. In: *GRB Coordinates Network* 28135 (July 2020), p. 1.
- [303] T. N. Ukwatta et al. “GRB 200716C: Swift detection of a burst with an optical counterpart”. In: *GRB Coordinates Network* 28124 (July 2020), p. 1.
- [304] A. Ursi et al. “GRB 200716C: AGILE/MCAL detection”. In: *GRB Coordinates Network* 28133 (July 2020), p. 1.
- [305] S. Torii et al. “GRB 200716C: CALET Gamma-Ray Burst Monitor detection”. In: *GRB Coordinates Network* 28139 (July 2020), p. 1.
- [306] W. C. Xue et al. “GRB 200716C: Insight-HXMT/HE detection”. In: *GRB Coordinates Network* 28145 (July 2020), p. 1.
- [307] D. Frederiks et al. “Konus-Wind observation of GRB 200716C”. In: *GRB Coordinates Network* 28147 (July 2020), p. 1.
- [308] P. D’Avanzo and CIBO Collaboration. “GRB 200716C: possible host galaxy from the SDSS”. In: *GRB Coordinates Network* 28132 (July 2020), p. 1.
- [309] B. Kumar et al. “GRB 200716C: Optical observations from HCT”. In: *GRB Coordinates Network* 28138 (July 2020), p. 1.
- [310] A. Pozanenko et al. “GRB 200716C: CrAO, Terskol, Assy-Turgen optical observations”. In: *GRB Coordinates Network* 28151 (July 2020), p. 1.
- [311] D. A. Kann et al. “GRB 200716C: CAHA optical observation // Anomalous light curve behavior?” In: *GRB Coordinates Network* 28152 (July 2020), p. 1.
- [312] Y. Wang et al. “GRB 200716C: Evidence for a Short Burst Being Lensed”. In: *ApJ* 918.2, L34 (Sept. 2021), p. L34. DOI: [10.3847/2041-8213/ac1ff9](https://doi.org/10.3847/2041-8213/ac1ff9). arXiv: [2107.10796](https://arxiv.org/abs/2107.10796) [[astro-ph.HE](#)].
- [313] X. Yang et al. “Evidence for Gravitational Lensing of GRB 200716C”. In: *ApJ* 921.2, L29 (Nov. 2021), p. L29. DOI: [10.3847/2041-8213/ac2f39](https://doi.org/10.3847/2041-8213/ac2f39). arXiv: [2107.11050](https://arxiv.org/abs/2107.11050) [[astro-ph.HE](#)].
- [314] J. K. Adelman-McCarthy et al. “The Sixth Data Release of the Sloan Digital Sky Survey”. In: *ApJS* 175.2 (Apr. 2008), pp. 297–313. DOI: [10.1086/524984](https://doi.org/10.1086/524984). arXiv: [0707.3413](https://arxiv.org/abs/0707.3413) [[astro-ph](#)].
- [315] M. J. Hardcastle et al. “LOFAR/H-ATLAS: a deep low-frequency survey of the Herschel-ATLAS North Galactic Pole field”. In: *MNRAS* 462.2 (Oct. 2016), pp. 1910–1936. DOI: [10.1093/mnras/stw1763](https://doi.org/10.1093/mnras/stw1763). arXiv: [1606.09437](https://arxiv.org/abs/1606.09437) [[astro-ph.GA](#)].
- [316] E. L. Wright et al. “The Wide-field Infrared Survey Explorer (WISE): Mission Description and Initial On-orbit Performance”. In: *AJ* 140.6 (Dec. 2010), pp. 1868–1881. DOI: [10.1088/0004-6256/140/6/1868](https://doi.org/10.1088/0004-6256/140/6/1868). arXiv: [1008.0031](https://arxiv.org/abs/1008.0031) [[astro-ph.IM](#)].
- [317] R. H. Becker, R. L. White, and D. J. Helfand. “The FIRST Survey: Faint Images of the Radio Sky at Twenty Centimeters”. In: *ApJ* 450 (Sept. 1995), p. 559. DOI: [10.1086/176166](https://doi.org/10.1086/176166).

- [318] J. J. Condon et al. “The NRAO VLA Sky Survey”. In: *AJ* 115.5 (May 1998), pp. 1693–1716. DOI: [10.1086/300337](https://doi.org/10.1086/300337).
- [319] E. A. K. Adams et al. “First release of Apertif imaging survey data”. In: *arXiv e-prints*, arXiv:2208.05348 (Aug. 2022), arXiv:2208.05348. arXiv: [2208.05348](https://arxiv.org/abs/2208.05348) [[astro-ph.IM](#)].
- [320] J. B. Oke. “Faint Spectrophotometric Standard Stars”. In: *AJ* 99 (May 1990), p. 1621. DOI: [10.1086/115444](https://doi.org/10.1086/115444).
- [321] K. I. Kellermann et al. “VLA Observations of Objects in the Palomar Bright Quasar Survey”. In: *AJ* 98 (Oct. 1989), p. 1195. DOI: [10.1086/115207](https://doi.org/10.1086/115207).
- [322] B. L. Fanaroff and J. M. Riley. “The morphology of extragalactic radio sources of high and low luminosity”. In: *MNRAS* 167 (May 1974), 31P–36P. DOI: [10.1093/mnras/167.1.31P](https://doi.org/10.1093/mnras/167.1.31P).
- [323] R. D. Baldi, A. Capetti, and G. Giovannini. “The new class of FR 0 radio galaxies”. In: *AN* 337.1-2 (Feb. 2016), p. 114. DOI: [10.1002/asna.201512275](https://doi.org/10.1002/asna.201512275). arXiv: [1510.04272](https://arxiv.org/abs/1510.04272) [[astro-ph.GA](#)].
- [324] M. Giroletti, G. Giovannini, and G. B. Taylor. “Low power compact radio galaxies at high angular resolution”. In: *A&A* 441.1 (Oct. 2005), pp. 89–101. DOI: [10.1051/0004-6361:20053347](https://doi.org/10.1051/0004-6361:20053347). arXiv: [astro-ph/0506497](https://arxiv.org/abs/astro-ph/0506497) [[astro-ph](#)].
- [325] R. D. Baldi, A. Capetti, and F. Massaro. “FR0CAT: a FIRST catalog of FR 0 radio galaxies”. In: *A&A* 609, A1 (Jan. 2018), A1. DOI: [10.1051/0004-6361/201731333](https://doi.org/10.1051/0004-6361/201731333). arXiv: [1709.00015](https://arxiv.org/abs/1709.00015) [[astro-ph.GA](#)].
- [326] M. Murgia et al. “Dying radio galaxies in clusters”. In: *A&A* 526, A148 (Feb. 2011), A148. DOI: [10.1051/0004-6361/201015302](https://doi.org/10.1051/0004-6361/201015302). arXiv: [1011.0567](https://arxiv.org/abs/1011.0567) [[astro-ph.CO](#)].
- [327] W. Voges et al. “The ROSAT all-sky survey bright source catalogue”. In: *A&A* 349 (Sept. 1999), pp. 389–405. arXiv: [astro-ph/9909315](https://arxiv.org/abs/astro-ph/9909315) [[astro-ph](#)].
- [328] A. Palmese et al. “Evidence for Dynamically Driven Formation of the GW170817 Neutron Star Binary in NGC 4993”. In: *ApJ* 849.2, L34 (Nov. 2017), p. L34. DOI: [10.3847/2041-8213/aa9660](https://doi.org/10.3847/2041-8213/aa9660). arXiv: [1710.06748](https://arxiv.org/abs/1710.06748) [[astro-ph.HE](#)].
- [329] W. Fong et al. “The Electromagnetic Counterpart of the Binary Neutron Star Merger LIGO/Virgo GW170817. VIII. A Comparison to Cosmological Short-duration Gamma-Ray Bursts”. In: *ApJ* 848.2, L23 (Oct. 2017), p. L23. DOI: [10.3847/2041-8213/aa9018](https://doi.org/10.3847/2041-8213/aa9018). arXiv: [1710.05438](https://arxiv.org/abs/1710.05438) [[astro-ph.HE](#)].
- [330] M. Contini. “NGC 4993 and other short gamma-ray burst host galaxies. Modelling line and continuum spectra”. In: *A&A* 620, A37 (Nov. 2018), A37. DOI: [10.1051/0004-6361/201834040](https://doi.org/10.1051/0004-6361/201834040).
- [331] Q. Wu, J. Feng, and X. Fan. “The Possible Submillimeter Bump and Accretion-jet in the Central Supermassive Black Hole of NGC 4993”. In: *ApJ* 855.1, 46 (Mar. 2018), p. 46. DOI: [10.3847/1538-4357/aaac28](https://doi.org/10.3847/1538-4357/aaac28). arXiv: [1710.09590](https://arxiv.org/abs/1710.09590) [[astro-ph.HE](#)].
- [332] C. Xie et al. “On the Host Galaxy of GRB 150101B and the Associated Active Galactic Nucleus”. In: *ApJ* 824.2, L17 (June 2016), p. L17. DOI: [10.3847/2041-8205/824/2/L17](https://doi.org/10.3847/2041-8205/824/2/L17). arXiv: [1606.00140](https://arxiv.org/abs/1606.00140) [[astro-ph.GA](#)].
- [333] B. Argence and F. Lamareille. “Emission-lines calibrations of the star formation rate from the Sloan Digital Sky Survey”. In: *A&A* 495.3 (Mar. 2009), pp. 759–773. DOI: [10.1051/0004-6361:20066998](https://doi.org/10.1051/0004-6361:20066998). arXiv: [0811.2420](https://arxiv.org/abs/0811.2420) [[astro-ph](#)].
- [334] M. Mouhcine et al. “The [OII] λ 3727/H α ratio of emission-line galaxies in the 2dF Galaxy Redshift Survey”. In: *MNRAS* 362.4 (Oct. 2005), pp. 1143–1156. DOI: [10.1111/j.1365-2966.2005.09211.x](https://doi.org/10.1111/j.1365-2966.2005.09211.x). arXiv: [astro-ph/0511809](https://arxiv.org/abs/astro-ph/0511809) [[astro-ph](#)].

- [335] A. Tsvetkova et al. “The Konus-Wind Catalog of Gamma-Ray Bursts with Known Redshifts. I. Bursts Detected in the Triggered Mode”. In: *ApJ* 850.2, 161 (Dec. 2017), p. 161. DOI: [10.3847/1538-4357/aa96af](https://doi.org/10.3847/1538-4357/aa96af). arXiv: [1710.08746](https://arxiv.org/abs/1710.08746) [[astro-ph.HE](#)].
- [336] L. Nava et al. “A complete sample of bright Swift long gamma-ray bursts: testing the spectral-energy correlations”. In: *MNRAS* 421.2 (Apr. 2012), pp. 1256–1264. DOI: [10.1111/j.1365-2966.2011.20394.x](https://doi.org/10.1111/j.1365-2966.2011.20394.x). arXiv: [1112.4470](https://arxiv.org/abs/1112.4470) [[astro-ph.HE](#)].
- [337] T. Eftekhari et al. “Late-time Radio and Millimeter Observations of Superluminous Supernovae and Long Gamma-Ray Bursts: Implications for Central Engines, Fast Radio Bursts, and Obscured Star Formation”. In: *ApJ* 912.1, 21 (May 2021), p. 21. DOI: [10.3847/1538-4357/abe9b8](https://doi.org/10.3847/1538-4357/abe9b8). arXiv: [2010.06612](https://arxiv.org/abs/2010.06612) [[astro-ph.HE](#)].
- [338] S. D. Barthelmy et al. “GRB 200716C: Swift-BAT refined analysis”. In: *GRB Coordinates Network* 28136 (July 2020), p. 1.
- [339] P. Kumar and B. Zhang. “The physics of gamma-ray bursts & relativistic jets”. In: *Phys. Rep.* 561 (Feb. 2015), pp. 1–109. DOI: [10.1016/j.physrep.2014.09.008](https://doi.org/10.1016/j.physrep.2014.09.008). arXiv: [1410.0679](https://arxiv.org/abs/1410.0679) [[astro-ph.HE](#)].
- [340] A. Cucchiara et al. “A Photometric Redshift of $z \sim 9.4$ for GRB 090429B”. In: *ApJ* 736.1, 7 (July 2011), p. 7. DOI: [10.1088/0004-637X/736/1/7](https://doi.org/10.1088/0004-637X/736/1/7). arXiv: [1105.4915](https://arxiv.org/abs/1105.4915) [[astro-ph.CO](#)].
- [341] C. L. Fryer et al. “Properties of High-redshift Gamma-Ray Bursts”. In: *ApJ* 929.2, 111 (Apr. 2022), p. 111. DOI: [10.3847/1538-4357/ac5d5c](https://doi.org/10.3847/1538-4357/ac5d5c). arXiv: [2112.00643](https://arxiv.org/abs/2112.00643) [[astro-ph.HE](#)].
- [342] J. Paynter, R. Webster, and E. Thrane. “Evidence for an intermediate-mass black hole from a gravitationally lensed gamma-ray burst”. In: *Nature Astronomy* 5 (Jan. 2021), pp. 560–568. DOI: [10.1038/s41550-021-01307-1](https://doi.org/10.1038/s41550-021-01307-1). arXiv: [2103.15414](https://arxiv.org/abs/2103.15414) [[astro-ph.HE](#)].
- [343] A. B. Congdon and C. Keeton. *Principles of Gravitational Lensing: Light Deflection as a Probe of Astrophysics and Cosmology*. 2018.
- [344] P. Veres et al. “Fermi-GBM Observations of GRB 210812A: Signatures of a Million Solar Mass Gravitational Lens”. In: *ApJ* 921.2, L30 (Nov. 2021), p. L30. DOI: [10.3847/2041-8213/ac2ee6](https://doi.org/10.3847/2041-8213/ac2ee6). arXiv: [2110.06065](https://arxiv.org/abs/2110.06065) [[astro-ph.HE](#)].
- [345] S.-J. Lin et al. “A Search for Millilensing Gamma-Ray Bursts in the Observations of Fermi GBM”. In: *ApJ* 931.1, 4 (May 2022), p. 4. DOI: [10.3847/1538-4357/ac6505](https://doi.org/10.3847/1538-4357/ac6505). arXiv: [2112.07288](https://arxiv.org/abs/2112.07288) [[astro-ph.HE](#)].
- [346] Z. Paragi, M. A. Garrett, and A. D. Biggs. “Observing ULXs with VLBI: the quest for intermediate-mass black holes”. In: *VI Microquasar Workshop: Microquasars and Beyond*. Jan. 2006, 61.1, p. 61.1.
- [347] E. J. Weller et al. “Dynamics of intermediate-mass black holes wandering in the milky way galaxy using the illustris TNG50 simulation”. In: *MNRAS* 511.2 (Apr. 2022), pp. 2229–2238. DOI: [10.1093/mnras/stac179](https://doi.org/10.1093/mnras/stac179). arXiv: [2201.07234](https://arxiv.org/abs/2201.07234) [[astro-ph.GA](#)].
- [348] P. Kaaret et al. “Chandra High-Resolution Camera observations of the luminous X-ray source in the starburst galaxy M82”. In: *MNRAS* 321.2 (Feb. 2001), pp. L29–L32. DOI: [10.1046/j.1365-8711.2001.04064.x](https://doi.org/10.1046/j.1365-8711.2001.04064.x). arXiv: [astro-ph/0009211](https://arxiv.org/abs/astro-ph/0009211) [[astro-ph](#)].
- [349] J. M. Miller et al. “X-Ray Spectroscopic Evidence for Intermediate-Mass Black Holes: Cool Accretion Disks in Two Ultraluminous X-Ray Sources”. In: *ApJ* 585.1 (Mar. 2003), pp. L37–L40. DOI: [10.1086/368373](https://doi.org/10.1086/368373). arXiv: [astro-ph/0211178](https://arxiv.org/abs/astro-ph/0211178) [[astro-ph](#)].
- [350] J. -P. Lasota et al. “The Origin of Variability of the Intermediate-mass Black-hole ULX System HLX-1 in ESO 243-49”. In: *ApJ* 735.2, 89 (July 2011), p. 89. DOI: [10.1088/0004-637X/735/2/89](https://doi.org/10.1088/0004-637X/735/2/89). arXiv: [1102.4336](https://arxiv.org/abs/1102.4336) [[astro-ph.HE](#)].

- [351] H. M. Earnshaw et al. “A variable ULX and possible IMBH candidate in M51a”. In: *MNRAS* 456.4 (Mar. 2016), pp. 3840–3854. DOI: [10.1093/mnras/stv2945](https://doi.org/10.1093/mnras/stv2945). arXiv: [1512.04825](https://arxiv.org/abs/1512.04825) [[astro-ph.HE](#)].
- [352] K. Atapin, S. Fabrika, and M. D. Caballero-García. “Ultraluminous X-ray sources with flat-topped noise and QPO”. In: *MNRAS* 486.2 (June 2019), pp. 2766–2779. DOI: [10.1093/mnras/stz1027](https://doi.org/10.1093/mnras/stz1027). arXiv: [1904.04905](https://arxiv.org/abs/1904.04905) [[astro-ph.HE](#)].
- [353] D. Cseh et al. “On the radio properties of the intermediate-mass black hole candidate ESO 243-49 HLX-1”. In: *MNRAS* 446.4 (Feb. 2015), pp. 3268–3276. DOI: [10.1093/mnras/stu2363](https://doi.org/10.1093/mnras/stu2363). arXiv: [1411.1306](https://arxiv.org/abs/1411.1306) [[astro-ph.HE](#)].
- [354] M. Mezcuca et al. “The extended radio jet of an off-nuclear low-mass AGN in NGC 5252”. In: *MNRAS* 480.1 (Oct. 2018), pp. L74–L78. DOI: [10.1093/mnrasl/sly130](https://doi.org/10.1093/mnrasl/sly130). arXiv: [1807.03792](https://arxiv.org/abs/1807.03792) [[astro-ph.GA](#)].
- [355] J. P. McKean et al. “High-resolution imaging of the anomalous flux ratio gravitational lens system CLASS B2045+265: dark or luminous satellites?” In: *MNRAS* 378.1 (June 2007), pp. 109–118. DOI: [10.1111/j.1365-2966.2007.11744.x](https://doi.org/10.1111/j.1365-2966.2007.11744.x). arXiv: [astro-ph/0611215](https://arxiv.org/abs/astro-ph/0611215) [[astro-ph](#)].
- [356] M. Haas et al. “3C 220.3: A Radio Galaxy Lensing a Submillimeter Galaxy”. In: *ApJ* 790.1, 46 (July 2014), p. 46. DOI: [10.1088/0004-637X/790/1/46](https://doi.org/10.1088/0004-637X/790/1/46). arXiv: [1406.2872](https://arxiv.org/abs/1406.2872) [[astro-ph.GA](#)].
- [357] D. Paraficz et al. “ALMA view of RX J1131-1231: Sub-kpc CO (2-1) mapping of a molecular disk in a lensed star-forming quasar host galaxy”. In: *A&A* 613, A34 (May 2018), A34. DOI: [10.1051/0004-6361/201731250](https://doi.org/10.1051/0004-6361/201731250). arXiv: [1705.09931](https://arxiv.org/abs/1705.09931) [[astro-ph.GA](#)].
- [358] C. Spingola et al. “A novel search for gravitationally lensed radio sources in wide-field VLBI imaging from the mJIVE-20 survey”. In: *MNRAS* 483.2 (Feb. 2019), pp. 2125–2153. DOI: [10.1093/mnras/sty3189](https://doi.org/10.1093/mnras/sty3189). arXiv: [1811.09152](https://arxiv.org/abs/1811.09152) [[astro-ph.GA](#)].
- [359] C. Casadio et al. “SMILE: Search for Milli-LEnses”. In: *MNRAS* 507.1 (Oct. 2021), pp. L6–L10. DOI: [10.1093/mnrasl/slab082](https://doi.org/10.1093/mnrasl/slab082). arXiv: [2107.06896](https://arxiv.org/abs/2107.06896) [[astro-ph.CO](#)].
- [360] R. Ahumada et al. “The 16th Data Release of the Sloan Digital Sky Surveys: First Release from the APOGEE-2 Southern Survey and Full Release of eBOSS Spectra”. In: *ApJS* 249.1, 3 (July 2020), p. 3. DOI: [10.3847/1538-4365/ab929e](https://doi.org/10.3847/1538-4365/ab929e). arXiv: [1912.02905](https://arxiv.org/abs/1912.02905) [[astro-ph.GA](#)].
- [361] R. Salvaterra et al. “A Complete Sample of Bright Swift Long Gamma-Ray Bursts. I. Sample Presentation, Luminosity Function and Evolution”. In: *ApJ* 749.1, 68 (Apr. 2012), p. 68. DOI: [10.1088/0004-637X/749/1/68](https://doi.org/10.1088/0004-637X/749/1/68). arXiv: [1112.1700](https://arxiv.org/abs/1112.1700) [[astro-ph.CO](#)].
- [362] G. Ghirlanda et al. “Radio afterglows of a complete sample of bright Swift GRBs: predictions from present days to the SKA era”. In: *MNRAS* 435.3 (Nov. 2013), pp. 2543–2551. DOI: [10.1093/mnras/stt1466](https://doi.org/10.1093/mnras/stt1466). arXiv: [1307.7704](https://arxiv.org/abs/1307.7704) [[astro-ph.HE](#)].
- [363] G. Ghirlanda et al. “The faster the narrower: characteristic bulk velocities and jet opening angles of gamma-ray bursts”. In: *MNRAS* 428.2 (Jan. 2013), pp. 1410–1423. DOI: [10.1093/mnras/sts128](https://doi.org/10.1093/mnras/sts128). arXiv: [1210.1215](https://arxiv.org/abs/1210.1215) [[astro-ph.HE](#)].
- [364] H. van Eerten, A. van der Horst, and A. MacFadyen. “Gamma-Ray Burst Afterglow Broadband Fitting Based Directly on Hydrodynamics Simulations”. In: *ApJ* 749.1, 44 (Apr. 2012), p. 44. DOI: [10.1088/0004-637X/749/1/44](https://doi.org/10.1088/0004-637X/749/1/44). arXiv: [1110.5089](https://arxiv.org/abs/1110.5089) [[astro-ph.HE](#)].
- [365] G. E. Anderson et al. “The Arcminute Microkelvin Imager catalogue of gamma-ray burst afterglows at 15.7 GHz”. In: *MNRAS* 473.2 (Jan. 2018), pp. 1512–1536. DOI: [10.1093/mnras/stx2407](https://doi.org/10.1093/mnras/stx2407). arXiv: [1709.06232](https://arxiv.org/abs/1709.06232) [[astro-ph.HE](#)].

- [366] N. M. Lloyd-Ronning and C. L. Fryer. “On the lack of a radio afterglow from some gamma-ray bursts - insight into their progenitors?” In: *MNRAS* 467.3 (May 2017), pp. 3413–3423. DOI: [10.1093/mnras/stx313](https://doi.org/10.1093/mnras/stx313). arXiv: [1609.04686](https://arxiv.org/abs/1609.04686) [[astro-ph.HE](#)].
- [367] N. M. Lloyd-Ronning et al. “A Comparison between Radio Loud and Quiet Gamma-Ray Bursts, and Evidence for a Potential Correlation between Intrinsic Duration and Redshift in the Radio Loud Population”. In: *ApJ* 871.1, 118 (Jan. 2019), p. 118. DOI: [10.3847/1538-4357/aaf6ac](https://doi.org/10.3847/1538-4357/aaf6ac).
- [368] A. Chakraborty et al. “Radio-bright versus radio-dark gamma-ray bursts - more evidence for distinct progenitors”. In: *MNRAS* 520.4 (Apr. 2023), pp. 5764–5782. DOI: [10.1093/mnras/stad438](https://doi.org/10.1093/mnras/stad438). arXiv: [2210.12972](https://arxiv.org/abs/2210.12972) [[astro-ph.HE](#)].
- [369] K. Zhang et al. “How are gamma-ray burst radio afterglows populated?” In: *MNRAS* 503.3 (May 2021), pp. 3262–3278. DOI: [10.1093/mnras/stab465](https://doi.org/10.1093/mnras/stab465). arXiv: [2010.12749](https://arxiv.org/abs/2010.12749) [[astro-ph.HE](#)].
- [370] A. Shahmoradi. “A Multivariate Fit Luminosity Function and World Model for Long Gamma-Ray Bursts”. In: *ApJ* 766.2, 111 (Apr. 2013), p. 111. DOI: [10.1088/0004-637X/766/2/111](https://doi.org/10.1088/0004-637X/766/2/111). arXiv: [1209.4647](https://arxiv.org/abs/1209.4647) [[astro-ph.HE](#)].
- [371] A. Shahmoradi and R. J. Nemiroff. “Short versus long gamma-ray bursts: a comprehensive study of energetics and prompt gamma-ray correlations”. In: *MNRAS* 451.1 (July 2015), pp. 126–143. DOI: [10.1093/mnras/stv714](https://doi.org/10.1093/mnras/stv714). arXiv: [1412.5630](https://arxiv.org/abs/1412.5630) [[astro-ph.HE](#)].
- [372] J. A. Osborne, F. Bagheri, and A. Shahmoradi. “Are there radio-loud and radio-quiet gamma-ray bursts?” In: *MNRAS* 502.4 (Apr. 2021), pp. 5622–5630. DOI: [10.1093/mnras/stab425](https://doi.org/10.1093/mnras/stab425). arXiv: [2010.08877](https://arxiv.org/abs/2010.08877) [[astro-ph.HE](#)].
- [373] L. Amati et al. “The THESEUS space mission concept: science case, design and expected performances”. In: *Advances in Space Research* 62.1 (July 2018), pp. 191–244. DOI: [10.1016/j.asr.2018.03.010](https://doi.org/10.1016/j.asr.2018.03.010). arXiv: [1710.04638](https://arxiv.org/abs/1710.04638) [[astro-ph.IM](#)].
- [374] P. Mészáros and M. J. Rees. “Population III Gamma-ray Bursts”. In: *ApJ* 715.2 (June 2010), pp. 967–971. DOI: [10.1088/0004-637X/715/2/967](https://doi.org/10.1088/0004-637X/715/2/967). arXiv: [1004.2056](https://arxiv.org/abs/1004.2056) [[astro-ph.HE](#)].
- [375] D. Burlon et al. “Gamma-ray bursts from massive Population-III stars: clues from the radio band”. In: *MNRAS* 459.3 (July 2016), pp. 3356–3362. DOI: [10.1093/mnras/stw905](https://doi.org/10.1093/mnras/stw905). arXiv: [1604.03946](https://arxiv.org/abs/1604.03946) [[astro-ph.HE](#)].